

Dissertation zur Erlangung des Doktorgrades
der Fakultät für Chemie und Pharmazie
der Ludwig-Maximilians-Universität München

Nanoporous Metal Oxides Templated by Nanocrystalline Cellulose

–

Synthesis and Applications in
Photovoltaics and Photocatalysis

Alesja Ivanova

aus

Riga, Lettland

2015

Erklärung

Diese Dissertation wurde im Sinne von § 7 der Promotionsordnung vom 28. November 2011 von Herrn Prof. Dr. Thomas Bein betreut.

Eidesstattliche Versicherung

Diese Dissertation wurde eigenständig und ohne unerlaubte Hilfe bearbeitet.

München, den 14. Juli 2015

.....
Alesja Ivanova

Dissertation eingereicht am: 14.07.2015

1. Gutachter: Prof. Dr. Thomas Bein

2. Gutachter: Prof. Dr. Dina Fattakhova-Rohlfing

Mündliche Prüfung am: 14.08.2015

ACKNOWLEDGEMENT

Foremost I would like to thank Prof. Thomas Bein for his advice and guidance throughout all the stages of my PhD studies. I wish to thank him for inspiring me to explore the challenging yet exciting topic that has fully fulfilled my expectations regarding my self-realization and the spectrum of expertise I have mastered. I very much appreciate the large degree of independence and freedom given to me to design experiments, to choose the collaborators and to attend scientific events. Additionally, I wish to thank Thomas for providing me with all the facilities required for the successful completion of my doctoral thesis, as well as for his help and promotion while applying for the external funding.

I greatly acknowledge the German Academic Exchange Service (DAAD) for awarding me a three-year scholarship to conduct doctoral research in Germany. Furthermore, I thank Nanosystems Initiative Munich (NIM), Center for NanoScience (CeNS) and Gesellschaft Deutscher Chemiker (GDCh) for their grants covering the costs of books, language courses and conference travel expenses.

I am very grateful to Prof. Dina Fattakhova-Rohlfing, who supported me throughout all my doctoral research. I greatly appreciate her openness to discussions, the creative ideas and an exceptional devotion to work. I am particularly thankful for Dina's contribution in manuscript preparation and her guidance in the paper submission process.

I would also like to acknowledge our collaborators, namely Jiri Rathouský for his excellent expertise in photocatalysis and krypton sorption analysis; Tom Savenije and Maria Fravventura for the outstanding knowledge and experience in the field of microwave conductivity measurements, as well as Patrick Zeller for his proficiency in surface spectroscopy. Thank you for your interest in the projects, your enthusiastic work and invaluable contributions!

I wish to thank students working on the projects related to my doctoral research. Bugra Eymen Kayaalp, Pirmin Ganter, Liana Movsesyan, Anna Sanina, Yury Vilks, Adrien Sthoer and Feng An, thank you for your excellent help and for the experience I got while mentoring you!

I am very much grateful to Steffen Schmidt, Markus Döblinger, Florian Auras and Benjamin Mandlmeier who performed electron microscopy analysis and introduced me to scanning electron microscopy. I wish to thank Christian Minke for the nuclear magnetic resonance measurements. I thank the group of Prof. Peter Klüfers for providing cotton linters. I am grateful to Tina Reuther for performing some of the analytics on my samples and for the assistance in obtaining chemicals and laboratory utilities. I very much appreciate Regina Huber's help in many organizational and administrative issues I encountered while working at LMU.

I wish to thank all my colleagues I have met during these years. It was a lot of fun to celebrate Christmas with you, to go to conferences and to participate in numerous get-together events (Stammtische)! My sincere thanks to my office mates: Florian, Basti, Stefan, Andi, Noggi, Tina, Askhat, Meltem, Hongi, Nadja for their pleasant company, support and help. Furthermore, I greatly appreciate the discussions we had during the water splitting and photovoltaic subgroup meetings with Halina, Dina, Markus, Ksenia, Ilina, Alex, Peter, Krissi, Fabi, Johann, Hans, Norma, Enrico, Askhat, Flo and Benni. Additionally, I would like to thank the perovskite subgroup: Pablo, Mihi, Meltem, Hongi, Nadja, and Charles for their international spirit and for all the nice events we organized together.

I especially thank Dana for our morning chats and for her hilarious Jewish jokes. Many thanks to Ksenia and Askhat for being very reliable colleagues and friends, as well as for training me to cook Russian food. I am grateful to all the nice people I met in Munich, for their friendship and support during my stay in Germany.

Moreover, I wish to express my gratitude to my teachers at Riga 37 Secondary School and at St. Petersburg State Institute of Technology, as well as to the lecturers of Advanced Materials Science master program, who have made a great impact on my personality and stimulated my interest to science. Without their enthusiasm and the knowledge I gained during my undergraduate and graduate studies it would not have been possible for me to pursue the PhD.

Most importantly I wish to thank my family for believing in me, encouraging me and supporting me throughout my education and the rest of my life.

ABSTRACT

Porous materials play an important role in numerous environmental applications including energy storage, energy conversion and environmental remediation systems. Reducing structural features down to the nanoscale drastically alters materials properties and leads to the enhancement of materials performance. The successful fabrication of efficient functional materials requires a high degree of control over their morphology addressing the needs of target applications.

The goal of this work was to develop a versatile general approach towards the synthesis of nanoporous metal oxides by using biogenic cellulose nanocrystals. Nanocrystalline cellulose (NCC) is an abundant biological nanomaterial that can be extracted from natural bulk celluloses. The present thesis demonstrates that the unique properties of NCC enable the efficient synthesis of porous titania and $\alpha\text{-Fe}_2\text{O}_3$ (hematite) thin films by using sacrificial templating with cellulose nanocrystals. In particular, this study reveals the mechanism of metal oxide formation in the presence of cellulose, as well as the effect of NCC-templated porous scaffolds on titania performance in photocatalysis and dye sensitized solar cells.

Chapter 1 provides general information about properties, application areas and common synthesis methods of nanoporous metal oxides, with an emphasis put on titanium oxide materials and biotemplating approaches. Chapter 2 discusses the basic principles of analytical methods employed to characterize porous nanomaterials. Chapters 3–6 reveal the experimental procedures towards NCC-templated porous titania and hematite thin films, their characterization and their applications.

First, the extraction of cellulose crystals from bulk celluloses is discussed. Different cellulose sources, as well as variable hydrolysis parameters have been employed to define the optimal procedure for the NCC preparation. Cotton fibers have provided the best results regarding the crystallinity, purity and shape of extracted cellulose crystals. Furthermore, repeated washings have been shown to narrow down the size distribution and to improve the crystallinity of cotton NCC.

Chapter 4 focuses on the synthesis of porous titania thin films assisted by nanocrystalline cellulose. The tunable porosity of titania thin films is a key factor for successful applications in photovoltaics, sensing and photocatalysis. To synthesize NCC-templated titania, the cellulose nanocrystals are introduced to a titania precursor solution. The colloidal mixtures can be directly spin- or dip- coated on glass, silicon and transparent conducting oxide (TCO) substrates and then calcined to remove the template and to crystallize the titania porous network. The obtained structures are highly porous anatase morphologies having well-defined, narrow pore size distribution.

We show that by varying the titania-to-template ratio it is possible to tune the surface area, pore size, pore anisotropy and dimensions of titania crystallites in the films. Post-treatment at high humidity and subsequent slow template removal promote pore widening; this treatment is also beneficial for the multilayer deposition of thick films. The NCC-templated mesoporous titania films show very high activity in the photocatalytic NO (nitrogen(II) oxide) conversion and in the degradation of 4-chlorophenol. Furthermore, the films are successfully applied as anodes in dye-sensitized solar cells.

Chapter 5 presents a strategy toward enhancement of the photocatalytic activity of NCC-templated titania thin films by introducing solvothermally synthesized preformed anatase nanoparticles into a sol-gel based biotemplated titania scaffold. The synthesis is based on the self-assembly of two types of precursors, namely crystalline and sol-gel titania, directed by the biogenic NCC template. Due to the shape persistence of the template, the NCC-templated titania scaffolds can accommodate large amounts of preformed titania without a significant reduction of the film porosity.

The resulting dual source titania thin films containing different amounts of preformed crystalline species were investigated with time resolved microwave conductivity (TRMC) measurements and tested in the photocatalytic conversion of 4-chlorophenol. The gradual addition of preformed nanoparticles leads to a consistent increase of the mean size of titania crystalline domains, whereas the porosity of the composite is well-preserved due to the rigid nature of the NCC template. The microwave conductivity studies establish increased photoconductivity of the films containing preformed anatase nanoparticles, in comparison to that of films made without the nanoparticles.

The synergistic features of the dual source titania, namely the improved crystalline properties brought by the preformed nanocrystals in combination with the high surface area provided by the NCC-templated sol-gel titania, result in a very high photocatalytic activity of the films in the photocatalytic decomposition of 4-chlorophenol. In quantitative terms, the dual source titania films prepared with 75% nanoparticles exhibit a first order degradation rate constant of 0.53 h^{-1} , strongly outperforming the activity of commercial P90 nanopowder showing a rate constant of 0.17 h^{-1} under the same conditions.

We have also adapted the NCC templating protocol for the fabrication of porous $\alpha\text{-Fe}_2\text{O}_3$ (hematite) thin films. Chapter 6 discusses the formation of porous iron oxide nanostructures via sol-gel transformations of molecular precursors in the confined space of self-organized cellulose nanocrystals used as a shape-persistent template. The obtained structures are highly porous hematite morphologies featuring pronounced anisotropic porosity. The character of the porous nanostructure depends on the iron salt used as precursor and on the heat treatment, respectively. Moreover, a post-synthetic hydrothermal treatment of the NCC/iron salt composites strongly affects the crystal growth, as well as the porous nanomorphology of the obtained hematite scaffolds. We demonstrate that the hydrothermal treatment alters the crystallization mechanism of the molecular iron precursors, which proceeds via the formation of anisotropic iron oxyhydroxide species.

The present study reveals that the nanocellulose templating technique enables a straightforward fabrication of a variety of porous crystalline scaffolds with well-defined mesoporous structure. For the first time the NCC has been used for the fabrication of homogeneous porous metal oxide films on different substrates, in contrast to the previously reported powders or free-standing membranes. The versatility and flexibility of the NCC templating approach offers broad perspectives towards the generalization of this method for the fabrication of different types of nanoporous metal oxides.

TABLE OF CONTENTS

1	Introduction.....	1
1.1	Porous Metal Oxides for Environmental Applications	1
1.1.1	Photocatalysis.....	2
1.1.2	Dye Sensitized Solar Cells.....	5
1.1.3	Synthesis Strategies towards Porous Metal Oxides	6
1.2	Nanostructuring with Biogenic Materials.....	11
1.2.1	Biotemplates.....	13
1.2.2	Nanocrystalline Cellulose	17
1.2.3	Metal Oxides Templated with Nanocrystalline Cellulose	22
1.3	References.....	25
2	Characterization.....	33
2.1	Sorption.....	33
2.2	X-Ray Diffraction.....	37
2.3	Electron Microscopy.....	40
2.3.1	Transmission Electron Microscopy.....	41
2.3.2	Scanning Electron Microscopy	43
2.4	X-ray Photoelectron Spectroscopy.....	46
2.5	Ultraviolet-Visible Spectroscopy.....	47
2.6	Nuclear Magnetic Resonance.....	49
2.7	Thermogravimetric Analysis	50
2.8	Dynamic Light Scattering	51
2.9	Photocatalytic Activity.....	52
2.10	Photovoltaic Characterization.....	53
2.10.1	DSC Assembly	53
2.10.2	<i>I-V</i> Characteristics.....	55
2.11	References.....	57
3	Extraction of Cellulose Nanocrystals	59
3.1	Introduction	59
3.2	Results and Discussion	62
3.2.1	Cellulose Sources.....	62

3.2.2	Acid Hydrolysis	64
3.2.3	Reaction Yield and Crystallinity.....	67
3.2.4	Fractionation.....	70
3.2.5	Nanocrystals Isolated from Cotton.....	75
3.3	Conclusions.....	77
3.4	Experimental.....	78
3.4.1	Synthesis	78
3.4.2	Characterization	79
3.5	References.....	81
3.6	Appendix.....	83
4	Tailoring the Morphology of Mesoporous Titania Thin Films through Bioteemplating with Nanocrystalline Cellulose	85
4.1	Introduction	85
4.2	Results and Discussion	87
4.2.1	Morphology Tuning.....	87
4.2.2	Film Performance in Photocatalysis	94
4.2.3	Film Performance in Dye Sensitized Solar Cells	96
4.3	Conclusions.....	97
4.4	Experimental.....	98
4.4.1	Synthesis	98
4.4.2	Characterization	100
4.5	References.....	103
4.6	Appendix.....	106
5	Nanocellulose-Templated Porous Titania Scaffolds Incorporating Presynthesized Titania Nanocrystals	113
5.1	Introduction	113
5.2	Experimental.....	115
5.2.1	Synthesis	115
5.2.2	Characterization	117
5.3	Results and Discussion	119
5.3.1	Effect of Preformed Anatase on Morphology.....	119
5.3.2	Microwave Conductivity	123

5.3.3	Photocatalytic Performance	125
5.4	Conclusions.....	129
5.5	References.....	130
5.6	Appendix.....	132
6	Nanocellulose-Assisted Formation of Porous Hematite Morphologies.....	137
6.1	Introduction	137
6.2	Results and Discussion	139
6.2.1	Effect of Precursor Salt and Calcination Procedure	139
6.2.2	Effect of Post-Synthetic Delayed Humidity Treatment.....	143
6.3	Conclusions.....	148
6.4	Experimental.....	149
6.4.1	Synthesis	149
6.4.2	Characterization	150
6.5	References.....	152
6.6	Appendix.....	154
7	Conclusion and Outlook.....	159
8	Appendix.....	163
8.1	List of Abbreviations	163
8.2	List of Symbols	165
9	Curriculum Vitae.....	167
10	Publications and Presentations.....	169
10.1	Publications.....	169
10.2	Oral Presentations.....	170
10.3	Poster Presentations	170

1 Introduction

1.1 Porous Metal Oxides for Environmental Applications

*A hole is nothing at all,
but you can break your neck in it.*

Austin O'Malley

Dramatically increasing worldwide demand for energy and the negative impact of human-caused environmental pollution on Earth's climate are some of the greatest challenges humankind has to address in the near future. The way towards a sustainable future requires the development of inexpensive alternative energy sources based on environmentally-friendly materials and methods.¹

Metal oxides, and particularly transition metal oxides such as titania and iron oxide play an important role in the development of novel sustainable technologies. Suitable semiconducting properties, abundance and chemical stability make them key components in numerous applications such as photocatalysis, photovoltaics, electrochemical energy storage and photoelectrochemistry. The efficiency of those applications critically depends on the charge transfer and charge transport processes at the interface and in the bulk of the active materials. Therefore, optimization of nanomorphology^{2,3} can greatly enhance the materials performance via the effects brought about by the increasing surface area and the diminishing bulk size.

One of the most straightforward ways to enlarge the specific surface area of a metal oxide is to introduce empty voids, i.e. pores, into the bulk. Porous morphologies feature high accessible surface areas in combination with an interconnected network of the metal oxide phase. The porous materials are classified according to the International Union of Pure and Applied Chemistry (IUPAC) into micro-, meso- and macroporous, with corresponding pore sizes of <2 nm, 2–50 nm and >50 nm, respectively.

Mesoporous metal oxide films are used in numerous applications such as dye-sensitized solar cells, electrochromic devices, antifogging, antibacterial, self-cleaning coatings, water splitting systems and many others. The fabrication of efficient porous films requires thorough control over their morphology, as well as additional adjustment of the specific film parameters, such as film thickness, homogeneity, mechanical stability and adhesion to the substrate.

Furthermore, control over the charge transport properties in the films is extremely important for the fabrication of semiconducting devices. Their efficiency depends on the crystallinity of the metal oxide porous framework and the connectivity between the crystalline domains. Thus, the synthesis strategy and the film processability are critical factors affecting the properties of functional thin films of porous metal oxides.

The next chapters give a brief introduction into the operation principles of important environmental applications based on mesoporous semiconducting metal oxides, followed by an overview of common strategies for the synthesis of inorganic oxides with defined porosity. Finally, the biotemplating approaches to nanostructured porous materials are introduced. A particular emphasis is put on the nanocrystalline cellulose (NCC) acting as a natural sacrificial template. The following chapters discuss in detail the NCC assisted synthetic routes towards porous titania and hematite scaffolds, as well as their performance in devices designed for environmental purposes.

1.1.1 Photocatalysis

Titanium dioxide is an n-type wide band gap semiconductor⁴ with a band gap of about 3.2 eV.^{5,6} There are three main allotropic forms of titania, namely a thermodynamically stable rutile phase (tetragonal) and metastable phases of anatase (tetragonal) and brookite (orthorhombic). Anatase is the most common phase of nanosized titania obtained by different nanofabrication methods.

Due to its large band gap, titania absorbs in the ultra-violet (UV) range of the electromagnetic spectrum. Under UV-light illumination titania can act as a photocatalysts, which finds practical applications in the field of water and air purification, disinfection, as well as in the fabrication of self-cleaning surfaces.

The photocatalytic decomposition of a pollutant proceeds via surface reactions at the interphase between titanium dioxide and the medium to be purified.^{7,8,9} Absorption of UV-light causes an electron transfer from the valence band (VB) to the conduction band (CB) creating a hole in the VB of the bulk oxide (Figure 1.1). The photogenerated electrons migrate to the surface and react there with molecular oxygen to produce superoxide anions O_2^- and radicals $\cdot O_2^-$, whereas the photogenerated holes react with water to produce hydroxyl radicals, $\cdot OH$. The species formed during redox reactions at the surface of the photocatalyst are highly reactive and can be used to decompose undesired organic compounds, e.g., pollutants, or bacteria.

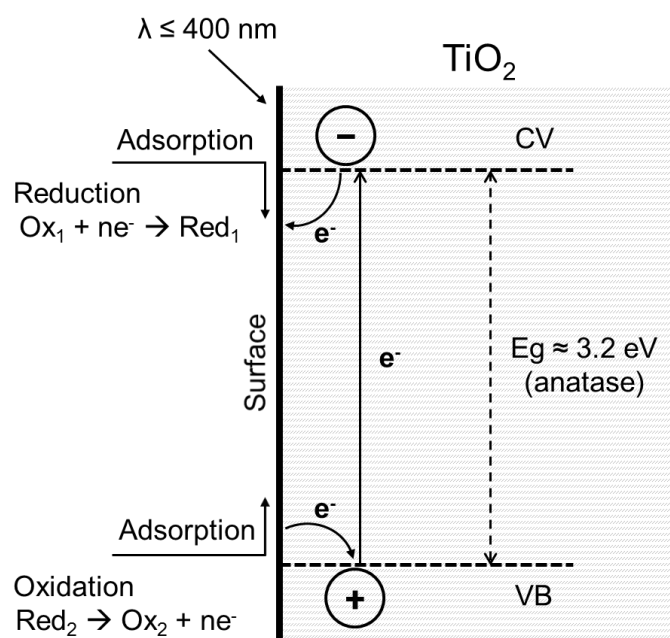


Figure 1.1. Schematic illustration of possible electron-transfer processes in and on titanium dioxide under UV light illumination. Adapted from Ref.⁸

Pelizzetti et al.⁹ suggested that the mechanism of photocatalytic reactions on titania surface involves the following reaction steps: charge generation (1.1), electron-hole recombination (1.2), electron transfer by adsorbed acceptors (1.3, 1.4) and electron transfer by donors (1.5, 1.6):





Ideally, an environmental photocatalyst (i) demonstrates high photoactivity, (ii) absorbs in the ultraviolet or visible range; is (iii) chemically inert, (iv) is stable to photocorrosion, and is (v) cheap and (vi) non-toxic.¹⁰ Titania fulfills all these requirements. Furthermore, its photocatalytic activity can be adjusted by tailoring its morphology. Nanostructured porous titania shows improved performance compared to flat bulk materials. First, the porosity increases the surface able to accommodate large amounts of pollutant molecules. Second, the diffusion distances of charge-carriers in nano-sized particles are much shorter than in the corresponding macroscopic materials. Therefore, the charge carriers photogenerated in nanostructured semiconductors can be scavenged without significant recombination losses.¹¹

Hydrogen production from water is another promising concept supporting clean energy systems.¹²⁻¹⁴ The mechanisms of water splitting to hydrogen and oxygen using semiconducting oxides acting as photocatalysts is similar to that demonstrated in Figure 1.1. Photogenerated electrons and holes reduce water to form H₂ and oxidize it to form O₂. The width of the band gap and the relative positions of the conduction and valence bands compared to the relevant redox levels of water are important criteria for the suitability of a semiconductor for the water splitting reaction. Iron oxide has a suitable band position for the oxygen evolution reaction. Its stable modification, hematite, has a narrow band gap of 2.1 eV that permits the absorption of visible light.¹⁰ Therefore, hematite has been intensively investigated as a visible light photocatalyst for the photocatalytic water splitting. Hematite nanoarchitectures were shown to play an important role in enhancing its photocatalytic performance.¹⁵

1.1.2 Dye Sensitized Solar Cells

Sun provides Earth with as much energy every hour as human civilization uses every year. Therefore even a small amount of sun light captured and converted to electricity would be already sufficient to stop emissions of greenhouse gases from conventional power plants.¹⁶

Solar cells are photovoltaic (PV) devices designed to convert energy of the sun to electrical energy. The commercial solar cell market is dominated by silicon solar cells that deliver relatively high conversion efficiencies of up to about 27%,¹ however their drawbacks are high fabrication costs and non-compatibility with flexible substrates. Alternative solar cell systems, for example dye-sensitized solar cells (DSC)^{11,17-19} or perovskite solar cells²⁰ are capable to lower the production costs and to overcome some other limitations of crystalline silicon photovoltaics.

Figure 1.2 demonstrates the working principle of a DSC.¹¹

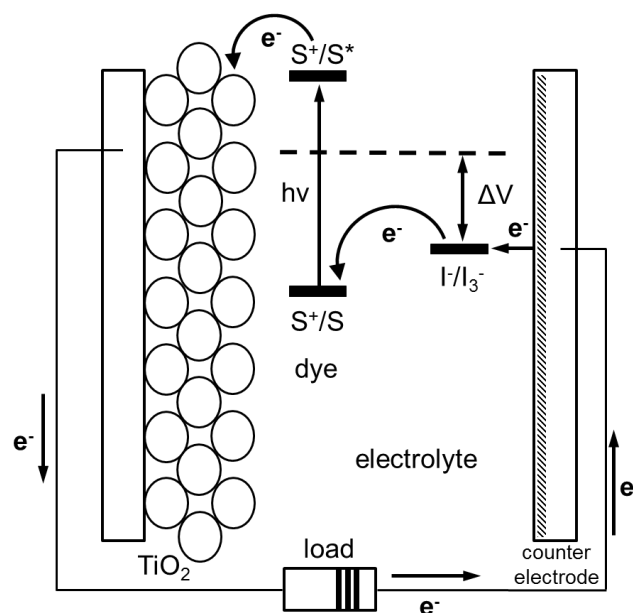


Figure 1.2. Schematic layout of a dye-sensitized solar cell showing its principle of operation. Adapted from Ref.¹¹

The key component of the cell is a mesoscopic film of titanium oxide in contact with a redox electrolyte or an organic hole conductor. The TiO₂ surface is covered by a

monolayer of dye acting as a photosensitizer. Upon photoexcitation the dye injects electrons into the conduction band of the titanium dioxide. Then the dye molecules are regenerated by electron donation from the electrolyte iodide/triiodide redox couple, which itself is regenerated at the counter electrode.

The operation principle of the DSC suggests that the maximization of the titania electrode surface is desirable, since the amount of injected electrons directly depends on the amount of dye/TiO₂ interactions. Mesoporous titania films are able to accumulate large amounts of dye molecules, so that the film thickness can be minimized to prevent long diffusion paths of the electrons to a current collector. Therefore, the porous morphology of the titania film is a key requirement for the successful operation of the DSC system.

The next chapter covers the common synthetic methods for the fabrication of nanostructured mesoporous thin films that can be employed in photocatalysis and as anodes for the fabrication of DSCs.

1.1.3 Synthesis Strategies towards Porous Metal Oxides

Porous materials can be obtained by a broad range of chemical and physical methods, which can be broadly divided into template-free and templated approaches.²¹

Sintering of nanoparticles is a common way to obtain porous metal oxide in a template-free approach. For instance, titania nanoparticles can be synthesized in a separate reaction and then deposited as a film on a substrate. Sintering of such film provides connectivity between titania nanoparticles and generates porosity arising from the interstitial voids. The disadvantage of this method is a poor control over porous morphology, as the porosity is defined solely by the initial shape and packing of the preformed nanoparticles.

Nanostructuring by using sacrificial templates offers a much greater control over the obtained porous structure. This method is based on the formation of metal oxides via wet chemistry, i.e. sol-gel routes, in the presence of structure directing additives.

In a sol-gel process²²⁻²⁸ a molecular metal oxide precursor is converted to a metal oxide via hydrolysis and polycondensation reactions followed by calcination. Metal salts, such

as chlorides, sulfates, etc., as well as metal alkoxides ($M(OR)_4$, where $M = Ti$ and $R = C_2H_5$ in the case of titanium(IV) ethoxide (TEOT)) are common metal precursors employed in wet synthesis.

The chemistry involved in the sol-gel process is often based on inorganic polymerization reactions occurring in aqueous systems. For example, addition of water to titanium alkoxide causes hydrolysis and the replacement of alkyl groups (R) by hydroxyl groups (OH) (1.7):²⁹



After the hydrolysis the condensation occurs, leading to the formation of titanium oxopolymers (1.8 and 1.9):



where $n \leq 4$ and R is an ethyl group, in the case of TEOT.

Complete polymerization of metal oxide precursor and solvent evaporation leads to the transition from the liquid sol into a gel phase. In the final step, the wet gels are dried by evaporation, providing so-called xerogels, or by using other techniques (e.g. supercritical or freeze drying) that provide aerogels. Subsequent heat treatment consolidates the gel and ultimately can convert it into a dense metal oxide.²¹

The exact mechanism of sol-gel reactions depends on many parameters, such as the nature of metal oxide precursor, type of the solvent, pH and the solution temperature. A careful control of all these parameters enables fine-tuning the structure and the size of the resulting sols and, subsequently, the morphology of the final metal oxides.

For the fabrication of porous thin films by templating, the metal oxide precursor sols are combined with structure directing molecules or other templates. Then the colloidal mixture is deposited on substrates using suitable coating techniques such as spin-coating, dip-coating or drop-casting. Finally, the film is calcined to remove the template and to crystallize the metal oxide.

First successful attempts of the templated fabrication of periodic porous metal oxides

have been demonstrated for silica by using surfactants as templates.^{30,31} Surfactants are amphiphilic molecules containing hydrophobic and hydrophilic parts. At a certain critical concentration they self-organize into micelles owing to electrostatic, van der Waals and hydrogen bonding interactions. Metal oxide precursors dissolved in such suspension can take part in co-assembly and organize around the micelles. Later the organic part of the hybrid system can be removed by heat treatment or by CO₂ extraction, such that pores are formed in place of the micelles (Figure 1.3).^{32,33}

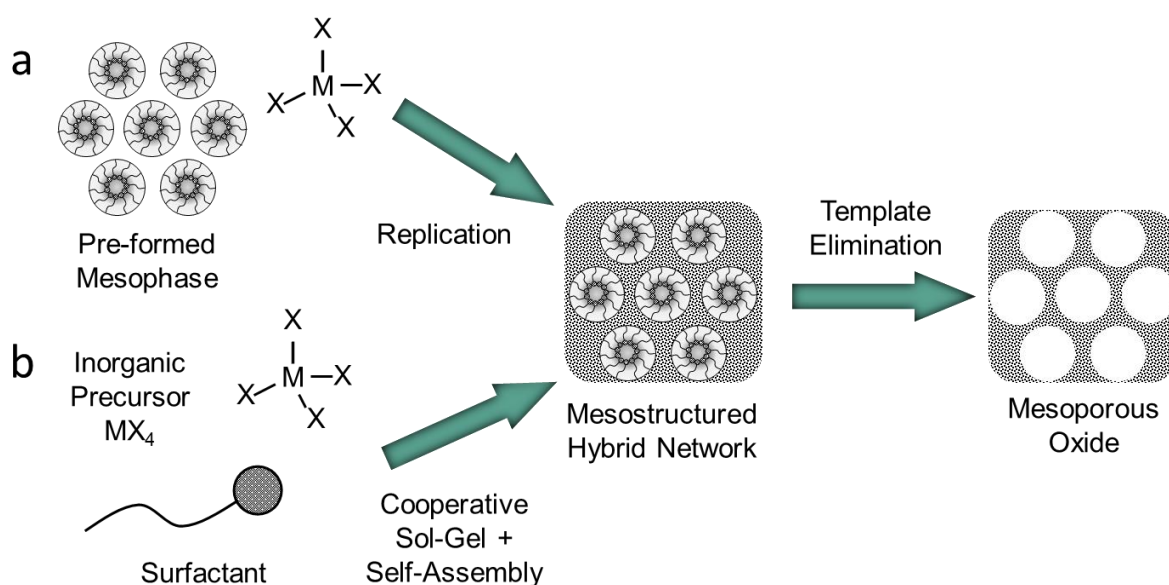


Figure 1.3. Synthetic approaches to mesostructured materials templated by surfactants. The mesostructure can be previously formed (a), or a cooperative process can take place (b). Adapted from Ref.³²

The dimensions of the resulting pores typically correlate with the size of the micelles, which in turn depends on the dimensions of the templating polymer, its concentration, type of the solvent and the presence of additives.³⁴ The “soft” surfactant templates such as CTABr (cetyltrimethylammonium bromide) and block-copolymers generally provide pores of meso dimensions, namely with a mean diameter of around 3 to 50 nm.

The crucial parameters affecting the morphology of micelle aggregates are defined by the micellar packing parameter g described in Equation 1.10, where V_{hc} is the volume of the hydrophobic core, A_o is the area of the head group and L is the alkyl chain length of a surfactant.³⁵ The g value predicts the geometries of surfactant self-assemblies in solution.

$$g = \frac{V_{hc}}{A_0 \times L} \quad (1.10)$$

During the film deposition, the mesostructural arrangement can also be achieved via a so-called evaporation-induced self-assembly (EISA)³⁶ with an additional more volatile solvent such as ethanol, as shown schematically in Figure 1.4. First, the disordered sol separates to into micellar and inorganic phases. Then, upon solvent evaporation, the position in the micellar phase diagram shifts, and the inorganic network condenses to form a stable hybrid mesostructure. Finally, the film is heated to decompose the template and to crystallize the inorganic scaffold, if so desired.

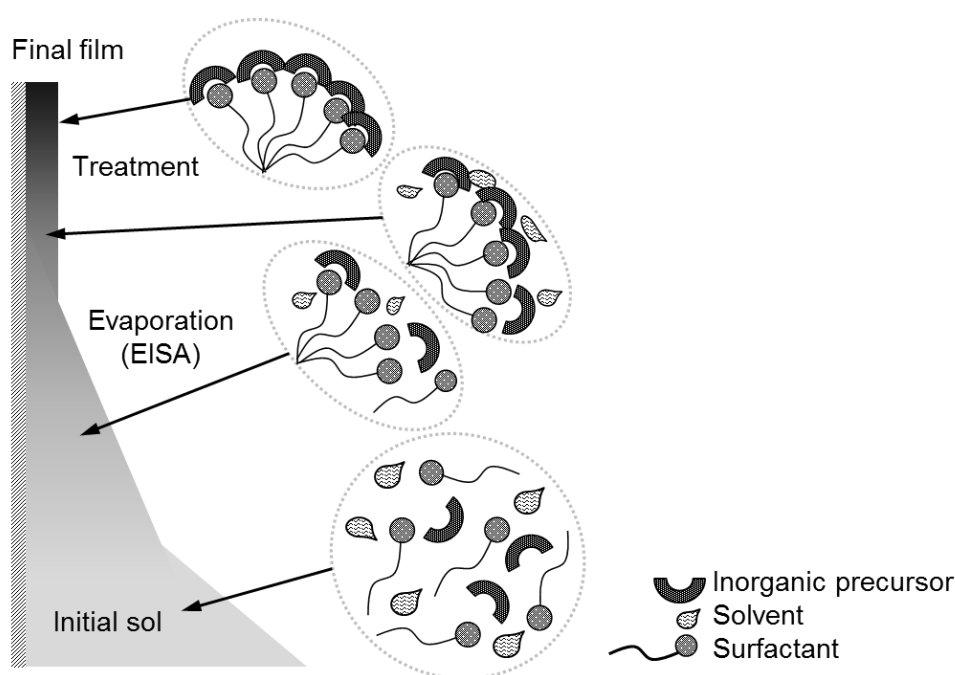


Figure 1.4. Formation of mesostructured thin film initiated by evaporation-induced self-assembly (EISA) during dip-coating. Adapted from Ref.³⁶

EISA routes are often applied to fabricate non-siliceous transition metal oxides, such as titania thin films.³⁷ However, the hydrolysis of transition metal compounds is significantly faster compared to silicon oxide precursors. Therefore the sol-gel synthesis of transition metal oxides requires more careful adjustment of synthesis parameters than in the case of silica.

One of important and challenging issues in the soft templating processing of the mesoporous films is the control of crystallinity of the metal oxide scaffold. Crystallization often hampers the cooperative self-organization and co-assembly and

therefore hinders formation of well-ordered porosity. Furthermore, thermal treatment required to enhance the film crystallinity often leads to a partial or a complete collapse of the periodic porous structure derived by the soft templates.

In contrast to the soft templates, hard templates can sustain more stress during the solution synthesis and subsequent heat treatment. Materials with well-defined rigid shapes such as mesoporous silica, silica beads etc. have been successfully employed in the synthesis of porous crystalline titanium dioxides.²¹ However, high thermal and chemical stability of the majority of conventional hard templates makes their removal rather difficult and is not always compatible with the processing conditions. For example, silica hard template is typically removed via chemical etching with diluted hydrofluoric acid or concentrated alkali metal hydroxide, which can damage the metal oxide scaffold and/or the underlying substrate.

Therefore, one attractive approach to fabricate crystalline metal oxides with a periodic mesoporous nanostructure is to use shape-persistent organic templates. Additionally, replacing expensive synthetic polymers by natural biopolymers would lead to more cost-effective fabrication of functional metal oxides. In the current study we employ natural cellulose crystals to fabricate thin films of porous titania and hematite. The next chapter introduces the general approaches to biotemplating and describes common properties of cellulosic materials.

1.2 Nanostructuring with Biogenic Materials

What nature delivers to us is never stale.

Because what nature creates has eternity in it.

Isaac Bashevis Singer

The way how nature creates materials has long fascinated scientists with chemical, physical or biological backgrounds. Nature-derived materials exhibit not only topological variability and diversity, but also sophisticated multifunctionality.³⁸ Hierarchically constructed biological objects such as butterfly wings, lotus leaves, silk, nacre, or bone tissue demonstrate astonishing functionalities resulting from the arrangement of extremely small features. The hierarchical structuring is a unique natural phenomenon, which deserves to be understood and imitated in various bio-inspired or bio-mimicking approaches to create novel functional materials.

There are several ways to implement the natural approaches to design novel functional materials. One possibility is to imitate natural processes performed by biogenic materials; as for instance the replication of photosynthetic reactions for photocatalytic water splitting and reduction of carbon dioxide by using synthetic inorganic materials. Another possibility is to employ biomaterials directly in the synthesis. This method takes advantage of the diversity and sustainability of natural materials thus offering new opportunities in tuning morphological, chemical and physical characteristics of target products. To date materials synthesis assisted by biological materials is a very fast-growing research area in the field of nanotechnology.³⁹⁻⁴²

The biotemplate-assisted fabrication of nanomaterials involves two main processing steps (Figure 1.5): i) the disintegration of bulk biomaterials by bottom-down approaches to isolate the desired nanoscale units, and ii) the bottom-up co-assembly of biogenic species with target materials or their precursors.

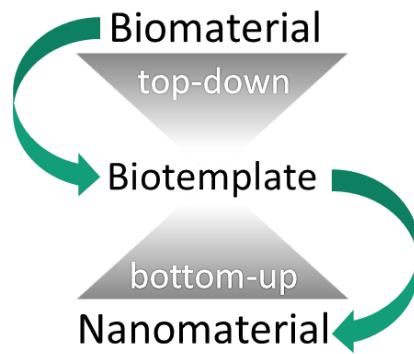


Figure 1.5. Schematic representation of a general approach towards the biotemplate-assisted synthesis of nanomaterials.

Depending on the desired nanomaterial, the general scheme in Figure 1.5 can be further extended by defining the type of biotemplate, the conditions of top-down and bottom up routes, as well as post-synthetic treatments required to prepare target materials. In the following the focus is put on the fabrication of porous metal oxides assisted by naturally occurring materials.

There are many different ways to obtain nanostructured metal oxides by using biotemplates. Boury et al.⁴⁰ have classified the strategies to associate metal oxides and biotemplates in the following main groups:

- (i) addition of soluble biotemplates to the metal oxide precursors in order to control the growth of metal oxide nanoparticles;
- (ii) preparation of hollow or porous structures by using insoluble biotemplates acting as moulds for replication;
- (iii) reaction of biotemplates with a metal-containing reagent leading to mineralized composites;
- (iv) combination of inorganics, i. e. metal oxide nanoparticles, and a biological material to form nanocomposites, where the latter acts as a filler.

The diverse possibilities of integrating biological materials into artificial synthesis routes has stimulated the development of a great variety of novel bio-based materials, namely aerogels,⁴³ hybrid nanocomposites,⁴⁴ composite hydrogels,⁴⁵ porous oxides,⁴⁶ chiral materials⁴⁷⁻⁵⁰ and photonic materials,⁵¹ applicable in fields such as medicine,⁵²⁻⁵⁴

catalysis,^{55,56} energy storage and conversion,^{46,57-62} chemical sensors,⁶³ thermal materials,⁶⁴ etc..

Currently, bio-based inorganic-organic composite materials and biotemplated porous materials are the two most common types of metal oxides prepared by bio-assisted nanostructuring. In the first case the green template acts as a filler to support or to reinforce the nanoscale metal oxides, while in the latter one the template is removed to introduce the porosity into metal oxide. The most common “green” materials employed to assist nanostructuring are described in the next chapter.

1.2.1 Biotemplates

The great advantages of the natural materials assisting the synthesis of novel nanomaterials are their availability and the unique hierarchical constitution. Cellulose is the most abundant polymeric raw material in the world, present primarily in wood biomass (Figure 1.6).⁶⁵

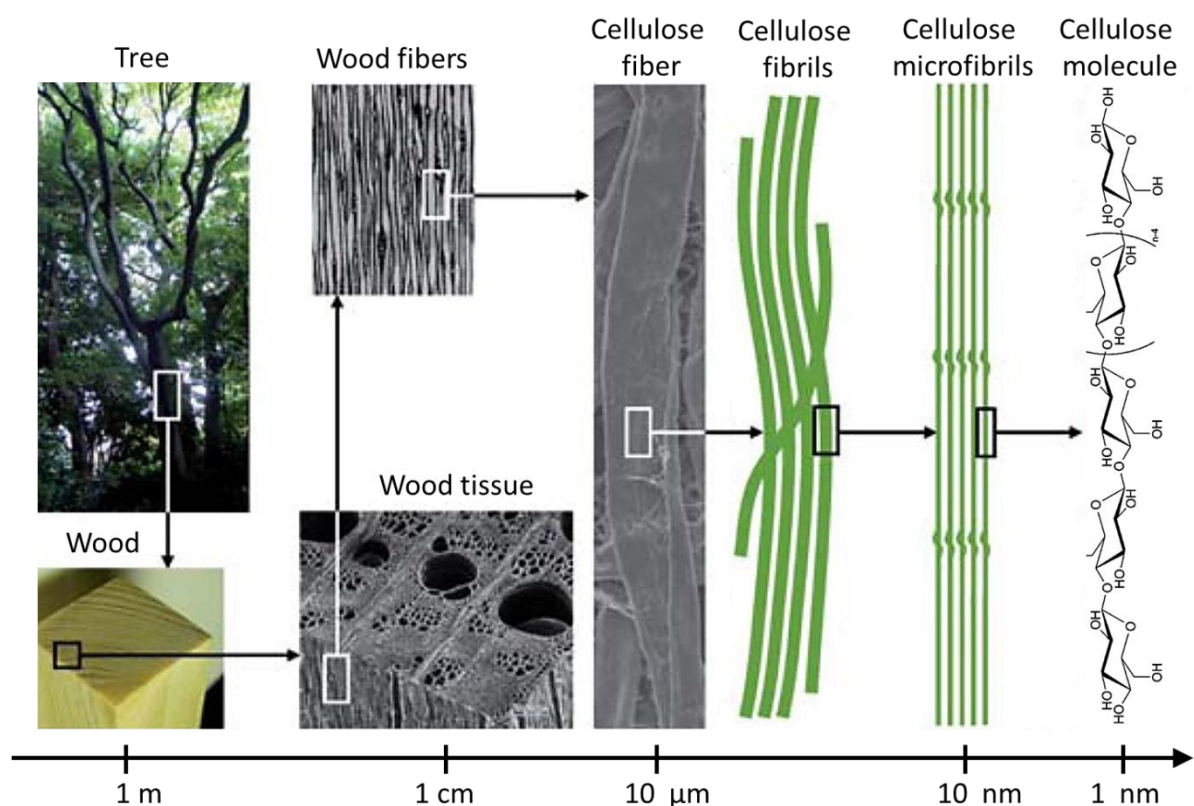


Figure 1.6. Hierarchical structure of wood. Adapted from Ref.^{66,67}

Wood demonstrates a fascinating hierarchical morphology with distinct structural units of variable dimensions: starting from a large plant trunk of several meters in size, down to a cellulose molecule of only several angstroms in width (Figure 1.6).

Due to their complex hierarchical structure, plants can be disintegrated to provide different secondary materials with dimensions defined by the degree of decomposition. Thus, it is possible to extract separate cellulose fibers, fibrils and microfibrils from wood with dimensions decreasing from several micrometers down to only a few nanometers, respectively.

Microfibrils can be further decomposed into cellulose molecules, whose chemical structure is shown in Figure 1.7.

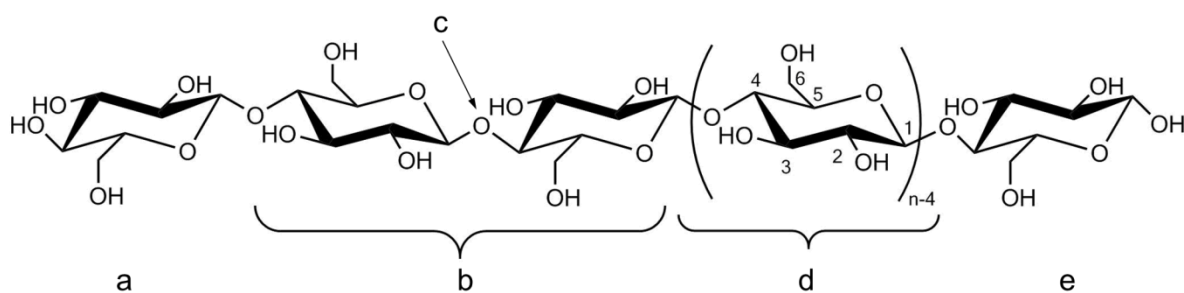


Figure 1.7. Chemical formula of cellulose revealing the non-reducing (a) and reducing (e) chain ends, the cellobiose unit (b) with the glycosidic link (c), as well as the anhydroglucose unit including atom numbering (d).⁶⁸

Cellulose is a trivial name for (1→4)-β-D-glucopyranan, i.e., a linear homopolysaccharide composed of β-D-anhydroglucopyranose (also referred to as anhydroglucose and glucopyranose) and connected by β(1→4) ether bonds called glycosidic links. β-D-anhydroglucopyranose is a six-membered heterocycle with an anomeric carbon (labelled as C1 in Figure 1.7), and it is usually found in the chair conformation.⁶⁸

The cellulose units are positioned such that their adjacent rings form intramolecular hydrogen bonds between oxygen in the ring and the hydrogen atom of C3 hydroxyl of a neighboring ring. Additionally, intermolecular hydrogen bonds form between the hydrogen atom of C6 hydroxyl and oxygen in a ring of an adjacent molecule. Intra- and intermolecular hydrogen bonding results in a stiffening of the cellulose chain and directs crystalline packing of the cellulose macromolecules.⁶⁸

The two ends of a cellulose chain are chemically different due to their different relative orientation. The one end has a free alcohol function on C4 and is non-reducing, the other end has a free anomeric atom providing reducing properties. This imparts some degree of polarity into native cellulose.⁶⁹

Furthermore, each cellulose monomer has three hydroxyl groups available for different kinds of reactions. This specific property of cellulose has been successfully used to modify the surface of nanounits extracted from the bulk celluloses. The grafting of carboxylated or sulphuric groups increases the dispersibility of the cellulose and changes its reactivity towards other chemical substances, thus expanding the practical applications of the cellulosic nanomaterials.

Cellulose is not the only example of a natural polysaccharide gaining broad attention for their application as a template in bio-inspired synthesis. Other important representatives of polysaccharides are, for instance, starch, glycogen, dextran, agarose, carrageenan, chitin, chitosan and alginate.⁷⁰⁻⁷² Although the polymeric structure of these substances is similar to cellulose, they differ either in the type of linkage between glucose monomers or by the functional groups attached to the monomers (Figure 1.8).

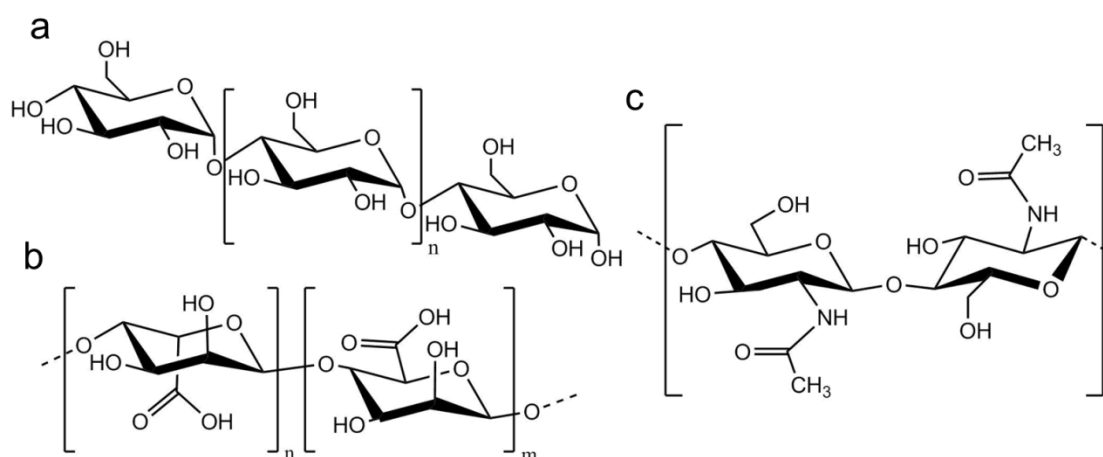


Figure 1.8. Chemical structures of natural polysaccharides: amylose found in starch (a), alginate (b) and chitin (c).

Apart from cellulose, several other polysaccharides assemble into multi-scale hierarchical structures. For example, starch appears in nature in the form of 2–100 μm granules.⁶⁹ Starch granules consist of rings of blocklets with amorphous and crystalline lamellae made of amylopectin and amylose chains. Different starch substructures such

as microscaled granules or nanoscaled platelet-like crystals^{73,74} have been employed in the synthesis of novel nanocomposites,^{75,76} as well as in the nanostructuring of porous oxides.⁷⁷⁻⁷⁹ However, the extraction of starch nanoparticles of well-defined shapes is challenging due to starch gelation at elevated temperatures, causing irreversible swelling of starch. Dextran also lacks crystallinity, furthermore, unlike cellulose and starch it is water soluble and therefore it can be used only as a sacrificial soft template.^{80,81}

In contrast to dextran and starch, chitin demonstrates rigidity and morphological properties very similar to cellulose. This biopolymer is widely found in nature, for instance, in the exoskeleton of crustaceans, insects and as well as in mushroom cellular walls.⁶⁹ Chitin has the same chemical structure as cellulose, with the only difference that one hydroxyl group in a monomer is replaced by an acetylamino group (Figure 1.8).

Because of strong hydrogen bonding, chitin macromolecules organize into stiff microfibrils, i.e, rod-like crystalline nanodomains resembling cellulose nanocrystals. Chitin nanowhiskers have been applied to prepare silica nanocomposites,^{44,82} porous silica and organosilica,⁸³ and have served as additive to control the crystallization of superconducting nanowires.⁸⁴

Apart from the polysaccharides, other biological materials have demonstrated their potential for being employed as templates for metal oxides such as for example bacteria,^{41,85} viruses,⁸⁶ proteins,^{87,88} silk fibroins,⁸⁹ egg white,⁹⁰ or diatoms.⁹¹ Furthermore, macroscale hierarchical materials such as green leaves,^{92,93} pollen particles,^{94,95} flagellar filaments⁶¹ and butterfly wings⁹⁶ have been shown to direct the formation of nanostructured materials.

To sum up, the common feature of biotemplates is their natural origin and organic composition, which makes them unique candidates for assisting nanofabrication approaches. The simple chemical composition assures straightforward handling and direct template removal. In addition, physical and chemical properties of biopolymers can be tuned by modifying their surface groups, which expands the variety of methods employing biotemplates. Nanodimensions, high crystallinity and anisotropy of nanocrystalline cellulose facilitate the straightforward application of the crystals for the wet chemical synthesis of sacrificially templated porous metal oxides.

1.2.2 Nanocrystalline Cellulose

Nanocrystalline cellulose (NCC), also referred in the literature as cellulose nanocrystals, nanowhiskers or nanocrystallites, as well as crystalline nanocellulose (CNC)⁶⁹ is a crystalline part of native cellulose synthesized by plants and bacteria.^{97,98} The biological role of rigid cellulose crystals is to provide stiffness to different parts of plants. Microorganisms synthesize cellulose as a protective barrier layer around their cells. Therefore, the main features of crystalline cellulose are nanoscale dimensions, elongated rod-like shape and a very high crystallinity.

Cellulose nanocrystals are hierarchically assembled cellulose macromolecules connected via intra- and intermolecular hydrogen bonding. The diverse possibilities of hydrogen bonding result in the different types of arrangements of polysaccharide chains, i.e., various cellulose polymorphs defined as I_α , I_β , II, III_I, III_{II}, IV_I and IV_{II} celluloses.^{97,99} Native celluloses consist of cellulose I polymorphs. The submodification I_α prevails in bacterial cellulose, whereas the I_β cellulose is more common for green plants.

Figure 1.9 demonstrates the schematic representation of a cross-section of a I_β cellulose nanocrystal, that has been shown to be square or rectangular.^{68,99}

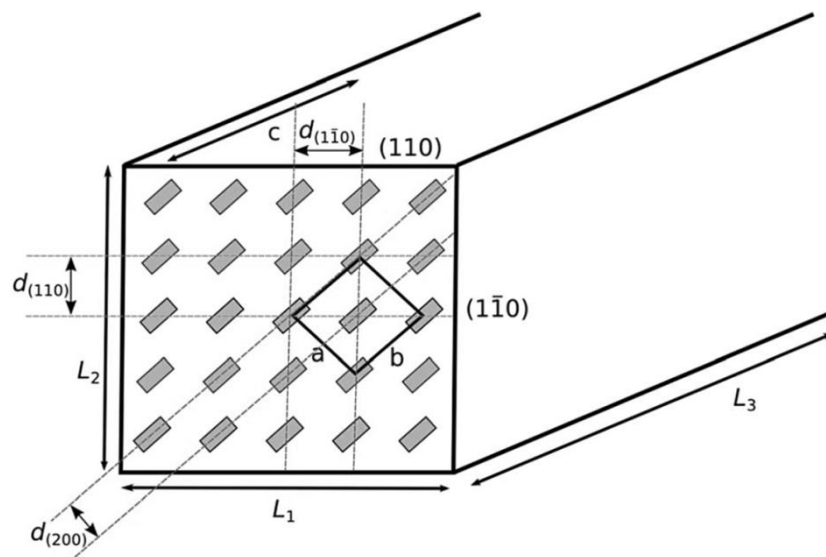


Figure 1.9. Schematic representation of a cross-section of a I_β cellulose nanocrystal showing the cellulose chain ends (grey spots), the unit cell and the directions of crystal planes.⁶⁸

The I_{β} crystal unit cell consists of two cellulose chains in monoclinic $P2_1$ arrangement with cell parameters: $a = 7.784 \text{ \AA}$, $b = 8.201 \text{ \AA}$, c (chain direction and unique axis) = 10.38 \AA and $\gamma = 96.5^\circ$.¹⁰⁰ The geometry of a cross-section and overall crystal dimensions depend on the cellulose origin.^{101,102} Generally the width of the cellulose crystals is in the range of 5–50 nm and the length is of about 100–1000 nm, where the larger longitudinal dimensions are characteristic for bacterial celluloses.^{97,103}

The first attempts to isolate rigid crystalline species from bulk celluloses were made in the late forties and early fifties of the last century by Ranby and Mukherjee et al.¹⁰⁴⁻¹⁰⁶ They performed an acid hydrolysis of native celluloses and obtained colloidal suspensions of rod-shaped particles. The properties of extracted cellulose were further investigated by Marchessault et al., who were the first to report the birefringence caused by self-assembly of cellulose species in aqueous suspensions.¹⁰⁷

The early studies on extraction of crystalline cellulose via hydrolysis have led to the development of a commercial product, microcrystalline cellulose (MCC) launched on the market in the early sixties.¹⁰⁸ The MCC is a powder of crystalline cellulose with particle dimensions in the range of several micrometres. The new material immediately found plenty of applications in various fields such as pharmaceuticals, medicine and food industry.

For the second time, crystalline cellulose has attracted intensive attention in the nineties. Owing to a significant progress in analytical and especially in imaging tools, it became possible to reveal the specific properties of the cellulose on the nanoscale.

Revol et al. have studied the self-organization of nanosized cellulose in aqueous solutions and reported the formation of stable chiral nematic (cholesteric) phases.¹⁰⁹⁻¹¹¹ Cellulose nanocrystals extracted by sulphuric acid are well-dispersed in water and form stable suspensions. At a certain critical concentration randomly oriented species self-organize into chiral-nematic patterns as shown in Figure 1.10. The ordered arrangement is characterized by a half pitch value, namely the distance over which a 180° rotation of the chiral nematic director is observed.

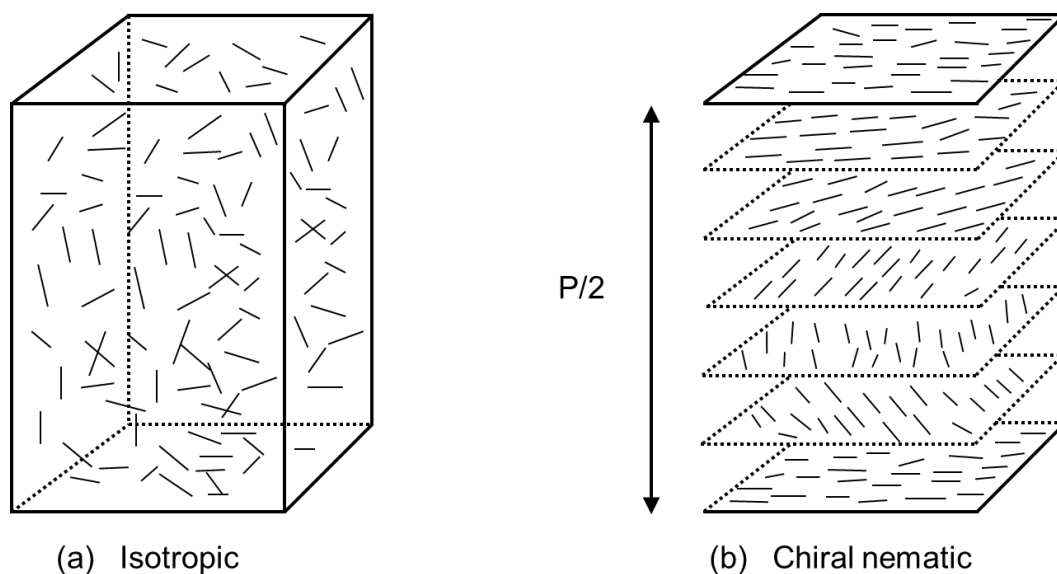


Figure 1.10. The schematic representation of the self-organization of cellulose nanocrystals in a suspension. (a) Randomly orientated cellulose nanocrystals. (b) Aligned cellulose nanocrystals. The arrow indicates the direction of the chiral nematic axis, and P stays for the chiral nematic pitch. The dotted lines are the guiding lines for the schematic visualization of nematic planes.¹¹¹

A similar phenomenon of helicoidal organization has been observed for other elongated species, for instance for viruses and DNA fragments⁹⁷ and for natural materials such as plant cell walls, chitin in arthropod cuticle and collagen in skeletal tissues.^{109,112}

The driving force for the self-alignment is presumably the initial screw symmetry of the polyglucose superstructures¹¹³ and their helical arrangement in cellulose microfibrils. The nanoscale chirality induces a spontaneous formation of a chiral nematic phase on a large scale.^{109,112,114} The critical concentration of the spontaneous phase separation into isotropic and anisotropic phases depends on the geometry of the crystals, their aspect ratio, surface charge, as well as on the ionic strength of the solution.^{109,110}

Marchessault et al. have observed the birefringence of a cellulose suspension at a concentration of 13 wt %.¹⁰⁷ In contrast, Revol et al.¹¹⁰ reported the critical volume fraction of 0.03, which corresponds to a cellulose concentration of about 4 wt %. The latter study reveals the dimensions of the chiral pitch in the range of 12–70 μm . Additionally, the authors demonstrate the sensitivity of the crystal self-organization in solution to external magnetic fields.

Upon complete water removal, dense cellulose films retain the self-organization of cellulose species. Typically, the chiral nematic pitch is about 10–20 μm and the free

standing films appear transparent. However, if the pitch size (P) matches the visible range of the electromagnetic spectrum, the films reflect light of selective wavelength λ_{max} and appear iridescent or colored:

$$\lambda_{max} = n_{avg} \times P, \quad (1.11)$$

where n_{avg} is the average refractive index.^{115,116}

The dimensions of the chiral nematic pitch, and hence the optical properties of the NCC assemblies, can be tuned via adjusting the ionic strength of the suspensions, for example by introducing inorganic salts to the suspensions and via controlling the evaporation conditions.^{111,117}

Another attractive property of the cellulose nanocrystals is the presence of hydroxyl groups on their surface, which can be replaced by other functional groups to modify the physical and chemical properties of the crystals.^{68,99}

Over the past few decades, significant progress has been made in expanding the application areas of nanocrystalline cellulose.

The main motivation for the rapid popularization of the NCC is the abundancy and eco-friendly nature of the bulk celluloses. Moreover, nanoscale crystalline cellulose demonstrates some unique properties required in many applications. High mechanical strength of the cellulose crystals, i.e., a crystal modulus of 100–160 GPa¹¹⁸ assures excellent reinforcing properties of NCC in the manufacturing of composite materials. In addition, the nano-dimensions of the NCC enable their homogeneous distribution in a polymer matrix. The nanocellulose-based composites can be used, for example, in the production of eco-friendly plastic automotive body panels.¹¹⁹

Another intriguing application of the NCC is the fabrication of mechanically stable and optically transparent NCC paper sheets.¹²⁰ Cast NCC films can also serve as membranes for blocking water vapors and oxygen.¹²¹ Electrically conductive NCC nanopapers and aerogels are obtained in the form of nanocomposites through addition of carbon nanotubes,^{122,123} and conductive polymers.¹²⁴

NCC composite films incorporating metal nanoparticles or metal oxides are applied as antimicrobial filters, as catalytic remedies for air and water purification and as

biosensors.¹²⁰ Freeze drying of cellulose nanocrystals leads to the formation of highly porous sponges, which can act as oil-spill absorbers (Figure 1.11).¹²⁵

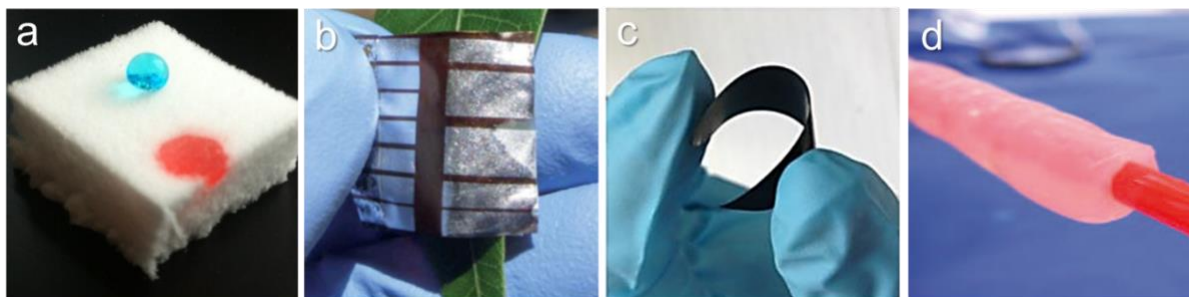


Figure 1.11. Digital photos demonstrating the diversity of NCC applications. (a) Porous silylated nanocellulose sponge acting as an oil-absorber (red drop) and a water-repellent (blue drop),¹²⁵ (b) transparent and conductive nanocellulose paper as a substrate for printed solar cells,¹²⁶ (c) free-standing lithium titanate/carbon nanotube/nanocellulose nanofiber hybrid used in lithium-ion batteries¹²⁷ (d) a tube of bacterial nanocellulose aimed to substitute a blood-vessel.⁹⁸

Biodegradability and biocompatibility of the NCC are especially beneficial for various medical applications aimed at wound healing, tissue engineering and implant fabrication.^{66,98,128-130} The utilization of the nanocellulose in energy conversion devices is another highly promising application field. NCC has already been demonstrated to assist in the fabrication of electrode materials for solar and fuel cells, as well as for lithium-ion batteries.^{120,126,131}

High demand for nanocelluloses aiding in the fabrication of novel functional materials for environmental and medical applications has stimulated the development of their industrial production. There are several companies aimed at launching the large-scale manufacture of nanocelluloses. Among them are FPIinnovations (Canada), Innventia (Sweden) and Melodea (Israel). Additionally, the opening of industrial facilities by Borregaard in Norway and Sappi in South Africa has been recently reported.^{132,133}

To sum up, nanocrystalline cellulose is currently gaining extensive attention due to its advanced properties enabling the assistance in the development of advanced functional materials. The next chapter focuses explicitly on the role of cellulose nanocrystals in the synthesis of porous metal oxides.

1.2.3 Metal Oxides Templated with Nanocrystalline Cellulose

Sacrificial biotemplating of porous metal oxides can be achieved by using natural materials such as cellulose nanocrystals as molds or templates. The function of the biotemplates is similar to that of the soft templates, i.e., block-copolymers that are employed in the sol-gel template-assisted synthesis (see Chapter 1.1.3). Analogous to the soft templates, the cellulose nanocrystals first direct the formation of metal oxides, and then introduce the porosity after being decomposed.

The first biomimetic replication of silica by nematically organized cellulose nanocrystals has been demonstrated by Dujardin et al.¹¹⁴ They reported birefringent mesoporous silica demonstrating high surface area and organized channel-like pores. Antonietti et al.¹³⁴ have prepared silica morphologies nanostructured by using self-aligned cholesteric cellulose derivatives, such as hydroxypropyl cellulose.

Shopsowitz et al. have employed NCC-assisted nanocasting to obtain free-standing films of chiral porous silica revealing unique optical properties.¹¹⁶ The cast NCC silica hybrids demonstrate various colors before and after the template removal. The color is adjusted by changing the fraction of silica precursor relative to the NCC. Furthermore, the light reflectance can be modified by adding different metal ions to NCC/silica precursor suspensions.¹³⁵

The recent progress in templating with NCC has stimulated the discovery of a whole family of new chiral functional materials.⁴⁹ NCC-aided nanocasting has been successfully employed for the fabrication of materials other than silica chiral, such as chiral mesoporous carbon,¹³⁶ flexible iridescent organosilicas,¹³⁷ chiral mesoporous silicon carbide,¹³⁸ silver nanoparticles supported by a chiral silica matrix¹³⁹ and flexible photonic resins.¹⁴⁰

We note that the most successful examples of cholesteric sacrificial templating are related to the fabrication of amorphous materials that do not undergo crystallization during the thermal template removal. However, the majority of technologically important semiconducting metal oxides (such as for instance titanium dioxide and hematite) needs to be crystalline for efficient performance. Obviously, the fabrication of crystalline metal oxides featuring both high crystallinity and high porosity requires the development of special synthesis methods.

Although titania has been successfully templated by natural materials of macroscopic dimensions, such as green leaves,¹⁴¹ corn stalks,¹⁴² natural cellulose fibers,^{29,46,143} filter paper,¹⁴⁴⁻¹⁴⁷ nanocellulose aerogels,^{148,149} starch gel,¹⁵⁰ bacterial cellulose^{151,152} etc., the studies on titania nanostructured by nanoscale colloidal cellulose crystals are rather scarce.

Zhou et al.¹⁵³ have applied cellulose nanocrystals in the synthesis of titania nanocubes. Chen et al.¹⁵⁴ prepared hierarchically nanostructured titania powders via one-pot hydrolysis of a titania precursor in the presence of cellulose nanocrystals. Nanocrystalline cellulose sponges obtained by freeze-drying were employed as scaffolds to obtain porous titania monoliths. Nanocellulose aerogels have been used as a template for porous titania nanoparticles.¹⁵⁵

Carbonization of titania has been realized by vacuum heating of composites containing cellulose nano-whiskers.¹⁵⁶ Composites of titania and cotton-nanofibers have been studied for applications in drug delivery.¹⁵⁷ Shopsowitz et al. have translated the chiral nematic organization of the cellulose nanocrystals to porous titania by a two-step sacrificial templating approach.¹⁵⁸ Here, NCC derived chiral silica was employed as a hard template to replicate chiral titania.

The fabrication of different nanoporous metal oxides by combining the cellulosic templates¹⁵⁹ and polysaccharide nanoparticles⁴⁰ with metal precursors became a very popular technique due to the straightforward synthesis and availability of the templates. The as-prepared powders and free-standing films are mostly employed in photocatalysis,^{29,147,151,154} however more elaborated devices such as solar cells^{46,160} and Li-ion batteries have been reported as well.

Besides titania, other porous metal oxides or composite materials such as alumina, tin dioxide and iron oxide have been prepared using cellulosic materials and biological nanocrystals. Mesoporous alumina featuring elongated mesopores has been obtained using chitin nanocrystals as a sacrificial template.¹⁶¹ Porous tin dioxide has been achieved by templating with hydroxypropyl cellulose (HPC),¹⁶² while flexible nanocomposites of iron oxides and bacterial nanocellulose reveal pronounced magnetic properties.¹⁶³

In the present thesis the nanocrystalline cellulose was employed as a supramolecular template for the fabrication of mesoporous titania and hematite thin films. It is the first time that the NCC has been used for the direct fabrication of homogeneous porous inorganic oxide thin films on different substrates. The goal of this thesis was to reveal the benefits of colloidal cellulose nanocrystals in the fabrication of porous titania and hematite thin films and thereby to extend the scope of templating methods based on sustainable, green materials.

1.3 References

- (1) *Fundamentals of materials for energy and environmental sustainability*; Ginley, D. S., Ed.; Cambridge University Press: Cambridge, 2012.
- (2) Ozin, G. A.; Arsenault, A.; Cademartiri, L. *Nanochemistry: A Chemical Approach to Nanomaterials*; The Royal Society of Chemistry: Cambridge, 2009.
- (3) Cao, G., *Nanostructures and nanomaterials*; Imperial College Press: London, 2008.
- (4) Atkins, P. W.; De Paula, J. *Atkins' Physical Chemistry*; Oxford University Press: Oxford, 2010.
- (5) Carp, O.; Huisman, C. L.; Reller, A. *Prog. Solid State Chem.* **2004**, *32*, 33.
- (6) Chen, X.; Mao, S. S. *Chem. Rev.* **2007**, *107*, 2891.
- (7) Fujishima, A.; Rao, T. N.; Tryk, D. A. *J. of Photochem. and Photobiol., C: Photochem. Rev.* **2000**, *1*, 1.
- (8) Herrmann, J.-M. *Appl. Catal., B: Environ.* **2010**, *99*, 461.
- (9) Pelizzetti, E.; Minero, C. *Electrochim. Acta* **1993**, *38*, 47.
- (10) Mishra, M.; Chun, D.-M. *Appl. Catal., A* **2015**, *498*, 126.
- (11) Kalyanasundaram, K. In *Dye-sensitized solar cells*; Kalyanasundaram, K., Ed.; EPFL Press: Lausanne, 2010, pp 1–43.
- (12) Kudo, A.; Miseki, Y. *Chem. Soc. Rev.* **2009**, *38*, 253.
- (13) Chen, X.; Li, C.; Grätzel, M.; Kostecki, R.; Mao, S. S. *Chem. Soc. Rev.* **2012**, *41*, 7909.
- (14) Chen, X.; Shen, S.; Guo, L.; Mao, S. S. *Chem. Rev.* **2010**, *110*, 6503.
- (15) Tilley, S. D.; Cornuz, M.; Sivula, K.; Grätzel, M. *Angew. Chem. Int. Ed.* **2010**, *49*, 6405.
- (16) Morton, O. *Nature* **2006**, *443*, 19.
- (17) O'Regan, B.; Grätzel, M. *Nature* **1991**, *353*, 737.
- (18) Grätzel, M. *Nature* **2001**, *414*, 338.
- (19) Grätzel, M. *Inorg. Chem.* **2005**, *44*, 6841.
- (20) Liu, M.; Johnston, M. B.; Snaith, H. J. *Nature* **2013**, *501*, 395.
- (21) Fattakhova-Rohlfing, D.; Zaleska, A.; Bein, T. *Chem. Rev.* **2014**, *114*, 9487.
- (22) Livage, J.; Lemerle, J. *Ann. Rev. Mater. Sci.* **1982**, *12*, 103.
- (23) Livage, J.; Henry, M.; Sanchez, C. *Prog. Solid State Chem.* **1988**, *18*, 259.
- (24) Livage, J.; Sanchez, C.; Henry, M.; Doeuff, S. *Solid State Ionics* **1989**, *32–33, Part 2*, 633.
- (25) Brinker, J. C.; Scherer, G. W. *Sol-gel Science: The Physics and Chemistry of Sol-gel*; Academic Press: London, 1990.

- (26) Henry, M.; Jolivet, J.; Livage, J. In *Chemistry, Spectroscopy and Applications of Sol-Gel Glasses*; Reisfeld, R., Jjørgensen, C. K., Eds.; Springer Berlin Heidelberg: 1992; Vol. 77, p 153.
- (27) Sakka, S.; Yoko, T. In *Chemistry, Spectroscopy and Applications of Sol-Gel Glasses*; Reisfeld, R., Jjørgensen, C. K., Eds.; Springer Berlin Heidelberg: 1992; Vol. 77, p 89.
- (28) Livage, J.; Ganguli, D. *Sol. Energy Mater. Sol. Cells* **2001**, *68*, 365.
- (29) Postnova, I.; Kozlova, E.; Cherepanova, S.; Tsybulya, S.; Rempel, A.; Shchipunov, Y. *RSC Adv.* **2015**, *5*, 8544.
- (30) Kresge, C. T.; Leonowicz, M. E.; Roth, W. J.; Vartuli, J. C.; Beck, J. S. *Nature* **1992**, *359*, 710.
- (31) Beck, J. S.; Vartuli, J. C.; Roth, W. J.; Leonowicz, M. E.; Kresge, C. T.; Schmitt, K. D.; Chu, C. T. W.; Olson, D. H.; Sheppard, E. W. *J. Am. Chem. Soc.* **1992**, *114*, 10834.
- (32) Soler-Illia, G. J. d. A. A.; Sanchez, C.; Lebeau, B.; Patarin, J. *Chem. Rev.* **2002**, *102*, 4093.
- (33) Sanchez, C.; Boissière, C.; Grosso, D.; Laberty, C.; Nicole, L. *Chem. Mater.* **2008**, *20*, 682.
- (34) Choucair, A.; Eisenberg, A. *Eur. Phys. J. E* **2003**, *10*, 37.
- (35) Israelachvili, J. N.; Mitchell, D. J.; Ninham, B. W. *J. Chem. Soc., Faraday Trans. 2: Mol. Chem. Phys.* **1976**, *72*, 1525.
- (36) Grosso, D.; Cagnol, F.; Soler-Illia, G. J. d. A. A.; Crepaldi, E. L.; Amenitsch, H.; Brunet-Bruneau, A.; Bourgeois, A.; Sanchez, C. *Adv. Funct. Mater.* **2004**, *14*, 309.
- (37) Crepaldi, E. L.; Soler-Illia, G. J. d. A. A.; Grosso, D.; Cagnol, F.; Ribot, F.; Sanchez, C. *J. Am. Chem. Soc.* **2003**, *125*, 9770.
- (38) Sanchez, C.; Arribart, H.; Giraud Guille, M. M. *Nat. Mater.* **2005**, *4*, 277.
- (39) Gu, J.; Zhang, W.; Su, H.; Fan, T.; Zhu, S.; Liu, Q.; Zhang, D. *Adv. Mater.* **2015**, *27*, 464.
- (40) Boury, B.; Plumejeau, S. *Green Chem.* **2015**, *17*, 72.
- (41) Selvakumar, R.; Seethalakshmi, N.; Thavamani, P.; Naidu, R.; Megharaj, M. *RSC Adv.* **2014**, *4*, 52156.
- (42) Zhao, N.; Wang, Z.; Cai, C.; Shen, H.; Liang, F.; Wang, D.; Wang, C.; Zhu, T.; Guo, J.; Wang, Y.; Liu, X.; Duan, C.; Wang, H.; Mao, Y.; Jia, X.; Dong, H.; Zhang, X.; Xu, J. *Adv. Mater.* **2014**, *26*, 6994.
- (43) Cai, J.; Liu, S.; Feng, J.; Kimura, S.; Wada, M.; Kuga, S.; Zhang, L. *Angew. Chem.* **2012**, *124*, 2118.
- (44) Alonso, B.; Belamie, E. *Angew. Chem. Int. Ed.* **2010**, *49*, 8201.
- (45) Yang, J.; Zhang, X.-M.; Xu, F. *Macromolecules* **2015**, *48*, 1231.
- (46) Ghadiri, E.; Taghavinia, N.; Zakeeruddin, S. M.; Grätzel, M.; Moser, J.-E. *Nano Lett.* **2010**, *10*, 1632.
- (47) Liu, B.; Cao, Y.; Huang, Z.; Duan, Y.; Che, S. *Adv. Mater.* **2015**, *27*, 479.
- (48) Schlesinger, M.; Giese, M.; Blusch, L. K.; Hamad, W. Y.; MacLachlan, M. J. *Chem. Commun.* **2015**, *51*, 530.

- (49) Giese, M.; Blusch, L. K.; Khan, M. K.; MacLachlan, M. J. *Angew. Chem. Int. Ed.*, **2015**, *54*, 2888.
- (50) Giese, M.; Krappitz, T.; Dong, R. Y.; Michal, C. A.; Hamad, W. Y.; Patrick, B. O.; MacLachlan, M. J. *J. Mater. Chem. C* **2015**, *3*, 1537.
- (51) Khan, M. K.; Bsoul, A.; Walus, K.; Hamad, W. Y.; MacLachlan, M. J. *Angew. Chem.* **2015**, *54*, 4304.
- (52) Tampieri, A.; Iafisco, M.; Sandri, M.; Panseri, S.; Cunha, C.; Sprio, S.; Savini, E.; Uhlarz, M.; Herrmannsdörfer, T. *ACS Appl. Mater. Interfaces* **2014**, *6*, 15697.
- (53) San, B. H.; Kim, J. A.; Kulkarni, A.; Moh, S. H.; Dugasani, S. R.; Subramani, V. K.; Thorat, N. D.; Lee, H. H.; Park, S. H.; Kim, T.; Kim, K. K. *ACS Nano* **2014**, *8*, 12120.
- (54) Chen, P.-H.; Liao, H.-C.; Hsu, S.-H.; Chen, R.-S.; Wu, M.-C.; Yang, Y.-F.; Wu, C.-C.; Chen, M.-H.; Su, W.-F. *RSC Adv.* **2015**, *5*, 6932.
- (55) Primo, A.; Marino, T.; Corma, A.; Molinari, R.; García, H. *J. Am. Chem. Soc.* **2011**, *133*, 6930.
- (56) Liu, S.; Bian, W.; Yang, Z.; Tian, J.; Jin, C.; Shen, M.; Zhou, Z.; Yang, R. *J. Mater. Chem. A* **2014**, *2*, 18012.
- (57) Yan, D.; Zhang, H.; Chen, L.; Zhu, G.; Li, S.; Xu, H.; Yu, A. *ACS Appl. Mater. Interfaces* **2014**, *6*, 15632.
- (58) Xiong, W.; Gao, Y.; Wu, X.; Hu, X.; Lan, D.; Chen, Y.; Pu, X.; Zeng, Y.; Su, J.; Zhu, Z. *ACS Appl. Mater. Interfaces* **2014**, *6*, 19416.
- (59) Zhang, X.; Hou, Y.; He, W.; Yang, G.; Cui, J.; Liu, S.; Song, X.; Huang, Z. *Nanoscale* **2015**, *7*, 3356.
- (60) Wang, L.; Xue, J.; Gao, B.; Gao, P.; Mou, C.; Li, J. *RSC Adv.* **2014**, *4*, 64744.
- (61) Beznosov, S. N.; Veluri, P. S.; Pyatibratov, M. G.; Chatterjee, A.; MacFarlane, D. R.; Fedorov, O. V.; Mitra, S. *Sci. Rep.* **2015**, *5*, 7736.
- (62) Lee, Y. M.; Kim, Y. H.; Lee, J. H.; Park, J. H.; Park, N.-G.; Choe, W.-S.; Ko, M. J.; Yoo, P. J. *Adv. Funct. Mater.* **2011**, *21*, 1160.
- (63) Jur, J. S.; Sweet, W. J.; Oldham, C. J.; Parsons, G. N. *Adv. Funct. Mater.* **2011**, *21*, 1993.
- (64) Tao, P.; Shang, W.; Song, C.; Shen, Q.; Zhang, F.; Luo, Z.; Yi, N.; Zhang, D.; Deng, T. *Adv. Mater.* **2015**, *27*, 428.
- (65) Klemm, D.; Heublein, B.; Fink, H.-P.; Bohn, A. *Angew. Chem. Int. Ed.* **2005**, *44*, 3358.
- (66) Lin, N.; Dufresne, A. *Eur. Polym. J.* **2014**, *59*, 302.
- (67) Isogai, A.; Saito, T.; Fukuzumi, H. *Nanoscale* **2011**, *3*, 71.
- (68) Eyley, S.; Thielemans, W. *Nanoscale* **2014**, *6*, 7764.
- (69) Dufresne, A. *Nanocellulose - From Nature to High Performance Tailored Materials*; Walter de Gruyter GmbH & Co.KG: Berlin, 2012.
- (70) Zollfrank, C.; Cromme, P.; Rauch, M.; Scheel, H.; Kostova, M. H.; Gutbrod, K.; Gruber, S.; Van Opdenbosch, D. *Bioinspir. Biomim. Nanobiomater.* **2012**, *1*, 13.

- (71) Lin, N.; Huang, J.; Dufresne, A. *Nanoscale* **2012**, *4*, 3274.
- (72) Tingaut, P.; Zimmermann, T.; Sebe, G. *J. Mater. Chem.* **2012**, *22*, 20105.
- (73) Putaux, J.-L.; Molina-Boisseau, S.; Momaour, T.; Dufresne, A. *Biomacromolecules* **2003**, *4*, 1198.
- (74) Le Corre, D.; Bras, J.; Dufresne, A. *Biomacromolecules* **2010**, *11*, 1139.
- (75) Le Corre, D.; Angellier-Coussy, H. *React. Funct. Polym.* **2014**, *85*, 97.
- (76) Haaj, S. B.; Thielemans, W.; Magnin, A.; Boufi, S. *ACS Appl. Mater. Interfaces* **2014**, *6*, 8263.
- (77) Zhang, B.; Davis, S. A.; Mann, S. *Chem. Mater.* **2002**, *14*, 1369.
- (78) Wang, F.; Zhou, Y.; Li, P.; Li, H.; Tu, W.; Yan, S.; Zou, Z. *RSC Adv.* **2014**, *4*, 43172.
- (79) Bao, S.-J.; Lei, C.; Xu, M.-W.; Cai, C.-J.; Cheng, C.-J.; Li, C. M. *Cryst. Eng. Comm.* **2013**, *15*, 4694.
- (80) Walsh, D.; Arcelli, L.; Ikoma, T.; Tanaka, J.; Mann, S. *Nat. Mater.* **2003**, *2*, 386.
- (81) Kim, Y.-Y.; Neudeck, C.; Walsh, D. *Polym. Chem.* **2010**, *1*, 272.
- (82) Ogasawara, W.; Shenton, W.; Davis, S. A.; Mann, S. *Chem. Mater.* **2000**, *12*, 2835.
- (83) Nguyen, T.-D.; Shopsowitz, K. E.; MacLachlan, M. J. *Chem. Eur. J.* **2013**, *19*, 15148.
- (84) Hall, S. R. *Adv. Mater.* **2006**, *18*, 487.
- (85) Shim, H.-W.; Park, S.; Song, H. J.; Kim, J.-C.; Jang, E.; Hong, K. S.; Kim, T. D.; Kim, D.-W. *Chem. Eur. J.* **2015**, *21*, 4655.
- (86) Huang, Y.; Chiang, C.-Y.; Lee, S. K.; Gao, Y.; Hu, E. L.; Yoreo, J. D.; Belcher, A. M. *Nano Lett.* **2005**, *5*, 1429.
- (87) Huggins, K. N. L.; Schoen, A. P.; Arunagirinathan, M. A.; Heilshorn, S. C. *Adv. Funct. Mater.* **2014**, *24*, 7737.
- (88) de la Rica, R.; Chow, L. W.; Horejs, C.-M.; Mazo, M.; Chiappini, C.; Pashuck, E. T.; Bitton, R.; Stevens, M. M. *Chem. Commun.* **2014**, *50*, 10648.
- (89) Fei, X.; Li, W.; Shao, Z.; Seeger, S.; Zhao, D.; Chen, X. *J. Am. Chem. Soc.* **2014**, *136*, 15781.
- (90) Liu, Y.; Lv, H.; Hu, J.; Li, Z. *Mater. Lett.* **2015**, *139*, 401.
- (91) Lang, Y.; Finn, D. P.; Caruso, F.; Pandit, A. *RSC Adv.* **2014**, *4*, 44418.
- (92) Li, X.; Fan, T.; Zhou, H.; Chow, S.-K.; Zhang, W.; Zhang, D.; Guo, Q.; Ogawa, H. *Adv. Funct. Mater.* **2009**, *19*, 45.
- (93) Han, L.; Yang, D.-P.; Liu, A. *Biosens. Bioelectron.* **2015**, *63*, 145.
- (94) Wang, X.-X.; Tian, K.; Li, H.-Y.; Cai, Z.-X.; Guo, X. *RSC Adv.* **2015**, *5*, 29428.
- (95) Gomez, I. J.; Goodwin, W. B.; Sabo, D.; Zhang, Z. J.; Sandhage, K. H.; Meredith, J. C. *J. Mater. Chem. C* **2015**, *3*, 632.

- (96) Zhang, W.; Gu, J.; Liu, Q.; Su, H.; Fan, T.; Zhang, D. *Phys. Chem. Chem. Phys.* **2014**, *16*, 19767.
- (97) Habibi, Y.; Lucia, L. A.; Rojas, O. J. *Chem. Rev.* **2010**, *110*, 3479.
- (98) Klemm, D.; Kramer, F.; Moritz, S.; Lindström, T.; Ankerfors, M.; Gray, D.; Dorris, A. *Angew. Chem. Int. Ed.* **2011**, *50*, 5438.
- (99) Moon, R. J.; Martini, A.; Nairn, J.; Simonsen, J.; Youngblood, J. *Chem. Soc. Rev.* **2011**, *40*, 3941.
- (100) Nishiyama, Y.; Langan, P.; Chanzy, H. *J. Am. Chem. Soc.* **2002**, *124*, 9074.
- (101) Garvey, C. J.; Parker, I. H.; Simon, G. P. *Macromol. Chem. Phys.* **2005**, *206*, 1568.
- (102) Ju, X.; Bowden, M.; Brown, E. E.; Zhang, X. *Carbohydr. Polym.* **2015**, *123*, 476.
- (103) Peng, B. L.; Dhar, N.; Liu, H. L.; Tam, K. C. *Can. J. Chem. Eng.* **2011**, *89*, 1191.
- (104) Ranby, B. G. *Acta Chem. Scand.* **1949**, *3*, 649.
- (105) Ranby, B. G. *Discuss. Faraday Soc.* **1951**, *11*, 158.
- (106) Mukherjee, S. M.; Woods, H. J. *Biochim. Biophys. Acta* **1953**, *10*, 499.
- (107) Marchessault, R. H.; Morehead, F. F.; Walter, N. M. *Nature* **1959**, *184*, 632.
- (108) Charreau H.; Foresti, M. L. V. A. *Recent Pat. Nanotechnol.* **2013**, *7*, 56
- (109) Revol, J. F.; Bradford, H.; Giasson, J.; Marchessault, R. H.; Gray, D. G. *Int. J. Biol. Macromolec.* **1992**, *14*, 170.
- (110) Revol, J. F. G., L.; Dong, X. M.; Gray, D. G.; Chanzy H.; Maret, G.; *Liq. Cryst.* **1994**, *16*, 127.
- (111) Revol, J. F. G., L.; Gray, D. G.; *J. Pulp Pap. Sci.* **1998**, *24*, 146.
- (112) Revol, J. F.; Marchessault, R. H. *Int. J. Biol. Macromolec.* **1993**, *15*, 329.
- (113) Kaushik, M.; Basu, K.; Benoit, C.; Cirtiu, C. M.; Vali, H.; Moores, A. J. *Am. Chem. Soc.* **2015**, *137*, 6124.
- (114) Dujardin, E.; Blaseby, M.; Mann, S. J. *Mater. Chem.* **2003**, *13*, 696.
- (115) De Vries, H. *Acta Crystallogr.* **1951**, *4*, 219.
- (116) Shopsowitz, K. E.; Qi, H.; Hamad, W. Y.; MacLachlan, M. J. *Nature* **2010**, *468*, 422.
- (117) Dumanli, A. G.; Kamita, G.; Landman, J.; van der Kooij, H.; Glover, B. J.; Baumberg, J. J.; Steiner, U.; Vignolini, S. *Adv. Opt. Mater.* **2014**, *2*, 646.
- (118) Eichhorn, S. J. *Soft Matter* **2011**, *7*, 303.
- (119) ACS Chemistry for Life Home Page. <http://www.acs.org/content/acs/en/pressroom/newsreleases/2011/march/green-cars-could-be-made-from-pineapples-and-bananas.html> (accessed Feb 20, **2015**).
- (120) Wei, H.; Rodriguez, K.; Renneckar, S.; Vikesland, P. J. *Environ. Sci. Nano* **2014**, *1*, 302.
- (121) Sirviö, J. A.; Kolehmainen, A.; Visanko, M.; Liimatainen, H.; Niinimäki, J.; Hormi, O. E. O. *ACS Appl. Mater. Interfaces* **2014**, *6*, 14384.

- (122) Hamed, M. M.; Hajian, A.; Fall, A. B.; Håkansson, K.; Salajkova, M.; Lundell, F.; Wågberg, L.; Berglund, L. A. *ACS Nano* **2014**, *8*, 2467.
- (123) Huang, H.-D.; Liu, C.-Y.; Zhang, L.-Q.; Zhong, G.-J.; Li, Z.-M. *ACS Sustain. Chem. Eng.* **2015**, *3*, 317.
- (124) Zhang, X.; Wu, X.; Lu, C.; Zhou, Z. *ACS Sustain. Chem. Eng.* **2015**, *3*, 675.
- (125) Zhang, Z.; Sèbe, G.; Rentsch, D.; Zimmermann, T.; Tingaut, P. *Chem. Mater.* **2014**, *26*, 2659.
- (126) Hu, L.; Zheng, G.; Yao, J.; Liu, N.; Weil, B.; Eskilsson, M.; Karabulut, E.; Ruan, Z.; Fan, S.; Bloking, J. T.; McGehee, M. D.; Wagberg, L.; Cui, Y. *Energ. Environ. Sci.* **2013**, *6*, 513.
- (127) Cao, S.; Feng, X.; Song, Y.; Xue, X.; Liu, H.; Miao, M.; Fang, J.; Shi, L. *ACS Appl. Mater. Inter.* **2015**, DOI: 10.1021/acsami.5b02693.
- (128) Chinga-Carrasco, G.; Syverud, K. *J. Biomater. Appl.* **2014**, *29*, 423.
- (129) Kan, K. H. M.; Li, J.; Wijesekera, K.; Cranston, E. D. *Biomacromolecules* **2013**, *14*, 3130.
- (130) Torres-Rendon, J. G.; Femmer, T.; De Laporte, L.; Tigges, T.; Rahimi, K.; Gremse, F.; Zafarnia, S.; Lederle, W.; Ifuku, S.; Wessling, M.; Hardy, J. G.; Walther, A. *Adv. Mater.* **2015**, DOI: 10.1002/adma.201405873.
- (131) Fang, Z.; Zhu, H.; Yuan, Y.; Ha, D.; Zhu, S.; Preston, C.; Chen, Q.; Li, Y.; Han, X.; Lee, S.; Chen, G.; Li, T.; Munday, J.; Huang, J.; Hu, L. *Nano Lett.* **2013**, *14*, 765.
- (132) Borregaard Home Page. <http://www.borregaard.com/News/Borregaard-invests-NOK-225-million-in-a-production-facility-for-Exilva-microfibrillar-cellulose> (accessed Feb 20, **2015**).
- (133) Sappi Home Page. <http://www.sappi.com/regions/eu/service/News/Pages/Sappi-and-Edinburgh-Napier-University-discover-new-low-cost-process-to-make-nanocellulose.aspx> (accessed Feb 20, **2015**).
- (134) Thomas, A.; Antonietti, M. *Adv. Funct. Mater.* **2003**, *13*, 763.
- (135) Kelly, J. A.; Shopsowitz, K. E.; Ahn, J. M.; Hamad, W. Y.; MacLachlan, M. J. *Langmuir* **2012**, *28*, 17256.
- (136) Shopsowitz, K. E.; Hamad, W. Y.; MacLachlan, M. J. *Angew. Chem. Int. Ed.* **2011**, *50*, 10991.
- (137) Shopsowitz, K. E.; Hamad, W. Y.; MacLachlan, M. J. *J. Am. Chem. Soc.* **2012**, *134*, 867.
- (138) Nguyen, T.-D.; Kelly, J. A.; Hamad, W. Y.; MacLachlan, M. J. *Adv. Funct. Mater.* **2015**, *25*, 2175.
- (139) Qi, H.; Shopsowitz, K. E.; Hamad, W. Y.; MacLachlan, M. J. *J. Am. Chem. Soc.* **2011**, *133*, 3728.
- (140) Khan, M. K.; Giese, M.; Yu, M.; Kelly, J. A.; Hamad, W. Y.; MacLachlan, M. J. *Angew. Chem. Int. Ed.* **2013**, *52*, 8921.
- (141) Li, X.; Fan, T.; Zhou, H.; Chow, S.-K.; Zhang, W.; Zhang, D.; Guo, Q.; Ogawa, H. *Adv. Funct. Mater.* **2009**, *19*, 45.
- (142) Jiang, P.; Lin, H.; Xing, R.; Jiang, J.; Qu, F. *J. Sol-Gel Sci. Technol.* **2012**, *61*, 421.

- (143) Kim, M.-H.; Woo, H.-G. *Mater. Lett.* **2014**, *134*, 229.
- (144) Liu, X.; Gu, Y.; Huang, J. *Chem. Eur. J.* **2010**, *16*, 7730.
- (145) Zhao, J.; Gu, Y.; Huang, J. *Chem. Commun.* **2011**, *47*, 10551.
- (146) Gu, Y.; Huang, J. *J. Mater. Chem.* **2009**, *19*, 3764.
- (147) Luo, Y.; Huang, J. *Chem. Eur. J.* **2015**, *21*, 2568.
- (148) Kettunen, M.; Silvennoinen, R. J.; Houbenov, N.; Nykänen, A.; Ruokolainen, J.; Sainio, J.; Pore, V.; Kemell, M.; Ankerfors, M.; Lindström, T.; Ritala, M.; Ras, R. H. A.; Ikkala, O. *Adv. Funct. Mater.* **2011**, *21*, 510.
- (149) Korhonen, J. T.; Hiekkataipale, P.; Malm, J.; Karppinen, M.; Ikkala, O.; Ras, R. H. A. *ACS Nano* **2011**, *5*, 1967.
- (150) Iwasaki, M.; Davis, S.; Mann, S. *J. Sol-Gel. Sci. Technol.* **2004**, *32*, 99.
- (151) Sun, D.; Yang, J.; Wang, X. *Nanoscale* **2010**, *2*, 287.
- (152) Zhang, D.; Qi, L. *Chem. Commun.* **2005**, 2735.
- (153) Zhou, Y.; Ding, E.-Y.; Li, W.-D. *Mater. Lett.* **2007**, *61*, 5050.
- (154) Chen, T.; Wang, Y.; Wang, Y.; Xu, Y. *RSC Adv.* **2015**, *5*, 1673.
- (155) Cai, H.; Mu, W.; Liu, W.; Zhang, X.; Deng, Y. *Inorg. Chem. Commun.* **2015**, *51*, 71.
- (156) Vuorema, A.; Shariki, S.; Sillanpaa, M.; Thielemans, W.; Nelson, G. W.; Foord, J. S.; Dale, S. E. C.; Bending, S.; Marken, F. *Phys. Chem. Chem. Phys.* **2011**, *13*, 9857.
- (157) Galkina, O. L.; Ivanov, V. K.; Agafonov, A. V.; Seisenbaeva, G. A.; Kessler, V. G. *J. Mater. Chem. B* **2015**, *3*, 1688.
- (158) Shopsowitz, K. E.; Stahl, A.; Hamad, W. Y.; MacLachlan, M. J. *Angew. Chem. Int. Ed.* **2012**, *51*, 6886.
- (159) Huang, J.; Kunitake, T. *J. Am. Chem. Soc.* **2003**, *125*, 11834.
- (160) Li, C.; Wang, F.; Yu, J. C. *Energ. Environ. Sci.* **2011**, *4*, 100.
- (161) Sachse, A.; Cardoso, L.; Kostov, K. L.; Gérardin, C.; Belamie, E.; Alonso, B. *Chem. Eur. J.* **2015**, *21*, 3206.
- (162) Nagai, K.; Gu, Q.; Yasuda, Y.; Norimatsu, T.; Fujioka, S.; Nishimura, H.; Miyanaga, N.; Izawa, Y.; Mima, K. *J. Polym. Sci. A: Polym. Chem.* **2009**, *47*, 4566.
- (163) Zeng, M.; Laromaine, A.; Feng, W.; Levkin, P. A.; Roig, A. *J. Mater. Chem. C* **2014**, *2*, 6312.

2 Characterization

This chapter explains the physical principles of the analytical methods employed to characterize nanomaterials. Porous materials templated by cellulose nanocrystals were analyzed to reveal their chemical composition and morphological properties. Additionally, cellulose and titania nanoparticles were investigated to determine their dimensions, as well as their colloidal and thermal stabilities. Finally, the photocatalytic and photovoltaic activities of NCC-templated titania thin films were tested by performing photocatalytic degradation measurements and by measuring the current-voltage characteristics of dye sensitized solar cells.

2.1 Sorption

Gas sorption measurements are widely used for determining the surface area and pore size distribution of porous solids.¹⁻³ To examine mesoporous metal oxide materials, nitrogen sorption at the boiling point of nitrogen, 77 K, is commonly performed. The analysis is based on monitoring the physisorption of gas molecules on the surface of a porous metal oxide at constant temperature.

In a sorption experiment, a known quantity of gas is admitted to a confined volume containing the adsorbent. As adsorption takes place, the pressure falls until equilibrium is established. By gradual admission (adsorption) and withdrawal (desorption) of known amounts of gas a sorption isotherm is constructed. The isotherm reveals the amounts of adsorbed/desorbed gas as a function of the relative pressure. The relative pressure is defined as the p/p_0 ratio, where p is the equilibrium pressure and p_0 is the saturation vapor pressure.³

The shape of the sorption isotherm varies depending on the intrinsic properties of porous materials. According to the IUPAC classification, there are six main types of sorption isotherms as shown in Figure 2.1.³

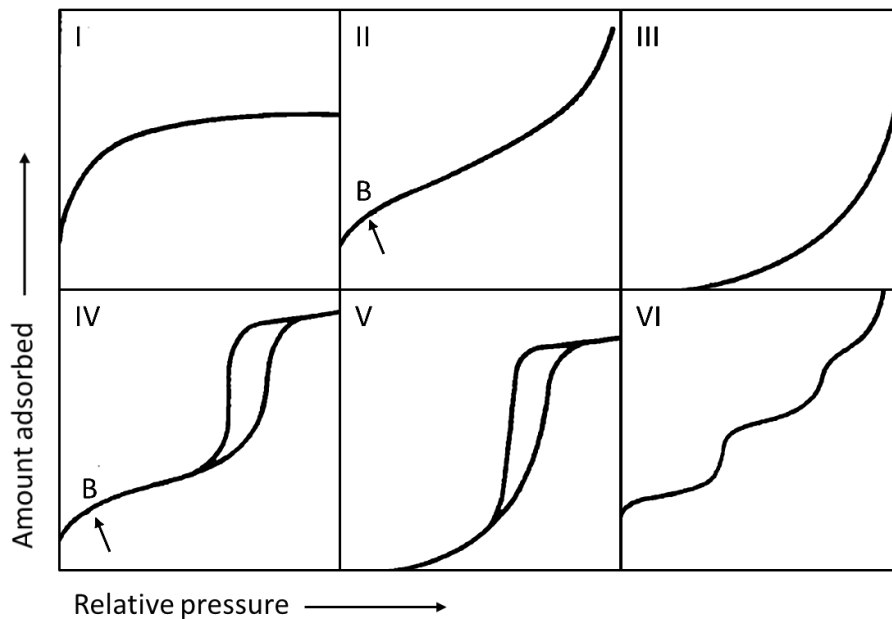


Figure 2.1. Different types of physisorption isotherms.³

The type I isotherm is characteristic for microporous (<2 nm) solids having relatively small external surfaces, for example in the case of activated carbons or molecular sieve zeolites. The type II isotherm represents unrestricted monolayer-multilayer adsorption and it is commonly obtained with nonporous or macroporous (>50 nm) adsorbents. Point B designates the stage at which monolayer coverage is complete and multilayer adsorption begins. Type III and type V curves indicate weak adsorbent-adsorbate interactions. Type III isotherm is convex over the complete p/p_0 range, whereas the type V isotherm shows a hysteresis loop and saturates at high relative pressures. The type VI isotherm represents a stepwise multilayer adsorption on a uniform non-porous surface. Isotherms of type III, V and VI are relatively rare.

Mesoporous materials (2–50 nm) provide type IV isotherms. The initial part of the curve is attributed to the monolayer-multilayer adsorption similar to the type II isotherm provided by non-porous materials. At higher relative pressures the capillary condensation in mesopores occurs, which is often accompanied by a hysteresis. The shape of a hysteresis loop reveals the specific structure of the mesopores.

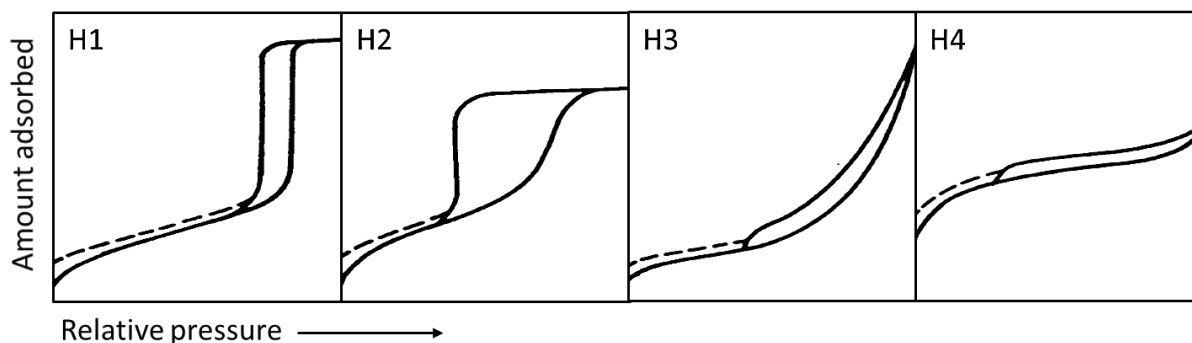


Figure 2.2. Different types of hysteresis loops.³

The narrow hysteresis loop of type H1 in Figure 2.2 is characteristic for materials with narrow pore size distributions, whereas the H2 shape reveals porous networks with less defined pore shapes, for instance in the case of ink-bottle pores (Figure 2.3). Type H3 and H4 are obtained for slit-shaped pores of aggregated plate-like particles and for narrow slit-pores of microporous materials, respectively.

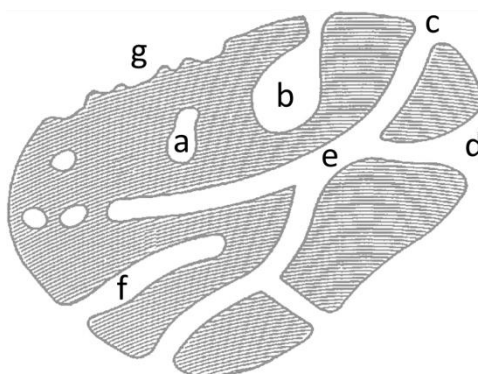


Figure 2.3. A schematic cross-section of a porous solid with different pores: (a) close, (b) open at one end (blind), ink-bottle shaped, (c) open cylindrical, (d) open funnel shaped, (e) through pores, (f) blind cylindrical pores. The roughness of the external surface is shown as (g).¹

Furthermore, the detailed analysis of sorption isotherms provides the porosity parameters, such as (i) the specific surface area, (ii) the total pore volume and (iii) the pore size distribution within the porous sample.

The specific surface area is commonly calculated by using the Brunauer-Emmett-Teller (BET) method. In this method, the surface area is estimated by multiplying the number of adsorbed molecules in the first monolayer by a cross-sectional area of the gas molecule:

$$a_s = \frac{n_m^a \cdot N_A \cdot a_m}{m_s}, \quad (2.1)$$

where a_s is the specific surface area, n_m^a is the monolayer capacity, N_A is the Avagadro constant, a_m is the area occupied by a single gas molecule in the first monolayer (the molecular cross-sectional area) and m_s is the sample mass.

The monolayer capacity n_m^a is defined by using the BET equation:

$$\frac{p}{n^a \cdot (p_0 - p)} = \frac{1}{n_m^a \cdot C} + \frac{(C-1)}{n_m^a \cdot C} \cdot \frac{p}{p_0}, \quad (2.2)$$

where n^a is the amount adsorbed at the relative pressure p/p_0 , n_m^a is the monolayer capacity and C is the BET constant related to the adsorbent-adsorbate interactions. In practice, the value of monolayer capacity n_m^a is calculated by constructing the BET plot, which is a linear relation of $p/n^a(p_0 - p)$ versus p/p_0 .

Assuming that the pores are completely filled with adsorptive at high relative pressure, it is possible to derive the total pore volume from the amounts of gas adsorbed at relative pressure close to unity.

The calculations of pore sizes in mesoporous materials are based on analysing the capillary condensation in mesopores, since the curvature of the liquid meniscus and the surface tension of the liquid condensate strongly depend on the pore geometry.

To evaluate the pore size distribution, the DFT (Density Functional Theory) methods, in particular NLDFT (Non-local DFT) are commonly applied. Although the latter method requires some knowledge of pore and surface structures, i.e., a proper choice of kernel, this approach provides good fits between theoretical and experimental data and, hence reliable values of pore sizes.⁴

The nitrogen sorption experiments with titania and hematite samples templated by NCC were performed on a Quantachrome Autosorb-1 at 77 K. The powders were degassed for 12 h at 150 °C. The surface area, mesopores volume and total pore volume were evaluated by using Quantachrome Instruments' Autosorb-1 software. The pore size distributions were obtained by the DFT method by using silica cylindrical pore and slit/cylindrical pore NLDFT equilibrium models.

Thin films of NCC-templated titania were also investigated by using Kr sorption. Kr has a low saturated vapor pressure at 77 K, therefore it can be used to assess the structural properties of very small amounts of porous materials, such as thin films.⁵ Kr sorption measurements were performed and evaluated by Dr. Jiri Rathouský at the J. Heyrovský Institute of Physical Chemistry in Prague. The analysis of Kr adsorption isotherms at the boiling point of liquid nitrogen (approx. 77 K) was carried out by using an ASAP 2010 apparatus (Micromeritics). Prior to the adsorption experiments, the sample was outgassed overnight at 200 °C.

2.2 X-Ray Diffraction

Today, 120 years after the discovery of X-rays by Röntgen, the devices based on X-ray radiation are of great importance in many application fields including analytical chemistry, medicine, microscopy and astronomy.⁶

Bragg and von Laue were the first to demonstrate that X-rays can be used to solve the crystal structure of chemical substances.⁷ They showed that the analysis of X-ray diffraction (XRD) induced by crystalline compounds can provide information about the atom arrangements in crystal lattices.

Crystalline materials consist of periodically arranged atoms with interatomic distances of the same order of magnitude as the wavelength of the X-rays, which is typically on the order of 1 Å.⁸ Therefore, when probing crystalline materials with X-rays, the atomic planes interact with X-ray radiation and affect the propagation of the radiation.⁸⁻¹⁰

In particular, when an X-ray beam of wavelength λ impinges on the crystal at an angle θ , it is scattered in different directions by the atoms of lattice planes. In some directions an increased intensity of reflected waves is observed due to the constructive interference. Figure 2.4 reveals the conditions for the constructive interference.¹⁰

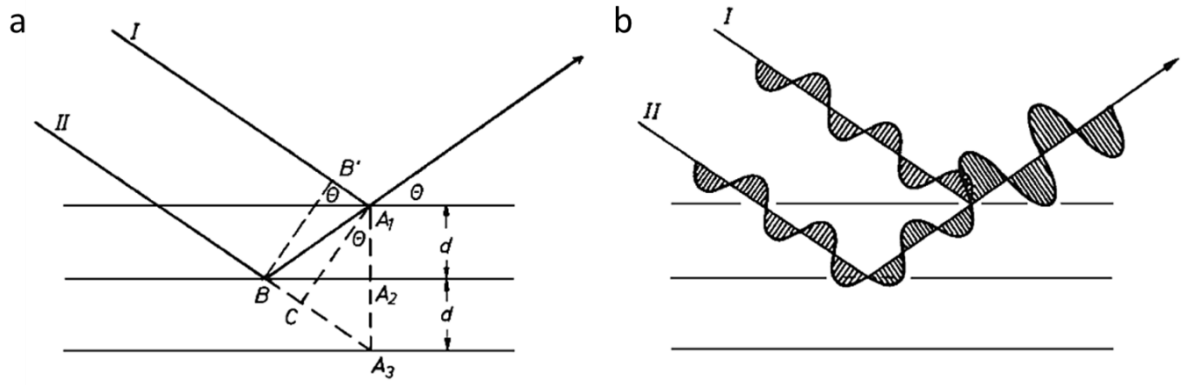


Figure 2.4. The schematic representation of X-rays impinging on the crystal planes revealing the conditions for the constructive interference (a, b).¹⁰

The parallel monochromatic X-rays I and II are reflected as A_1 and B . Their path difference Δ is equal to:

$$\Delta = BA_1 - A_1B' = BA_3 - BC = CA_3, \quad (2.3)$$

where $BA_1 = BA_3$ and $B'A_1 = BC$.

Therefore,

$$\sin\theta = \frac{\Delta}{2d} \quad (2.4)$$

The interference maximum is observed only if:

$$\Delta = n \cdot \lambda, \quad (2.5)$$

where n is an integer.

Therefore, the conditions for constructive interference can be expressed as following:

$$n \cdot \lambda = 2d \cdot \sin\theta \quad (2.6)$$

The Equation 2.6 is a Bragg's law telling that the constructive interference is observed for X-rays that are reflected from the lattice planes at the angle θ , if the path length difference between X-rays scattered from different crystals planes is an integer times n the wavelength λ .

Thus, by scanning crystalline samples with X-rays at different specular angles, one can obtain information about the interplanar atomic distance d :

$$d = \frac{n \cdot \lambda}{2 \sin \theta}, \quad (2.7)$$

where λ is the wavelength of the X-rays, θ is the Bragg angle and n is an integer.

Furthermore, the crystallite size of crystalline metal oxides can be estimated from their diffraction pattern by using the Scherrer equation:¹¹⁻¹³

$$D_{hkl} = \frac{k \cdot \lambda}{\beta_{hkl} \cdot \cos \theta}, \quad (2.8)$$

where D_{hkl} is the crystallite size in the direction perpendicular to the lattice planes, hkl are the Miller indices of the planes being analyzed, k is a numerical crystallite-shape factor generally approximated to 0.9, λ is the wavelength of the X-rays, β_{hkl} is a diffraction broadening, i.e., full width at half maximum of the X-ray diffraction signal in radians, θ is the Bragg angle.

The experimental setups for XRD analysis can be divided into different types of devices, namely working in reflection and transmission modes. Additionally, the information obtained from the diffraction patterns depends on the range of scanning angles probed during the measurements. The WAXS (Wide Angle X-ray Scattering) technique analyzes the samples in the range of about $5\text{--}80^\circ 2\theta$, whereas the SAXS (Small Angle X-ray Scattering) methods are based on screening samples at low angles of about $0\text{--}5^\circ 2\theta$. The latter method is usually employed to investigate the periodic arrangement in mesopores thin films.¹⁴

XRD measurements of nanocrystalline cellulose and NCC-templated titania thin films were performed on a Bruker diffractometer (D8 Discover, Cu-K α 1 radiation) operating in reflection mode equipped with a VÅNTEC-1 detector. Additionally, the powder samples of NCC-templated titania and hematite were analyzed by using a STOE powder diffractometer in transmission geometry (Cu-K α 1) equipped with a position-sensitive Mythen-1K detector. To define the crystal structure of the samples, the diffraction patterns were compared with the patterns from the data base provided by the International Centre for Diffraction Data (ICDD).

2.3 Electron Microscopy

Electron microscopy is one of the basic analytical tools that is capable of revealing the structure of materials on an atomistic scale.^{9,15-18}

In electron microscopy the sample is probed by a beam of accelerated electrons. The interaction of the electrons with the specimen generates different types of radiation (Figure 2.5) that can be detected and then analysed to obtain the specific information about the sample.

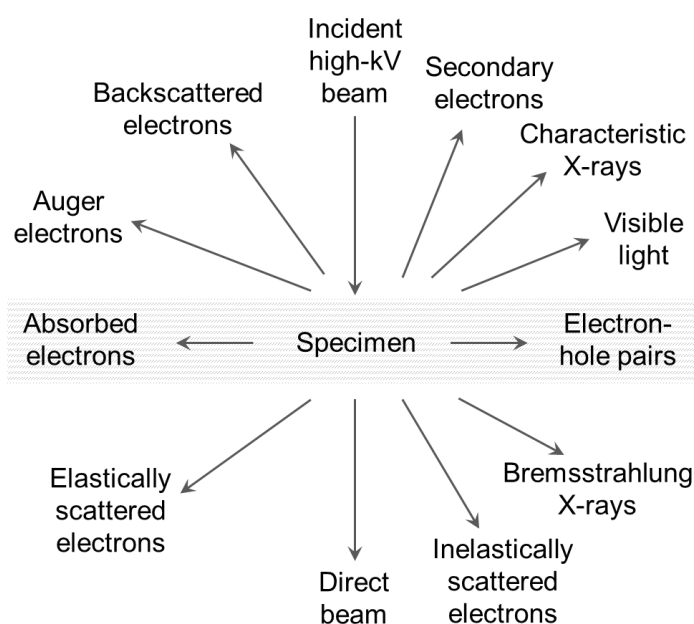


Figure 2.5. Signals generated when a high-energy beam of electrons interacts with a specimen. Most of these signals can be detected with different types of electron microscopy.¹⁵

The working principle of electron microscopy is analogous to light microscopy. However, the imaging with electrons provides resolution up to a sub-Ångstrom level, which is significantly higher than in the case of light microscopy.

Depending on the operation mode, there are two different types of electron microscopes. A transmission electron microscope (TEM) operates in the transmission mode and detects the signals transmitted through the specimen, therefore it is employed to study the structure of very thin specimens. In contrast, a scanning electron microscope (SEM) detects the signals from the sample surface, hence it is capable of

imaging the topography of thicker samples. The next chapters describe the working principles of the microscopy techniques.

2.3.1 Transmission Electron Microscopy

In a transmission electron microscope (TEM) the beam of accelerated electrons penetrates the ultra-thin sample, interacts with it and then the transmitted electrons are collected to construct the image in real space or to record an electron diffraction pattern in reciprocal space. Thus, TEM analysis can reveal the sample morphology and the phase composition at high magnifications.

High resolution imaging is achieved due to the wave-particle character of the electrons. According to the Louis de Broglie relationship the wavelengths of electrons depend on their velocity:⁹

$$\lambda = \frac{h}{mv}, \quad (2.9)$$

where λ is the wavelength, h is the Plank's constant, m is the mass and v is the velocity of the electron.

Therefore, by applying high accelerating voltages it is possible to reduce the wavelength of electrons down to the dimensions of the interatomic distances. For example, the energy of an electron beam of 50 kV corresponds to the wavelength of about 0.005 nm.¹⁸ Accelerating voltages of modern TEM devices are in the range of 100–300 kV⁹ assuring high resolution and deep penetration depth.

Figure 2.6 shows the principle of the image formation in TEM. First, the high energy electrons are generated in the electron gun placed at the top of the microscope column kept under vacuum. The common electron source is a field emission gun equipped with a tungsten tip. This source provides a coherent electron beam with small effective size of less than 0.01 μm .⁹

The electromagnetic condenser lens system controlled through the lens currents focuses the electrons on the specimen. Then the elastically scattered electrons that escape the specimen are focused by the objective lens system, also controlled by lens

currents. Afterwards, a series of additional imaging lenses including the projector lens enlarge the image to the final magnification.

The image contrast in TEM is associated with the differences in the mass-thickness of a sample, coherent diffraction or with the phase contrast resulting from the interference between diffracted beams.

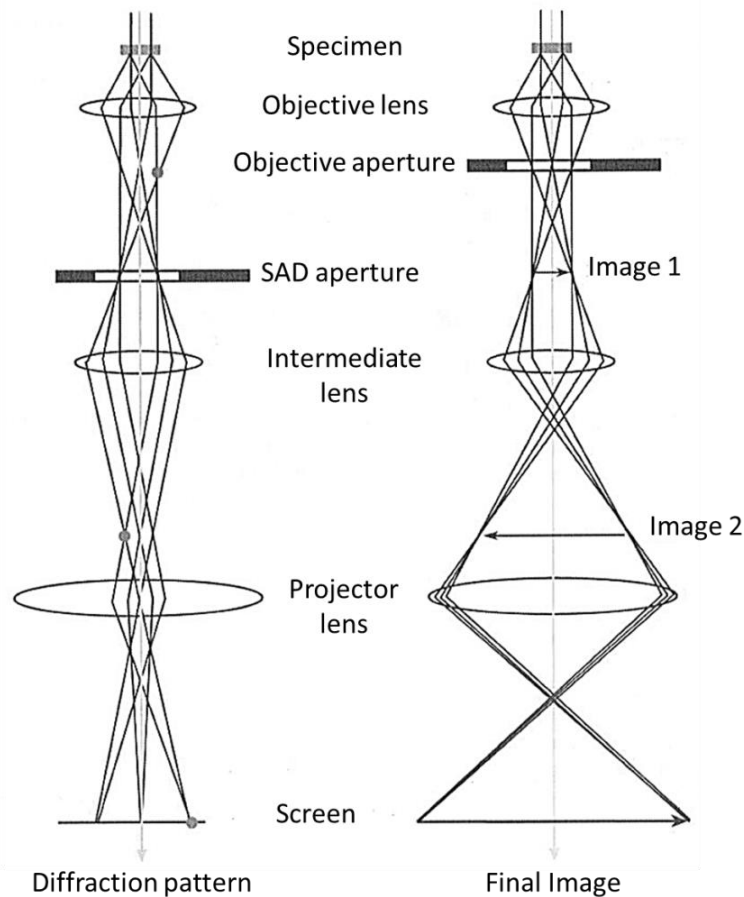


Figure 2.6. Ray-diagram of the TEM imaging system showing the projection of a diffraction pattern (left) and the image (right) onto the screen. In each case the intermediate lens selects either the back focal plane or the image plane of the objective lens as its object, respectively. SAD stands for the selected-area diffraction.¹⁵

In STEM (Scanning Transmission Electron Microscopy) the image contrast can be controlled by choosing the appropriate position of the detectors. The high-angle annular dark-field (HAADF) detector analyses the inelastically scattered electrons. The STEM-HAADF imaging provides images with enhanced mass contrast, which is especially important for the analysis of the porous morphology of nanostructured materials.⁹

In this study cellulose nanocrystals, hematite and titania porous powders and thin films have been analysed by using TEM. For the imaging of cellulose nanocrystals, a water suspension of NCC was dropped on holey-carbon coated copper grid and dried overnight. Then the samples were investigated by using a FEI Titan 80-300 transmission electron microscope equipped with a field emission gun operating at 80 kV.

For the imaging of thin films of NCC-templated titania and hematite, the coatings were removed from substrates and then placed on a holey-carbon coated copper grid. Powders of porous titania and hematite were carefully ground and dispersed in ethanol. Then suspensions were dropped on a holey-carbon coated copper grid. The imaging was performed on a FEI Titan 80-300 transmission electron microscope equipped with a field emission gun operating at 300 kV. High-resolution transmission electron microscopy (HRTEM) of the thin film cross-sections was performed at 300 kV by using STEM-HAADF mode.

2.3.2 Scanning Electron Microscopy

The operation of a scanning electron microscope (SEM) is related to that of a transmission electron microscope. However, the principal difference lies in the mechanism of image formation. The SEM image is formed by detecting electrons released from the specimen, whereas in TEM the transmitted electrons are analyzed.

In SEM the primary electrons are focused into a small-diameter electron probe that is scanned across the specimen. By scanning simultaneously in two perpendicular directions, a rectangular area of specimen is covered and a raster image is formed.

The main components of the scanning microscope are shown in Figure 2.7. The device consists of the microscope column, the signal detector system, the computer hardware and software responsible for the data processing, and the display.^{9,18}

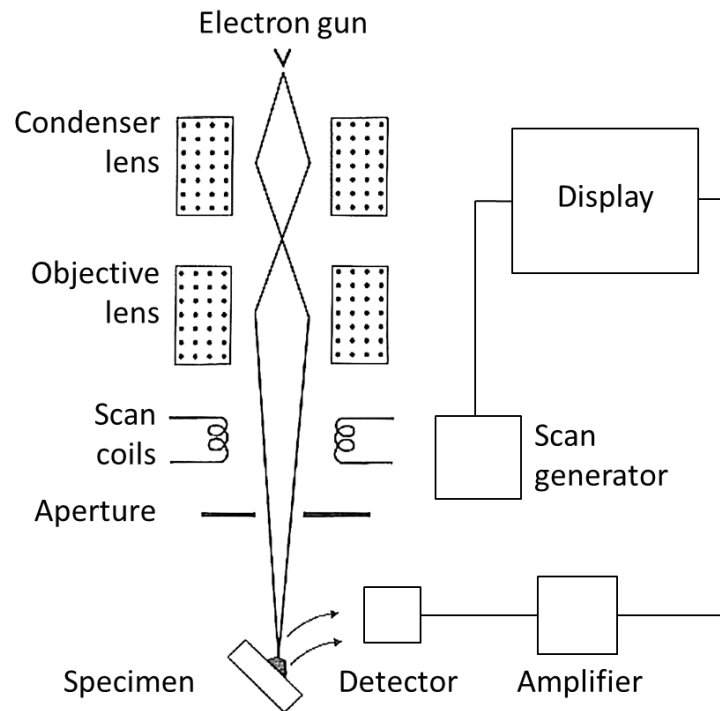


Figure 2.7. Schematic diagram showing the main components of a scanning electron microscope.¹⁶

Analogous to TEM devices, an SEM column has a source of high energy electrons and a condenser system. However, in an SEM the objective lens responsible for the ultimate resolution is above the specimen. The function of this lens is to focus the electron probe, rather than to collect the image signal like it is in a TEM. Then the focused electron beam hits the specimen and induces the radiation that is analysed by the detector.

The energy of the SEM electron beam is typically in the range of 3–30 keV.⁹ This power is sufficient to generate different types of signals in the specimen. The ability of the signals to escape the sample and to be collected depends on the sample nature and the energy of the primary electrons.

Figure 2.8 shows the schematic representation of the beam-specimen interaction volume. The inelastically scattered secondary electrons have low energy, therefore they can be detected close to the impact point of the incident beam. This is the most common signal detected in SEM. It provides information about the surface morphology of the sample.

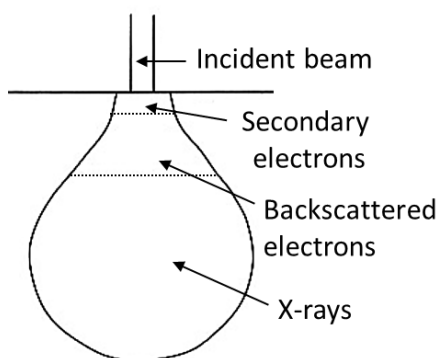


Figure 2.8. The interaction volume and the regions from which different radiation types can be detected.¹⁶

Backscattered electrons are able to escape from deeper regions of the specimen. The probability of elastic scattering of these electrons strongly depends on the sample density. Therefore, it is possible to resolve variations in mass density and atomic number by employing the backscattered electron detector.

X-rays are commonly used for the chemical analysis. The X-ray spectrum emitted by the sample can be analysed to determine the qualitative and quantitative composition of the sample.

In this study the imaging of mesoporous titania and hematite coated on conductive glass or silicon was performed on a JEOL JSM-6500F scanning electron microscope equipped with a field emission gun operating at 5 kV.

Cellulose powders were deposited on a carbon pad and sputtered with carbon in a BAL-TEC MCS 010 sputter coater prior to the analysis. The imaging was carried on a JEOL JSM-6500F scanning electron microscope equipped with a field emission gun operating at 2 kV.

The SEM analysis of cellulose nanocrystals deposited on a silicon wafer from NCC aqueous dispersions was performed on a Verios XHR 460L microscope operating at 0.5 kV.

2.4 X-ray Photoelectron Spectroscopy

X-ray photoelectron spectroscopy (XPS) is a surface-sensitive emission spectroscopy employed to analyze the elemental composition and electronic states of the elements within the sample.^{9,19}

In an XPS experiment (Figure 2.9) the X-rays hit the sample surface, the energy is absorbed by atoms, and the secondary electrons are released with the kinetic energy E_s equal to:

$$E_s = h\nu - (E_b + \phi), \quad (2.10)$$

where $h\nu$ is the energy of the incident photon, E_b is the binding energy required to bring the excited electron to the Fermi level and ϕ is the workfunction required to move the electron from the Fermi level to the vacuum level.

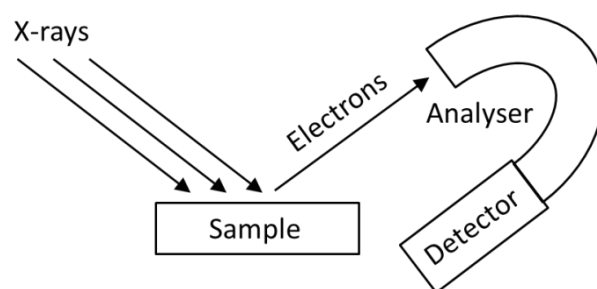


Figure 2.9. Schematic representation of the working principle of X-ray photoelectron spectroscopy.

The energies of the released electrons are measured by using an X-ray photoelectron spectrometer. Generally, prior to the actual analysis the sample surface is cleaned by argon-ion sputtering. During the measurement the photoelectron signal is generated by incident X-rays with wavelength at the order of 0.1–1 nm.⁹ The emitted electrons are analysed electrostatically with a hemispherical energy analyser and then counted by a detector.

The output of the XPS experiment is a photoemission spectrum revealing the number of counted electrons as a function of the kinetic energy. The spectrum can be used as a fingerprint of the sample. The intensive peaks in the spectrum correspond to the emission of electrons from the energy levels in the inner electron shells of sample

atoms. The background signal arises from scattered secondary electrons generated in deep layers of the sample.

The photoemission of the same atoms but in different oxidation states generates multiple peaks that can be detected and assigned, hence XPS analysis can provide information about the chemical state of the atom.

The XPS analysis was carried out in order to study the composition of NCC/iron oxide sol nanocomposites. The analysis was performed with a VSW TA10 X-ray source, providing non-monochromated Mg K_{α} radiation, and a VSW HA100 hemispherical analyzer. The samples were cleaned before measurement by 15 min Ar^{+} sputtering (VSW AS10 ion source, 1 kV, $\sim 7 \mu A$). The recorded elemental peaks were fitted with a Doniach-Sunjić line shape convoluted with a Gaussian and linear background subtraction.²⁰

2.5 Ultraviolet-Visible Spectroscopy

Ultraviolet-visible (UV-Vis) spectroscopic analysis is based on the ability of the substances to absorb light with wavelengths in the ultraviolet and visible spectral range.^{19,21} The absorption occurs due to electronic transitions in the materials promoted by the incident UV-Vis radiation.

The nature of the transitions depends on the molecular/atomic structure of the sample, hence each kind of electron transition corresponds to a particular amount of energy absorbed. $\sigma \rightarrow \sigma^{*}$ transitions are transparent in the visible region, they occur below 200 nm. $\pi \rightarrow \pi^{*}$ and $n(\text{non-bonding}) \rightarrow \pi^{*}$ absorptions are characteristic for colored substances such as chromophores and take place in the near ultraviolet and visible region.²¹ Coloring of some inorganic substances is often due to d electron transitions $d \rightarrow d^{*}$. Another type of transitions is due to charge transfer, for example in organo-metallic compounds, when an electron from an orbital of the ligand is transferred to an unfilled orbital of a metal and vice-versa.

UV-Vis spectra can reveal the structure of molecules in a compound and provide qualitative and quantitative information about the sample composition.

The UV-Vis spectrometer measures the light intensity I after passing through a sample, and compares it to the light intensity I_0 before it passes through the sample. The detected signal is the transmittance T in percent:

$$T = \frac{I}{I_0} \quad (2.11)$$

The transmittance can be converted into absorbance A :

$$A = -\log \frac{T}{100} \quad (2.12)$$

The UV-Vis active molecules or materials can be quantified by using the Beer-Lambert Law. The law reveals that the intensity of adsorbed light or absorbance A , depends on the path length l , the concentration c of the absorbing species and the absorptivity ε :

$$A = \varepsilon \cdot c \cdot l \quad (2.13)$$

Optical properties of semiconducting metal oxides are important characterization criteria, since light-induced photocatalytic reactions are governed by the ability of the catalyst to absorb light. Semiconductors absorb light below a threshold wavelength λ_g depending on the band gap energy E_g :²²

$$\lambda_g = 1240/E_g \quad (2.14)$$

Furthermore, within the semiconductor the extinction of light changes exponentially:

$$I = I_0 \cdot \exp(-\alpha \cdot l), \quad (2.15)$$

where l is the penetration distance of the light and α is the reciprocal absorption length.

The absorbance of thin films coated on transparent substrates has to be corrected to exclude the absorption of the substrate.²³ For that purpose, the supported films are measured both in transmission and reflection modes. Then the absorption is calculated as follows:

$$A = 100 - R - T, \quad (2.16)$$

where A , R , T is the amount of absorbed, reflected and transmitted light in percent (%), respectively.

In the present work UV Vis spectroscopy was performed to measure the transmittance of NCC free-standing and NCC-titania-sol composites. Additionally, thin films of NCC-templated porous titania were studied to reveal their transmittance in the UV-Vis region. The measurements were performed on a Hitachi U-3501 spectrophotometer and on a Perkin Elmer Lambda 1050 UV/Visible/NIR spectrophotometer equipped with an integrating sphere.

2.6 Nuclear Magnetic Resonance

Nuclear magnetic resonance spectroscopy (NMR) probes the magnetic properties of NMR active atomic nuclei and can reveal the quantitative and qualitative composition of a sample.^{19,24,25}

In an NMR experiment, NMR active nuclei are exposed to a magnetic field, an electromagnetic pulse is applied and the energy from the pulse is absorbed by the nuclei. The induced signal is detected and amplified to record a free-induction decay (FID). Then a computer program converts the time domain of the FID to the frequency domain and constructs an NMR spectrum.

The NMR spectrum shows the intensity of the detected signals depending on the chemical shift values. The chemical shift value is the resonance frequency expressed as the difference between the resonance frequency of the analyzed nucleus and that of a reference standard. NMR signals occur at specific resonance frequencies that depend on the magnetic properties of an atomic nucleus, hence enabling a qualitative analysis.

The magic angle spinning (MAS) NMR method is commonly employed to analyze solid samples.²⁴ A sample is rotated at a frequency of up to about 50 kHz at the magic angle $\theta_m = 54.74^\circ$ with respect to the direction of the magnetic field. The rotation modulates anisotropic spin interactions and provides a much better resolution of the powder spectra. The signal can be further enhanced by integrating crosspolarization (CP) between different nuclei in the pulse sequence.

CP-MAS ^{13}C -solid-state NMR spectroscopy was carried out in order to evaluate the crystallinity of NCC powders. ^{13}C is an NMR-active carbon isotope, thus enabling the

characterization of organic compounds. The NMR measurements were performed on a Bruker Avance 500 spectrometer equipped with a 11.75 T magnet. The spectra were recorded in the range from -250 to 450 ppm.

2.7 Thermogravimetric Analysis

Thermogravimetric analysis (TGA) belongs to the group of thermal methods that measure changes in physico-chemical properties of samples as a function of temperature.²⁶⁻²⁸ A thermal analysis provides information about different physical and chemical phenomena, such as crystalline and second-order transitions, fusion, sublimation, sorption, degradation, decomposition, solid-state reactions, etc..

The set-up for the thermal analysis consists of (i) the sample container, (ii) sensors to measure the temperature and the particular sample property (iii) the enclosure within which the conditions such as temperature, gas atmosphere etc. can be controlled, (iv) and the computer for controlling the experimental parameters and for collecting the data from the sensors (Figure 2.10)

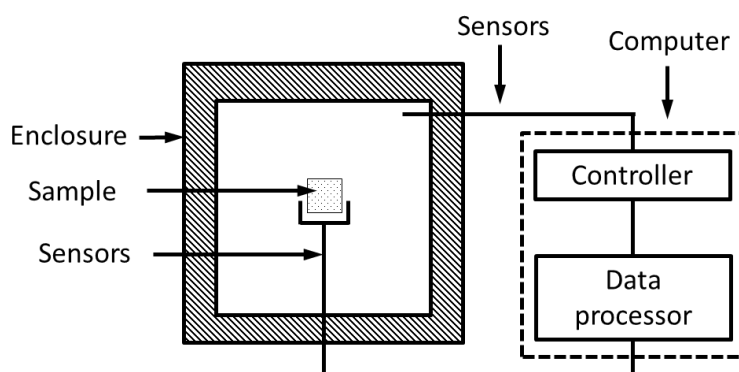


Figure 2.10. Schematic of general thermal analysis or calorimetry apparatus.²⁶

In a TGA experiment, the mass of a sample in a controlled atmosphere is recorded as a function of temperature or time while heating a sample. The measurement data are plotted as a thermogravimetric (TG) curve that shows mass or mass percentage as a function of time or temperature.

Instruments for TGA measurements are equipped with a furnace and a sensitive microbalance, referred to as a thermobalance. The balances are thermally isolated from

the oven and are able to detect changes in mass as small as 0.1 μg .²⁷ The temperature in the system is measured by thermocouples located close to the sample container. Modern devices use electronic routines of temperature control by comparing the output data of the thermocouple to the electronically stored reference.

Differential scanning calorimetry (DSC) is often used as a complementary analysis to TGA measurements. In DSC a sample and a reference are heated at a given temperature ramp, simultaneously the instrument detects the difference in heat flow between the sample and the reference. The output is the differential thermogram revealing the rate of energy change versus temperature.

DSC is a quantitative technique and provides additional information that is not accessible by TGA, for example in the case of processes occurring without a change in weight, e.g., crystalline transitions, solid-state reactions, etc..

Thermogravimetric measurements of cellulose powders and nanocellulose-iron oxide precursor composites were carried out on a Netzsch STA 440 C TG/DSC instrument with heating rates of 2 $^{\circ}\text{C min}^{-1}$ or 10 $^{\circ}\text{C min}^{-1}$ in a stream of synthetic air of about 25 mL/min.

2.8 Dynamic Light Scattering

Dynamic light scattering (DLS) is an analytical technique for measuring the size of colloidal particles in solutions by probing the solution dynamics.²⁷ The working principle of DLS is based on monitoring the changes in Raylight-scattering of light induced by the Brownian motion of the particles.

A DLS device consists of a laser source, a sample cell, a photodetector and a computer. In the experiment the laser beam is focused into a cuvette containing a dispersion of particles. With the help of the photodetector, the time-dependent light intensity fluctuations are monitored. The intensity of light fluctuations depends on particle size and particle motions, which are in turn affected by particle dimensions. Hence, the detected DLS signal can be correlated to define the translational diffusion coefficient of

the particles D_T , which provides the value of the hydrodynamic particle diameter d_n as follows:

$$d_n = \frac{k_B T}{3\pi \cdot \eta_m \cdot D_T}, \quad (2.17)$$

where k_B is the Boltzmann's constant, T is the temperature and η_m the viscosity of the medium.

The DLS measurements were performed to estimate the size of titania nanoparticles and cellulose nanocrystallites in aqueous suspensions by using a Malvern Zetasizer-Nano instrument equipped with a 4 mW He-Ne laser (633 nm) and an avalanche photodiode.

2.9 Photocatalytic Activity

The working principle of titania acting as a photocatalyst is described in Chapter 1.1.1. In general, the photocatalytic degradation tests are based on monitoring the decreasing concentration of a specific compound in the presence of a photocatalyst activated by light.²⁹⁻³²

NCC-templated porous titania thin films were employed as photocatalysts to degrade nitrogen(II) oxide and 4-chlorophenol in gaseous and liquid phases, respectively. The photocatalytic tests were performed and analyzed by Dr. Jiri Rathouský at the J. Heyrovský Institute of Physical Chemistry in Prague.

The experimental set-up for the NO photocatalytic decomposition consisted of a gas supply part, the photoreactor, and a chemiluminiscent NO-NO_x gas analyzer (Horiba ambient monitor APNA-360). The gaseous reaction mixture was prepared by mixing streams of dry air, wet air and 50 ppm NO in nitrogen, in order to obtain a final NO concentration of 1 ppm at 50% relative humidity. Prior to the photocatalytic tests, the photoreactor was purged with the NO/water vapor/air mixture without illumination until a steady NO concentration was achieved at the outlet. Then the photoreactor was illuminated by four 8 W black lights providing the UV light with 1 mW/cm² intensity, and the concentration of NO gas was monitored.

4-chlorophenol was photocatalytically degraded in a vessel 55 mL in volume, its initial concentration being 1×10^{-4} mol/L. A Sylvania Lynx-S 11 W BLB lamp irradiated the films with a UV light power achieving 1 mW cm^{-2} at the film surface. Then the aliquots of the solution in the reaction vessel were taken at regular time intervals and analyzed by high-performance liquid chromatography (HPLC).

2.10 Photovoltaic Characterization

NCC-templated titania thin films coated on conductive glass substrates were employed as active electrodes in dye-sensitized solar cells (DSC). Chapter 1.1.2 introduces the basic operation principle of a DSC, whereas the following two chapters explain in detail the fabrication and characterization procedures of DCS devices assembled from porous NCC-templated titania anodes.

2.10.1 DSC Assembly

Dye-sensitized solar cells (DSCs)³³ of a sandwich-type configuration were assembled according to the procedure developed by Ito et al.³⁴

A DSC device consisted of the following key components: (i) the active electrode made of a porous titania film coated on conductive glass and loaded with dye molecules (ii) the liquid iodine-based electrolyte and (iii) the counter electrode with a Pt layer coated on a conductive glass. These components were brought into contact by sealing the cell with polymer spacers (Figure 2.11).

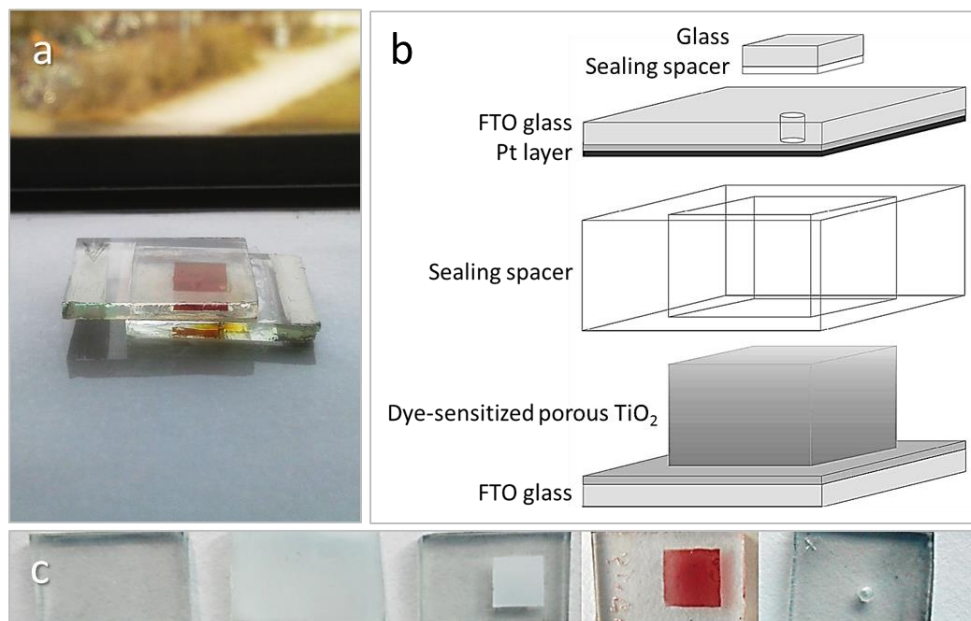


Figure 2.11. (a) Digital photo of a dye-sensitized solar cell (DSC). (b) Sandwich-type layout of a DSC.³⁴ (c) Titania electrode at different stages of preparation. From left to right: FTO substrate, porous titania coated on FTO, reduced area of titania film, dye-loaded titania film, counter Pt-electrode.

To prepare active electrodes, the precursor solution of NCC-templated titania was coated on a conductive FTO (fluorine-doped tin dioxide) glass substrate (Pilkington, TEC7) with a titania blocking layer of about 60 nm pre-deposited from the mixture of tetraethyl orthotitanate in tetrahydrofuran and hydrochloric acid (for details see description in Chapter 4.4.1). The film was heated at 500 °C to remove the templating cellulose nanocrystals and to calcine titania. Afterwards the area of porous titania was reduced to form a square with dimensions of $0.55 \times 0.55 \text{ cm}^2$.

The substrate was heated at 70 °C on a hot plate and then it was immersed into a dye solution. The sensitizer was prepared by dissolving the N719 dye powder ($[\text{RuL}_2(\text{NCS})_2]:2\text{TBA}$, where L = 2,2'-bipyridyl-4,4'-dicarboxylic acid and TBA = tetra-n-butylammonium) in a mixture of acetonitrile and tert-butyl alcohol. The porous titania film was kept overnight in the dye solution. Then the substrate was washed with acetonitrile to remove the dye residues weakly attached to the titania surface.

Counter Pt-electrodes were prepared by chemical deposition of hexachloroplatinic acid on an FTO substrate. The acid was diluted with ethanol and deposited on an FTO substrate with subsequent heating at 450 °C.

The titania and Pt electrodes were sealed on a hot plate set to 100 °C by using a 25 μm thick Surlyn spacer. Then the “sandwich” was vacuum back filled with the electrolyte through the pre-drilled hole. The electrolyte contained butylmethylimidazolium iodide, iodine, guanidinium thiocyanate and 4-tert-butylpyridine dissolved in a mixture of acetonitrile and valeronitrile with ratios described elsewhere.³⁴

Finally, the hole was sealed by Surlyn foil with a glass slide on top. Subsequently, the cell was analyzed to determine its current-voltage characteristics, as described in the next chapter.

2.10.2 *I-V* Characteristics

The performance of a DSC device can be estimated by measuring its current-voltage characteristics recorded in a solar simulator.³⁵ The data obtained during the measurement are displayed in an *I-V* curve showing the dependency of current *I* (or current density) of the applied external voltage *V*. (Figure 2.12).

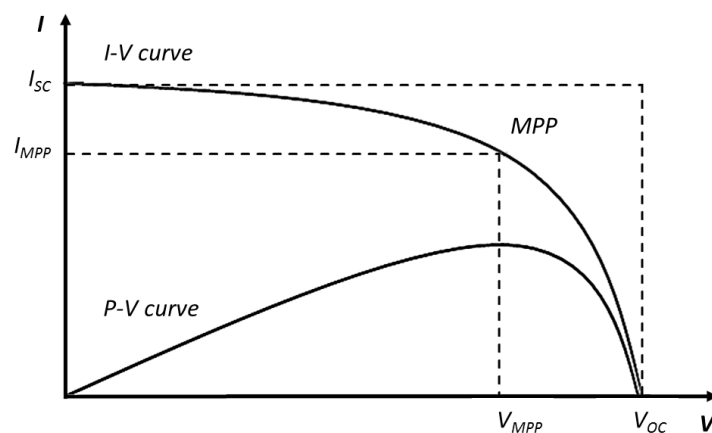


Figure 2.12. A schematic representation of *I-V*-characteristics of a solar cell under illumination, showing the maximum power point *MPP* and the corresponding current I_{MPP} and voltage V_{MPP} . The fill factor is estimated by calculating the ratio of the dashed area defined by I_{MPP} and V_{MPP} to the dashed area with the short circuit current I_{SC} and the open circuit voltage V_{OC} .

The analysis of the curve provides the critical parameters of solar cell performance, such as a short circuit current I_{SC} , the open circuit voltage V_{OC} , the fill factor *FF* and the power conversion efficiency η .

The short circuit current I_{SC} and the open circuit voltage V_{OC} are defined by the intercepts of the *I-V* curve at $V = 0$ and $I = 0$, respectively (Figure 2.12).

The fill factor describes the deviation of the solar cell power achieved at maximum power point P_{MPP} from the ideal power obtained with I_{sc} and V_{oc} . The FF is calculated as follows:

$$FF = \frac{P_{MPP}}{I_{sc} \cdot V_{oc}} = \frac{I_{MPP} \cdot V_{MPP}}{I_{sc} \cdot V_{oc}}, \quad (2.18)$$

where I_{mpp} and V_{mpp} are the current density and the voltage at the maximum power point, respectively.

The key value describing solar cell performance is the power conversion efficiency η :

$$\eta = \frac{P_{out}}{P_{in}} = \frac{P_{MPP}}{P_{in}} = \frac{I_{sc} \cdot V_{oc} \cdot FF}{P_{in}}, \quad (2.19)$$

where P_{out} is the maximum power delivered by a solar cell and P_{in} is the incident light power.

Solar cells assembled from NCC-templated titania anodes were measured on an AM 1.5 G solar simulator (Solar Light Model 16S) equipped with a 150 W xenon lamp under 100 mW/cm^2 white light illumination. The light intensity was adjusted by using a Fraunhofer ISE certified silicon reference cell.

2.11 References

- (1) Rouquero, J.; Avnir, D.; Fairbridge, C. W.; Everett, D. H.; Haznes, J. H.; Pernicone, N.; Ramsay, J. D. F.; Sing, K. S. W.; Unger, K. K. *Pure Appl. Chem.* **1994**, *66*, 1739.
- (2) Rouquerol, F.; Rouquerol, J.; Sing, K. S. W. *Adsorption by powders and porous solids, principles, methodology and applications*; Academic Press: San Diego, 1999.
- (3) Sing, K. S. W.; Everett, D. H.; Haul, R. A. W.; Moscou, L.; Pierotti, R. A.; Rouquerol, J.; Siemieniewska, T. *Pure Appl. Chem.* **1985**, *57*, 603.
- (4) Landers, J.; Gor, G. Y.; Neimark, A. V. *Colloids Surf., A* **2013**, *437*, 3.
- (5) Bartels, O.; Zukal, A. *J. Mater. Sci.* **2005**, *40*, 2603.
- (6) Kirz, J. *Science* **1995**, *270*, 934.
- (7) Hildebrandt, G. *Cryst. Res. Technol.* **1993**, *28*, 747.
- (8) *Powder Diffraction: Theory and Practice*; Dinnebier, R. E., Billinge, S. J. L., Eds.; The Royal Society of Chemistry: Cambridge, 2008.
- (9) Brandon, D.; Kaplan, W. D. *Microstructural Characterization of Materials*; Wiley: Chichester, 2008.
- (10) Borchardt-Ott, W.; Sowa, H. *Kristallographie*; Springer Spectrum: Berlin, 2013.
- (11) Holzwarth, U.; Gibson, N. *Nat. Nanotechnol.* **2011**, *6*, 534.
- (12) Alexander, L.; Klug, H. P. *J. Appl. Phys.* **1950**, *21*, 137.
- (13) Scherrer, P. *Nachr. Ges. Wiss. Göttingen* **1918**, *26*, 98.
- (14) Fratzl, P. *J. Appl. Crystallogr.* **2003**, *36*, 397.
- (15) Williams, D. B.; Carter, C. B. *Transmission electron microscopy: a textbook for materials science*; Plenum Press: New York, 1996.
- (16) Goodhew, P. J.; Humphreys, J.; Beanland, R. *Electron Microscopy and Analysis*; Taylor & Francis: London, 2001.
- (17) Goldstein, J. I.; Newbury, D. E.; Echlin, P.; Joy, D. C.; Lyman, C. E.; Lifshin, E.; Sawyer, L.; Michael, J. R. *Scanning electron microscopy and x-ray microanalysis*; Kluwer Academic/Plenum Publishers: New York, 2003.
- (18) Egerton, R. F. *Physical principles of electron microscopy: an Introduction to TEM, SEM, and AEM*; Springer Science+Business Media, Inc: Boston, 2005.
- (19) Atkins, P. W.; De Paula, J. *Atkins' Physical Chemistry* Oxford University Press: Oxford, 2010.
- (20) Doniach, S.; Sunjic, M. *J. Phys. C: Solid State Phys.* **1970**, *3*, 285.
- (21) Anderson, R. J.; Bendell, D. J.; Groundwat, P. W. *Organic Spectroscopic Analysis*; Royal Society of Chemistry: Cambridge, 2004.
- (22) Hagfeldt, A.; Graetzel, M. *Chem. Rev.* **1995**, *95*, 49.
- (23) Klahr, B. M.; Martinson, A. B. F.; Hamann, T. W. *Langmuir* **2011**, *27*, 461.

- (24) Levit, M. H. *Spin dynamics: basics of Nuclear Magnetic Resonance*; Wiley, Chichester, 2008.
- (25) Mitchell, T. N.; Costisella, B. *NMR-From Spectra to Structures*; Springer: Berlin, 2004.
- (26) *Principles of thermal analysis and calorimetry*; Heines, P. J, Ed.; Royal Society of Chemistry: Cambridge, 2002.
- (27) Skoog, D. A.; Holler, F. J.; Crouch, S. R. *Principles of instrumental analysis*; Thomson: Belmont, 2007.
- (28) Coats, A. W.; Redfern, J. P. *Analyst* **1963**, *88*, 906.
- (29) Fujishima, A.; Rao, T. N.; Tryk, D. A. *J. Photochem. Photobiol., C* **2000**, *1*, 1.
- (30) Hoffmann, M. R.; Martin, S. T.; Choi, W.; Bahnemann, D. W. *Chem. Rev.* **1995**, *95*, 69.
- (31) Linsebigler, A. L.; Lu, G.; Yates, J. T. *Chem. Rev.* **1995**, *95*, 735.
- (32) Hashimoto, K.; Irie, H.; Fujishima, A. *J. Appl. Phys.* **2005**, *44*, 8269.
- (33) O'Regan, B.; Gratzel, M. *Nature* **1991**, *353*, 737.
- (34) Ito, S.; Murakami, T. N.; Comte, P.; Liska, P.; Grätzel, C.; Nazeeruddin, M. K.; Grätzel, M. *Thin Solid Films* **2008**, *516*, 4613.
- (35) Kalyanasundaram, K. In *Dye-sensitized solar cells*; Kalyanasundaram, K., Ed.; EPFL Press: Lausanne, 2010.

3 Extraction of Cellulose Nanocrystals

This chapter describes the extraction of cellulose nanocrystals employed as sacrificial templates in the synthesis of mesoporous materials presented in the following chapters.

3.1 Introduction

Cellulose nanocrystals have been known since the late 40ies of the last century, when Ranby reported for the first time the aqueous colloids of crystalline “micelles” isolated from native cellulose.¹ The stable colloidal dispersions were achieved by boiling wood and cotton in sulfuric acid, leading to a partial destruction of pristine cellulose. The straightforward acid hydrolysis of hierarchically organized plant celluloses (Figure 3.1) was successfully employed to extract cellulose crystals in several further studies.²⁻¹³

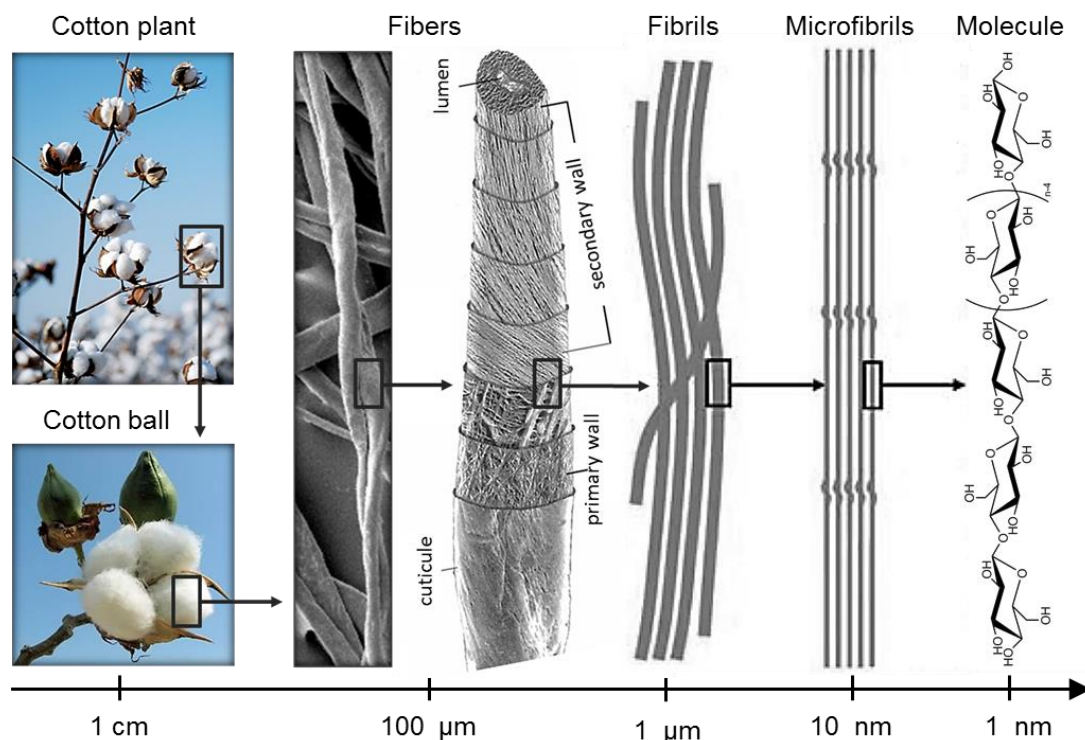


Figure 3.1. The hierarchical structure of cotton. Adapted from Ref.¹⁴

The success of this method is based on the fact that cellulose fibers initially consist of low-ordered (amorphous) regions and highly ordered domains of cellulose nanocrystals. The latter ones are stable and they can sustain the hydrolysis, whereas the amorphous regions are less resistant and therefore they are easily decomposed by strong acids (Figure 3.2).^{15,16}

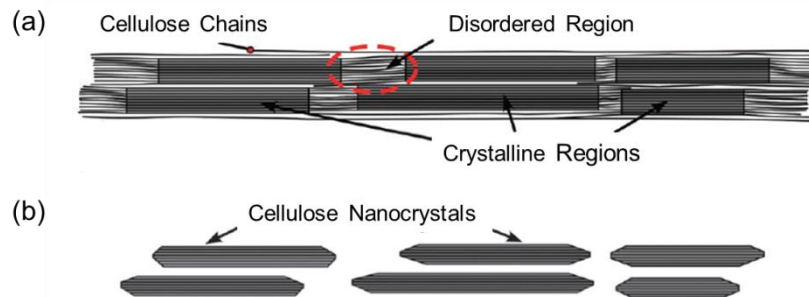


Figure 3.2. (a) Schematic representation of a cellulose microfibril showing the alternation of crystalline and amorphous domains. (b) Cellulose nanocrystals after dissolving the disordered regions by acid hydrolysis.¹⁶

The properties of the crystalline material obtained *via* hydrolysis depend on hydrolysis conditions and to a large extent on the nature of the initial cellulose. The key parameters here are the phase composition and crystalline quality, namely content, distribution and dimensions of crystalline nanodomains in pristine cellulose. Wood pulps, plants, bacterial cellulose, marine animals, algae and microcrystalline celluloses have been demonstrated to be suitable starting materials for the NCC isolation.^{17,18} As the degree of crystallinity, crystallite sizes and distribution of crystalline regions vary for these different celluloses, the dimensions of the isolated nanocrystals depend directly on the source material.^{16,18} Cotton, wood and microcrystalline cellulose provide crystals with nanometer-scale lengths, whereas celluloses derived from tunicin, bacteria and algae typically have a higher degree of polymerization and longer crystalline regions, hence providing cellulose whiskers up to several μm in length.^{18,20}

Although many different types of acids can be used for cellulose hydrolysis, hydrochloric and sulfuric acids are among the most effective ones. The acid penetrates into cellulose fibers and breaks down the glycosidic bonds, so that the length of the cellulosic polymer chains decreases. The hydrolysis route involves the protonation of glucosidic oxygen (reaction 1 in Figure 3.3) or cyclic oxygen (reaction 2 in Figure 3.3), followed by splitting of glucosidic bonds induced by the addition of water.^{21,22} In

contrast to hydrochloric acid, sulfuric acid additionally results in sulfonation of cellulose.^{1,5} Sulfate ester groups ($-\text{OSO}_3^-$) grafted on the surface induce negative charging of cellulose nanocrystals, hence promoting their colloidal stability. Due to this effect, the hydrolysis with sulfuric acid remains the most popular method for the preparation of nanocrystalline cellulose easily dispersible in water.

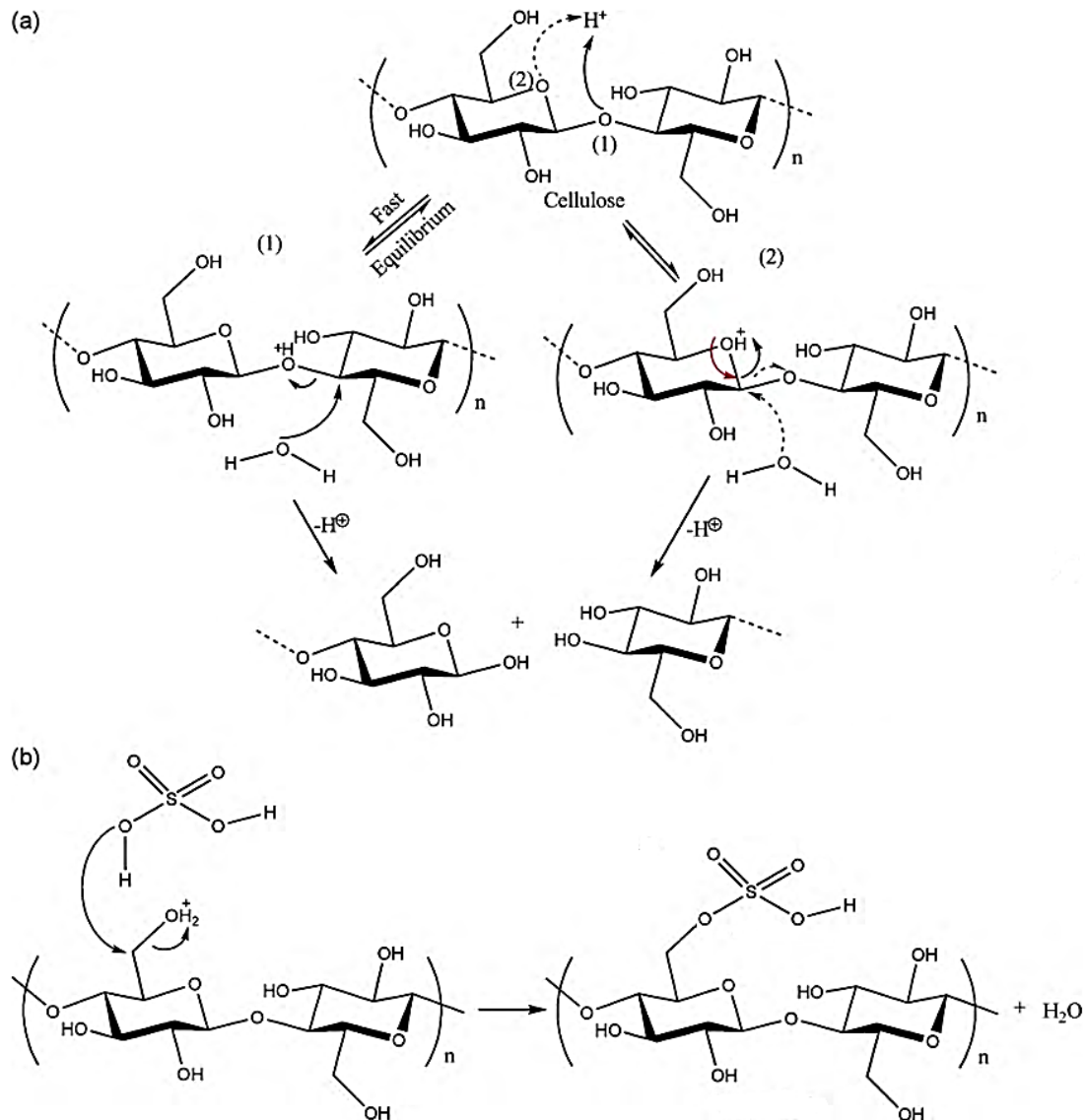


Figure 3.3. (a) Schematic illustration of the mechanism of cellulose disintegration during acid hydrolysis. (b) Esterification of cellulose due to the hydrolysis with sulfuric acid.²¹

The hydrolysis conditions, namely reaction time, temperature, type and concentration of the acid, as well as the acid-to cellulose ratio affect the properties of the released nanocrystals^{2,4,23-27} and define the reaction yield.^{28,29} Dong et al.⁷ have investigated hydrolysis of filter paper Whatman No. 1 in 64% sulfuric acid and established that the

optimal hydrolysis temperature and time correspond to about 45 °C and 60 min, respectively. They found that at lower temperatures the reaction yield decreases, while longer hydrolysis times reduced the dimensions of the released crystals. Since every type of cellulose requires thorough optimization of the hydrolysis conditions, we have modified the procedure suggested by Dong et al. and adapted it for available cellulose sources.

This chapter focuses on the preparation of cellulose nanocrystals by hydrolysis of different cellulose materials with sulfuric acid. First, different bulk celluloses are characterized and explored for their use as an NCC (nanocrystalline cellulose) source. Then the detailed investigation of cotton hydrolysis in sulfuric acid is discussed. Finally, we demonstrate the effect of post-hydrolysis fractionation on the crystallinity and mean dimensions of the cellulose nanocrystals.

3.2 Results and Discussion

3.2.1 Cellulose Sources

We have explored different bulk celluloses for their use as a starting cellulose source for the isolation of nanocrystalline cellulose (NCC). In particular, we have employed celluloses originating from wood, cotton and commercial microcrystalline cellulose. Hardwood (Lwarcel) and softwood (Domsjo and ASPA) Kraft pulp sheets, cotton linters and microcrystalline cellulose (Avicel® PH-101) are commercial products commonly applied in paper, textile and pharmaceutical industries, respectively. These celluloses have been purified by various chemical pretreatments of pristine biomasses.

Wood pulp is fabricated by the Kraft process and bleaching to remove non-cellulosic impurities, for example lignin. Avicel® is a pure depolymerized microcrystalline cellulose manufactured from wood pulp by deep hydrolysis with mineral acids. Cotton is a natural fiber that grows around the seeds of cotton plants and consists mainly of pure cellulose.

SEM images in Figures 3.4 and A3.1 in the Appendix show the morphology of different types of cellulose materials. Cotton linters and Avicel® feature fibrous morphology with

fibers of several micrometers in size (Figure A3.1 in the Appendix). SEM images at higher magnification reveal that the surface of cotton fibers is composed of very fine elongated features of about 20 nm in diameter (Figure 3.4 a). In contrast, the fibers of Avicel® at similar magnification appear more dense, being composed of large fibers of about 500 nm in width (Figure 3.4 b). The surface of wood pulp sheets indicates the presence of some fine elongated substructures (Figure 3.4 c), however they are much less pronounced than in the SEM images of the cotton linters.

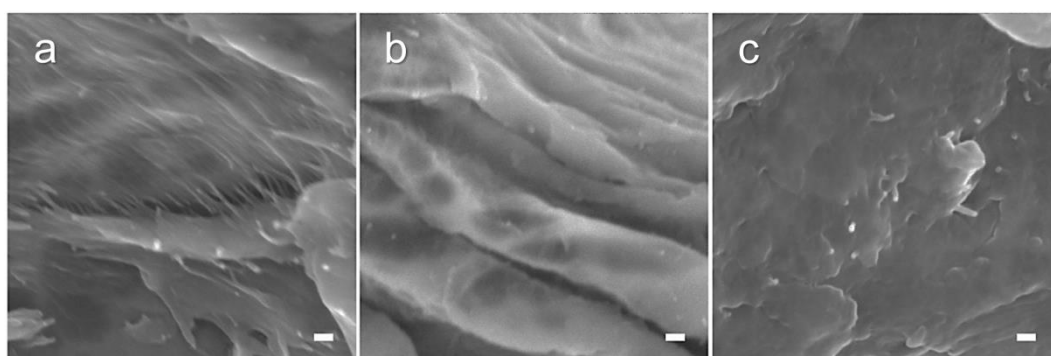


Figure 3.4. SEM images of bulk celluloses: (a) cotton linters, (b) microcrystalline cellulose Avicel®, (c) dried soft wood pulp (Domsjo). The scale bars correspond to 100 nm.

The XRD analysis shown in Figure 3.5 reveals the presence of I_{β} cellulose for all the cellulose sources. However, the shapes of the patterns vary for different cellulose types, which points to the different contents and dimensions of crystalline domains in the samples. The proportion of crystalline and amorphous cellulose in the bulk celluloses can be estimated by using the peak-height method suggested by Segal et al.^{30,31} In this method, the crystallinity defined as the crystallinity index γ_{XRD} is determined from the ratio of the minimum signal intensity at ca. $18^{\circ} 2\theta$ arising from amorphous cellulose (I_{18}) to the intensity of the most intensive cellulose XRD reflection at ca. $22.7^{\circ} 2\theta$ ($I_{22.7}$) corresponding to the crystalline cellulose (Equation 3.1).

$$\gamma_{XRD} = \left(\frac{I_{22.7} - I_{18}}{I_{22.7}} \right) \times 100\% \quad (3.1)$$

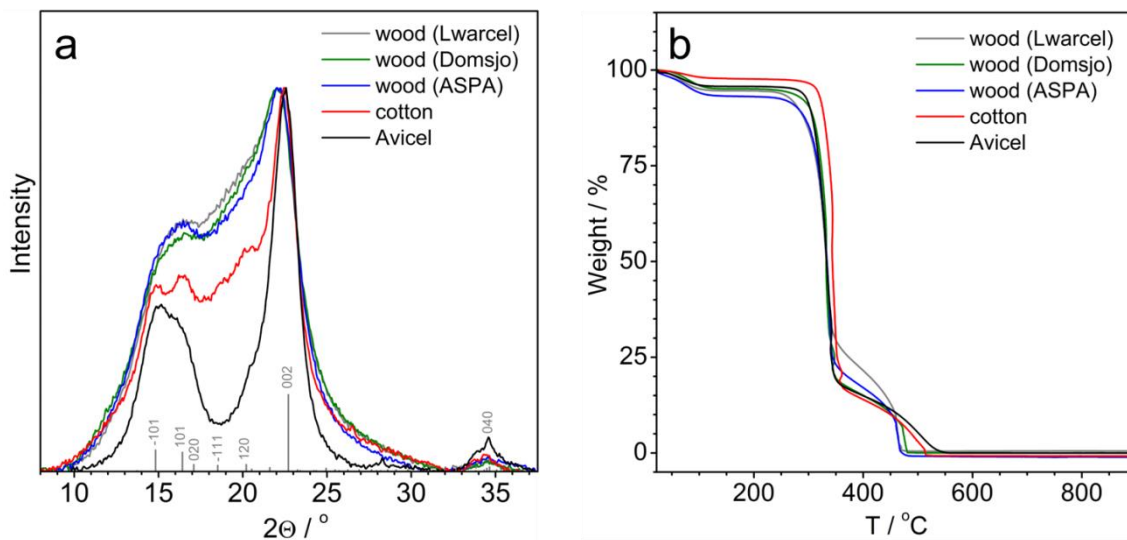


Figure 3.5. X-ray diffraction patterns (a) and TGA curves (b) of microcrystalline cellulose, wood pulps and cotton. The assigned reflections correspond to the I_β cellulose (ICDD pattern 00-060-1502). The background-subtracted diffraction patterns were normalized to the most intense reflections (the original patterns are shown in Figure A3.2 in the Appendix).

The crystallinity derived from XRD patterns in Figure 3.5 is of about 35%, 56% and 87% for wood pulps, cotton and microcrystalline cellulose, respectively. The microcrystalline cellulose shows the highest crystallinity compared to the other cellulose sources, whereas the wood pulps are the least crystalline. The cotton linters have a moderate crystallinity, which can be advantageous for the NCC extraction, because amorphous regions decompose in acid and facilitate the release of crystals, whereas a high content of crystalline domains is necessary to achieve high reaction yields.

The difference in the morphology and crystallinity of the above bulk celluloses indicates that the disintegration of these celluloses results in nanocrystalline celluloses of different quality. Next we compare the nanocrystalline cellulose (NCC) extracted from different cellulose sources by acid hydrolysis at similar conditions.

3.2.2 Acid Hydrolysis

Typically the isolation of nanocellulose from bulk cellulose consists of three main steps: (i) purification of pristine cellulose (ii) dissolution of amorphous regions by hydrolysis and (iii) washing of the remaining crystalline phase.¹⁷ We have performed the acid hydrolysis based on a modified procedure developed by Dong et al.⁶ We mixed different bulk celluloses with 64% H_2SO_4 at constant ratios of 1:8.75 g/mL and heated the mixtures under reflux at similar conditions (Table 3.1).

Table 3.1 Hydrolysis conditions, reaction yields and properties of the final dispersions of the nanocellulose extracted from wood and cotton. The hydrolysis was performed with 64% sulfuric acid and 1:8.75 g/mL cellulose-to acid ratio

Cellulose source	Hydrolysis			NCC dispersion		
	$\tau_1@RT, h^a$	$T, ^\circ C$	$\tau_2@T, min^b$	pH	$c, wt \%^c$	$Yield, \%^d$
Cotton	1	58	20	2.5	2.0	19
Wood (Domsjo)	1	45	25	2.4	2.6	10
Wood (ASPA)	1	45	25	2.3	4.7	14

^a stirring time

^b hydrolysis time

^c NCC concentration in wt % after washing

^d yield with respect to the initial amount of bulk cellulose

We found that when hydrolysed the cellulose-acid mixture changes its color from white to yellow-brownish or ivory, as shown in Figure 3.6-a.

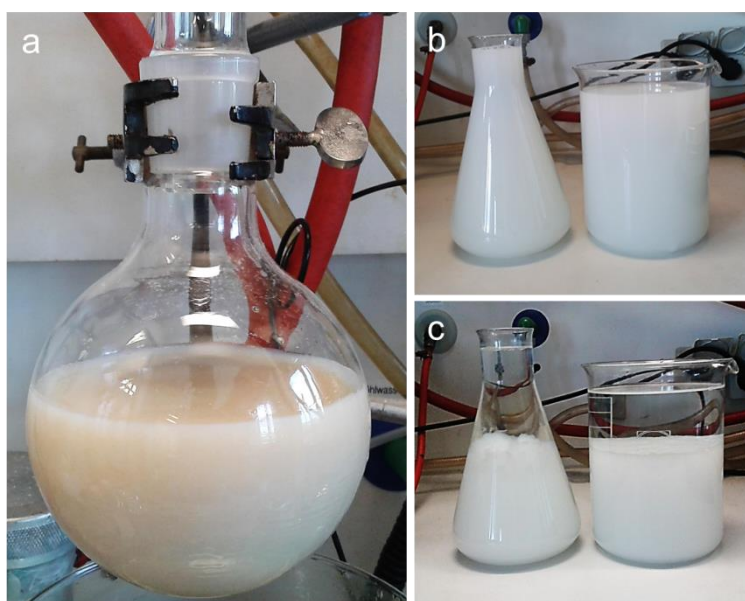


Figure 3.6. Digital images showing the extraction of cellulose nanocrystals from cotton linters. (a) A cellulose suspension after the hydrolysis with 64% sulfuric acid for 45 min at 55 °C. (b) A ten-fold diluted cellulose suspension in water. (c) Phase separation of the suspension after ca. 15 h.

To stop the hydrolysis the suspension is diluted with a tenfold amount of deionized water and left overnight to sediment the NCC-containing fraction (Figure 3.6-b, c, respectively). Later, the upper liquid phase is decanted and the NCC-rich lower phase is washed with water via successive centrifugation.

We have observed that after each subsequent washing by repeated centrifugation, the supernatants appear more and more turbid (Figure 3.7 a).

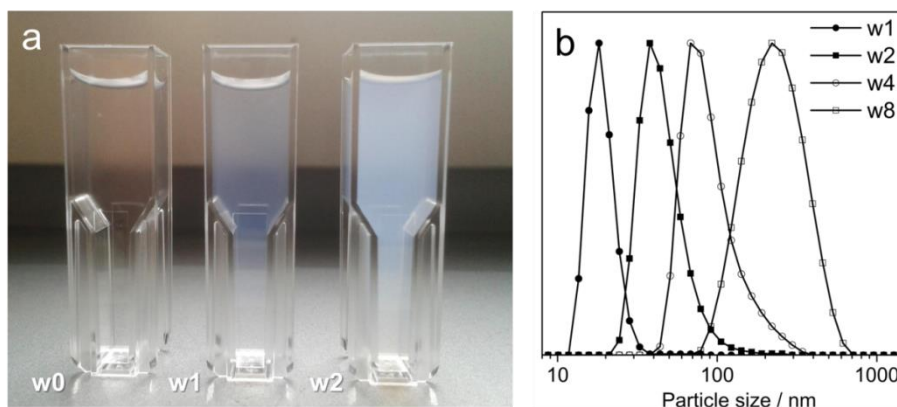


Figure 3.7. (a) Digital photo and normalized DLS data (b) of the supernatants obtained after the first centrifugation (w0) and after subsequent washing for 1–8 times (w1–w8) applied to aqueous dispersion of cellulose nanocrystals.

Moreover, the DLS signal shifts right (Figure 3.7-b), indicating the enlargement of particle dimensions in the solutions. The size of the particles after eight washing steps is in the range of several hundreds of nanometers, which largely exceeds the size of the single cellulose nanocrystals. These observations suggest the high sensitivity of NCC colloidal stability to ionic strength and to pH of the solution. However, we note that the common DLS analysis can only provide a rough estimate of the NCC size due to the non-spherical shape of the crystals.

We have applied only two washing cycles for all subsequent experiments, since continuous washing of nanocrystals results in significant losses of the product. NCC dispersions described in Table 3.1 were concentrated via rotary evaporation to achieve concentration of about 10 wt %. Afterwards, we cast the dispersions to dry at room temperature, in order to form about 80 μm thick NCC free-standing films that were then pulverized for the XRD analysis.

The XRD patterns of NCCs in Figure 3.8-a show distinct and sharp reflections and only a minor presence of broad amorphous background characteristic for disordered cellulose. The shapes of the NCC patterns indicate a significant improvement of crystallinity of hydrolyzed samples compared to the pristine celluloses (Figure 3.8-a vs. Figure 3.5-a). The main cellulose XRD reflection at about $22.7^\circ 2\theta$ in Figure 3.8-a becomes more prominent, whereas the amorphous background at $18^\circ 2\theta$ diminishes. Therefore, the

isolated crystals show a higher crystallinity index than bulk celluloses. In quantitative terms the achieved crystallinity values are 53%, 70% and 87% for the hydrolysed wood pulps ASPA, Domsjo and cotton, respectively.

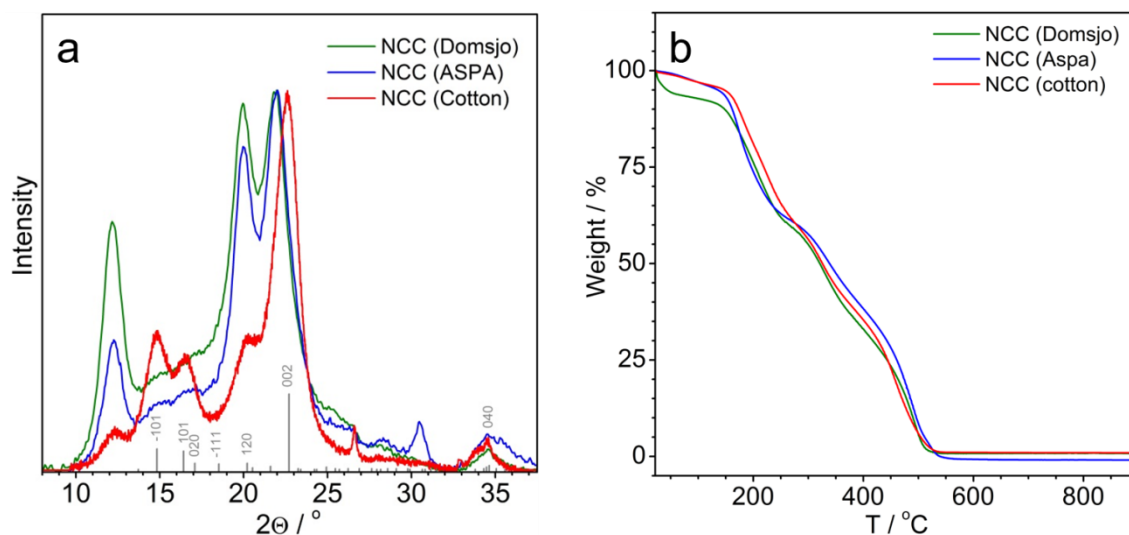


Figure 3.8. X-ray diffraction patterns (a) and TGA curves (b) of nanocrystalline cellulose obtained from soft wood pulps and cotton. The assigned reflections correspond to the I_β cellulose (ICDD pattern 00-060-1502). The background-subtracted diffraction patterns were normalized to the maximum reflections (the original patterns are shown in Figure A3.3 in the Appendix).

The change of the shape of the TGA curve also confirms the successful extraction of crystalline material from pristine celluloses (Figure 3.8-b). The crystalline cellulose is more resistant to thermal degradation, therefore it demonstrates a more gradual mass loss than pristine celluloses (Figure 3.5-b). The degradation curves of NCCs in Figure 3.8-b are consistent with the previously recorded TGA of nanocrystalline cellulose.^{21,32}

To sum up, the above initial results show that cotton and wood pulp sheets are suitable sources for the NCC preparation. Avicel® has initially a high crystallinity (based on XRD, TGA and SEM analysis), hence extraction of distinct crystalline nano-species from this material is rather challenging. Therefore, in the following section we will focus on the optimization of nanocellulose isolation from wood pulps and cotton linters.

3.2.3 Reaction Yield and Crystallinity

To study the effect of hydrolysis in more detail, we have hydrolysed cotton and wood pulps at different temperatures and reaction times, while keeping the acid

concentration, cellulose to-acid ratio and washing protocol identical for all the samples (Table 3.2).

Table 3.2. Reaction yields and crystallinity γ_{XRD} of nanocrystalline cellulose depending on the cellulose source, reaction time τ and temperature T . The hydrolysis was performed with 64% sulfuric acid and 1:8.75 g/mL cellulose-to acid ratio

Sample	$\tau_1@RT$, h	T , °C	$\tau_2@T$, min	Yield, % ^a	γ_{XRD} , %
NCC cotton-1	-	45	25	7	77
NCC cotton-2	17	45	15	10	80
NCC cotton-3	-	45	40	13	81
NCC cotton-4	1	58	20	19	84
NCC cotton-5	-	45	60	6	86
NCC cotton-6	1	60	60	13	86
NCC cotton-7	1	55	25	14	90
NCC cotton-8	-	55	30	nd ^b	nd
NCC cotton-9	-	60	60	nd	nd
NCC wood Domsjo-1	1	45	25	10	70
NCC wood Domsjo-2	1	55	15	4	80
NCC wood ASPA-1	1	45	25	14	80
NCC wood ASPA-2	1	55	25	4	85

^a yield with respect to the initial amount of bulk cellulose.

^b not determined; starting suspensions for fractionation (see Chapter 3.2.4)

Figure 3.9 shows XRD patterns of the nanocrystalline cellulose extracted by using different hydrolysis parameters.

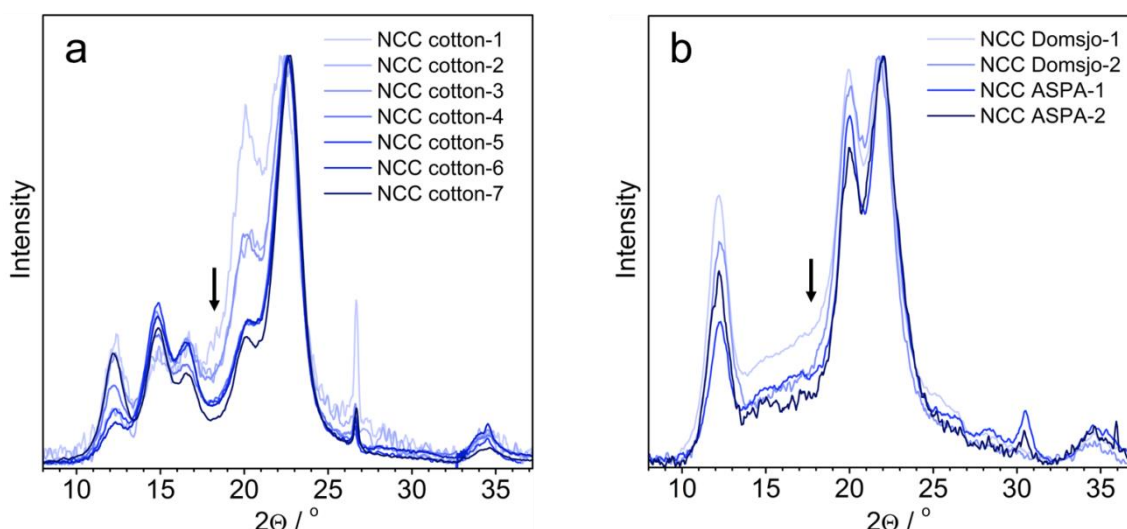


Figure 3.9. XRD patterns of NCC prepared from cotton (a) and dry soft wood pulps (b) at different hydrolysis conditions described in Table 3.2. The arrows point to the decreasing signal at ca. $18^\circ 2\theta$ corresponding to amorphous cellulose.

The variation of the shapes of the patterns indicates the change in the crystalline quality of the resulting celluloses. We found that temperature increase and longer hydrolysis times favor better disintegration of the amorphous cellulose. The most significant crystallinity increase, namely the noticeable reduction of amorphous background at ca. $18^\circ 2\theta$ has been observed for the sample NCC cotton-7 that was hydrolysed at 55°C for 25 min (Figure 3.9, Table 3.2).

The XRD data imply that more drastic hydrolysis conditions, i.e. higher temperatures and longer reaction times in the ranges examined, are more effective for the extraction of crystalline cellulose. However, a further increase of hydrolysis time and temperature can negatively affect the yield of the reaction or the crystallinity.

As an example, Figure 3.10 shows the dependence of the yield on the reaction time, revealing that both short and long hydrolysis times result in rather low yields. Thus, there is an optimum hydrolysis time for the isolation of nanocellulose species assuring high hydrolysis yields.

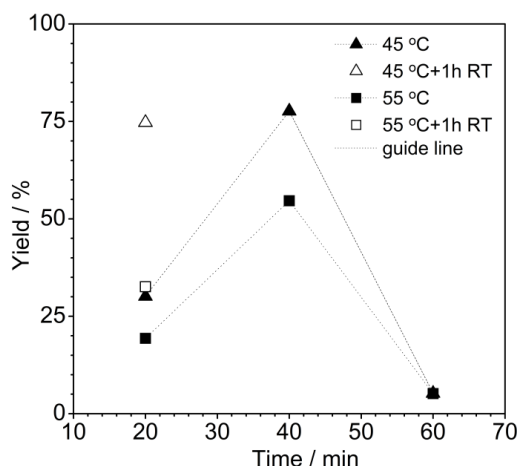


Figure 3.10. Reaction yields of the hydrolysis of dry hard wood pulp (Lwarcel) with 64% sulphuric acid and cellulose-to-acid ratio 1:8.75 g/mL depending on hydrolysis time and reaction temperature.

We note that the reaction yields are calculated as a ratio of cellulose after hydrolysis and washing procedure with respect to the amount of pristine cellulose, without considering the cellulose crystallinity. Although the hard wood pulp demonstrates very high reaction yields of up to 75% (Figure 3.10), the quality of the crystals extracted from this type of wood is lower compared to cotton. The hardwood cellulose is generally a less popular source for isolation of nanocrystalline cellulose than softwoods, since it is more complex and heterogeneous in structure and it has shorter fibers and a more rigid constitution.³²

To sum up, the conditions of the hydrolysis reaction play an important role in NCC extraction, since they affect the NCC quality and the reaction yield. The best results regarding the NCC crystallinity and the reaction yield were obtained for cotton NCC hydrolysed at RT for 1 h followed by heating at temperatures of 45–55 °C for about 25 min. We note that if the stirring time prior the hydrolysis is reduced to 20 min, the hydrolysis at elevated temperatures can be prolonged up to 45 min. Typically the hydrolysis should be stopped as soon as large cellulose aggregates dissolve and the color of the reaction mixture changes to ivory white, as shown in Figure 3.6-a.

3.2.4 Fractionation

Fractionation by differential centrifugation is a well-known approach to obtain colloidal dispersions of increased uniformity. We have performed differential centrifugation³⁴ of

NCC aqueous dispersions prepared by different hydrolysis routes, in order to decrease the contents of aggregates and narrow the size distribution of the cellulose crystals. Figure 3.11 shows the fractionation procedures employed for the NCC dispersions.

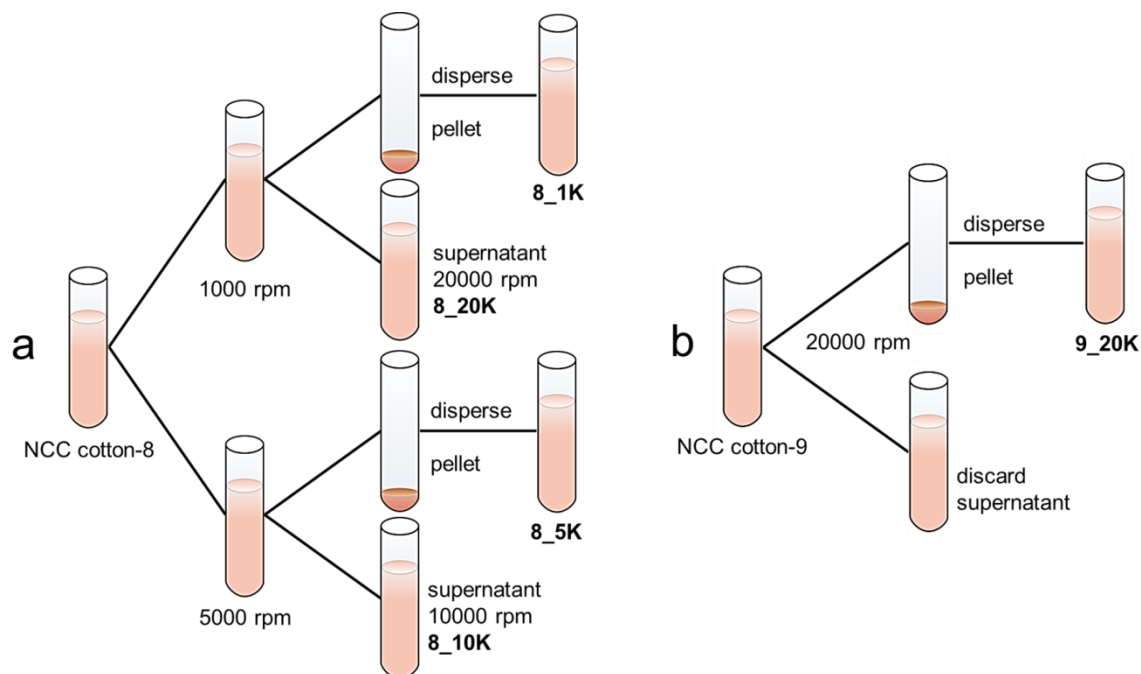


Figure 3.11. Schematic representation of the differential centrifugation of hydrolysed and washed cotton dispersions: NCC cotton-8 (a) and NCC cotton-9 (b). The sample notation indicates the NCC batch and the final centrifugation speed, e.g., 8_1K stands for the NCC cotton-8 dispersion and 1000 rpm centrifugation speed, respectively.

The NCC batch assigned as NCC cotton-8 was extracted at relatively mild hydrolysis conditions, namely at lower temperature and shorter times compared to the batch assigned as NCC cotton-9 (Table 3.2). After the hydrolysis, both dispersions were diluted and washed as previously described.

The fractionated NCC solutions were analysed by using electron microscopy to evaluate the size of the crystals in each fraction. XRD, NMR, IR and TGA analysis revealed the crystallinity and thermal stability of the as-fractionated nanocellulose.

Table 3.3 shows average dimensions of the nanocrystalline cellulose calculated from TEM images. Cellulose crystals appear in the TEM images in Figure 3.12 as elongated bundled species of around 8 to 12 nm in width and of about 100–170 nm in length, depending on the NCC fraction.

Table 3.3. Effect of fractionation on the mean dimensions (width D and length L) of cellulose nanocrystals revealed by TEM analysis. The crystals were extracted from cotton and fractionated at centrifugation speeds 1000, 5000 and 2000 rpm for 8_1K, 8_5K and 9_20K, respectively. The NCC dimensions were estimated by measuring the lengths and widths of about 40 whiskers for each sample

Sample	D , nm	L , nm	L_{min} , nm	L_{max} , nm
8_1K	12 ± 2	173 ± 60	97	280
8_5K	10 ± 2	123 ± 40	62	209
9_20K	8 ± 2	101 ± 35	36	193

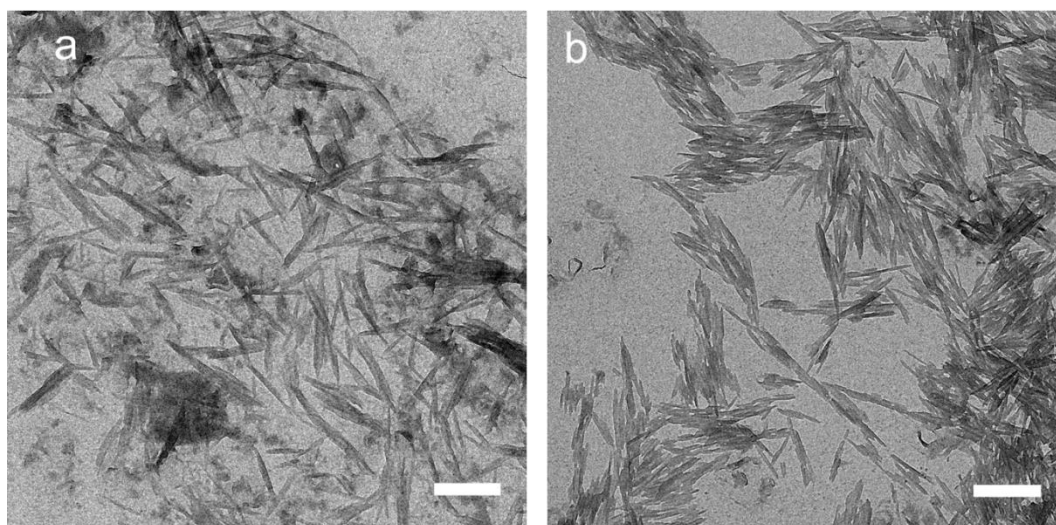


Figure 3.12. TEM images of cellulose nanocrystals extracted from cotton and fractionated by differential centrifugation at (a) 1000 rpm (8_1K) and (b) 20000 rpm (9_20K). The scale bars correspond to 200 nm.

The nanocellulose 8_1K separated at 1000 rpm shows rather long and thick bundled structures of about 200×12 nm in size (Figure 3.12). In contrast, the 9_20K dispersion exposed to stronger hydrolysis and fractionated at higher speed of 20000 rpm is more homogeneous and has the smallest crystallites of about 100×8 nm. The intermediate centrifugation speed 5000 rpm provides the average crystal dimensions of 150×10 nm. Hence there is a tendency of decreasing cellulose dimensions and reduced aggregation due to the fractionation.

Next, we studied the effect of fractionation on the cellulose crystallinity by using NMR and XRD techniques (Figure 3.13).

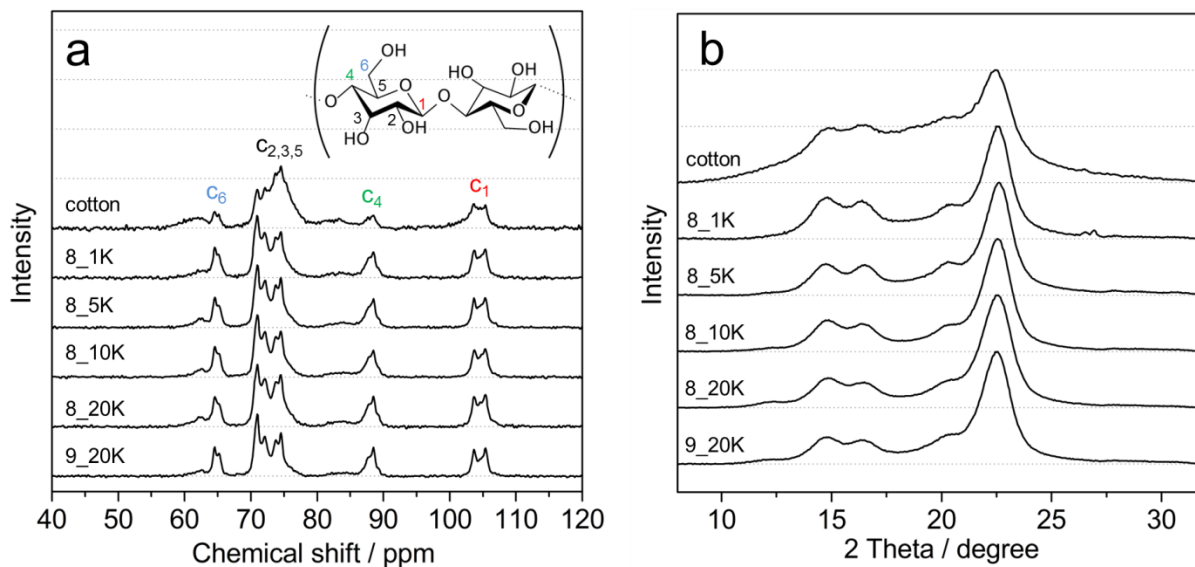


Figure 3.13. ^{13}C CP-MAS NMR spectra (a) and XRD patterns (b) of bulk cotton and nanocrystalline cellulose depending on hydrolysis conditions and fractionation speed. Sample 9_20K was hydrolyzed at 60 °C for 60 min and fractionated at 20000 rpm. The samples from the NCC cotton-8 batch were hydrolyzed for 30 min at 55 °C and fractionated at centrifugation speeds of 1000 (8_1K), 5000 (8_5K), 10000 (8_10K) and 20000 (8_20K) rpm, respectively.

In solid state ^{13}C -NMR spectroscopy, the amorphous cellulose can be distinguished from the crystalline one by comparing the shape of the signals. The ordered crystalline materials give sharp NMR peaks, whereas for the disordered domains broad signals are characteristic.³⁵ Furthermore, a cellulose ^{13}C CP-MAS NMR spectrum can be analyzed to estimate the crystallinity index of a cellulose powder. We note that due to the crosspolarization conditions the NMR peak areas are not necessarily quantitative with respect to the amount of carbon. However, due to the similarity of the materials relative trends can be obtained.

The degree of crystallinity γ_{NMR} is determined by dividing the integrated area of the NMR signal in the range of 86–92 ppm corresponding to the crystalline cellulose (C_4 region in Figure 3.13 a) by the total area of the signal at 72–92 ppm arising from both crystalline and amorphous cellulose:^{35,36}

$$\gamma_{NMR} = \left(\frac{I(86 \text{ ppm} - 92 \text{ ppm})}{I(79 \text{ ppm} - 92 \text{ ppm})} \right) \times 100\% \quad (3.2)$$

Table 3.4 summarizes the calculated crystallinities for each NCC fraction estimated from the spectra shown in Figure 3.13 a.

Table 3.4. Effect of fractionation on crystallinity of hydrolyzed cellulose revealed by NMR γ_{NMR} and XRD γ_{XRD} analysis. The crystals were extracted from cotton (Table 3.2) and fractionated at centrifugation speeds of 1000, 5000, 10000 and 20000 rpm for samples 8_1K, 8_5K, 8_10K, 8_20K and 9_20K, respectively

Sample	γ_{NMR} , %	γ_{XRD} , %
Cotton	37	56
8_1K	71	87
8_5K	72	91
8_10K	72	90
8_20K	72	90
9_20K	77	92

The NMR results imply that, whereas substantial increase in crystallinity is achieved by the implemented acid hydrolysis, the crystallinity γ_{NMR} of most fractionated phases is rather similar, of about 70%. However, the 9_20K sample demonstrates the highest crystallinity according to the γ_{NMR} calculations (and to the XRD data, see below), which may be explained by the fact that this sample was exposed to longer hydrolysis times at higher temperature than batch 8. In contrast, 8_1K possesses the lowest crystallinity, as a consequence of the mild hydrolysis and low-speed fractionation.

Crystallinity indexes calculated by the XRD peak-height method (Table 3.4, Equation 3.1) confirm the general trend established by the NMR analysis. The strongly hydrolyzed sample 9_20K contains the lowest amorphous cellulose amounts, whereas the lowest crystallinity is observed for the NCC low-speed fraction 8_1K. The fractions separated at intermediate speeds show rather similar crystallinities.

We note that the crystallinity values calculated by using NMR and XRD based methods differ noticeably. This phenomenon has been previously discussed in several studies.^{31,37} The XRD-peak-height approach usually gives a slightly higher percentage of crystallinity compared to the NMR analysis. This could be caused by quantification issues related to the use of cross-polarization techniques in the NMR. On the other hand, the XRD method is rather sensitive to the measurement and analysis conditions, namely the background subtraction. Nevertheless, the XRD peak-height method remains the most popular and straightforward approach, which shows the same quantitative trends as the NMR analysis.

To sum up, the NMR and XRD investigations clearly confirm that acid hydrolysis of bulk cotton leads to an increase in cellulose crystallinity, which can be further improved by differential centrifugation due to removal of amorphous and aggregated cellulose. We found that the fractionation at lower speeds such as ≤ 1000 rpm is more effective than centrifugations at higher speeds, namely at 5000 and 10000 rpm.

3.2.5 Nanocrystals Isolated from Cotton

The experiments described before revealed the optimal conditions for the isolation of cellulose nanocrystals. We found that the best NCC in terms of the purity, crystallinity and size homogeneity is obtained by hydrolysing cotton linters in 64% sulfuric acid for 1 hour at RT and then for 30 min at 55 °C, followed by washing and fractionation at 500 rpm. Figures 3.14, 3.15, 3.16 reveal the properties of cellulose nanocrystals extracted by the latter method.

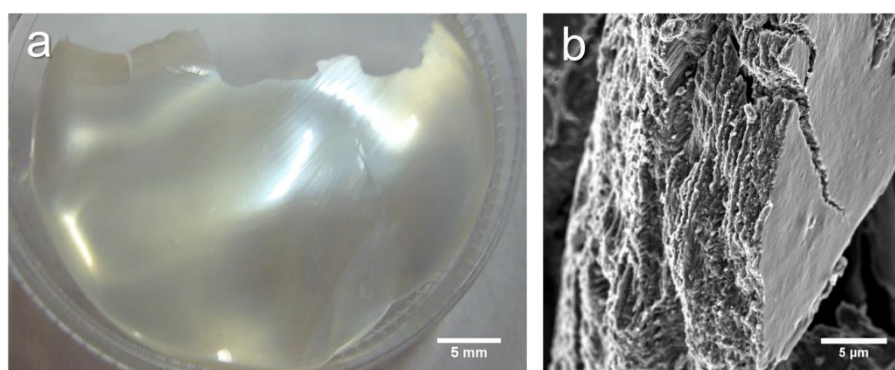


Figure 3.14. (a) Digital image of a free-standing film cast from a water dispersion of cellulose nanocrystals extracted from cotton. (b) SEM cross-section of NCC free-standing film.

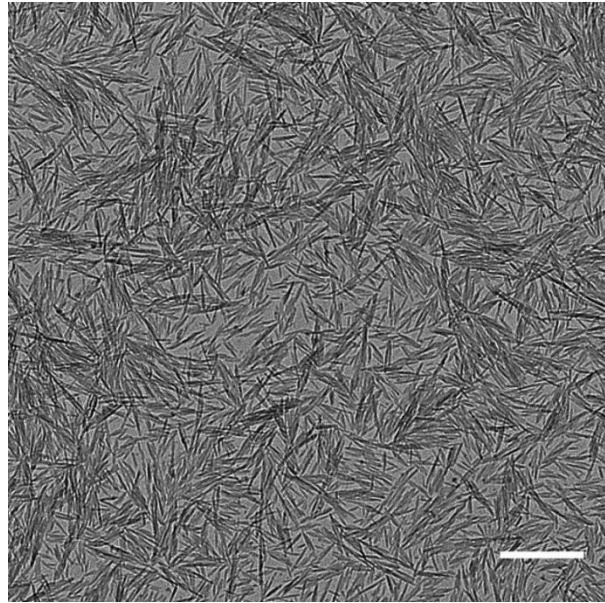


Figure 3.15. TEM image of cellulose nanocrystals extracted from cotton by 64% sulfuric acid hydrolysis at 55 °C for 30 min. The scale bar corresponds to 500 nm.

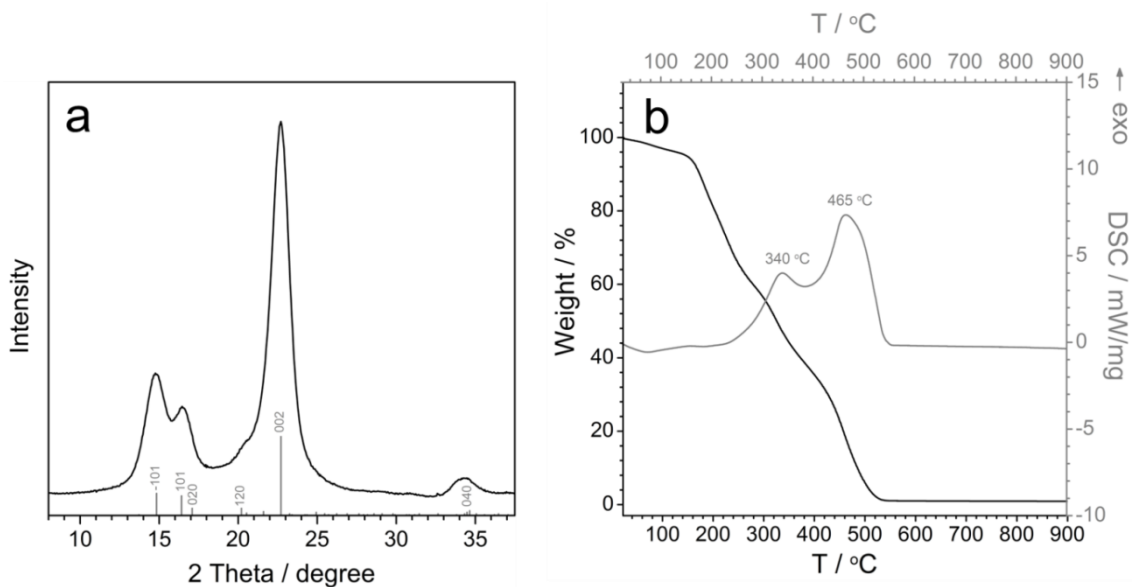


Figure 3.16. (a) XRD pattern of cellulose nanocrystals extracted from cotton by 64% sulfuric acid hydrolysis at 55 °C for 30 min. The assigned reflections correspond to the I_β cellulose (ICDD pattern 00-060-1502). (b) Mass loss and DSC data of the nanocrystalline cellulose extracted from cotton at 55 °C for 30 min.

The TEM analysis (Figure 3.15) reveals the distinct rod-shaped crystals with mean dimensions of 10 ± 2 nm in width and 117 ± 34 nm in length (average values obtained by measuring width and length of 75 and 50 crystals, respectively).

The as-prepared nanocrystals decompose up to about 500 °C under the conditions of the thermal analysis (10 °C/min heating rate of in a stream of synthetic air of about 25

mL/min) (Figure 3.16). The decomposition of nanocellulose is a step-wise process with several successive degradation steps involving evaporation of adsorbed water, depolymerization, dehydration, and decomposition of glycosyl units followed by the formation of a charred residue. The mass loss above 460 °C is attributed to the oxidation and breakdown of the charred residue to lower molecular weight gaseous products.³²

Aqueous dispersions of the cellulose nanocrystals demonstrate a unique ability to form nematic liquid crystalline phases at certain concentrations. Above the critical concentration, upon solvent removal, the suspensions dry out and form free-standing films with domains aligned parallel to the substrate (Figure 3.14). The free-standing film in Figure 3.14 shows some iridescence, which indicates that the material consists of successive layers at the nanoscale level.³⁸

3.3 Conclusions

In this chapter we have explored different bulk celluloses as starting sources for the isolation of cellulose nanocrystals. Among various bulk celluloses, namely cotton, wood pulp and commercial microcrystalline cellulose, we found cotton to be the most suitable for the release of nanocrystalline domains via sulphuric acid hydrolysis. Cotton initially consists of pure cellulose, hence it requires less chemical pre-treatments compared to wood celluloses. Moreover, cotton has average relative contents of amorphous and crystalline domains assuring the effective release of crystalline cellulose and good reaction yields.

We found that nanocrystalline cellulose can be successfully extracted from cotton with 64% sulfuric acid hydrolysis and 1:8.75 g/mL cotton-to acid ratio within the temperature ranges from 45 to 55 °C and reaction times of 20–40 min. The hydrolysis time and temperature affect the reaction yield and the crystallinity of the released crystals. Furthermore, we suggest performing a differential centrifugation on freshly hydrolysed and washed NCC dispersions. We have demonstrated that fractionation at low centrifugation speeds, i.e. ≤ 1000 rpm, effectively removes large cellulose aggregates containing undesirable non-crystalline cellulose.

3.4 Experimental

3.4.1 Synthesis

Bulk celluloses. Four different types of bulk celluloses have been employed for the preparation of nanocrystalline cellulose, namely soft- and hardwood pulps, cotton and microcrystalline cellulose. ASPA (Monksjö Aspa Bruck AB, Sweden) is an elemental chlorine free (ECF) bleached softwood kraft dry pulp, produced from pine (*Picea abies*) and spruce (*Pinus silvestris*) wood fibers. Lwarcel (Lwarcel Cellulose, Brasil) is an ECF bleached kraft dry pulp originating from Eucalyptus wood. Domsjö (Domsjö Fabriker AB, Sweden) is a softwood cellulose manufactured by two-stage sodium based cooking followed by alkali and hydrogen peroxide closed-loop bleaching. The cotton linters were supplied by Peter Temming AG (Germany). Microcrystalline cellulose Avicel® PH-101 was purchased from Fluka.

Hydrolysis of cellulose. The wood pulp sheets were cut to small pieces and then milled to powder by using a Fritsch Planetary Pulverisette 6 ball mill at a rotation speed of 250 rpm for about 50 min. Cotton linters were washed with deionized water and dried in an oven at 60 °C. To perform the hydrolysis, the cellulose was gradually introduced into a round bottom flask containing 64% (w/w) sulfuric acid (at room temperature, RT) at a cellulose-to acid ratio of 1:8.75 g/mL. The mixture was stirred at RT for 20–60 min and then heated in an oil bath under reflux at 20–58 °C for 20–60 min, depending on the sample batch (see Tables 3.1 and 3.2). After the desired time had passed, the mixture was ten-fold diluted with deionized water to stop the hydrolysis. As-diluted cellulose dispersion was stored overnight to reach the phase separation, i.e. a segregated nanocrystal-rich bottom phase and a transparent upper phase. The upper phase was decanted and the bottom one washed by repeated centrifugation with deionized water. The NCC suspension was washed twice in 40 mL tubes by centrifugation at 20000 rpm (47808 g relative centrifugal force (RFC)) for 20 min in a Thermo Scientific High-Speed centrifuge equipped with a Thermo Scientific SS-34 rotor. Finally, the suspensions were concentrated by rotary evaporation at 55 mbar and 40 °C.

Differential centrifugation. A freshly washed NCC suspension was centrifuged in several successive times at rotation speeds in the range from 1000 rpm (120 g RCF) to 20000

(47808 g RCF) as shown in Figure 3.11. After each centrifugation step the upper phase was isolated from the pellet. Later, the as-separated NCC dispersions were concentrated in a rotating evaporator at 55 mbar and 40 °C until the concentration and pH-values reached about 7 wt % and pH 2, respectively. The concentrated suspensions were dried at room temperature and pulverized in a mortar for the further analysis.

3.4.2 Characterization

Scanning electron microscopy (SEM) of bulk and nanocrystalline celluloses was performed by using a JEOL JSM-6500F microscope equipped with a field emission gun operated at 5 kV. The cellulose powders were deposited on a carbon pad and then sputtered with carbon in a BAL-TEC MCS 010 sputter coater.

Wide angle X-ray diffraction (XRD) of NCC powders was carried out in the reflection mode using a Bruker D8 Discover diffractometer with Ni-filtered Cu-K α -radiation ($\lambda = 1.5406 \text{ \AA}$), equipped with a Vantec-1 position sensitive detector. The powders were deposited on silicon wafer. The recorded XRD signals were assigned by using the database of The International Centre for Diffraction Data[®] (ICDD). To evaluate the crystallinity, the XRD patterns were baseline-corrected in Bruker DIFFRAC.SUITE EVA software by using a linear function with anchor points at about 9° and 32° 2 θ . The baseline-corrected patterns were analyzed according to Equation 3.1. The Scherrer equation was used to estimate the crystallite dimensions.

Thermogravimetric analysis was performed on a Netzsch STA 440 C TG/DSC instrument (heating rate of 10 °C/min in a stream of synthetic air of about 25 mL/min).

CP-MAS ¹³C-NMR Spectroscopy of NCC powders was carried out by using a Bruker Avance 500 spectrometer equipped with a 11.75 T magnet. The measurements were performed at room temperature in a 4 mm 1H/BB MAS probe at 10 kHz rotation frequency and the following acquisition parameters: 20.5 ms acquisition time, 5 ms crosspolarization (CP) contact time and 2 s scan delay. The spectra were recorded in the range from -250 to 450 ppm relative to tetramethylsilane. The crystallinity of the cellulose was estimated by applying Equation 3.2. The integrated signal areas corresponding to amorphous and crystalline celluloses were calculated with the software OriginLab.

Dynamic light scattering (DLS) was performed on a Malvern Zetasizer-Nano instrument equipped with a 4 mW He-Ne laser (633 nm) and an avalanche photodiode. The particle size calculations are based on the Stokes–Einstein equation assuming spherical shape of nanoparticles. Due to the rod-like shape of the NCC the DLS data can only indicate trends. To estimate the length of the crystals, DLS measured translational diffusion coefficients have to be further analysed by using particle diameter data obtained from TEM analysis.³⁹

Transmission electron microscopy (TEM) was performed using an FEI Titan 80–300 electron microscope equipped with a field emission gun operated at 80 kV. The samples were prepared by diluting the concentrated NCC suspensions to 0.15 wt % with ethanol followed by 5 minutes of ultrasonication. The TEM images were analyzed with ImageJ software. The mean dimensions of the crystals were calculated by assigning the lengths and widths of about 40 individual whiskers.

3.5 References

- (1) Ranby, B. G. *Acta Chem. Scand.* **1949**, *3*, 649–650.
- (2) Elazzouzi-Hafraoui, S.; Nishiyama, Y.; Putaux, J.-L.; Heux, L.; Dubreuil, F.; Rochas, C. *Biomacromolecules* **2008**, *9*, 57–65.
- (3) Marchessault, R. H.; Morehead, F. F.; Walter, N. M. *Nature* **1959**, *184*, 632–633.
- (4) Marchessault, R. H.; Koch, M. J.; Yang, J. T. *J. Colloid Sci.* **1961**, *16*, 327–344.
- (5) Revol, J.-F.; Bradford, J. G.; Giasson, R. H.; Marchessault, R. H.; Gray, D. G. *Int. J. Biol. Macromol.* **1992**, *14*, 170–172.
- (6) Dong, X. M.; Kimura, T.; Revol, J.-F.; Gray, D. G. *Langmuir* **1996**, *12*, 2076–2082.
- (7) Dong, X.; Revol, J.-F.; Gray, D. *Cellulose* **1998**, *5*, 19–32.
- (8) Beck-Candanedo, S.; Roman, M.; Gray, D. G. *Biomacromolecules* **2005**, *6*, 1048–1054.
- (9) Elazzouzi-Hafraoui, S.; Putaux, J.-L.; Heux, L. *J. Phys. Chem. B* **2009**, *113*, 11069–11075.
- (10) Zhou, Q.; Brumer, H.; Teeri, T. T. *Macromolecules* **2009**, *42*, 5430–5432.
- (11) Shopsowitz, K. E.; Qi, H.; Hamad, W. Y.; MacLachlan, M. J. *Nature* **2010**, *468*, 422–425.
- (12) Cranston, E. D.; Gray, D. G. *Biomacromolecules* **2006**, *7*, 2522–2530.
- (13) Hamad, W. Y.; Hu, T. Q. *Can. J. Chem. Eng.* **2010**, *88*, 392–402.
- (14) Isogai, A.; Saito, T.; Fukuzumi, H. *Nanoscale* **2011**, *3*, 71–85.
- (15) de Souza Lima, M. M.; Borsali, R. *Macromol. Rapid Commun.* **2004**, *25*, 771–787.
- (16) Moon, R. J.; Martini, A.; Nairn, J.; Simonsen, J.; Youngblood, J. *Chem. Soc. Rev.* **2011**, *40*, 3941–3994.
- (17) Dufresne, A. *Nanocellulose - From Nature to High Performance Tailored Materials*; Walter de Gruyter GmbH & Co.KG: Berlin, 2012.
- (18) Habibi, Y.; Lucia, L. A.; Rojas, O. J. *Chem. Rev.* **2010**, *110*, 3479–3500.
- (19) Sacui, I. A.; Nieuwendaal, R. C.; Burnett, D. J.; Stranick, S. J.; Jorfi, M.; Weder, C.; Foster, E. J.; Olsson, R. T.; Gilman, J. W. *Appl. Mater. Interfaces* **2014**, *6*, 6127–6138.
- (20) Grunert, M.; Winter, W. *J. of Polym. Environ.* **2002**, *10*, 27–30.
- (21) Lu, P.; Hsieh, Y.-L. *Carbohydr. Polym.* **2010**, *82*, 329–336.
- (22) Peng, B. L.; Dhar, N.; Liu, H. L.; Tam, K. C. *Can. J. Chem. Eng.* **2011**, *89*, 1191–1206.
- (23) Bondeson, D.; Mathew, A.; Oksman, K. *Cellulose* **2006**, *13*, 171–180.
- (24) Chen, Y.; Liu, C.; Chang, P. R.; Cao, X.; Anderson, D. P. *Carbohydr. Polym.* **2009**, *76*, 607–615.
- (25) Brito, B. L.; Pereira, F.; Putaux, J.-L.; Jean, B. *Cellulose* **2012**, *19*, 1527–1536.
- (26) Kargarzadeh, H.; Ahmad, I.; Abdullah, I.; Dufresne, A.; Zainudin, S.; Sheltami, R. *Cellulose* **2012**, *19*, 855–866.
- (27) Liu, Y.; Wang, H.; Yu, G.; Yu, Q.; Li, B.; Mu, X. *Carbohydr. Polym.* **2014**, *110*, 415–422.

- (28) Pirani, S.; Hashaikeh, R. *Carbohydr. Polym.* **2013**, *93*, 357–363.
- (29) Fan, J.-s.; Li, Y.-h. *Carbohydr. Polym.* **2012**, *88*, 1184–1188.
- (30) Segal, L.; Creely, J. J.; Martin, A. E.; Conrad, C. M. *Text. Res. J.* **1959**, *29*, 786–794.
- (31) Terinte, N.; Ibbett, R.; Schuster, K. C. *Lenzinger Berichte* **2011**, *89*, 118–131.
- (32) Roman, M.; Winter, W. T. *Biomacromolecules* **2004**, *5*, 1671–1676.
- (33) Stelte, W.; Sanadi, A. R. *Ind. Eng. Chem. Res.* **2009**, *48*, 11211–11219.
- (34) Bai, W.; Holbery, J.; Li, K. *Cellulose* **2009**, *16*, 455–3994.
- (35) Zuckerstätter, G.; Schild, G.; Wollboldt, P.; Röder, T.; Weber, K. H.; Sixta, H. *Lenzinger Berichte* **2009**, *87*, 38–46.
- (36) Atalla, R. H.; VanderHart, D. L. *Solid State Nucl. Magn. Reson.* **1999**, *15*, 1–19.
- (37) Park, S.; Baker, J.; Himmel, M.; Parilla, P.; Johnson, D. *Biotechnology for Biofuels* **2010**, *3*, 1–10.
- (38) Chen, Q.; Liu, P.; Nan, F.; Zhou, L.; Zhang, J. *Biomacromolecules* **2014**, *15*, 4343–4350.
- (39) Boluk, Y.; Danumah, C. J. *Nanopart. Res.* **2013**, *16*, 1–7.

3.6 Appendix

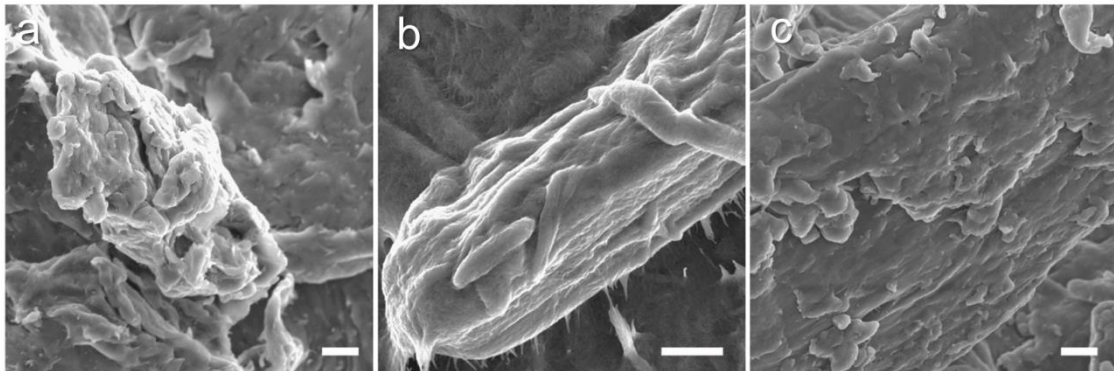


Figure A3.1. SEM images of (a) cotton linters, (b) microcrystalline cellulose Avicel®, (c) dried soft wood pulp (Domsjo). The scale bars correspond to 500 nm.

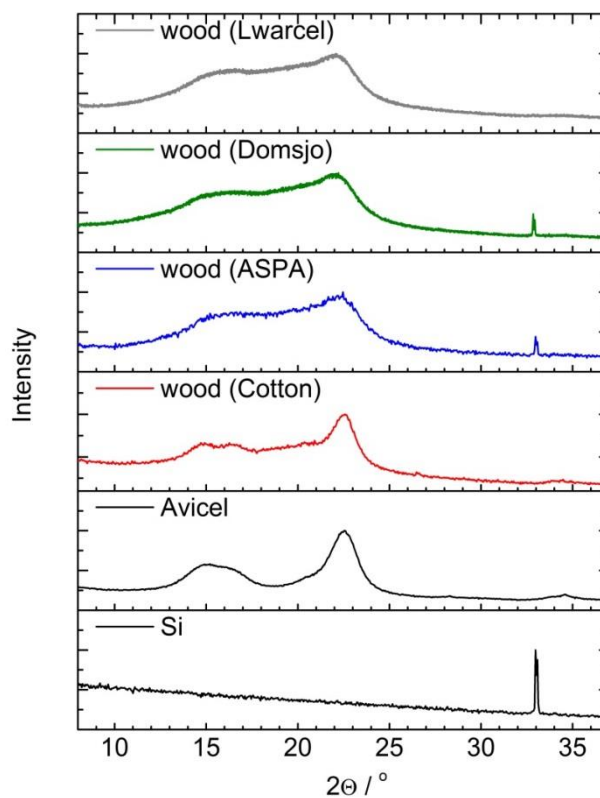


Figure A3.2. X-ray diffraction patterns of microcrystalline cellulose, wood pulps and cotton. The cellulose powders were measured on silicon wafer in reflection mode. The diffraction patterns were normalized to the most intense reflections.

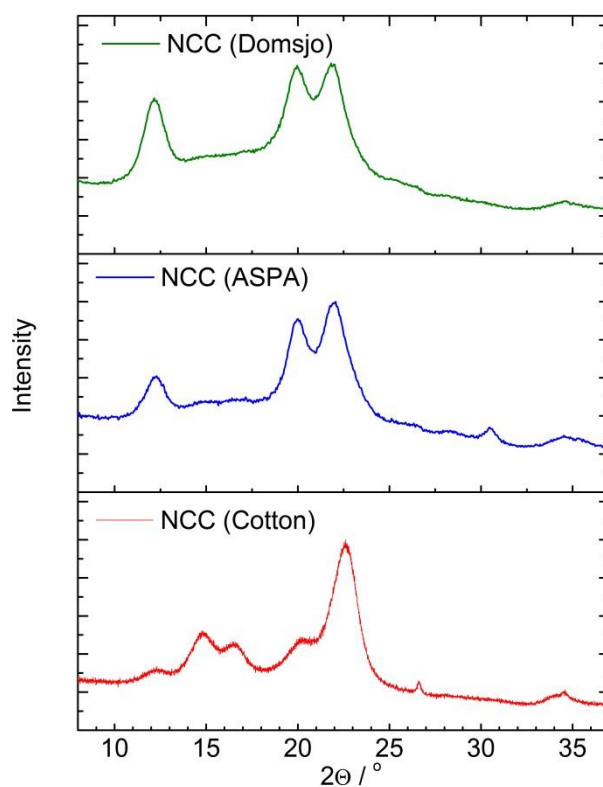
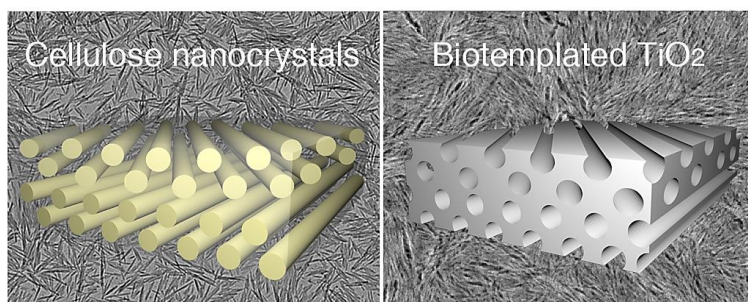


Figure A3.3. X-ray diffraction patterns of nanocrystalline cellulose obtained from soft wood pulps and cotton. The cellulose powders were measured on silicon wafer in reflection mode. The diffraction patterns were normalized to the most intense reflections.

4 Tailoring the Morphology of Mesoporous Titania Thin Films through Biotemplating with Nanocrystalline Cellulose



This chapter is based on the following publication:

*Alesja Ivanova, Dina Fattakhova-Rohlfing, Bugra Eymer Kayaalp, Jiri Rathouský, Thomas Bein. Tailoring the morphology of mesoporous titania thin films through biotemplating with nanocrystalline cellulose. J. Am. Chem. Soc. **2014**, 136, 5930.*

4.1 Introduction

Titania is a very important semiconductor material for photovoltaics, photocatalysis and electrochemistry. The efficient performance of titania-based devices often requires deposition of porous titania thin films possessing high surface area.¹ Generally, a successful device operation requires not only a high surface area, but also an optimization of the morphology of the titania films, including the crystallinity of the pore walls,² as well as the shape, orientation and size of the pores.

Evaporation-induced self-assembly³ is one of the most popular approaches for the formation of thin films with controlled mesoporosity. The method is based on the self-assembly of titania precursors and structure-directing micelles of amphiphilic molecules.⁴ The procedure relies on the formation of micellar aggregates, which is sensitive to the template-to-inorganic precursor ratio, the concentration of amphiphilic

molecules and the nature of the solvents. Considering these factors, the use of shape-persistent templates can be advantageous over molecular template aggregates. As the former templates^{5,6} have a defined shape that is maintained throughout the entire synthesis route, it is not influenced by the reaction conditions. Silica and alumina are among the most frequently used hard templates enabling shape persistent replication of various morphologies. However, removal of the solid inorganic templates without attacking the target material is usually challenging. In this respect, biomaterials are very attractive as shape persistent pore generators since they can provide a wide variety of shapes and sizes and generally they can be easily removed. Several examples of naturally grown biotemplates such as cell^{7,8} and peptide assemblies,⁹ egg-white,¹⁰ algae,¹¹⁻¹⁴ butterfly wings,¹⁵ weevil scales,¹⁶ chitin¹⁷ and calcium alginate¹⁸ have already demonstrated their potential for the synthesis of diverse porous titania morphologies.

Polysaccharides, in particular celluloses, attract special attention as versatile and abundant 'green' templates.¹⁹⁻²² Natural cellulose, either plant or bacterial, has a hierarchical structure covering a broad range of dimensions. The original fibers of several micrometer thickness can be disintegrated stepwise, first into fibril bundles, then into separate microfibrils and finally into the smallest nano-sized crystals composed of cellulose molecules.^{23,24} Microbial cellulose has a ribbon-like morphology with large longitudinal and small lateral dimensions. The plant cellulose fibers, in contrast, are much thicker but the aspect ratios of their crystals are lower than that of bacterial cellulose.

The dried nanocrystalline cellulose (NCC) extracted from wood pulp, cotton and algae has a rod-like shape being 5–70 nm in width and 100 nm to several micrometers in length.²⁵ The whiskers suspended in water show an remarkable ability to self-organize and to form chiral nematic liquid crystalline phases.²⁶ Dujardin²⁷ and Antonietti et al.²⁸ employed chiral cellulose suspensions in porous silica synthesis. This approach was further developed in the recent studies of Shopsowitz et al. showing a broad variety of NCC-templated chiral materials: coloured free-standing silica films,²⁹ carbon³⁰ and flexible organosilica.³¹ In a recent study³² the resulting chiral silica was used as a hard template for the structuring of titania via replication. Direct cellulose templating of titania has been done with nanocellulose aerogels,³³ microfibrillated cellulose,³⁴ bacterial cellulose,³⁵ nanocrystalline cellulose³⁶, filter paper³⁷ and green leaves.³⁸

However, in all these cases the final products were sponge-like titania monoliths, free-standing films or powders. Titania powders biotemplated with cotton fibers³⁹ and viruses⁴⁰ were further processed to a paste that was afterwards coated on conducting substrates and applied in solar cell assembly. The direct formation of cellulose-templated titania thin films on substrates has not been reported yet.

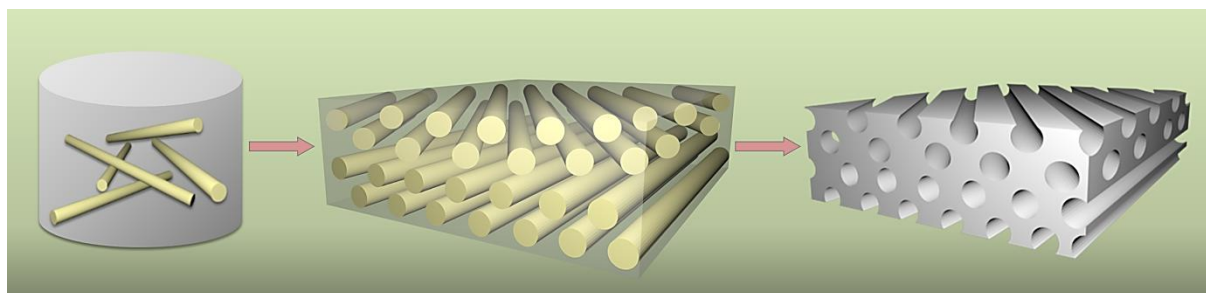
Here we present for the first time the formation of titania porous films on substrates using a direct NCC templating approach. The straightforward one-pot synthesis provides mesoporous TiO₂ thin films with anisotropic porosity deposited on different substrates, which can be used directly as electrodes in photovoltaic devices. The pore anisotropy, surface area and pore size of the NCC-templated titania can be easily tuned through processing conditions using the same template and without additional swelling agents. The porous morphology can be tailored by the variation of the precursor composition and post-treatment of the film at high humidity. We show a striking effect of the humidity on the templating cellulose crystals. NCC incorporated in the sol matrix swells and expands, which provides a straightforward tool for pore tuning.

Finally, we demonstrate the promising application potential of the cellulose-templated thin films in photovoltaic devices and in photocatalysis, namely in the NO (nitrogen(II) oxide) oxidation and 4-chlorophenol degradation in gaseous and liquid phases, respectively.

4.2 Results and Discussion

4.2.1 Morphology Tuning

For the fabrication of the NCC-templated titania films we added an aqueous suspension of nanocrystalline cellulose (NCC) containing rod-shaped cellulose species (Figure A4.1a in the Appendix) to pre-hydrolysed titanium(IV) ethoxide (TEOT). After stirring, the opaque colloidal dispersion was coated onto the substrate and the composite film was calcined at 450 °C to combust the template and to crystallize titania (Scheme 4.1).



Scheme 4.1. Synthesis approach for the NCC-templated mesoporous TiO_2 film.

The resulting porous structure (Figure 4.1b) exhibits slit-shaped mesopores and elongated thread-like pore walls consisting of anatase crystallites sized about 9 nm. The pore pattern replicates the parent NCC crystals (Figures 4.1 and A4.1 in the Appendix) that tend to aggregate in short-range bundle-like domains. A similar tendency towards the formation of oriented pore domains is observed in the titania network after template removal. The cross section of the film demonstrates that the domains are preferentially aligned parallel to the substrate, although some random orientation appears as well (Figure A4.2a in the Appendix). The variation of the template distribution in three dimensions enables the formation of a highly interconnected porous network.

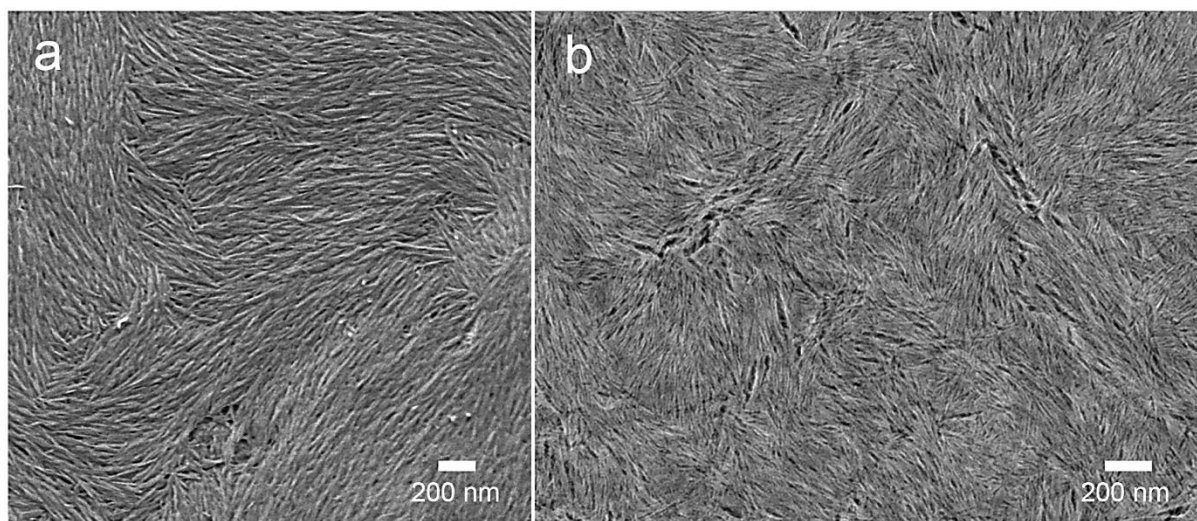


Figure 4.1. (a) SEM image of nanocrystalline cellulose film prepared by drop-casting a 2.5 wt % NCC aqueous dispersion on a silicon wafer. (b) SEM top view of NCC-templated porous titania thin film spincoated on a silicon wafer. The precursor solution was prepared by adjusting the TiO_2 /NCC mass ratio at 1.5 with 2.5 wt % NCC.

We found that the film morphology strongly depends on the titania precursor concentration in the solution. Accordingly, we studied the films coated from different

solutions containing the same NCC concentration but different amounts of the TEOT precursor (recalculated as TiO_2/NCC mass ratio, see the Experimental).

X-ray diffraction analysis reveals that the increase in the TiO_2/NCC mass ratio leads to a gradual growth of the average anatase crystallite size after calcination. At the same time, the morphology of the films also changes, as follows from the SEM images (Figures 4.2 and A4.3 in the Appendix).

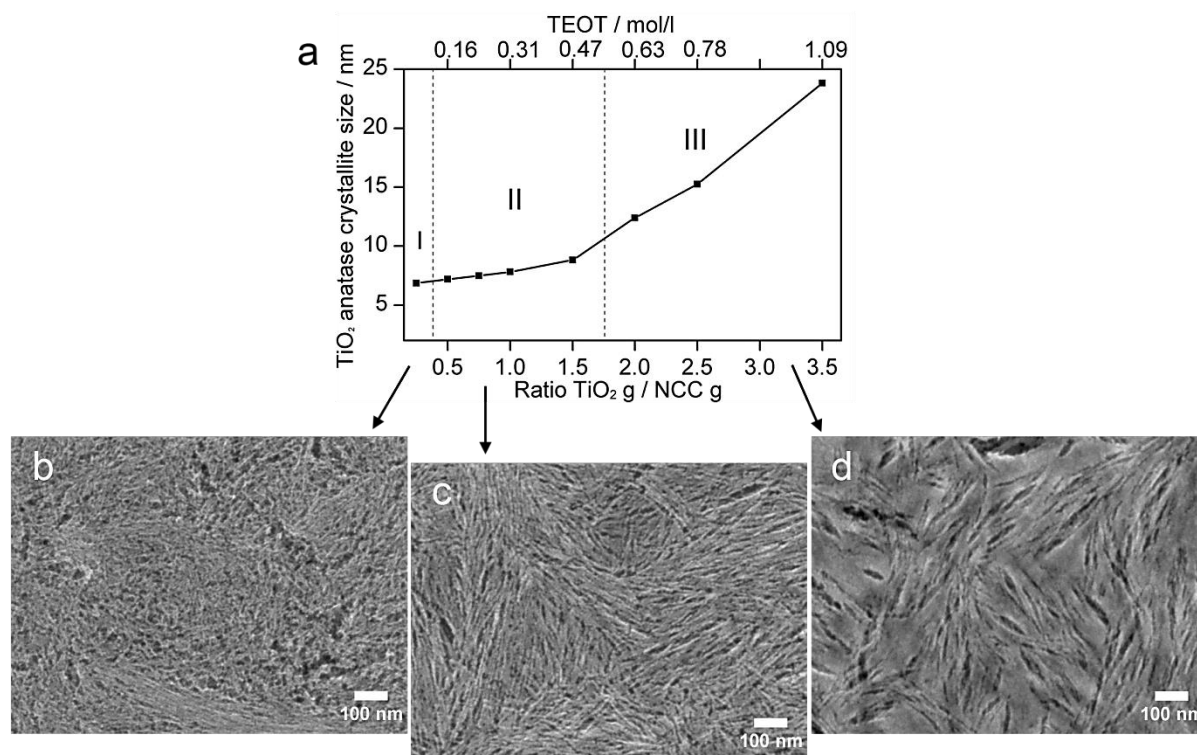


Figure 4.2. Morphology variation of cast (a) and spin-coated (b-d) NCC-templated titania films depending on TEOT amounts in 25 mg/mL NCC precursor solutions. **(a)** Development of the mean anatase crystallite size depending on the TiO_2/NCC mass ratio. Scanning electron microscopy top views of porous titania films prepared from the solutions with **(b)** $\text{TiO}_2/\text{NCC} = 0.25$ g/g, **(c)** 0.75 g/g and **(d)** 2.5 g/g corresponding to the regions I, II, III in the graph (a), respectively.

Depending on the TiO_2/NCC mass ratio in the precursor solution, one can differentiate three major types of porous structures that are formed after calcination. At the TiO_2/NCC ratio ≤ 0.25 , highly porous sponge-like titania is formed that consists of fine 6–7 nm anatase crystallites (region I in the Figure 4.2). Region II corresponds to the intermediate TiO_2/NCC ratios of 0.5–1.5. The titania films formed at these ratios feature pronounced pore anisotropy and high pore volume. When the relative TEOT concentration increases further (TiO_2/NCC ratio ≥ 2.0), the films become more dense

with large slit-like pores surrounded by closely packed large anatase crystallites (range III).

The best results regarding film processability, pore anisotropy and pore volume were obtained for the TiO₂/NCC ratios of 0.5–1.75 corresponding to the region II. The SEM top-views of these titania films show morphologies that closely resemble the shape of the NCC template. The confined space between the cellulose template crystals restricts the growth of titania crystals in composite materials during calcination. The anatase crystallites are 7–12 nm in size and are homogeneously integrated into the NCC rod pattern. A decrease in the relative NCC amount below this optimum ratio (region III) enables unrestricted growth of the titania crystallites reaching 23 nm after calcination. The NCC-templated titania networks show a BET surface area of 61 m²/g and 171 m²/g for the ratios 2.5 and 0.5, respectively. The reason of the marked decrease in the surface area with the increasing TiO₂/NCC weight ratio is the formation of non-porous bulk titania due to the insufficient content of NCC.

In order to investigate in more detail the effect of the NCC concentration on the morphology of the resulting titania films, we have kept the TEOT concentration at 0.27 mol/L and prepared solutions with different TiO₂/NCC weight ratios by varying the NCC contents. Nitrogen sorption isotherms of the samples prepared with 0.5–2.0 ratios correspond to the type IV characteristic for mesoporous materials (Figure 4.3a, c).

We found that the surface area and the pore volume of the porous titania gradually grow with increasing relative template content (Figures 4.3e and A4.4 in the Appendix). The observed upward trend clearly confirms the suppression of the formation of non-porous material with the increasing percentage of the templating NCC. A related porosity evolution with increasing amount of biogenic template has been observed for chitin-templated porous silica microparticles.^{41,42} The templated samples prepared with equal 0.27 mol/L TEOT concentration consisted of titania crystalline domains with dimensions of 7–10 nm (TEM images and XRD patterns in Figures A4.5 and A4.6b in the Appendix, respectively).

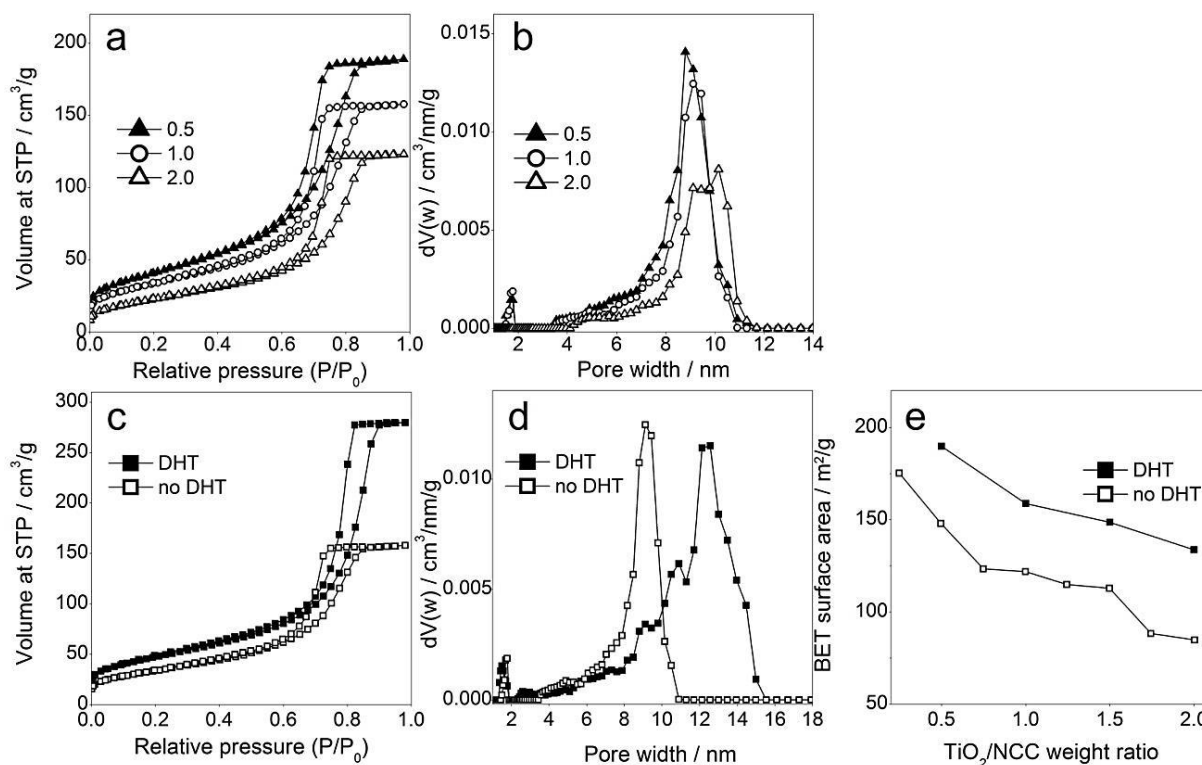


Figure 4.3. Nitrogen sorption isotherms **(a)** and corresponding pore size distributions **(b)** of NCC-templated titania prepared from 0.27 mol/L TEOT solutions with TiO₂/NCC g/g ratios of 0.5, 1.0 and 2.0. Effect of hydrothermal treatment (DHT) applied to NCC/titania-sol composite (TiO₂/NCC = 1.0 g/g) prior to calcination **(c, d, e)**. Nitrogen sorption isotherms **(c)** and pore size distributions **(d)** of porous titania after calcination. The sample marked with solid squares (■) was kept for 4 days at 70 °C in 80% relative humidity before calcination and the open square (□) sample was prepared without the post-synthetic humidity treatment. Variation of the BET surface area of porous titania prepared from precursor solutions with different TiO₂/NCC mass ratios with (solid squares) and without (open squares) DHT treatment **(e)**.

To elucidate the role of NCC in the structure formation we have prepared titania from a similar sol-gel titania solution but without NCC. The powders obtained at the otherwise identical conditions are practically nonporous, being composed of densely packed anatase crystalline domains with an average size of 17 nm obtained from XRD line broadening (Figure A4.6 in the Appendix). In contrast, titania derived from the NCC-containing solution is highly porous and consists of small (7–10 nm) anatase crystals (TEM images in Figures A4.2c, A4.5, A4.7b, A4.8 in the Appendix).

NCC fulfills a multiple function in the formation of the porous scaffold and in the crystal growth. The NCC significantly increases the viscosity of the precursor solution. Moreover, NCC rods may also provide an additional surface for the heterogeneous nucleation of titania. We propose that the nucleation of titania on the NCC surface in combination with the confinement effect of the shape-persistent NCC template control

the crystallization of the titania scaffold, leading to the formation of polycrystalline scaffolds consisting of extremely small titania crystallites.

As shown above, the variation of the concentration and the relative amount of titania and the NCC template leads to significant changes in the surface area and the crystallite size of the mesoporous titania formed after calcination, but only to a slight change in the pore size distribution (Figure 4.3b). The pore size is significantly influenced by controlling the NCC degradation during calcination and by applying a humidity treatment to the dried composites prior to their calcination (Figures 4.3c-e and A4.9 in the Appendix).

The humidity treatment (usually referred to as delayed humidity treatment (DHT) in the literature) has already been applied successfully for the synthesis of highly ordered tin oxide films⁴³ and silica.⁴⁴ It has been reported that the control over humidity improves the optical quality of films and affects the micelle organization,⁴⁵ however it does not significantly change the dimensions of the resulting pores.^{46,47} If pore swelling is of interest when using soft templates, more drastic intervention like addition of swelling agents such as alkylamines or triisopropylbenzene can be necessary.^{48,49}

Cellulose has a unique ability to hydrate and swell when exposed to humidity.⁵⁰ In addition, cellulose crystals withstand higher temperatures than the majority of amphiphilic molecular templates. Indeed, NCC in the presence of titania precursor and water degrades over a broad temperature range from 120 °C to 450 °C (Figure A4.10c in the Appendix). When the TiO₂/NCC composite is heated, the gradual NCC combustion proceeds simultaneously with the nucleation and growth of the titania crystallites. The control over these two parallel processes is an effective tool for pore size tuning.

When a larger pore size is desired, the NCC integrity in the composite should be preserved as long as possible during calcination. At the same time, the titania crystal growth should be slowed down. We found that these requirements can be fulfilled when the dried titania/NCC composite films are additionally treated at higher humidity and at elevated temperatures. Such a procedure can be considered as a hydrothermal treatment of the solid amorphous titania matrix in the confined space of the pre-arranged NCC template rods.

According to our observations, degradation of NCC in hydrothermal conditions is suppressed compared to combustion in dry air (Figure A4.10 in the Appendix). This implies that the NCC template is present during nucleation and crystallization of the titania phase, hence constraining the titania crystal growth in favour of smaller crystallites. Additionally, the NCC crystals remain in the swollen state under the hydrothermal conditions, which is advantageous for the formation of the larger pores.

The validity of this concept for enlarging the average pore diameter in the NCC-templated titania is confirmed by nitrogen sorption measurements. The data demonstrate an increase in the mean pore size and specific surface area (Figures 4.3c-e) for the samples treated hydrothermally before calcination. The effect of DHT becomes even more obvious when comparing the total pore volumes of 0.243 cm³/g and 0.446 cm³/g for the non-treated and humidity-treated samples, respectively. Despite the pore expansion, the surface area of the porous networks does not drop, but it increases. It appears that the pores mostly expand while they do not coalesce significantly. Also, the titania crystallites in the hydrothermally modified samples tend to be smaller than in the non-treated samples (Figure A4.6c in the Appendix).

The titania films based on the NCC-containing solutions are very smooth, transparent, have a very good adhesion to the substrate and good mechanical stability. Importantly, it is possible to obtain thick (up to about 700 nm) smooth films in a single coating step without adding any thickeners (Figure A4.2a in the Appendix). The absence of additional thickening agents assures the smoothness of the films on the nanometer scale (Figure A4.11 in the Appendix). The thickness of the NCC-templated titania films can be further increased by successive coating of several layers. The deposition of the following layers does not require any intermediate high temperature calcination, which is often the case for surfactant-templated films.^{51,52} For example, for the fabrication of anodes for dye-sensitized solar cells we have dip-coated four layers. Every subsequent layer was DHT-treated by keeping the films for 1 h in an oven (70 °C/30 min and 100 °C/30 min) in a desiccator with a saturated KCl solution. During the hydrothermal treatment the titania scaffold already starts to crystallize. At the same time the NCC does not dry out such that the film volume remains preserved. After the intermediate humidity treatment, the partially crystalline titania films sustained the final calcination at 500 °C/30 min and turned into a highly porous titania network. It is possible to tune

the final film thickness by controlling the drying conditions of each deposited layer, as well as by adjusting the NCC concentration in the precursor solution (not shown).

We note that the deposition protocol for the mesoporous films based on the NCC containing solutions is much more straightforward and less time-consuming than in the case of films templated by more traditional molecular surfactants. For example, the thickness of the titania films obtained by a sol-gel route from the solutions containing amphiphilic polymers is usually limited to about 300 nm. The main reason for this limitation is a drastic change in volume upon combustion of the polymer and crystallization of an initially amorphous mesostructured framework upon calcination, leading to cracking and even peeling off the substrate for the thicker titania coatings.

4.2.2 Film Performance in Photocatalysis

Mesoporous titania is important from the environmental point of view, as it can be used for the photocatalytic degradation of a number of pollutants. In the following we present two examples of the photocatalytic performance of the NCC-templated titania, namely in the oxidation of nitrogen oxide and in the degradation of 4-chlorophenol in aqueous media, serving as models for the purification of air and water, respectively. To assess the efficiency of the NCC-templated titania as a photocatalyst, its performance was compared with recently published data on mesoporous layers of TiO_2 .

For the photocatalytic experiments the film was spin-coated on a glass substrate from a precursor solution with a TiO_2 /NCC weight ratio of 0.75 and calcined at 500 °C. The film shows excellent transparency (Figure 4.4b) and high porosity according to the sorption measurements. The adsorption isotherm of Kr at the boiling point of liquid nitrogen (ca. 77 K) exhibits a broad hysteresis loop ranging from the relative pressure of ca. 0.5 to 1 (Figure 4.4a), which indicates the presence of some proportion of mesopores narrower than ca. 10 nm. As the adsorption isotherm does not reach a plateau at a relative pressure approaching 1 and keeps rising, the film must additionally contain a substantial proportion of pores wider than about 10 nm. This conclusion follows from the peculiar properties of krypton in narrow pores at ca. 77 K, which behaves as a supercooled liquid.

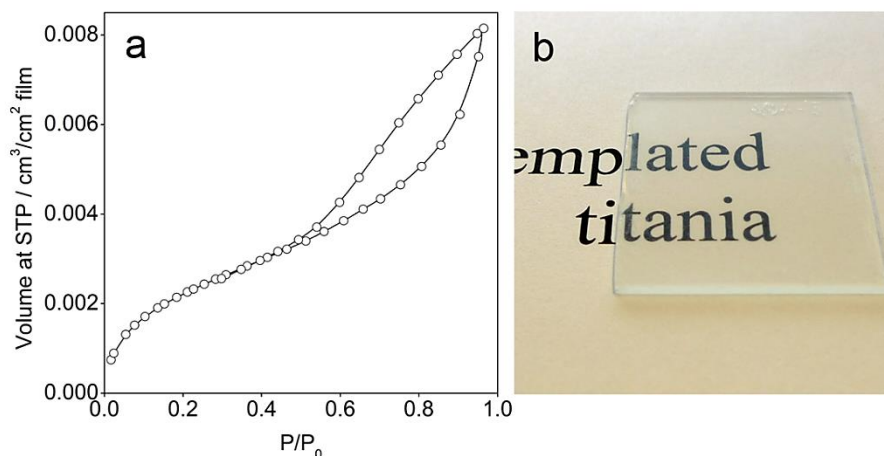


Figure 4.4. Transparent NCC-templated titania porous film of 850 nm in thickness coated on a $2.5 \times 2.5 \text{ cm}^2$ glass substrate; **(a)** adsorption isotherm of Kr at 77 K and **(b)** a photo.

The specific surface area of the film derived from Kr sorption measurements and related to substrate area, film total volume or film mass equals $112 \text{ cm}^2/\text{cm}^2$, $132 \text{ cm}^2/\text{cm}^3$ and $115 \pm 8 \text{ m}^2/\text{g}$, respectively. The estimated film porosity is 68% as calculated from the total volume of the film, its mass and anatase density. Using the pore volume calculated from the adsorption isotherm of Kr, the fraction of pores narrower than about 10 nm is 17%.

The nitrogen sorption data of the free-standing film prepared from the same precursor solution showed a BET surface area of $123 \text{ m}^2/\text{g}$. The similarity of the BET surface area of the powder determined by N_2 adsorption and that measured on the thin film by Kr sorption shows (i) that the films are homogeneous and (ii) that their porosity does not significantly change with the thickness and the deposition method.

Owing to the high porosity, high crystallinity and anatase phase present, the NCC-templated porous titania films deliver a high steady-state conversion efficiency of 16% in the photocatalytic oxidation of nitrogen(II) oxide. Its performance compares favourably with that of the “brick and mortar” mesoporous films templated by amphiphilic Pluronic polymer, which at the same conditions achieved a conversion of 10%.²

The reaction mechanism of the photocatalytic degradation of 4-chlorophenol is complicated but the overall decrease in the concentration of 4-chlorophenol can be described by a first-order reaction⁵³ (Figure A4.12 in the Appendix). The calculated first order rate constant for the photocatalytic decomposition of 4-chlorophenol on the NCC-

templated titania film equals 0.18 h^{-1} , which is 50% higher than the highest reported rate constant of 0.12 h^{-1} obtained at exactly the same conditions (especially the intensity of illumination and the illuminated area were identical) for a $1.5 \mu\text{m}$ and $456 \text{ cm}^2/\text{cm}^2$ roughness factor mesoporous sol-gel titania film prepared using Pluronic P123 block-copolymer.⁵³

4.2.3 Film Performance in Dye Sensitized Solar Cells

In addition to their high photocatalytic activity, the NCC-templated mesoporous titania films show excellent performance as thin anodes in dye-sensitized solar cells (DSCs) (Figure 4.5 and Table 4.1).

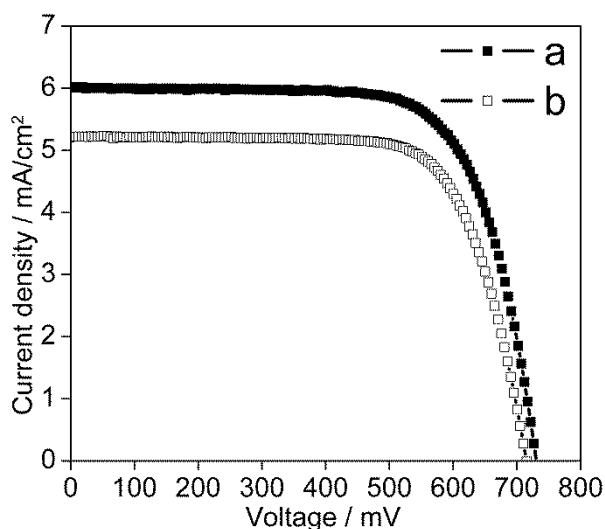


Figure 4.5. *I-V* curves of DSSCs prepared with (a) $1.8 \mu\text{m}$ NCC-templated mesoporous titania film acting as an active electrode (solid squares) compared to the performance of (b) a $2.5 \mu\text{m}$ thick anode made of sintered 20 nm titania nanoparticles (open squares). The anodes were sensitized with N719 dye and assembled in a sandwich-type cell with volatile I^-/I_3^- electrolyte and Pt-counter electrode. The photovoltaic performance was measured at AM 1.5 G at $100 \text{ mW}/\text{cm}^2$ full sunlight illumination. The active cell area was 0.159 cm^2 .

Table 4.1. Photovoltaic parameters of the dye-sensitized solar cells made with different titania anodes, N719 dye and I^-/I_3^- electrolyte. The cells were measured under AM 1.5 G at $100 \text{ mW}/\text{cm}^2$ full sun irradiation

Titania anode	Film thickness, μm	J_{sc} , mA/cm^2	V_{oc} , mV	FF , %	η , %
(a) NCC-templated	1.8	6.02	731	70.9	3.12
(b) Sintered NPs	2.5	5.24	715	72.2	2.70

A film of only 1.8 μm thickness obtained by the subsequent coating of 4 layers (see Experimental section for detailed description of the synthesis) delivers a short circuit current density J_{sc} of 6.02 mA/cm^2 at full sunlight (AM 1.5 G). A reference cell based on a 2.5 μm titania film made of 20 nm sintered titania nanoparticles tested at the same conditions showed a lower performance, which is due to the significantly lower surface area of the titania layer prepared by the sintering approach.

4.3 Conclusions

In this study we have demonstrated that novel porous titania thin film morphologies can be obtained by biotemplating with nanocrystalline cellulose (NCC). The main advantages of the NCC template compared to the traditionally used 'soft templates' such as surfactant micelles include shape persistence, higher temperature stability and tunable dimensions. The combination of these features permits tailoring the film morphology by varying the composition of the precursor mixture, the processing conditions, and post deposition treatments.

At a given NCC concentration, the concentration of the titania precursor is decisive for the resulting titania crystal size in the pore walls. To achieve the formation of a highly-porous structure, the crystal size should be smaller than 12 nm. The surface area can be varied in the range from 61 to 175 m^2/g by adjusting the template content. In addition, considerable pore expansion is achieved with a hydrothermal post-synthetic treatment, leading to a two-fold increase in the total pore volume and an increase in the mean pore size from 9 to 13.5 nm.

To sum up, considerable changes in the surface area, pore size and total pore volume can be realized with the same template by a moderate variation of the deposition conditions. We suggest that the pore formation in the NCC-templated titania is mainly influenced by (i) the initial dimensions of cellulose rods, (ii) titania crystallization rate around the NCC rods, (iii) the NCC arrangement in the precursor solution and during the film coating and (iv) the NCC thermal decomposition.

NCC templating offers the potential to supersede conventional approaches towards porous titania for diverse applications. The sustainable starting materials are widely

available, and NCC-templated titania networks can be easily modified according to the requirements for the resulting materials or devices. Moreover, recent work in our laboratories shows that due to the unique properties cellulose nanocrystals this approach can also be extended to the fabrication of crystalline mesoporous thin films of other oxides.

4.4 Experimental

4.4.1 Synthesis

NCC preparation. The cellulose crystals were extracted from cotton linters CP20 (Peter Temming AG) by sulfuric acid hydrolysis according to a modified procedure mentioned elsewhere.^{29,54} 300 mL 64% H₂SO₄ was added to 34 g cotton. After 1 h the mixture was heated to 55 °C for 30 min. The linters dissolved completely and the solution became slightly yellow. Then the suspension was tenfold diluted with deionized water. Afterwards it was left overnight to sediment the NCC-containing fraction. The upper liquid phase was decanted and the NCC-rich lower phase was washed three times with water via repeated centrifugation. The last centrifugation step was performed at 500 rpm in order to remove large cellulose aggregates. Finally, the suspension was concentrated up to 9–11 wt % at pH 1.7–2.3.

Precursor preparation. Concentrated HCl was added to titanium(IV) ethoxide (TEOT) and the mixture was stirred approximately 10 min. After the full dissolution of TEOT the required amounts of NCC suspension were introduced, and then water was added. The mixture was stirred for 2 h before the film deposition. The composition of precursor solutions is defined by the following parameters: titania to NCC mass ratio, Ti⁴⁺ concentration in mol/L and NCC wt % concentration. TiO₂/NCC ratio 1.0 means that the NCC amount in grams was equal to the titania amount in grams calculated from the titanium ethoxide content in a precursor solution. Ti⁴⁺ concentration in mol/L was calculated taking into account volumes of all liquid components of a precursor solution. NCC wt % concentration indicates the percentage of the NCC amount relative to the total precursor mass. For example, the precursor solution with a TiO₂/NCC ratio 0.75, 2.5 wt % NCC and 0.23 mol/L Ti⁴⁺ was prepared according to the following recipe:

0.2143 g (0.9395 mmol) titanium(IV) ethoxide, 153 mg (1.846 mmol) 37% HCl, 1.155 g of 8.70 wt % NCC water suspension and 2.49 mL H₂O.

Film fabrication. The thin films for the SEM analysis were deposited on a 1.5 × 2.0 cm² silicon wafer by spin-coating 80 µl precursor solution at 2000 rpm for 40 s. X-ray diffraction, nitrogen sorption and thermogravimetric analysis was performed on pulverized free-standing films. For their fabrication the precursor solution was cast into a plastic Petri dish and dried at RT. Then the films were exposed to humidity or calcined directly. For the *delayed humidity treatment (DHT)*, the free-standing films were placed into a 2 L desiccator containing 80 mL KCl saturated solution and kept in oven at 70 °C or 100 °C for 0.5–48 h. The films were calcined by using a stepwise 2 °C/min ramp with 2 h-steps of continuous heating at 100 °C, 360 °C and a final step 450 °C/30 min.

For the photocatalytic measurements and krypton sorption analysis, the 250 µl of precursor (TiO₂ g/NCC g = 0.75, 2.5 wt % NCC, 0.23 mol/L Ti⁴⁺) was spin-coated on 2.5 × 2.5 cm² optical glass at 1500 rpm for 30 s followed by 1 min film drying with a heat gun and N₂ flow. The spin-coating and drying were repeated 5 times. Then the film was calcined by using 2 °C/min ramp with 2 h-steps of continuous heating at 100 °C, 360 °C and final calcination at 500 °C/30 min. After the calcination additional 5 layers were deposited in a similar way and calcined at 500 °C/30 min. The weight of the 10-layered film coated on 2.5 × 2.5 cm² substrate was equal to 0.630 ± 0.05 mg measured by using Mettler Toledo analytical balances (0.01mg/0.1mg readability).

For the photovoltaic measurements, the NCC-templated titania films were fabricated on 1.5 × 2.0 cm² FTO TEC-7 glass substrates coated with a dense titania blocking layers (100 µl solution of tetraethyl orthotitanate (0.525 mL), hydrochloric acid (37%, 0.375 mL) and tetrahydrofuran (7 mL) spin-coated at 4000 rpm for 40 s). NCC containing precursor (TiO₂/NCC = 1.0 g/g, 2 wt % NCC, 0.28 mol/L Ti⁴⁺) was dip-coated with 6 mm/s speed on top of the blocking layers. Then the films were placed in a 2 L desiccator containing 50 mL saturated KCl solution and kept in an oven at 70 °C/30 min with subsequent heating at 100 °C/30 min. The dip-coating and hydrothermal treatment steps were repeated four times. After the second and fourth layer the films were calcined at 500 °C/30 min by using 2 °C/min ramp with 2 h continuous heating steps at 100 °C and 360 °C, respectively. The anodes for the reference solar cells were

obtained by diluting with ethanol and spin-coating Dyesol 18 NRT paste on a FTO glass with a blocking layer. The films were calcined at 500 °C for 30 min with a 1 h-ramp.

Solar cell assembly. Solar cells were prepared by using a liquid iodine-based electrolyte, Pt-counter electrodes and N719 dye according to the recipes and cell assemblage mentioned elsewhere.⁵⁵ The titania films were reduced (by removal from the surface) to an area of $0.55 \times 0.55 \text{ cm}^2$, heated at 70 °C and then immersed into a 0.5 mM solution of N719 dye in a mixture of acetonitrile and *tert*-butyl alcohol (1:1). After 16 h, the dye-coated electrodes were placed in acetonitrile for 1 h. Counter Pt-electrodes were prepared by chemical deposition from 10 mM H_2PtCl_6 ethanol solution and heated at 450 °C for 15 min. The anode and the counter electrode were sealed on a hot plate by using 25 μm Surlyn spacer. Then the “sandwich” was vacuum back filled with the electrolyte through the pre-drilled hole in the Pt-electrode. The electrolyte solution contained 0.6 M butylmethylimidazolium iodide (BMII), 0.03 M iodine, 0.10 M guanidinium thiocyanate and 0.50 M 4-*tert*butylpyridine in a mixture of acetonitrile and valeronitrile (85:15). Finally, the hole was sealed by $1.5 \times 1.5 \text{ cm}^2$ Surlyn foil and a glass slide on top.

4.4.2 Characterization

Film top view imaging was performed on a JEOL JSM-6500F scanning electron microscope (SEM) equipped with a field emission gun, at 5 kV. High-resolution transmission electron microscopy (HRTEM) and scanning transmission electron microscopy in high-angle annual dark field mode (STEM-HAADF) was performed using a FEI Titan 80–300 equipped with a field emission gun operated at 80 kV and 300 kV.

For the cellulose rod imaging, a water suspension of NCCs was dropped on holey-carbon coated copper grid and dried overnight. The TEM analysis was carried out at 80 kV. HRTEM of the film cross-sections was performed at 300 kV by using STEM-HAADF mode. For the imaging of porous titania we scratched a thin film from a substrate or ground a free-standing film. Then the sample was dispersed in ethanol and the solution was dropped on a holey-carbon coated copper grid. The imaging was performed at 300 kV.

X-ray diffraction analysis was carried out in reflection mode by using a Bruker D8 diffractometer with 1.5406 Å Ni-filtered Cu K α radiation, operating at 40 kV and 40 mA. The mean crystallite size was calculated from broadening of the (101) anatase reflection by using the Scherrer equation.

The nitrogen sorption isotherms were obtained at $-196\text{ }^{\circ}\text{C}$ using a Quantachrome Autosorb-1. For the measurements 27 ± 3 mg of the sample was outgassed at $150\text{ }^{\circ}\text{C}$ overnight. The specific surface area was determined with the Brunauer-Emmett-Teller method at $p/p_0 = 0.05\text{--}0.2$. The pore size distribution was determined with a DFT/Monte-Carlo method and a NLDFT equilibrium model by using the Quantachrome Instruments Autosorb-1 software.

The krypton sorption isotherms at the boiling point of liquid nitrogen were obtained using an ASAP2010 (Micromeritics) apparatus. Three $2.5 \times 2.5\text{ cm}^2$ glass slides coated with porous titania film were measured simultaneously. Prior to the adsorption experiments, the sample was outgassed overnight at $200\text{ }^{\circ}\text{C}$. The saturation pressure of solid krypton of ca. 1.6 torr and the cross-section of the krypton molecule of 0.21 nm^2 (as recommended by the producer of the equipment) were used.

Thermogravimetric measurements were performed on a Netzsch STA 440 C TG/DSC with a heating rate of 1 K/min in a stream of synthetic air of about 25 mL/min . UV-VIS spectra were recorded with a Hitachi U-3501 spectrophotometer.

The experimental set-up for the photocatalytic tests consisted of a gas supply part, the photoreactor, and a chemiluminiscent NO-NO $_x$ gas analyzer (Horiba ambient monitor APNA-360). The gaseous reaction mixture was prepared by mixing streams of dry air (1500 mL/min), wet air (1500 mL/min , relative humidity of 100%) and 50 ppm NO/N_2 (approx. 60 mL/min), in order to obtain a final concentration of NO of 1 ppm at a relative humidity of 50%. The photoreactor was illuminated by four 8 W black lights, the UV light intensity achieving 1 mW/cm^2 . The size of the photocatalytic layer was $5 \times 10\text{ cm}^2$. Prior to the photocatalytic tests, the photoreactor was purged with the NO/water vapor/air mixture without illumination until a steady NO concentration was achieved at the outlet. It is readily calculated that 100% NO conversion would be equivalent to a photonic efficiency of $\xi = 0.14\%$, assuming a mean irradiation wavelength of 350 nm .

4-Chlorophenol was photocatalytically degraded in a vessel 55 mL in volume, its initial concentration being 1×10^{-4} mol/L. The solution in the vessel was kept at 25 °C. Photocatalytic experiments were carried out without bubbling. The level of the liquid in the photoreactors was open to air under magnetic stirring, i.e., the concentration of dissolved oxygen was constant during the experiment owing to its equilibration with oxygen in the ambient air. A Sylvania Lynx-S 11 W BLB lamp irradiated the films with a UV light power achieving 1 mW cm^{-2} at the film surface. The irradiated area of the TiO_2 film was 12.5 cm^2 . In each experiment, eight 0.5 mL aliquots were taken from the solution in the reaction vessel at regular time intervals and analyzed by HPLC.

The solar cells were illuminated at 100 mW/cm^2 with white light from an AM 1.5 G solar simulator (Solar Light Model 16S) equipped with a 150 W xenon lamp. The light intensity was adjusted by using a Fraunhofer ISE certified silicon reference cell.

4.5 References

- (1) O'Regan, B.; Gratzel, M. *Nature* **1991**, *353*, 737–740.
- (2) Szeifert, J. M.; Fattakhova-Rohlfing, D.; Georgiadou, D.; Kalousek, V.; Rathouský, J.; Kuang, D.; Wenger, S.; Zakeeruddin, S. M.; Grätzel, M.; Bein, T. *Chem. Mater.* **2009**, *21*, 1260–1265.
- (3) Brinker, C. J.; Lu, Y.; Sellinger, A.; Fan, H. *Adv. Mater.* **1999**, *11*, 579–585.
- (4) Soler-Illia, G. J. d. A. A.; Crepaldi, E. L.; Grosso, D.; Sanchez, C. *Curr. Opin. Colloid Interface Sci.* **2003**, *8*, 109–126.
- (5) Lu, A. H.; Schüth, F. *Adv. Mater.* **2006**, *18*, 1793–1805.
- (6) Lee, K.-R.; Kwon, Y.-U. *Nano* **2010**, *05*, 75–87.
- (7) Sun, X.; Zheng, C.; Qiao, M.; Yan, J.; Wang, X.; Guan, N. *Chem. Commun.* **2009**, *31*, 4750–4752.
- (8) He, W.; Cui, J.; Yue, Y.; Zhang, X.; Xia, X.; Liu, H.; Lui, S. *J. Colloid Interface Sci.* **2011**, *354*, 109–115.
- (9) Han, T. H.; Oh, J. K.; Park, J. S.; Kwon, S.-H.; Kim, S.-W.; Kim, S. O. *J. Mater. Chem.* **2009**, *19*, 3512–3516.
- (10) Yang, F.; Ma, Y.; Zhou, Y.; Pei, C.; Luo, Q.; Zeng, M.; Dai, B. *Curr. Nanosci.* **2011**, *7*, 1004–1008.
- (11) Jeffryes, C.; Campbell, J.; Li, H.; Jiao, J.; Rorrer, G. *Energy Environ. Sci.* **2011**, *4*, 3930–3941.
- (12) Shi, N.; Li, X.; Fan, T.; Zhou, H.; Ding, J.; Zhang, D.; Zhu, H. *Energy Environ. Sci.* **2011**, *4*, 172–180.
- (13) Jia, Y.; Han, W.; Xiong, G.; Yang, W. *J. Colloid Interface Sci.* **2008**, *323*, 326–331.
- (14) Losic, D.; Triani, G.; Evans, P. J.; Atanacio, A.; Mitchell, J. G.; Voelcker, N. H. *J. Mater. Chem.* **2006**, *16*, 4029–4034.
- (15) Chen, J.; Su, H.; Song, F.; Moon, W.-J.; Kim, Y.-S.; Zhang, D. *J. Colloid Interface Sci.* **2012**, *370*, 117–123.
- (16) Galusha, J. W.; Jorgensen, M. R.; Bartl, M. H. *Adv. Mater.* **2010**, *22*, 107–110.
- (17) Sachse, A.; Hulea, V.; Kostov, K. L.; Marcotte, N.; Boltoeva, M. Y.; Belamie, E.; Alonso, B. *Chem. Commun.* **2012**, *48*, 10648–10650.
- (18) KimLing, M. C.; Caruso, R. A. *J. Mater. Chem.* **2012**, *22*, 4073–4082.
- (19) Zollfrank, C.; Cromme, P.; Rauch, M.; Scheel, H.; Kostova, M. H.; Gutbrod, K.; Gruber, S.; Van Opdenbosch, D. *Bioinspired, Biomimetic Nanobiomater.* **2012**, *1*, 13–25.
- (20) Lin, N.; Huang, J.; Dufresne, A. *Nanoscale* **2012**, *4*, 3274–3294.
- (21) Tingaut, P.; Zimmermann, T.; Sebe, G. *J. Mater. Chem.* **2012**, *22*, 20105–20111.
- (22) Gu, Y.; Huang, J. *J. Mater. Chem.* **2009**, *19*, 3764–3770.

- (23) Pääkkö, M.; Ankerfors, M.; Kosonen, H.; Nykänen, A.; Ahola, S.; Österberg, M.; Ruokolainen, J.; Laine, J.; Larsson, P. T.; Ikkala, O.; Lindström, T. *Biomacromolecules* **2007**, *8*, 1934–1941.
- (24) Isogai, A.; Saito, T.; Fukuzumi, H. *Nanoscale* **2011**, *3*, 71–85.
- (25) Klemm, D.; Kramer, F.; Moritz, S.; Lindström, T.; Ankerfors, M.; Gray, D.; Dorris, A. *Angew. Chem. Int. Ed.* **2011**, *50*, 5438–5466.
- (26) Revol, J. F.; Bradford, H.; Giasson, J.; Marchessault, R. H.; Gray, D. G. *Int. J. Biol. Macromol.* **1992**, *14*, 170–172.
- (27) Dujardin, E.; Blaseby, M.; Mann, S. *J. Mater. Chem.* **2003**, *13*, 696–699.
- (28) Thomas, A.; Antonietti, M. *Adv. Funct. Mater.* **2003**, *13*, 763–766.
- (29) Shopsowitz, K. E.; Qi, H.; Hamad, W. Y.; MacLachlan, M. J. *Nature* **2010**, *468*, 422–425.
- (30) Shopsowitz, K. E.; Hamad, W. Y.; MacLachlan, M. J. *Angew. Chem. Int. Ed.* **2011**, *50*, 10991–10995.
- (31) Shopsowitz, K. E.; Hamad, W. Y.; MacLachlan, M. J. *J. Am. Chem. Soc.* **2011**, *134*, 867–870.
- (32) Shopsowitz, K. E.; Stahl, A.; Hamad, W. Y.; MacLachlan, M. J. *Angew. Chem. Int. Ed.* **2012**, *51*, 6886–6890.
- (33) Kettunen, M.; Silvennoinen, R. J.; Houbenov, N.; Nykänen, A.; Ruokolainen, J.; Sainio, J.; Pore, V.; Kemell, M.; Ankerfors, M.; Lindström, T.; Ritala, M.; Ras, R. H. A.; Ikkala, O. *Adv. Funct. Mater.* **2011**, *21*, 510–517.
- (34) Korhonen, J. T.; Hiekkataipale, P.; Malm, J.; Karppinen, M.; Ikkala, O.; Ras, R. H. A. *ACS Nano* **2011**, *5*, 1967–1974.
- (35) Zhang, D.; Qi, L. *Chem. Commun.* **2005**, 2735–2737.
- (36) Chen, X.-Y.; Chen X.; Hong, S.-W.; Chen, X.; Huang, B. *Chin. J. Catal.* **2011**, *32*, 1762–1767.
- (37) Liu, X.; Gu, Y.; Huang, J. *Chem. Eur. J.* **2010**, *16*, 7730–7740.
- (38) Li, X.; Fan, T.; Zhou, H.; Chow, S.-K.; Zhang, W.; Zhang, D.; Guo, Q.; Ogawa, H. *Adv. Funct. Mater.* **2009**, *19*, 45–56.
- (39) Ghadiri, E.; Taghavinia, N.; Zakeeruddin, S. M.; Grätzel, M.; Moser, J.-E. *Nano Lett.* **2010**, *10*, 1632–1638.
- (40) Lee, Y. M.; Kim, Y. H.; Lee, J. H.; Park, J. H.; Park, N.-G.; Choe, W.-S.; Ko, M. J.; Yoo, P. J. *Adv. Funct. Mater.* **2011**, *21*, 1160–1167.
- (41) Alonso, B.; Belamie, E., *Angew. Chem. Int. Ed.* **2010**, *49*, 8201–8204.
- (42) Belamie, E.; Boltoeva, M. Y.; Yang, K.; Cacciaguerra, T.; Alonso, B., *J. Mater. Chem.* **2011**, *21*, 16997–17006.
- (43) Shao, S.; Dimitrov, M.; Guan, N.; Kohn, R. *J. Mater. Chem.* **2009**, *19*, 8411–8417.
- (44) Li, X.; Birnbaum, J. C.; Williford, R. E.; Fryxell, G. E.; Coyle, C. A.; Dunham, G. C.; Baskaran, S. *Chem. Commun.* **2003**, *20*, 2054–2055.
- (45) Crepaldi, E. L.; Soler-Illia, G. J. d. A. A.; Grosso, D.; Cagnol, F.; Ribot, F.; Sanchez, C. *J. Am. Chem. Soc.* **2003**, *125*, 9770–9786.

- (46) Fulvio, P. F.; Grabicka, B. E.; Grudzien, R. M.; Jaroniec, M. *Adsorpt. Sci. Technol.* **2007**, *25*, 439–449.
- (47) Morishige, K.; Tateishi, M.; Hirose, F.; Aramaki, K. *Langmuir* **2006**, *22*, 9220–9224.
- (48) Cao, L.; Man, T.; Kruk, M. *Chem. Mater.* **2009**, *21*, 1144–1153.
- (49) Sayari, A.; Kruk, M.; Jaroniec, M.; Moudrakovski, I. L. *Adv. Mater.* **1998**, *10*, 1376–1379.
- (50) Aulin, C.; Ahola, S.; Josefsson, P.; Nishino, T.; Hirose, Y.; Österberg, M.; Wågberg, L. *Langmuir* **2009**, *25*, 7675–7685.
- (51) Szeifert, J. M.; Fattakhova-Rohlfing, D.; Rathouský, J.; Bein, T. *Chem. Mater.* **2012**, *24*, 659–663.
- (52) Procházka, J.; Kavan, L.; Shklover, V.; Zúkalová, M. t.; Frank, O.; Kalbáč, M.; Zúkal, A. t.; Pelouchová, H.; Janda, P.; Mocek, K.; Klementová, M.; Carbone, D. *Chem. Mater.* **2008**, *20*, 2985–2993.
- (53) Rathousky, J.; Kalousek, V.; Kolar, M.; Jirkovsky, J. *Photochem. Photobiol. Sci.* **2011**, *10*, 419–424.
- (54) Dong, X. M.; Kimura, T.; Revol, J.-F.; Gray, D. G. *Langmuir* **1996**, *12*, 2076–2082.
- (55) Ito, S.; Murakami, T. N.; Comte, P.; Liska, P.; Grätzel, C.; Nazeeruddin, M. K.; Grätzel, M. *Thin Solid Films* **2008**, *516*, 4613–4619.

4.6 Appendix

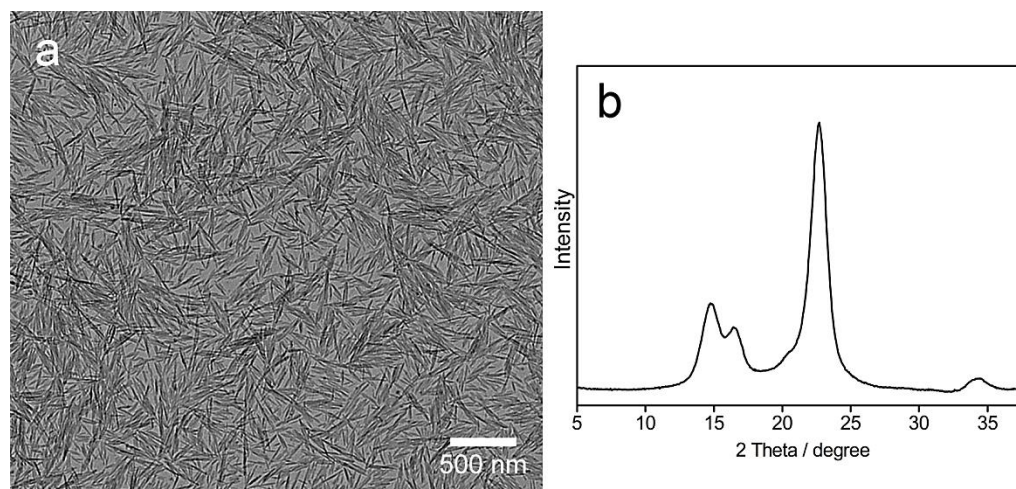


Figure A4.1. (a) TEM image of cellulose nanocrystals extracted from cotton. The image analysis reveals the mean crystal dimensions of 10 ± 2 nm in width and 117 ± 34 nm in length by measuring 75 and 50 nanocrystals, respectively. (b) XRD pattern of the nanocrystalline cellulose extracted from cotton. The diffraction pattern corresponds to the I_{β} cellulose with a domain size in [200] direction of about 7 nm.

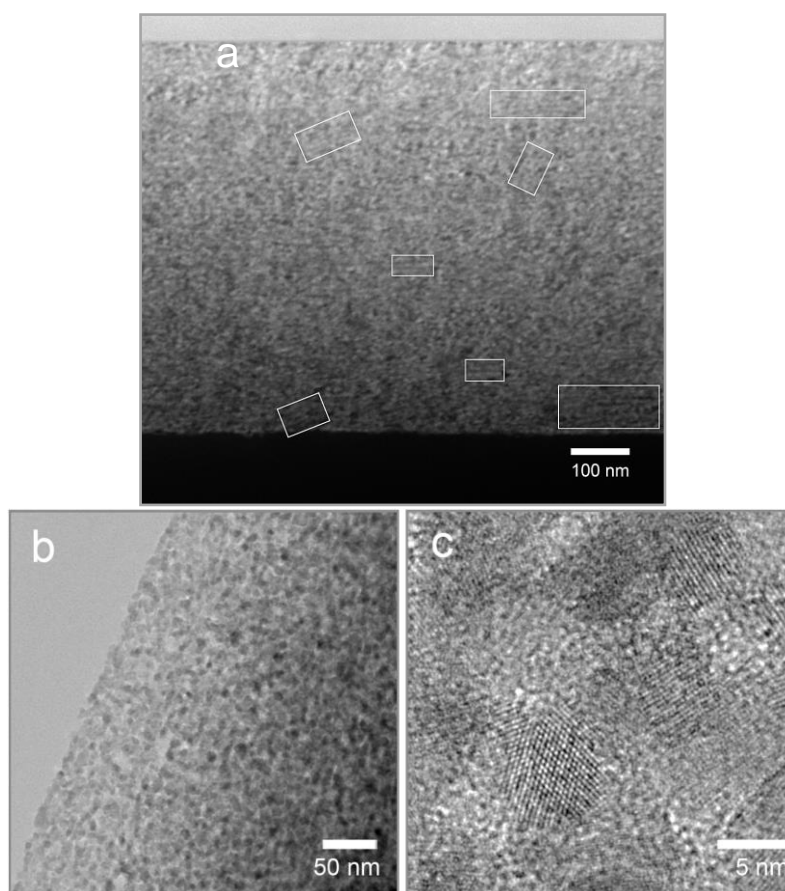


Figure A4.2. A HAADF-STEM cross section images at different magnifications (a-c) of the porous titania film dip-coated on a Si-wafer from a solution with a ratio $TiO_2/NCC = 0.5$ g/g, 4 wt % NCC and 0.27 mol/L Ti^{4+} . Highlighted areas represent domains of aligned titania “threads” (bright areas) and elongated pores in between (dark areas) (a).

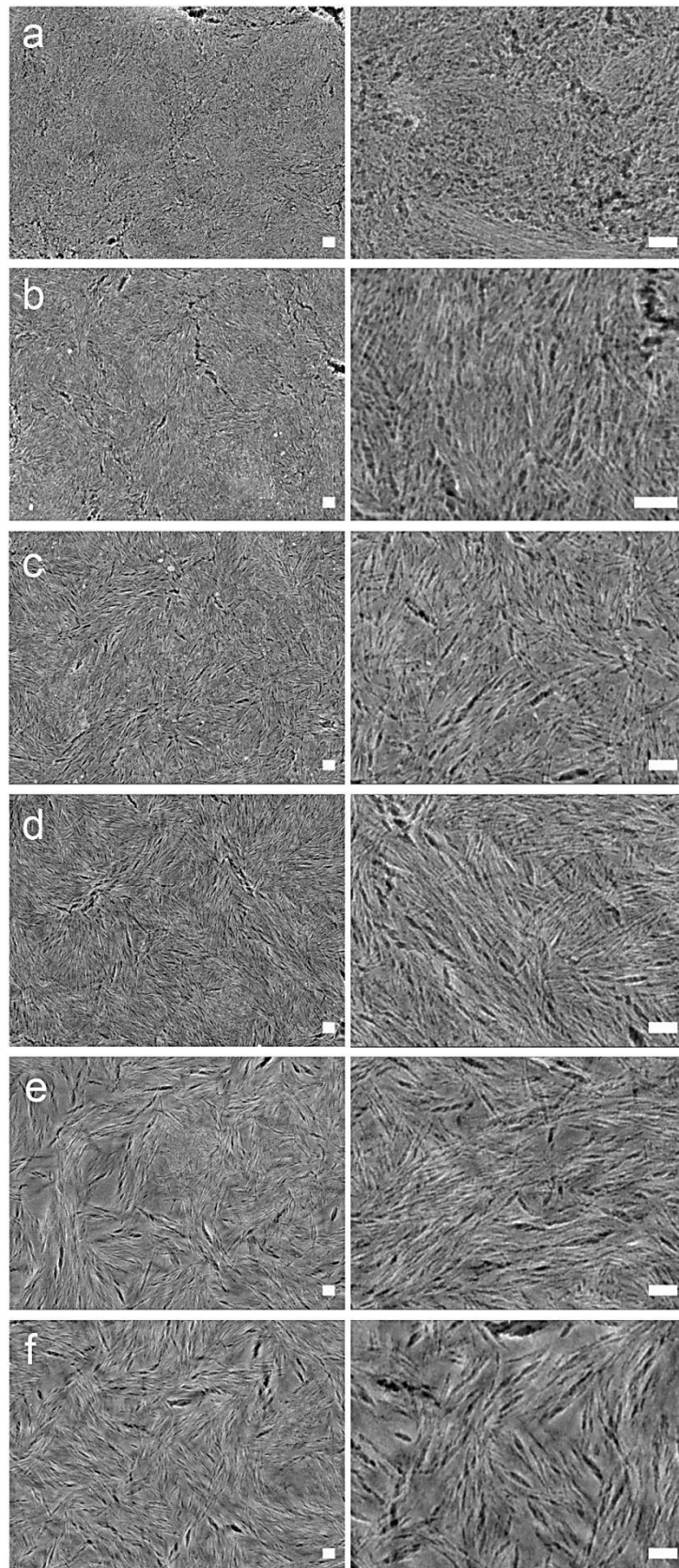


Figure A4.3. Low (left) and high (right) magnification top view SEM images showing the morphology changes of NCC-templated titania thin films depending on the TEOT concentration in the precursor solution: TiO_2/NCC mass ratios of 0.25 **(a)**, 0.5 **(b)**, 1.0 **(c)**, 1.5 **(d)**, 2.0 **(e)**, 2.5 **(f)** and NCC concentration 2.5 wt %. The scale bar corresponds to 100 nm.

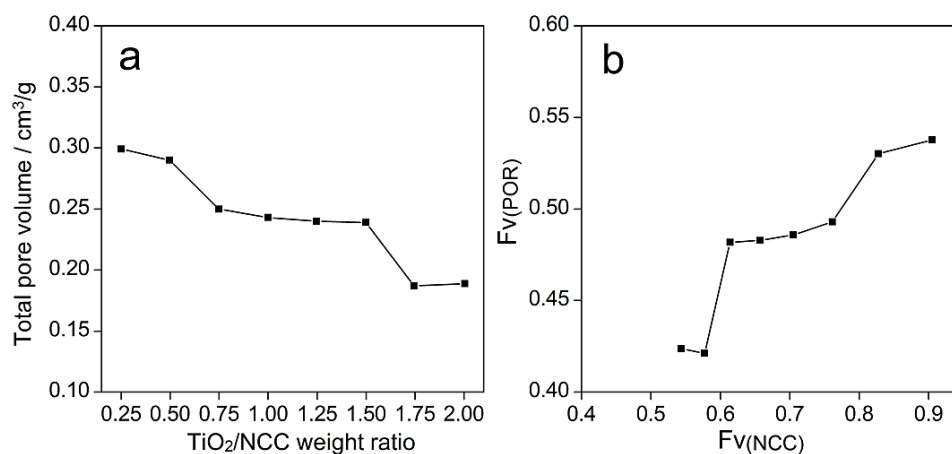


Figure A4.4. (a) Total pore volume of NCC-templated titania prepared from 0.27 mol/L TEOT solutions with different TiO₂/NCC weight ratios. The pore volume was calculated from N₂ sorption isotherms at $p/p_0 = 0.93$. **(b)** Variations of the pore volume fraction in titania $F_{V(\text{POR})}$ as a function of the estimated initial nanocellulose volume fraction $F_{V(\text{NCC})}$ in the composite prior to calcination. $F_{V(\text{POR})}$ was calculated from the adsorbed N₂ volume at $p/p_0 = 0.93$ and the anatase density of 3.89 cm³/g. $F_{V(\text{NCC})}$ was estimated by using the weight ratio of the titania to template in the precursor and a cellulose crystal density of 1.63 cm³/g.

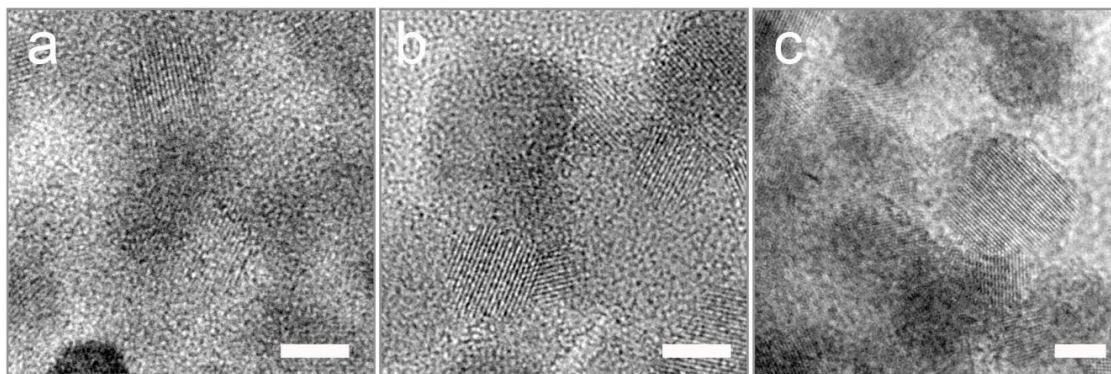


Figure A4.5. TEM images of free-standing films prepared from solutions with 0.25 **(a)**, 0.75 **(b)** and 2.0 **(c)** g/g oxide/template ratio. The scale bars correspond to 5 nm.

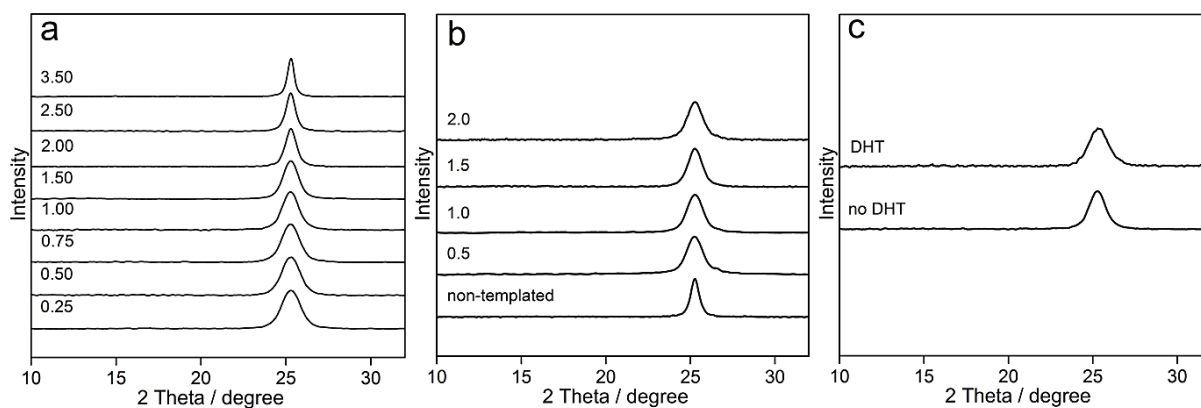


Figure A4.6. X-ray diffractograms of non-templated and NCC-templated TiO_2 after calcination. **(a)** X-ray diffraction patterns of titania prepared from precursor solutions with different TEOT contents and TiO_2/NCC mass ratios from 0.25 to 3.5. The TEOT concentration increase leads to the narrowing of the anatase signal. **(b)** X-ray diffraction patterns of non-templated samples and samples prepared from the 0.27 mol/L TEOT precursor solutions with different NCC contents and TiO_2/NCC mass ratios from 0.5 to 2.0. The NCC-templated samples show a broad anatase signal which shape does not significantly change upon increase in NCC concentration. **(c)** XRD patterns of biotemplated titania prepared with and without delayed humidity treatment (DHT and no DHT, respectively) prior to calcination. The greater line broadening of the DHT sample indicates smaller dimensions of the titania crystallites, compared to the non-treated sample. The mean crystallite sizes calculated from the anatase main reflections are 6.5 nm and 8 nm, respectively.

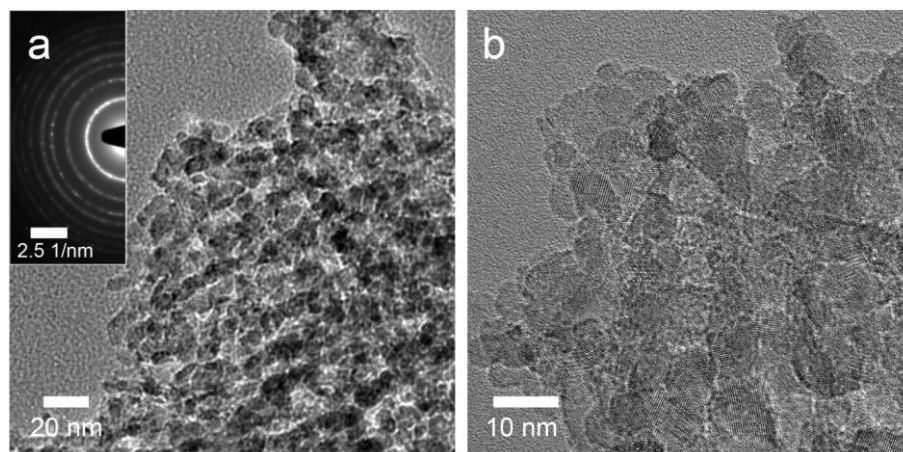


Figure A4.7. Low **(a)** and **(b)** high magnification top view TEM images of porous titania film templated by cellulose nanocrystals ($\text{TiO}_2/\text{NCC} = 1.5 \text{ g/g}$, 2.5 wt % NCC, 0.47 mol/L Ti^{4+}) spin-coated on a Si-wafer and isolated from the substrate for the TEM analysis.

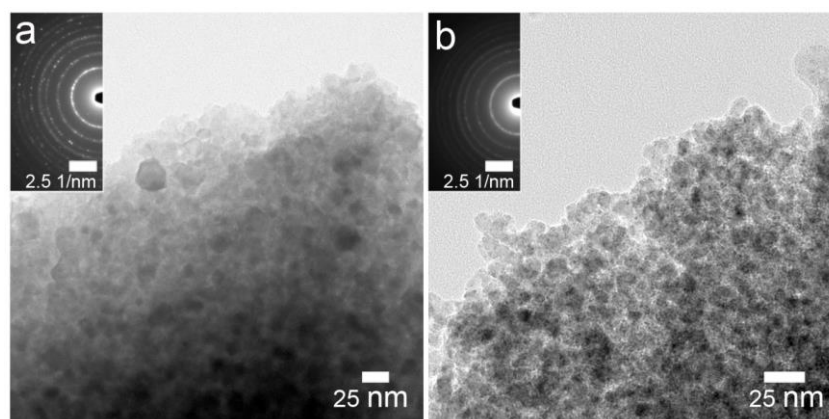


Figure A4.8. TEM images of TiO_2 cast film prepared without **(a)** and with **(b)** NCC template, the TiO_2/NCC mass ratio in the precursor solution equalling 0.75 g/g.

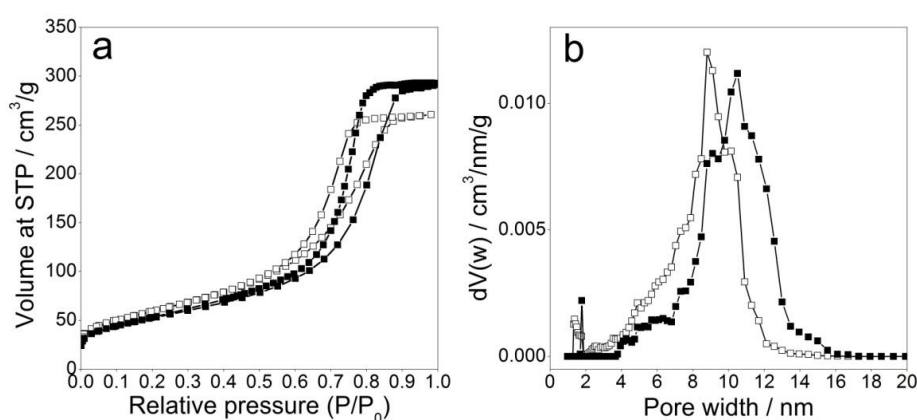


Figure A4.9. N_2 sorption isotherms **(a)** and pore size distributions **(b)** of porous titania calcined at $450\text{ }^\circ\text{C}$ for 30 min by using $3\text{ }^\circ\text{C}/\text{min}$ fast ramp (\square) and $2\text{ }^\circ\text{C}/\text{min}$ slow ramp with 2 h heating at $100\text{ }^\circ\text{C}$ and $360\text{ }^\circ\text{C}$ (\blacksquare).

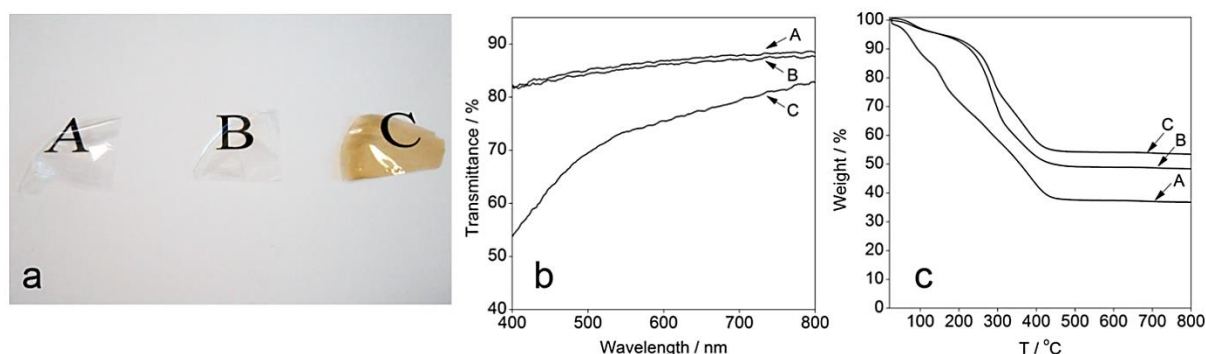


Figure A4.10. Digital photograph **(a)**, UV/VIS spectra **(b)** and TGA curves **(c)** of the NCC free-standing films (figures a, b) and NCC/ TiO_2 composite (figure c) before (A) and after (B, C) postsynthetic treatment. Sample C was heated at $70\text{ }^\circ\text{C}/30\text{ min}$ (figures a, b) or $100\text{ }^\circ\text{C}/48\text{ h}$ (figure c) in ambient air; Sample B was identically thermally treated as C but in extra humid atmosphere. The brownish colouring and transparency loss indicates the NCC degradation (sample C), which is noticeably retarded when the sample is heated in humidity (sample B) **(a,b)**. In addition, the weight loss TGA data reveal larger NCC content in the composite B posttreated in humidity then in the sample C heated in ambient air **(c)**.

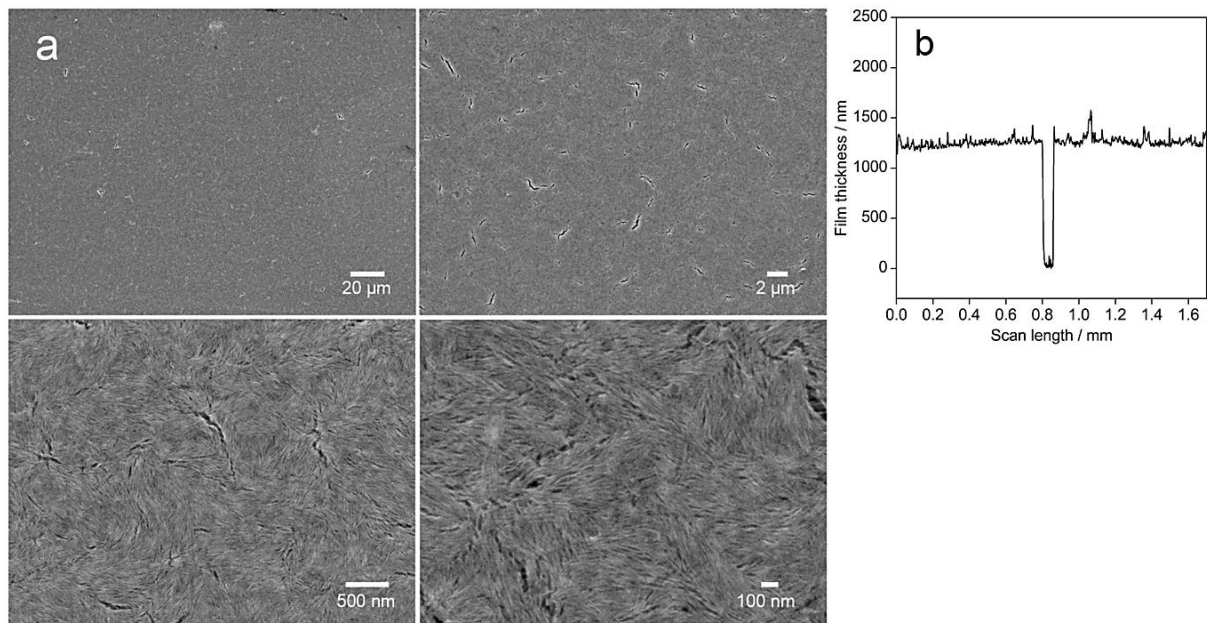


Figure A4.11. (a) SEM images of a 1.2 μm thick NCC-templated titania on FTO glass at different magnifications. (b) The surface profile revealing the film thickness. The film profile was measured over a thin scratch made in the middle of the film. The film was prepared by repeated dip-coating of a precursor solution ($\text{TiO}_2/\text{NCC} = 1.0 \text{ g/g}$, 2 wt % NCC, 0.28 mol/L Ti^{4+}) followed by DHT and calcination at 450 °C.

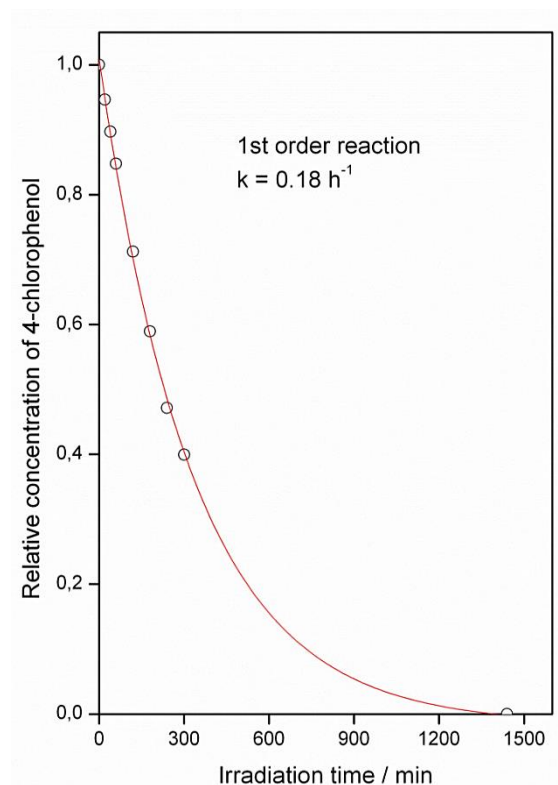
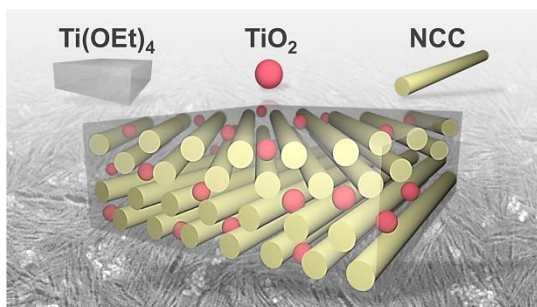


Figure A4.12. Photocatalytic degradation of 4-chlorophenol on NCC-templated titania porous film of 850 nm thickness coated on a $2.5 \times 2.5 \text{ cm}^2$ glass substrate.

5 Nanocellulose-Templated Porous Titania Scaffolds Incorporating Presynthesized Titania Nanocrystals



This chapter is based on the following publication:

Alesja Ivanova, Maria Fravventura, Dina Fattakhova-Rohlfing, Jiri Rathouský, Liana Movsesyan, Pirmin Ganter, and Thomas Bein. Nanocellulose-templated porous titania scaffolds incorporating presynthesized titania nanocrystals.

Chem. Mater. **2015**, DOI:0.1021/acs.chemmater.5b00770.

5.1 Introduction

Nanostructured titania films on solid supports offer significant benefits for photocatalytic applications^{1,2} compared to the commonly used powder morphologies. In contrast to powders, the immobilized titania can be easily separated from reaction mixtures. Furthermore, due to high mechanical stability and transparency, titania thin films are attractive for self-cleaning and antibacterial surface applications, where the optical appearance is important for practical use. However, a major challenge for the design of efficient photocatalytic coatings compared to powders is the low amount of photoactive material that can be deposited as a stable film. In order to achieve competitive conversion efficiencies, titania thin coatings require a high surface area, which is typically introduced by porosity. At the same time, a high crystallinity of the

titania scaffold is required for efficient charge separation and minimized recombination losses. Owing to the great practical importance of nanostructured crystalline titania films, numerous synthetic routes have already been developed.³⁻¹⁰ Various templating approaches including evaporation-induced self-assembly (EISA)¹¹ offer a high degree of control over the porous morphology. The latter method is based on a co-assembly of titania precursors (typically colloidal titania oligomers) and species acting as porosity template (such as supramolecular aggregates of amphiphilic molecules). EISA became a very popular technique for the fabrication of mesoporous titania films due to an unprecedented degree of control over the size, shape and spatial arrangement of the pores with very high specific surface areas, which is advantageous for photocatalytic applications. Nonetheless, the charge transport properties of the resulting titania scaffolds are usually inferior.¹² This can be attributed to limited control over the crystallization of the titania phase under the conditions of self-assembly, which additionally results in a partial loss of porosity.

More flexibility in obtaining the desirable high porosity crystalline scaffolds can be achieved by decoupling the process of crystallization from that of porous structure formation, hence enabling independent optimization of the crystallinity and porosity parameters, respectively. This can be realized by using preformed crystalline titania precursors for assembling the porous structure, or by a synergistic combination of different titania sources. One example of the latter strategy is the so called titania “brick and mortar” process introduced by our group, which combines the favorable features of crystalline and amorphous precursors.^{13,14} Here the formation of the fully crystalline interconnected porous titania is achieved by the fusion of preformed nanocrystalline “bricks” with a structure-directing matrix of surfactant-templated sol-gel titania.

The synergistic effect of both titania sources during calcination dramatically enhances the performance of the material, in particular the crystallinity and the photocatalytic activity of the films containing preformed nanoparticles. Nevertheless, further optimization of the properties of the titania scaffolds is restricted by the use of the soft surfactant templates, which limit the size range of the crystalline “bricks”, the processing parameters and calcination temperatures.¹⁵ As we show here, these limitations can be overcome by the use of rigid nanoscale templates, whose self-assembly is much less dependent on the film fabrication conditions.

Nanocrystalline cellulose (NCC) extracted from natural cellulose sources¹⁶⁻¹⁸ is a promising biogenic template for the generation of porosity in inorganic oxides.^{19,20,21,22} Cellulose nanocrystals act simultaneously as a thickener and as a porogen, thus enabling a straightforward deposition of mesoporous films on different substrates.²³ Owing to the rigidity and the thermal stability of the cellulose nanocrystals, the titania-cellulose composites can be calcined at high temperatures and produce fully crystalline titania networks with well-defined mesostructure.

Here we demonstrate the versatility and flexibility of the NCC templating approach for the formation of crystalline titania films with a highly porous structure. In particular we expand the synthesis route suggested in our previous work²³ by introducing pre-synthesized crystalline anatase particles into the NCC replicated titania scaffold. For the synthesis of the anatase nanocrystals we chose the hydrothermal procedure commonly used for the fabrication of high quality titania for photovoltaic purposes.²⁴

Our nanostructuring approach is based on the self-assembly of two types of precursors, namely crystalline and sol-gel titania, directed by the biogenic NCC template. We show that due to the shape persistence of the template, the NCC-templated titania scaffolds can accommodate large amounts of preformed titania without a significant reduction of the film porosity. This opens the possibility to tune the crystalline properties of the porous scaffold by using different types of preformed nanoparticles.

5.2 Experimental

5.2.1 Synthesis

Extraction of cellulose nanocrystals. The nanocrystalline cellulose (NCC) was extracted from Peter Temming AG cotton linters CP20 by hydrolysis with sulphuric acid.²⁵ The cotton fibers were washed with water and dried at 60 °C. 64% H₂SO₄ was added to cotton fibers at the ratio of 1 mL acid to 8.75 g cellulose. The mixture was kept at room temperature for 1 h. Then it was heated to 55 °C for 30 min under vigorous stirring until large cellulose aggregates dissolved. Afterwards the suspension was tenfold diluted with de-ionized water and stored overnight. The upper liquid phase was decanted and

the NCC-rich lower phase was washed three times with water via repeated centrifugation at 47808 g relative centrifugal force (RFC) for 15 min. The last centrifugation step was performed at 70 g RFC for 10 min in order to sediment cellulose aggregates and to collect the suspension of finely dispersed NCC. Finally, the suspension was concentrated in a rotary evaporator up to 6–10 wt % at pH 2.6–2.8.

Synthesis of preformed titania nanoparticles. Titania nanoparticles (NPs) were prepared according to a modified procedure mentioned elsewhere.²⁴ Acetic acid (1.00 g, 0.0167 mol) was added to titanium(IV) iso-propoxide (4.737 g, 0.0167 mol) under stirring and the solution was stirred for 15 min at room temperature. Then 24.2 mL water was quickly added. A white precipitate was formed. The hydrolysis continued while stirring the mixture for 1 h at room temperature. Following this step, 0.33 mL concentrated nitric acid was added. The mixture was then heated from room temperature to 80 °C within 40 minutes and peptized for 1h 15 min. An additional 0.57 mL water was introduced. Afterwards the mixture was placed in an autoclave and heated at 200 °C for 16 h 30 min. After the hydrothermal treatment, 0.2 mL of 65% nitric acid was added and the solution was sonicated for 10 min. Then the colloidal solution was washed three times with water via multiple centrifugation. At last, the dispersion was rotary evaporated to contain 11–14 wt % titania.

Preparation of precursor solutions for the NCC-templated dual source titania films. The films were prepared from precursors with a total Ti^{4+} concentration of 0.3 mol/L, 1.0 g/g titania to NCC weight ratio, 1.65 mol/mol 37% hydrochloric acid to titanium(IV) ethoxide (TEOT) and different contents of preformed titania nanoparticles (NPs). NP amounts were varied from 5 to 100% relative to the total amount of Ti^{4+} in the form of NPs and TEOT.

For the preparation of 75% NP precursor, 0.074 g (0.751 mmol) 37% hydrochloric acid was added to 0.1074 g (0.471 mmol) titanium(IV) ethoxide in a 5 mL vial under stirring. After the solution became clear, 0.9951 g of 11.3 wt % nanoparticle and 2.4431 g of 6.15 wt % nanocrystalline cellulose solutions were subsequently introduced. Finally, 3.25 g (0.181 mol) water was added. The 50% NP precursor solution contained 0.155 g (1.573 mmol) 37% hydrochloric acid, 0.2158 g (0.946 mmol) titanium(IV) ethoxide, 0.6668 g of 11.3 wt % NP solution, 2.4389 g of 6.15 wt % nanocrystalline cellulose solution and

3.62 g (0.201 mol) water. The 25% NP precursor solution contained 0.2280 g (2.314 mmol) 37% hydrochloric acid, 0.3213 g (1.409 mmol) titanium(IV) ethoxide, 0.3345 g of 11.3 wt % NP solution, 2.4483 g of 6.15 wt % nanocrystalline cellulose solution, and 3.63 g (0.202 mol) of extra-added water. The 0% NP thin films were deposited by using the precursor with 0.4293 g (1.882 mmol) titanium(IV) ethoxide, 0.306 g (3.105 mmol) 37% hydrochloric acid, 3.2555 g of 6.15 wt % NCC solution and 4.42 g (0.246 mol) of extra-added water. The 100% NP thin films were deposited by using the precursor with 1.3263 g of 11.3 wt % NP solution, 2.444 g of 6.15 wt % NCC solution and 1.75 g (0.097 mol) g of extra-added water. The precursor solutions were stirred for about 3 h prior the film deposition.

Film fabrication. For the morphological investigations the titania thin films were deposited on $1.5 \times 2.0 \text{ cm}^2$ silicon wafers by spin-coating a 100 μL precursor solution at 1500 rpm for 30 s. The rest of the solution was cast on a $6 \times 6 \text{ cm}^2$ Teflon surface. The films were calcined at 500 °C/30 min by using 2 °C/min ramp with 2 h continuous heating steps at 100 °C and 360 °C, respectively. Pulverized cast films were analyzed by using X-ray diffraction and nitrogen sorption measurements.

For the photocatalytic and microwave conductivity measurements 200 μL of precursor solution was spin-coated on $2.5 \times 2.5 \text{ cm}^2$ optical glass or quartz at 1500 rpm for 30 s followed by 1 min film drying with a heat gun and N_2 flow. The spin-coating and drying steps were repeated 4, 3, 2 and 2 times for 25, 50, 75 and 100% NP films respectively, to achieve about 1 μm thickness of the resulting film after calcination. The 0% NP film was prepared by spin-coating 10 layers at 1500 rpm for 30 s followed by 1 min film drying with a heat gun and N_2 flow with additional full calcination after coating the first 5 layers. To deposit a 100% NP non-templated film, 11 wt % aqueous dispersion of preformed nanoparticles was deposited and spin-coated 6 times. As a last step, the films were calcined at 500 °C with the stepwise ramp mentioned above.

5.2.2 Characterization

Film top view imaging was performed on a JEOL JSM-6500F scanning electron microscope (SEM) equipped with a field emission gun, at 5 kV. Transmission electron microscopy (TEM) was performed using a FEI Titan 80–300 equipped with a field

emission gun operated at 300 kV. An aqueous suspension of titania nanocrystallites was dropped on holey-carbon coated copper grid and dried overnight prior to TEM analysis. For the imaging of porous titania we removed the thin films from the substrate and dispersed them in ethanol. Then the dispersion was dropped on a holey-carbon coated copper grid. The imaging was performed at 300 kV.

X-ray diffraction (XRD) analysis was carried out in reflection mode by using a Bruker D8 diffractometer with 1.5406 Å Ni-filtered Cu K α radiation, operating at 40 kV and 40 mA. The mean crystallite size was calculated from the broadening of the (101) anatase reflection by using the Scherrer equation.

The nitrogen sorption isotherms were obtained at $-196\text{ }^{\circ}\text{C}$ using a Quantachrome Autosorb-1. The specific surface area was determined with the Brunauer-Emmett-Teller method at $p/p_0 = 0.05\text{--}0.2$. The pore size distribution was determined with a DFT/Monte-Carlo method and a cylindrical pore NLDFT equilibrium model for silica by using the Quantachrome Instruments Autosorb-1 software.

In photocatalytic activity tests the NCC-templated titania films on $2.5 \times 2.5\text{ cm}^2$ glass slides were employed to degrade 4-chlorophenol in a vessel 55 mL in volume with the initial concentration being $1 \times 10^{-4}\text{ mol/L}$. The solution in the vessel was kept at $25\text{ }^{\circ}\text{C}$. Three glass substrates with coated titania films were simultaneously measured, which corresponds to a total titania film mass of about 1.5 mg for each type of sample. Photocatalytic experiments were carried out without bubbling. The level of the liquid in the photoreactors was open to air under magnetic stirring, i.e., the concentration of dissolved oxygen was constant during the experiment owing to its equilibration with oxygen in the ambient air. A Sylvania Lynx-S 11 W BLB lamp irradiated the films with a UV light power achieving 1 mW cm^{-2} at the film surface. The irradiated area of the TiO $_2$ film was 12.5 cm^2 . In each experiment, eight 0.5 mL aliquots were taken from the solution in the reaction vessel at regular time intervals and analyzed by HPLC.

For the reference measurements 2.5 mg of powder AEROXIDE TiO $_2$ P90 (surface area of $90\text{ m}^2/\text{g}$, average primary particle size of approx. 14 nm, Evonik) was used to degrade 4-chlorophenol in a vessel 55 mL in volume, the initial chlorophenol concentration being $1 \times 10^{-4}\text{ mol/L}$. The solution in the vessel was kept at $25\text{ }^{\circ}\text{C}$. Photocatalytic experiments were carried out without bubbling. The level of the liquid in the

photoreactors was open to air under magnetic stirring, i.e., the concentration of dissolved oxygen was constant during the experiment owing to its equilibration with oxygen in the ambient air. The irradiation was exactly the same as in the experiments with films. In each experiment, eight 0.5 mL aliquots were taken from the solution in the reaction vessel at regular time intervals and analyzed by HPLC.

The microwave conductivity measurements were performed using the experimental setup fully described elsewhere.^{26–28}

5.3 Results and Discussion

5.3.1 Effect of Preformed Anatase on Morphology

For the fabrication of the NCC-templated dual source titania we added an aqueous suspension of nanocrystalline cellulose (NCC) to a mixed titania precursor system containing amorphous and crystalline titania at different ratios. The amorphous titania was prepared by the hydrolysis of titanium ethoxide (TEOT), while titania nanoparticles (NP) synthesized by hydrothermal reaction were used as the crystalline counterpart.²⁴

The hydrothermal synthesis route provides nearly spherical crystalline anatase nanoparticles with a mean size of around 11 nm and only a minor fraction of anisotropic and rhombic species (Figure A5.1 in the Appendix). The amount of preformed nanoparticles in the mixed titania precursor was varied from 0 to 100%, where the percentage is related to the total titania content (of both nanoparticles and TEOT) in the precursor solution. The precursor solutions were stirred for about 3 h at room temperature (RT), then spin-coated or drop-cast on substrates and subsequently calcined at 500 °C. After calcination the template was completely removed from the composite films leaving behind the porous scaffolds of crystalline titania (TGA curves are shown in Figure A5.2 in the Appendix).

The SEM images in Figure 5.1 and Figure A5.4 in the Appendix demonstrate that the titania films after calcination feature two distinct types of morphology depending on the percentage of the preformed nanoparticles in the precursor solution.

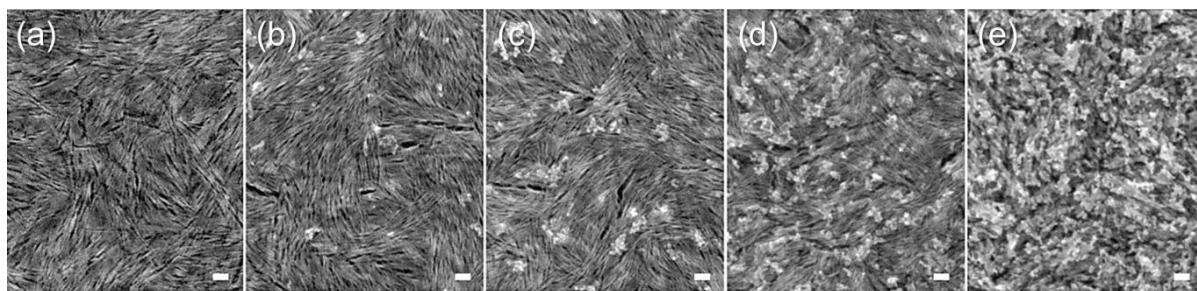


Figure 5.1. SEM images of porous dual source titania films showing the evolution of morphology depending on the content of preformed titania nanoparticles: 0% (a), 5% (b), 10% (c), 30% (d), and 50% (e). Scale bars correspond to 100 nm.

In Figure 5.1a the film prepared from amorphous precursor without the crystalline nanoparticles reveals a uniform mesoporous morphology composed of slit-shaped mesopores. The pore walls are formed by small intergrown anatase crystallites, which in fact replicate the shape of the NCC template rods. In contrast, the porosity of the films containing more than 50 wt % nanoparticles is disordered, featuring rather undefined pore shapes and higher roughness (Figure 5.1e and Figures A5.3, A5.4 in the Appendix). Hence, with high nanoparticle contents the effect of the NCC on the mesostructure becomes much less pronounced than in the case of a high fraction of amorphous titania precursor. Moderate amounts of nanoparticles (up to 30 wt %) gradually modify the character of the NCC-assisted porosity. Figures 5.1b-d reveal that in this case the nanoparticles are homogeneously distributed in the mesoporous network, although they tend to form clusters of a few nanometers in size.

The corresponding nitrogen sorption isotherms in Figure 5.2 show that the nature of the mesoporosity of the samples strongly depends on the content of nanoparticles. The films containing up to 10% nanoparticles feature type IV isotherms with the hysteresis between adsorption and desorption branches typical for mesoporous materials with relatively narrow pores.

The mean pore size obtained from the isotherms corresponds to about 10 nm. With increasing particle content above 10% the inflection points of the adsorption and desorption branches gradually shift towards higher relative pressures due to an increase in the pore size. The shapes of these isotherms correspond to a material with non-uniform pores with broad pore size distributions. The addition of nanoparticles slightly reduces the BET surface area from 156 to 113 m²/g for 0% and 100%

nanoparticle samples, respectively (Table 5.1). These textural changes can be attributed to the increasing pore wall thickness because of the incorporated nanoparticles.

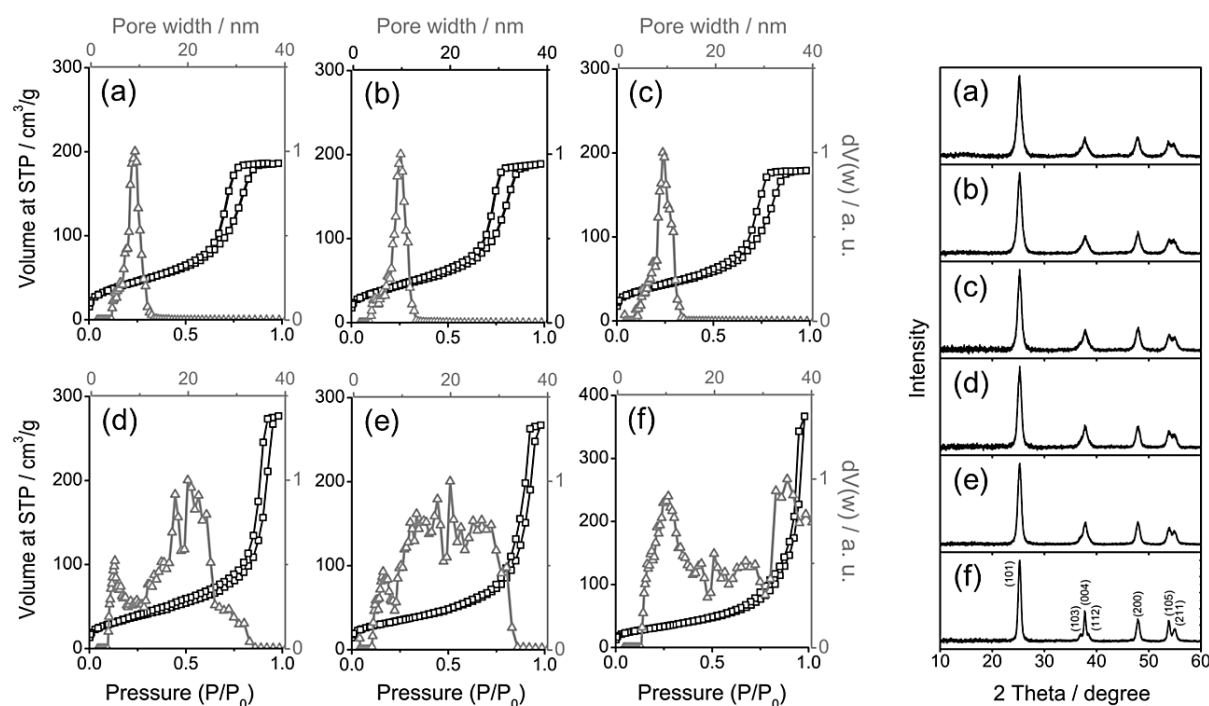


Figure 5.2. Nitrogen sorption isotherms with corresponding pore size distributions (left) and X-ray diffraction patterns (right) of calcined NCC-templated titania prepared by casting the precursor solutions with different amounts of preformed titania nanoparticles: (a) 0%, (b) 5%, (c) 10%, (d) 30%, (e) 50%, (f) 100%. The indexed reflections correspond to the anatase phase.

Table 5.1. Porosity data and average sizes of titania crystallites in NCC-templated titania after calcination depending on the content of preformed titania particles: 0%, 5%, 10%, 30%, 50% and 100%

NP content, %	Surface area ^a , $S_{BET}(N_2)$, m ² /g	Total pore volume at $p/p_0 = 0.95$ ^a , V , cm ³ /g	Pore width ^a , d_1 , nm	Mean crystallite size ^b , $d_2 \pm 0.5$, nm
0	156	0.288	9.1	8.1
5	148	0.291	9.8	8.4
10	147	0.277	9.1	9.5
30	130	0.327	19.9	10.2
50	117	0.385	19.9	10.5
100	113	0.352	35.0	14.6

^a calculated from N₂ sorption isotherms shown in Figure 5.2.

^b calculated from the broadening of the (101) anatase reflection by using the Scherrer equation.

As indicated by the narrowing of the XRD signals shown in Figure 5.2, the addition of preformed nanoparticles leads to a gradual increase in the mean size of crystalline

titania domains after calcination. The size of the crystalline domains increases from ca. 9 nm to about 15 nm for the films containing 0% and 100% nanoparticles, respectively (Table 5.1). TEM images in Figures 5.3 and A5.3b in the Appendix demonstrate that the films are completely crystalline after calcination, however the crystalline domains of the 75% nanoparticle sample are larger than in the pristine sol-gel templated titania (0% NP) with the mean dimensions of about 13 and 8 nm, respectively.

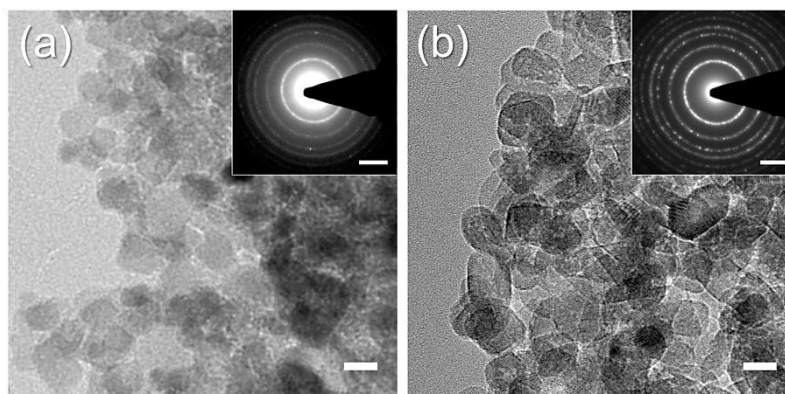


Figure 5.3. TEM images revealing the morphology and crystallinity of the NCC-templated titania thin films prepared from the titania sol-gel precursor (a, 0% nanoparticles) and from the precursor containing crystalline titania (b, 75% nanoparticles). The scale bars are 10 nm. The insets show the selected area electron diffraction (SAED) patterns of the corresponding images (the scale bars are 2.5 1/nm).

Although the calcination was performed at a high temperature of 500 °C, the titania crystals formed in the NCC-templated composite remain rather small. The average size of the crystalline domains in the films containing 0–10% nanoparticles is around 8.9 ± 0.5 nm, which is smaller than the initial mean size of the preformed nanocrystals prepared by hydrothermal synthesis at 200 °C. We attribute this effect to low mobility of the titania species in the dried NCC/sol-gel titania composite and to a restricted crystal growth due to the surrounding rigid cellulose matrix. Under the conditions of the hydrothermal reaction, titania crystals are formed in a solvent-rich environment and at high temperatures facilitating the efficient crystal feeding and the formation of defect-poor species.

Composites containing 30–50% nanoparticles exhibit an average particle size of about 10.4 ± 0.5 nm, which is larger than in the case of the sol-gel titania precursor. A substantially increased content of added crystalline nanoparticles facilitates the crystallization and crystal growth in the dual source titania films. We note that the growth of titania crystallites in the films prepared via particle sintering as well as in the

films nanostructured by soft templates (e.g. amphiphilic polymers) can be achieved by changing the calcination protocol, i. e. its temperature and duration, however only at the expense of drastically decreasing surface area.²⁹ In the dual source titania system we achieve an increase of the mean size of titania crystallites without changing the calcination temperature, while preserving the porosity generated by NCC to a large extent.

5.3.2 Microwave Conductivity

Intrinsic properties of semiconductors, namely the ability to generate and transfer charge carriers upon photoexcitation, play an important role in the kinetics of photocatalytic reactions. To elucidate the electronic properties of the porous dual source titania films, we performed time resolved microwave conductivity (TRMC) measurements. TRMC is a reliable contactless technique for the characterization of charge-carriers in low-conductivity media such as polycrystalline titania.

In TRMC analysis the sample is excited by a 3 ns laser pulse at a wavelength of 300 nm and probed by continuous X-band microwaves (~ 8.5 GHz). The charge carriers photogenerated in these conditions absorb a fraction $\Delta P(t)/P$ of the microwave power proportional to the photoconductance $\Delta G(t)$ induced in the sample, according to:

$$\frac{\Delta P(t)}{P} = -K \cdot \Delta G(t) \quad (5.1)$$

The sensitivity factor K has a value of $40 \times 10^3 \text{ S}^{-1}$ in our experimental conditions. $\Delta G(t)$ is directly proportional to the product of the yield of mobile charge carriers per incident photon, η and the sum of mobilities $\Sigma\mu$ of light-induced charge carriers according to:

$$\eta \Sigma\mu = \frac{\Delta G_{max}}{e\beta I_0} \quad (5.2)$$

Here, e is the elementary charge, β is the ratio between the broad and narrow inner dimensions of the microwave waveguide and I_0 is the incident photon fluence. It was previously reported that in anatase TiO_2 the electron mobility is more than one order of magnitude larger than the hole mobility, hence electron motion dominates the TRMC signal.³⁰ Owing to the weak electric field of the microwave probe ($\sim 100 \text{ V/cm}$), the measured mobilities refer to small displacements of the charge carriers (few nm),

describing mostly intra-particle rather than inter-particle electron mobility (especially if the TiO_2 nanocrystals are larger than 20 nm and not sintered together).

For the TRMC investigations the transparent anatase films were coated on quartz slides from precursor solutions with different fractions of preformed nanoparticles (Figures A5.5 and A5.6 in the Appendix). Since the films absorb more than 90% light at the photoexcitation wavelength of 300 nm, the presented data have not been normalized to the fraction of absorbed photons.

The transients recorded at 10^{14} photons/cm² in Figure 5.4a indicate that the films containing presynthesized titania species give a much higher photoconductance signal compared to the 0% NP sample. The signal intensities obtained from the 75% and 100% NP dual source titania are about four times larger compared to the 0% NP sample.

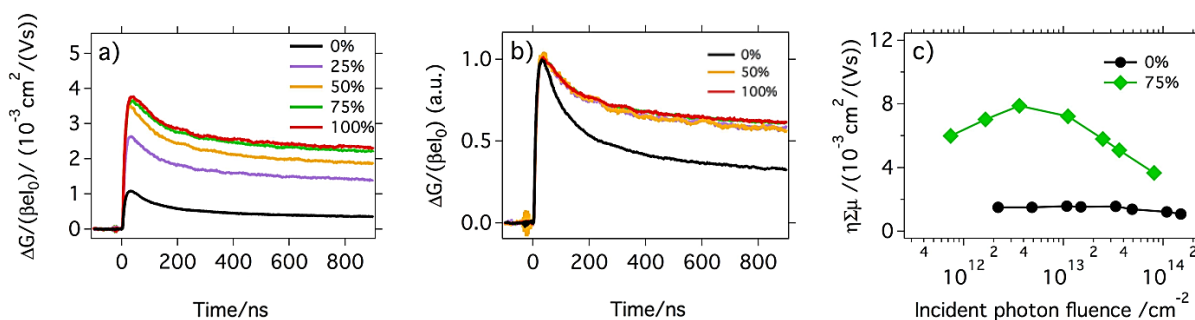


Figure 5.4. TRMC data measured upon 300 nm excitation of NCC-templated titania films prepared without (black lines) and with (colored lines) addition of preformed titania species (25–100%). (a) Decay kinetics and corresponding normalized decay kinetics (b) of TRMC traces recorded at about 10^{14} photons/cm² fluence. (c) Fluence dependence of the maxima of the TRMC traces.

The decays of the normalized photoconductance signals in Figures 5.4b reveal a rather similar behavior for the dual source titania films (colored lines), while the 0% NP titania sample exhibits significantly faster decay kinetics (black line). The decay profile of photoconductance is strongly determined by the time-dependent decrease in the population of charge carriers due to electron-hole recombination and electron diffusion towards deep traps. A high decay rate in titania photocatalysts has been previously attributed to the trapping of electrons.³¹ Therefore the decay profile exhibited by the pristine (sol-gel) NCC-templated scaffold points to a higher recombination and electron trapping compared to the NP containing samples. The overlap between the decay dynamics of the latter samples confirms that, as discussed above, we are probing the

motion of the same type of charge carriers (mainly conduction band electrons) experiencing the same relaxation paths.

For a more detailed analysis we investigated the evolution of the photoconductance response depending on the incident photon fluence for the most and least conductive samples, which are 75% and 0% NP films, respectively. The data in Figure 5.4c clearly show a strongly enhanced photoconductance of 75% NP titania film compared to the 0% NP sample in the whole range of measured photon fluences. The distinct bell-shape of the TRMC signals shown by the 75% NP film is typical for the nanocrystalline titania. The signal maximum is related to the presence of deep electron traps in the material. After reaching the maximum, the magnitude of the signal decreases; this behavior was previously assigned to higher order electron-hole recombination processes.^{30,32}

To sum up, the measured photoconductance responses differ significantly for the pure sol-gel and the nanoparticle-containing titania. The increase of the photoconductance and the reduced decay rates observed for the films containing preformed anatase nanoparticles indicate higher charge mobilities and slower recombination than in the unmodified NCC-templated titania.

We attribute the positive effect of nanoparticles on conductivity to the beneficial combination of titania of different origin and improved crystal quality of the resulting titania scaffolds. It is well known that the optoelectronic properties of titania strongly depend on the way of its fabrication and especially on the quality of the crystalline titania phase.^{33,34} Hydrothermally synthesized and commercially available titania species tend to outperform the sol-gel derived titania in numerous applications.³⁵ In addition to the crystal quality, the increasing size of titania crystalline domains in the mesoporous scaffold reduces the number of grain boundaries and enlarges the interparticle contact area, providing faster transport in the film.^{34,36} Thus, by modifying the NCC-templated films with preformed anatase particles we were able to prolong the lifetime of photogenerated charges and to reduce their recombination rate.

5.3.3 Photocatalytic Performance

In a next step, we investigated the effect of nanoparticle addition on photocatalytic performance of the titania films structured with NCC. The films coated on glass were

employed for the photodegradation of 4-chlorophenol in aqueous solutions. The decomposition of 4-chlorophenol on the surface of titania may depend on many factors, although the titania crystallinity and the amount of surface area accessible for the reactant are usually considered key factors. The effect of porosity induced by the NCC is evident from the comparison of the performance of the films prepared from nanoparticles with and without template (samples 100% NP (\blacktriangle) and 100% NP n-t (\bullet) in Figure 5.5 and Table 5.2, respectively).

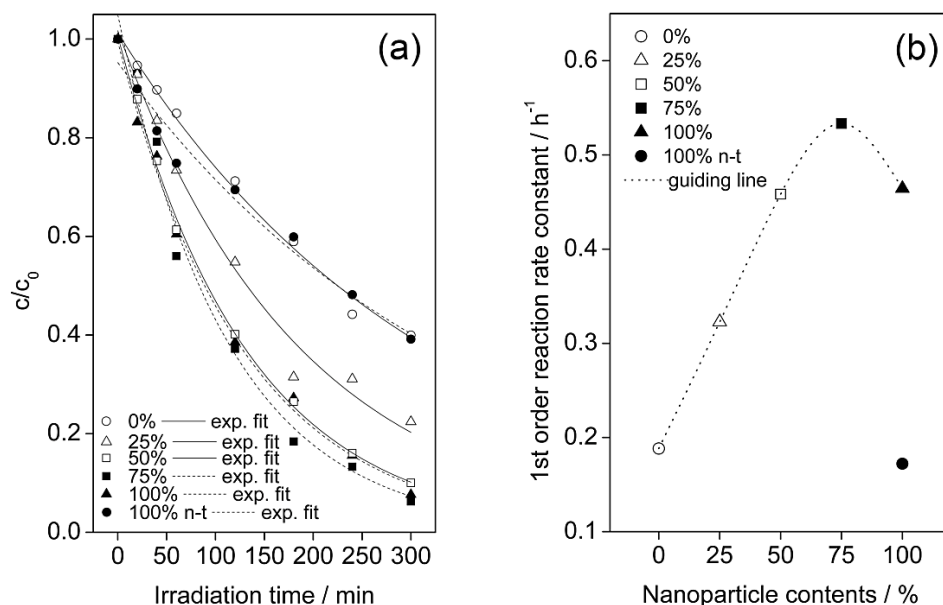


Figure 5.5. (a) The effect of the percentage of incorporated preformed anatase nanoparticles on the photocatalytic performance of the dual source NCC-templated titania films in the photodegradation of 4-chlorophenol. (b) Variation of the 1st order rate constant with the percentage of preformed anatase nanoparticles.

Table 5.2. Overview of the photocatalytic performance of dual source titania films templated by NCC with different contents of preformed anatase nanoparticles

NP content, %	Mean film thickness, μm	1 st order rate constant of the photocatalytic degradation of 4-chlorophenol, h^{-1}	Half life time of the photocatalytic degradation of 4-chlorophenol, min
0	1.0	0.19	221
25	0.7	0.30	129
50	1.5	0.46	90
75	1.0	0.53	78
100	1.7	0.46	90
100 n-t ^a	0.9	0.17	241

^a n-t = non-templated

The non-templated sample (n-t in Table 5.2) shows significantly slower photodegradation of 4-chlorophenol than the NCC replicated sample, although the crystallinity of the films is comparable in this case. This drastic change is due to the beneficial porosity induced by biogenic templating. The generated pores provide high accessibility of the surface and high local, intrapore concentration of the reactant, and thus accelerate the photocatalytic reactions.

Interestingly, the NCC-templated films prepared from amorphous titania (0% NP) show the lowest 1st order rate constant in 4-chlorophenol degradation compared to the other cellulose-replicated films, although this sample possesses the highest porosity (Table 5.1). On the other hand, less porous films prepared from nanoparticles only (100% NP) exhibit much higher photocatalytic activity than the purely sol-gel derived one. This indicates that high surface area is not the only decisive factor determining the performance of the NCC-templated dual source titania.

Figure 5.5b reveals that the preformed anatase nanoparticles significantly enhance the photocatalytic performance of the NCC-templated titania. Although all the films are crystalline after the calcination at 500 °C, the size of the crystalline domains and the quality of the titania phase differ depending on the titania source employed in the synthesis. According to the photoconductivity measurements, the preformed nanoparticles strongly enhance the photoconductivity, which can be due to the larger particle size and also due to the lower amount of bulk defects in the particles obtained in the hydrothermal synthesis compared to the sol-gel derived material. As shown before, the enhancement of crystallinity suppresses the surface recombination and assures more efficient charge separation. Moreover, it has been demonstrated that for titania particles smaller than 30 nm in size, the photoactivity strongly scales with the particle size.³⁷

We found that the highest rate constant of the photocatalytic degradation of 4-chlorophenol was obtained for the films containing 75% of preformed anatase species. The average size of the crystalline domains and the porosity of these films is neither the largest nor the smallest among the samples studied. According to our previous study, the addition of sol-gel titania improves the connectivity and crystallinity of the

performed anatase in “brick and mortar” films.¹³ A similar phenomenon is evidently valid for the NCC-templated dual source titania films discussed here.

Importantly, the photocatalytic activity of the NCC-templated porous films is significantly higher than that of the films templated with amphiphilic polymers. Owing to the thermal stability of cellulose nanocrystals, we could apply higher calcination temperatures than in the block-copolymer based “brick and mortar” approach without losing the porous texture. Therefore even the films prepared by only NCC templating (0% NP) already show higher activity compared to the “brick and mortar” mesoporous titania films templated with amphiphilic block copolymers.^{13,23}

The photocatalytic performance of thin titania layers is commonly compared to that of commercially available self-cleaning glasses, which feature a crystalline titania film of about 15 nm thickness.³⁸ However, due to the different intended application, the self-cleaning glasses are not sufficiently active in water purification, which requires an efficient degradation of rather stable compounds such as chlorophenols. Another option for a reliable reference is to prepare thin films from commercially available titania powders such as P25 and P90 titanium dioxide, which show high photocatalytic activity and are commonly taken as standard materials for various photocatalytic processes. The major issue with the use of powders for thin film applications is the difficulty in processing, as the films deposited without binders are not mechanically stable and consequently not sufficiently reproducible.

We have compared the performance of the NCC titanium dioxide films with that of the powder P90 in a well-stirred solution at exactly the same experimental conditions (concentration, reactor volume, temperature, stirring, illumination). The 1st order rate constants of the photocatalytic degradation of 4-chlorophenol of about 0.5 h⁻¹ for the most active NCC-templated samples (total film mass of about 1.5 mg) compares favorably with that obtained for a 2.5 mg dispersion of P90 (0.17 h⁻¹). Even if these data are not completely comparable (the activity of the dispersed powders is expected to be higher due to the absence of mass transport limitations), they clearly show that the NCC replicated titanium dioxide layers exhibit a very high photocatalytic activity in the degradation of 4-chlorophenol.

5.4 Conclusions

Different amounts of preformed anatase nanocrystals have been introduced into porous titania scaffolds replicated by nanocrystalline cellulose. By using this strategy we are able to tune the crystallinity of the films without changing the calcination temperature. Simultaneously, the dual source films demonstrate high surface areas and high porosities. We show that the gradual increase in the relative nanoparticle amounts significantly affects film morphology and its performance, namely conductivity and photocatalytic activity.

Time resolved microwave conductivity measurements demonstrate an enhanced photoconductivity of biotemplated titania containing preformed anatase nanoparticles. Furthermore, the photocatalytic performance of NCC-derived porous films drastically increases owing to the incorporation of preformed titania species. The dual source titania films show a more than two-fold enhancement in 4-chlorophenol degradation rate compared to the film prepared by simple sintering of nanoparticles.

The highest degradation rate of 0.53 h^{-1} among the studied samples was obtained for the NCC-templated titania containing 75% presynthesized nanoparticles. Hence by combining titania of different origins together with the efficient cellulose templating method we achieve a significant enhancement in the performance of the titania thin films. We anticipate that the network templated by nanocrystalline cellulose is a perfect matrix for the incorporation of species with target functionality due to its rigidity, defined porosity and straightforward synthesis. We conclude that NCC templating is a powerful and versatile approach for introducing photocatalytically active species into semiconducting oxides.

5.5 References

- (1) Fujishima, A.; Rao, T. N.; Tryk, D. A. *J. Photochem. Photobiol., C* **2000**, *1*, 1–21.
- (2) Han, F.; Kambala, V. S. R.; Srinivasan, M.; Rajarathnam, D.; Naidu, R. *Appl. Catal., A* **2009**, *359*, 25–40.
- (3) Antonelli, D. M.; Ying, J. Y. *Angew. Chem., Int. Ed. Engl.* **1995**, *34*, 2014–2017.
- (4) Yang, P.; Zhao, D.; Margolese, D. I.; Chmelka, B. F.; Stucky, G. D. *Nature (London)* **1998**, *396*, 152–155.
- (5) Grosso, D.; Soler-Illia, G. J. d. A. A.; Babonneau, F.; Sanchez, C.; Albouy, P.-A.; Brunet-Bruneau, A.; Balkenende, A. R. *Adv. Mater. (Weinheim, Ger.)* **2001**, *13*, 1085–1090.
- (6) Crepaldi, E. L.; de Soler-Illia, G. J.; Grosso, D.; Cagnol, F.; Ribot, F.; Sanchez, C. *J. Am. Chem. Soc.* **2003**, *125*, 9770–9786.
- (7) Bartl, M. H.; Boettcher, S. W.; Frindell, K. L.; Stucky, G. D. *Acc. Chem. Res.* **2005**, *38*, 263–271.
- (8) Galusha, J. W.; Jorgensen, M. R.; Bartl, M. H. *Adv. Mater.* **2010**, *22*, 107–110.
- (9) Marszewski, M.; Jaroniec, M. *Langmuir* **2013**, *29*, 12549–12559.
- (10) Fattakhova-Rohlfing, D.; Zaleska, A.; Bein, T. *Chem. Rev.*, **2014**, *114*, 9487–9558.
- (11) Sanchez, C.; Boissière, C.; Grosso, D.; Laberty, C.; Nicole, L. *Chem. Mat.* **2008**, *20*, 682–737.
- (12) Docampo, P.; Guldin, S.; Leijtens, T.; Noel, N. K.; Steiner, U.; Snaith, H. J. *Adv. Mater.* **2014**, *26*, 4013–4030.
- (13) Szeifert, J. M.; Fattakhova-Rohlfing, D.; Georgiadou, D.; Kalousek, V.; Rathouský, J.; Kuang, D.; Wenger, S.; Zakeeruddin, S. M.; Grätzel, M.; Bein, T. *Chem. Mater.* **2009**, *21*, 1260–1265.
- (14) Fulvio, P. F.; Mayes, R. T.; Wang, X.; Mahurin, S. M.; Bauer, J. C.; Presser, V.; McDonough, J.; Gogotsi, Y.; Dai, S. *Adv. Funct. Mater.* **2011**, *21*, 2208–2215.
- (15) Grosso, D.; Cagnol, F.; Soler-Illia, G. J. D. A. A.; Crepaldi, E. L.; Amenitsch, H.; Brunet-Bruneau, A.; Bourgeois, A.; Sanchez, C. *Adv. Funct. Mater.* **2004**, *14*, 309–322.
- (16) Ranby, B. G. *Acta Chem. Scand.* **1949**, *3*, 649–650.
- (17) Habibi, Y.; Lucia, L. A.; Rojas, O. J. *Chem. Rev.* **2010**, *110*, 3479–3500.
- (18) Dufresne, A. *Mater. Today* **2013**, *16*, 220–227.
- (19) Dujardin, E.; Blaseby, M.; Mann, S. J. *Mater. Chem.* **2003**, *13*, 696–699.
- (20) Shopsowitz, K. E.; Qi, H.; Hamad, W. Y.; MacLachlan, M. J. *Nature* **2010**, *468*, 422–425.
- (21) Shopsowitz, K. E.; Stahl, A.; Hamad, W. Y.; MacLachlan, M. J. *Angew. Chem. Int. Ed.* **2012**, *51*, 6886–6890.
- (22) Kelly, J. A.; Giese, M.; Shopsowitz, K. E.; Hamad, W. Y.; MacLachlan, M. J. *Acc. Chem. Res.* **2014**, *47*, 1088.

- (23) Ivanova, A.; Fattakhova-Rohlfing, D.; Kayaalp, B. E.; Rathouský, J.; Bein, T. *J. Am. Chem. Soc.* **2014**, *136*, 5930–5937.
- (24) Ito, S.; Murakami, T. N.; Comte, P.; Liska, P.; Grätzel, C.; Nazeeruddin, M. K.; Grätzel, M. *Thin Solid Films* **2008**, *516*, 4613–4619.
- (25) Dong, X. M.; Kimura, T.; Revol, J.-F.; Gray, D. G. *Langmuir* **1996**, *12*, 2076–2082.
- (26) Kroeze, J. E.; Savenije, T. J.; Warman, J. M. *J. Am. Chem. Soc.* **2004**, *126* (24), 7608–7618.
- (27) Dehaas, M. P.; Warman, J. M. *Chem. Phys.* **1982**, *73* (1–2), 35–53.
- (28) Savenije, T. J.; Ferguson, A. J.; Kopidakis, N.; Rumbles, G. *J. Phys. Chem. C* **2013**, *117*, 24085–24103.
- (29) Guldin, S.; Hüttner, S.; Tiwana, P.; Orilall, M. C.; Ulgut, B.; Stefik, M.; Docampo, P.; Kolle, M.; Divitini, G.; Ducati, C.; Redfern, S. A. T.; Snaith, H. J.; Wiesner, U.; Eder, D.; Steiner, U. *Energy Environ. Sci.* **2011**, *4*, 225–233.
- (30) Savenije, T. J.; de Haas, M. P.; Warman, J. M. *Z. Phys. Chem.* **1999**, *212*, 201–206.
- (31) Katoh, R.; Furube, A.; Yamanaka, K.-I.; Morikawa, T. *J. of Phys. Chem. Lett.* **2010**, *1*, 3261–3265.
- (32) Fravventura, M. C.; Deligiannis, D.; Schins, J. M.; Siebbeles, L. D. A.; Savenije, T. J. *J. Phys. Chem. C* **2013**, *117*, 8032–8040.
- (33) Carneiro, J. T.; Savenije, T. J.; Moulijn, J. A.; Mul, G. *J. Phys. Chem. C* **2009**, *114*, 327–332.
- (34) Emilio, C. A.; Litter, M. I.; Kunst, M.; Bouchard, M.; Colbeau-Justin, C. *Langmuir* **2006**, *22*, 3606–3613.
- (35) Kowalska, E.; Remita, H.; Colbeau-Justin, C.; Hupka, J.; Belloni, J. *J. Phys. Chem. C* **2008**, *112*, 1124–1131.
- (36) Villanueva-Cab, J.; Jang, S.-R.; Halverson, A. F.; Zhu, K.; Frank, A. J. *Nano Letters* **2014**, *14*, 2305–2309.
- (37) Almquist, C. B.; Biswas, P. *J. Catal.* **2002**, *212*, 145–156.
- (38) Mills, A.; Lepre, A.; Elliott, N.; Bhopal, S.; Parkin, I. P.; O'Neill, S. *J. Photochem. Photobiol. A* **2003**, *160*, 213–224.

5.6 Appendix

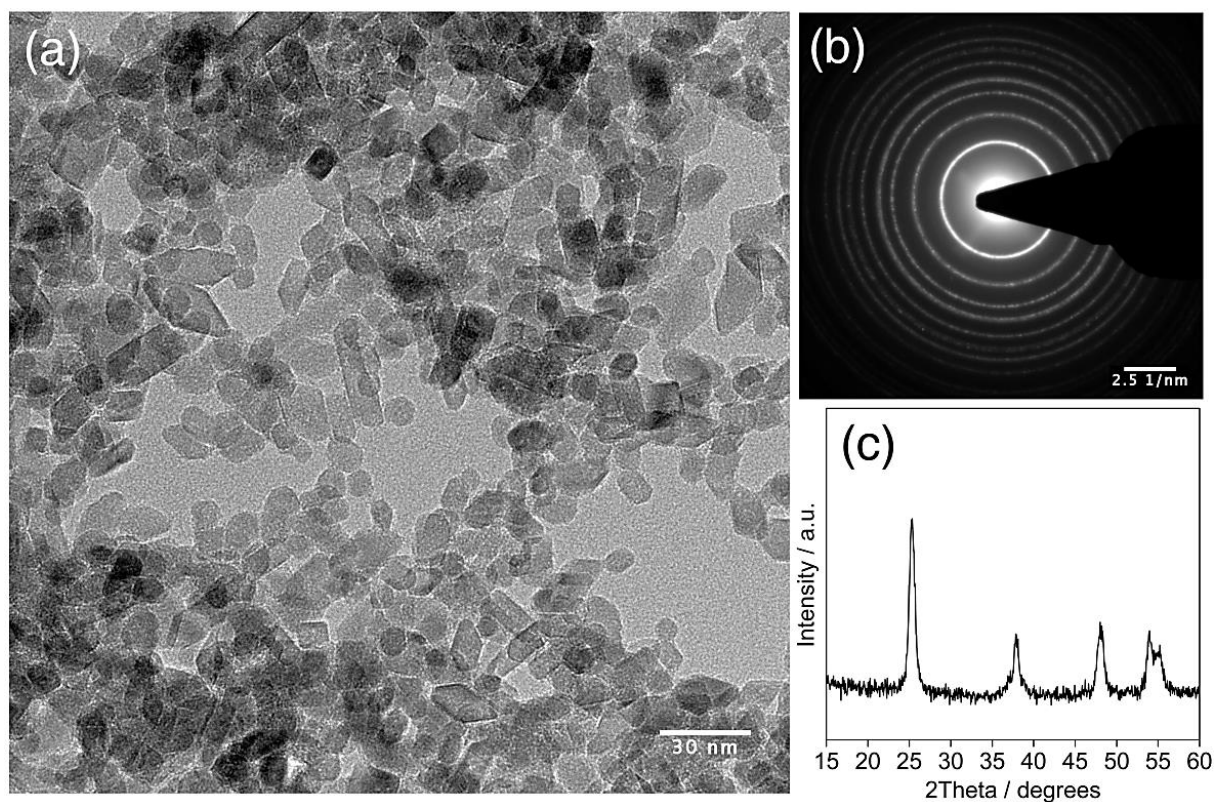


Figure A5.1. (a) TEM image, selected area electron diffraction (SAED) pattern (b) and XRD pattern (c) of hydrothermally synthesized titanium dioxide nanoparticles. The particles were used as crystalline titania source in the nanocellulose assisted synthesis of porous titania thin films.

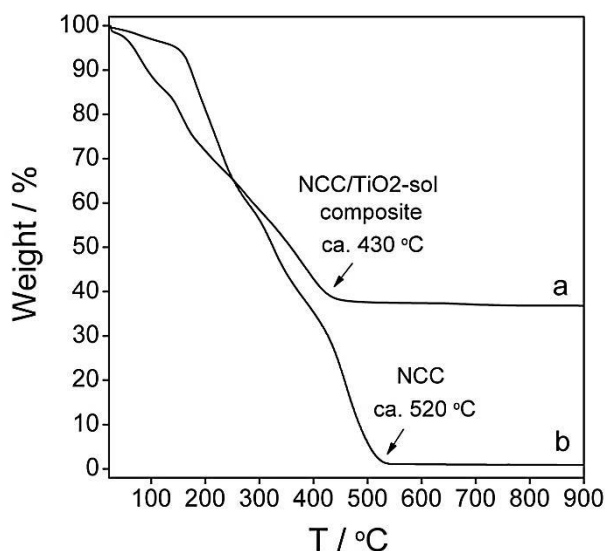


Figure A5.2. TGA curves revealing the mass loss of an NCC/TiO₂-sol composite (a) compared to a mass loss of a pristine NCC (b). The samples were cast from an NCC water dispersion and an NCC/titania precursor solution, respectively and dried overnight at RT. The analysis was performed at 10 K/min heating rate. The arrows indicate the approximate temperature of a complete NCC degradation. Thermogravimetric analysis was performed on a Netzsch STA 440 C TG/DSC instrument with heating rate of 10K/min in a stream of synthetic air of about 25 mL/min.

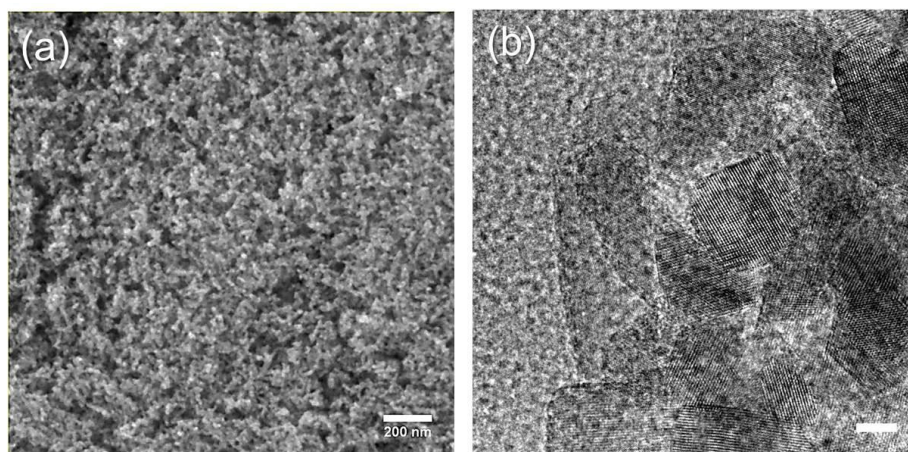


Figure A5.3. SEM and TEM images of the NCC-templated dual source titania thin film prepared from a precursor solution containing 75% preformed titania nanoparticles. (a) SEM top-view of NCC-templated dual source titania thin film coated on silicon wafer. (b) TEM image of the NCC-templated dual source titania thin film coated on silicon and isolated from the substrate for the TEM analysis. The scale bar is 5 nm.

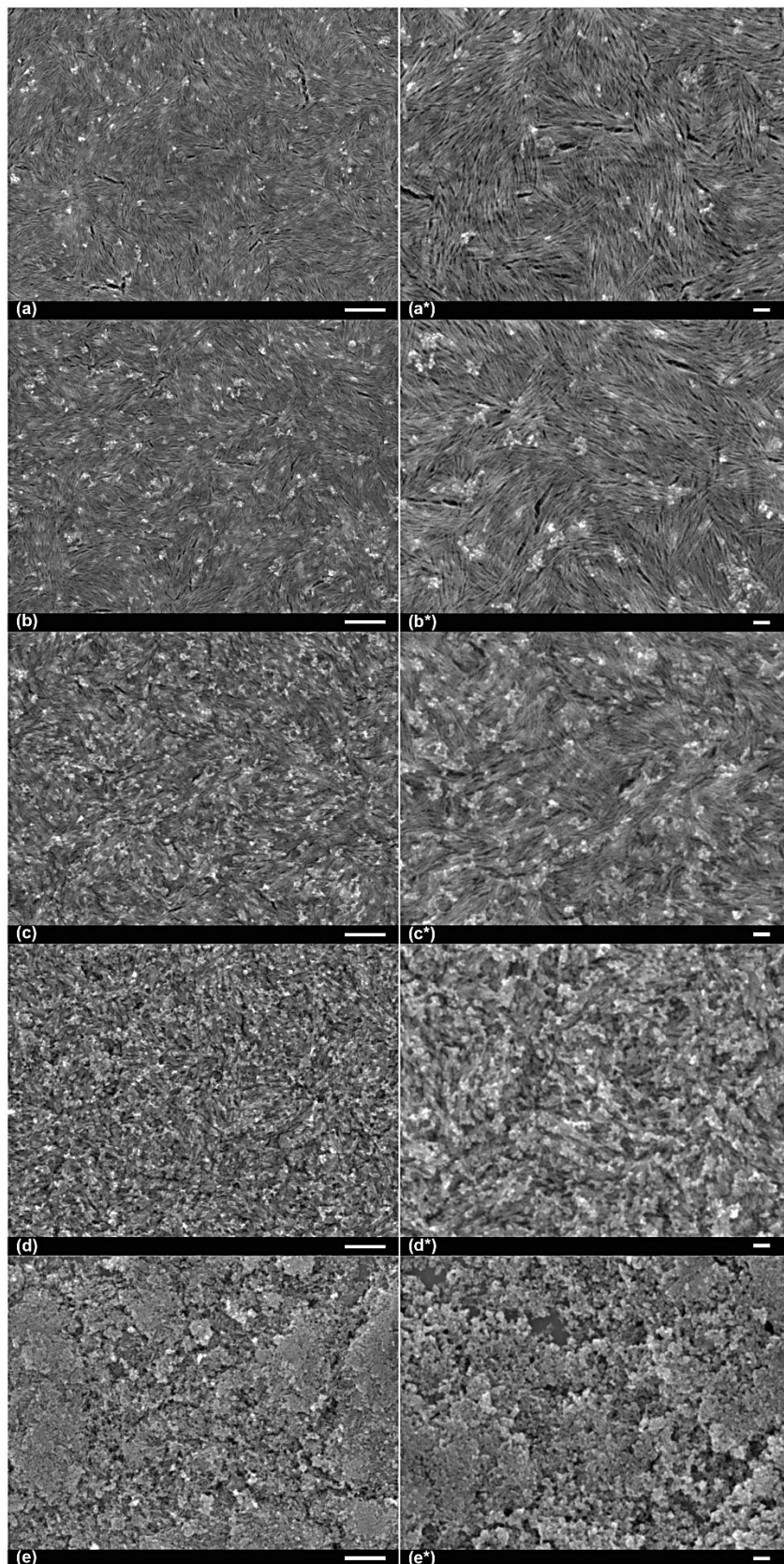


Figure A5.4. SEM images of the dual source titania thin films templated by nanocrystalline cellulose showing the morphology development depending on the titania nanoparticle content: (a) 5%, (b) 10% (c) 30% (d) 50% (e) 100%. The images taken at low and high (*) magnifications show scale bars of 500 and 100 nm, respectively.

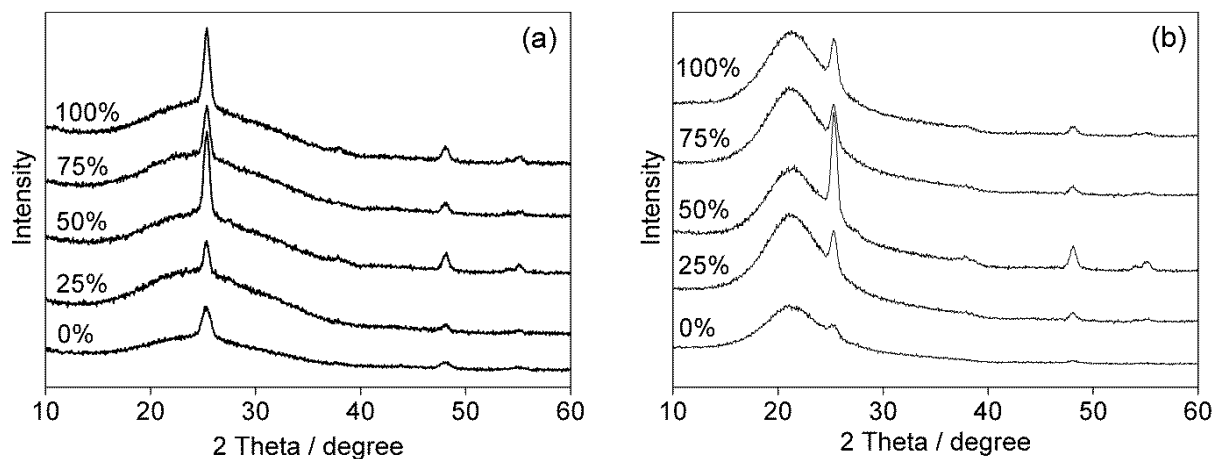


Figure A5.5. XRD patterns of the porous titania films containing different amounts of preformed anatase species (given in the figures) coated on glass (a) and quartz (b) slides.

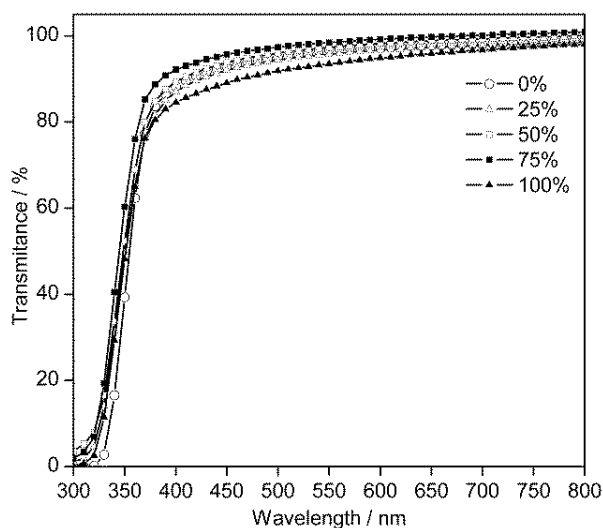
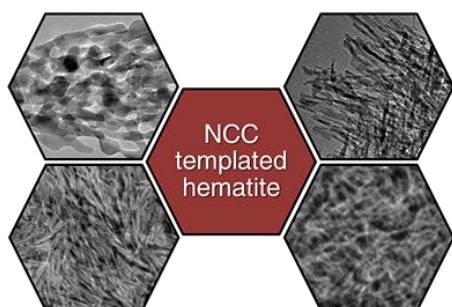


Figure A5.6. UV-Vis spectra revealing the transmittance of NCC templated porous titania films deposited on glass from precursor solutions with different contents of preformed titania nanoparticles (0–100%). The measurements were performed on a Perkin Elmer Lambda 1050 UV/Visible/NIR spectrophotometer equipped with an integrating sphere.

6 Nanocellulose-Assisted Formation of Porous Hematite Morphologies



This chapter is based on the following publication:

*Alesja Ivanova†, Ksenia Fominykh†, Dina Fattakhova-Rohlfing, Patrick Zeller, Markus Döblinger and Thomas Bein. Nanocellulose-assisted formation of porous hematite morphologies. *Inorg. Chem.*, **2015**, 54, 1129.*

†These authors contributed equally

6.1 Introduction

The combination of semiconducting properties with low cost, abundance and chemical stability makes iron oxides attractive materials for various energy conversion and storage applications. Among numerous iron oxide compounds, α -Fe₂O₃ (hematite) is the most studied material whose applications span from electrochemical energy storage and photoelectrochemical water splitting to photocatalytic degradation of air and water pollutants and gas sensing.¹⁻³ The performance of hematite in these applications critically depends upon mass transfer to the active surface sites, charge transfer at the interface, and charge and/or ion transport in the bulk. These processes are controlled to a large degree by the nanomorphology of the iron oxide, due to the role of interface-related processes caused by the large surface area, as well as the impact of the diminishing dimensions on its charge carrier and ion transport behavior.

Due to the interest in nanostructured hematite, several strategies have already been developed for the fabrication of nanostructured hematite morphologies with optimized properties.⁴⁻⁶ Still, a major synthetic challenge is control over the structure on different length scales, from the organization of atoms in the crystalline structure to the macroscopic morphology, which strongly influence the performance of hematite in different applications.

Templated approaches based on sol-gel transformations of molecular precursors can provide a high level of control over the porous nanostructure by using objects with a well-defined shape and 3D organization to guide the evolution of structure and morphology. Mesoporous nanocrystalline iron oxide thin films with high surface area have been prepared by so called soft templating methods using supramolecular aggregates (micelles) of amphiphilic molecules.^{7,8}

The practical benefits of soft templating include the straightforward formation of periodic porous structures based on the self-assembly processes, and the facile subsequent removal of the organic templates by thermal decomposition. However, the critical step in these transformations is the crystallization of the inorganic scaffold, which often leads to the collapse of the porous morphology due to uncontrolled crystal growth at elevated temperatures and requires a careful selection of the amphiphilic molecules and/or the processing conditions. Alternatively, hard-templating routes are advantageous regarding the formation of highly crystalline transition-metal oxide morphologies with well-defined porosity.⁹⁻¹¹ Thermally stable and robust templates such as porous silica or alumina have been demonstrated to sustain the crystallization of porous transition-metal oxides, but these methods are less suitable for the processing of porous coatings on different substrates due to the difficulties associated with the removal of the template under demanding conditions.

Nanocrystalline cellulose (NCC) extracted from natural cellulose sources^{12,13} is a promising biogenic template for the generation of porosity in inorganic oxides. The cellulose nanocrystals having an anisotropic rod-like shape show a remarkable ability to self-organize and to form chiral nematic liquid crystalline phases.^{14,15} Owing to the rigidity and the thermal stability of the cellulose nanocrystals, the NCC-based composites can sustain relatively high temperatures and provide fully crystalline metal

oxide scaffolds with well-defined mesostructure, therefore combining the advantages of soft templating and the shape-persistent hard templates.

Recent studies on the preparation of nanoscale iron oxide aided by cellulose have focused mainly on composite materials.¹⁶⁻²⁴ In these publications cellulose of different origins acts as a supporting matrix for the formation of iron oxide and as a filler for the homogeneous distribution of pre-synthesised crystalline nanospecies. Other biomaterials have been shown to assist in the nanofabrication of iron oxide, such as silk,²⁵ chitosan,²⁶⁻²⁸ chitin,²⁹ proteins,³⁰ yeast cells³¹ and butterfly wings.³² A few publications describing the fabrication of porous hematite morphologies aided by sacrificial cellulose templating³³⁻³⁵ deal only with macroscopic cellulose-based objects such as wood, filter paper or fibers fabricated from regenerated cellulose. On the contrary, in our study we employ distinct nanosized cellulose species for the synthesis of porous hematite nanostructures.

Recently we have established the high potential of cellulose nanocrystals in the fabrication of porous titania thin films.³⁶ Herein we explore the suitability of this promising approach for the synthesis of iron oxide films. We show for the first time the direct formation of porous hematite thin films on different substrates by a nanocellulose-assisted templating method. We demonstrate several strategies to alter the scaffold morphology. In particular, we investigate the effect of iron oxide precursors and calcination temperature on the film porosity and crystallinity. Furthermore, we reveal a striking effect of post-synthetic treatments on the crystallization of iron oxide in the nanocellulose matrix.

6.2 Results and Discussion

6.2.1 Effect of Precursor Salt and Calcination Procedure

For the fabrication of mesoporous iron oxide, aqueous dispersions of nanocrystalline cellulose (NCC) were mixed with different iron salts acting as iron oxide precursors in the sol-gel process. As such, we used hydrates of iron(III) nitrate [$\text{Fe}(\text{NO}_3)_3 \cdot 9\text{H}_2\text{O}$], iron(III) chloride ($\text{FeCl}_3 \cdot 6\text{H}_2\text{O}$), and iron(II) chloride ($\text{FeCl}_2 \cdot 4\text{H}_2\text{O}$), which are perfectly

soluble in the NCC dispersions without changing their colloidal stability. Fe(III) salts color the opaque cellulose suspensions yellow, whereas the Fe(II) chloride solution remains white. After dissolution, the precursor mixtures were processed to powders or films by drop casting on Teflon surfaces or spin-coating on different substrates (typically silicon wafers or fluorine-doped tin oxide, FTO), respectively. After drying, the composites were calcined in air at temperatures ranging from 300 °C to 600 °C to remove the cellulose under formation of mesoporous iron oxide scaffolds.

Thermogravimetric analysis of the pure NCC reveals that it dehydrates in several subsequent steps in the temperature range from 200 °C to 500 °C^{37,38} and that it is completely decomposed at 500 °C. Addition of iron salts leads to a decrease in the decomposition temperature, which depends on the type of precursor as demonstrated in Figure 6.1 (a1–a3).

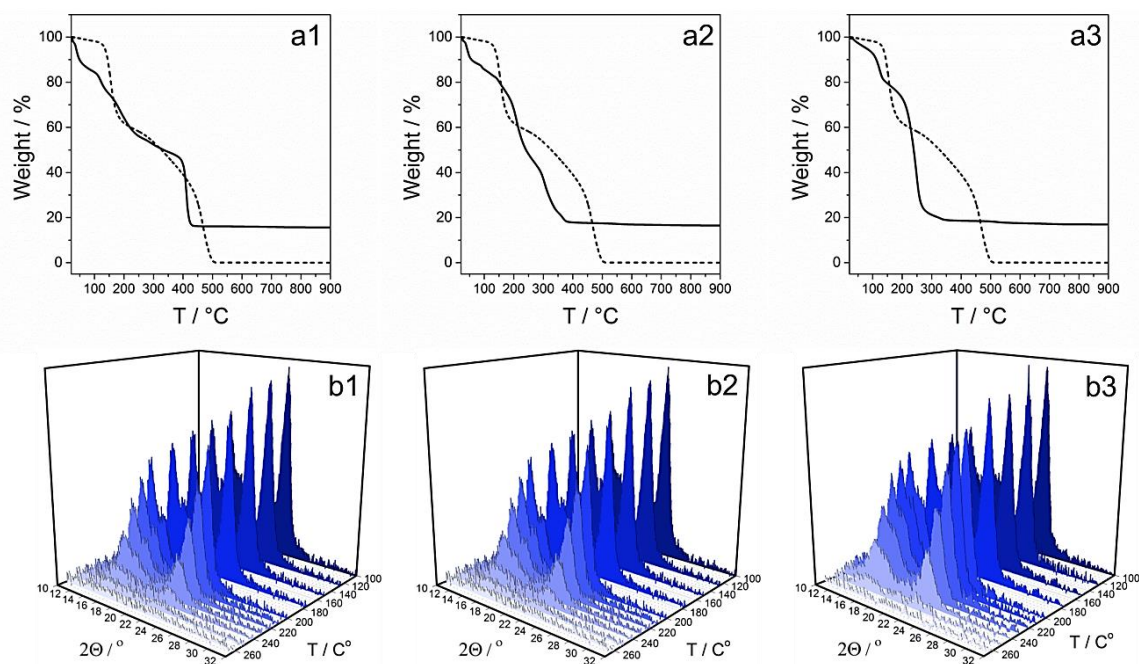


Figure 6.1. Degradation of nanocrystalline cellulose/iron-oxide-precursor composites containing different iron salts: $\text{FeCl}_3 \cdot 6\text{H}_2\text{O}$ (a1, b1), $\text{FeCl}_2 \cdot 4\text{H}_2\text{O}$ (a2, b2) and $\text{Fe}(\text{NO}_3)_3 \cdot 9\text{H}_2\text{O}$ (a3, b3). **Top row:** thermogravimetric analysis revealing mass loss of iron oxide precursor/NCC composites (black lines) compared to pristine NCC (dashed lines) (a1, a2, a3). The composites were dried at 35 °C prior to the analysis and heated with a ramp of 2 °C/min. **Bottom row:** *in-situ* X-ray diffraction patterns obtained upon gradual heating of 1 μm iron oxide precursor/NCC composite films coated on silicon wafers (b1, b2, b3).

According to the TGA measurements, the lowest decomposition temperature of ca. 290 °C was observed for the NCC- $[\text{Fe}(\text{NO}_3)_3 \cdot 9\text{H}_2\text{O}]$ composite, which could be attributed to the oxidative character of the nitrate ions. The addition of Fe(III) chloride leads to a

rather small decrease in decomposition temperature to ca. 450 °C, while in the Fe(II) chloride-containing composites the NCC is combusted at about 400 °C.

In order to investigate the degradation behavior of the nanocellulose in thin films, we performed *in-situ* X-ray diffraction (XRD) heating experiments on 1 μm thick composite films coated on silicon wafers. Parts b1–b3 in Figure 6.1 show a gradual reduction of the signals characteristic for native cellulose upon temperature increase (the NCC signal assignment is shown in Figure A6.1 in the Appendix). Although the XRD results indicate the complete degradation of crystalline cellulose at 250 °C, the optical appearance of the films calcined at this temperature implies the presence of template residues, as follows from the black coloring of the film (Figure A6.2-d in the Appendix), which is consistent with the thermogravimetric analysis revealing an incomplete decomposition of cellulose at 250 °C (Figure 6.1).

The degradation studies demonstrate that calcination of composite films at 300 °C to 600 °C should be sufficient to remove the NCC with the associated liberation of open pores. This is confirmed with scanning electron microscopy (SEM) images of the NCC-templated films, which demonstrate the formation of elongated slit-like pores characteristic for the NCC-derived porous scaffolds, closely replicating the shape of the initial NCC (Figure 6.2).

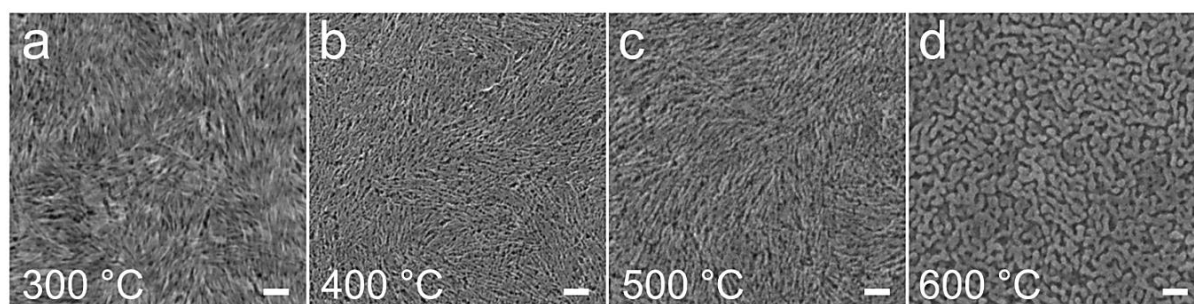


Figure 6.2. SEM top view images revealing the effect of calcination temperature on the morphology of NCC-templated α -Fe₂O₃ thin films. The films were coated on silicon wafers from solutions containing NCC and FeCl₃·6H₂O and calcined at 300 °C (a), 400 °C (b), 500 °C (c), and 600 °C (d). The scale bars correspond to 100 nm.

The mesoporous morphology obtained after calcination of the dried coatings is practically not influenced by the choice of iron precursors (SEM images in Figure 6.2 and Figure A6.3 in the Appendix). The porous texture only slightly changes with the increasing calcination temperature from 300 °C to 500 °C, corresponding to the stability

range of NCC. However, calcination at 600 °C leads to a significant crystal growth with formation of worm-like disordered porous layers typically observed for different solution-processed hematite films (Figure 6.2d).

Analysis by transmission electron microscopy (TEM) confirms the increase of the feature sizes for the NCC-templated film calcined at 600 °C compared to the one heated at 500 °C. The samples exhibit a highly porous structure and a crystalline morphology as can be seen in the high resolution and selected area electron diffraction (SAED) images (Figure 6.3 and Figure A6.4 in the Appendix). The determined *d*-spacing values are typical of hematite and agree very well with previous studies.³⁹

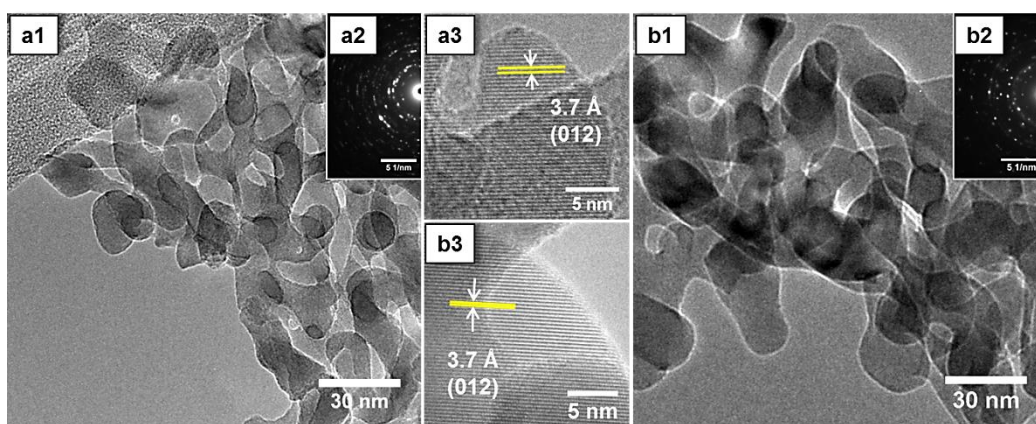


Figure 6.3. TEM images (a1, a3, b1, b3) and SAED patterns (a2, b2) of NCC-templated iron oxide thin films prepared from $\text{FeCl}_2 \cdot 4\text{H}_2\text{O}$ precursor solutions and calcined at 500 °C (a) and 600 °C (b).

In order to study the temperature-induced formation of crystalline iron oxide in the presence of nanocellulose, we performed XRD measurements on cast free-standing composites. Figure 6.4 and Figure A6.5a in the Appendix reveal the formation of $\alpha\text{-Fe}_2\text{O}_3$ phase for all precursors at temperatures higher than 300 °C.

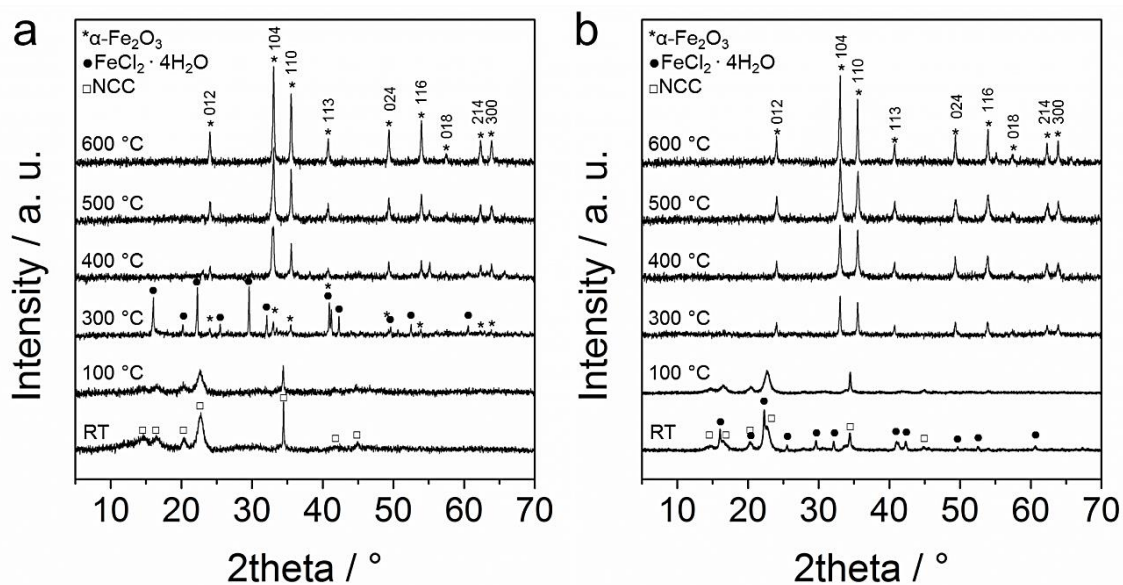


Figure 6.4. XRD patterns of NCC-templated iron oxide free-standing films cast from $\text{FeCl}_3 \cdot 6\text{H}_2\text{O}$ (a) and $\text{FeCl}_2 \cdot 4\text{H}_2\text{O}$ (b) precursor solutions. The composites were dried overnight (assigned as RT) and then heated either at 100 °C overnight or calcined at 300–600 °C for 30 min. The assigned signals correspond to a native cellulose (ICDD pattern C00-003-0289) (\square), iron(II) chloride tetrahydrate (ICDD pattern 00-016-0123) (\bullet) and hematite (ICDD pattern 00-003-0289) (*).

Surprisingly, the heating of the iron(III) chloride-NCC composite at 300 °C initially leads to the formation of hematite and iron(II) chloride, which could be due to a reaction of iron(III) chloride with NCC degradation products.

6.2.2 Effect of Post-Synthetic Delayed Humidity Treatment

To modify the crystallization of hematite, the dried composite films were post-treated at 100 °C in high humidity, also known as delayed humidity treatment (DHT). This procedure can be considered as a hydrothermal treatment of the iron salts in the confined space of the pre-arranged NCC template rods. The XRD analysis reveals the formation of a crystalline inorganic phase corresponding to crystalline iron oxyhydroxide ($\beta\text{-FeOOH}$, akaganeite) after the DHT treatment (Figure 6.5).

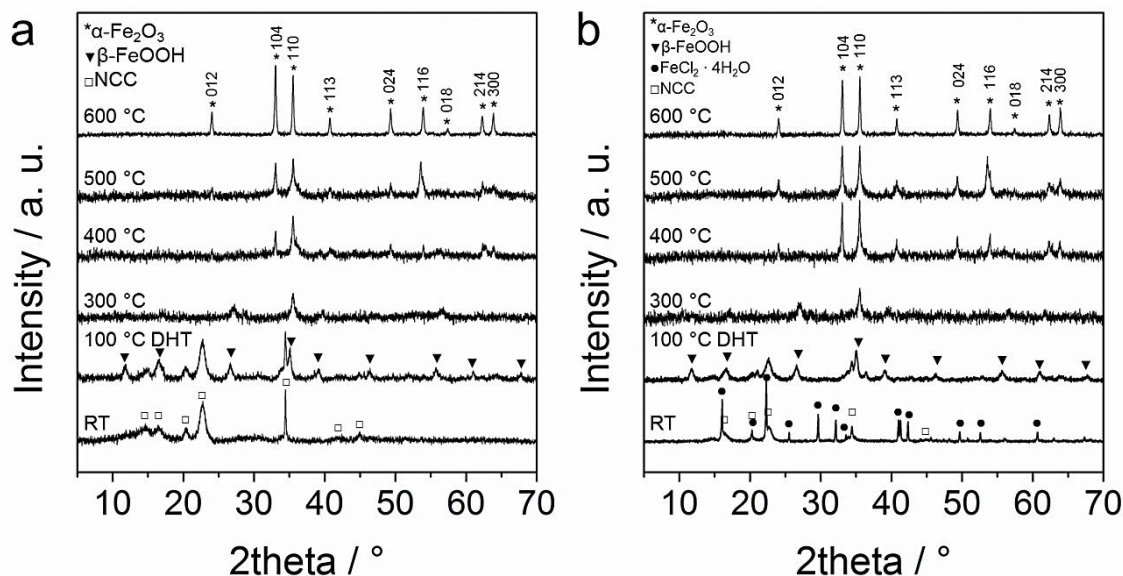


Figure 6.5. XRD patterns of NCC-templated iron oxide free-standing films cast from $\text{FeCl}_3 \cdot 6\text{H}_2\text{O}$ (a) and $\text{FeCl}_2 \cdot 4\text{H}_2\text{O}$ (b) precursor solutions. The dried composites (assigned as RT) were post-synthetically treated overnight at 100 °C in high humidity (set to 85% relative humidity at RT) and then calcined at 300–600 °C for 30 min. The assigned signals correspond to native cellulose (ICDD pattern 00-003-0289) (\square), iron (II) chloride tetrahydrate (ICDD pattern 00-016-0123) (\bullet), akaganeite (ICDD pattern 00-034-1266) (\blacktriangledown) and hematite (ICDD pattern 00-033-0664) (*).

We note that heating at 100 °C without the hydrothermal treatment does not lead to the formation of a crystalline phase (Figure 6.4). Our results imply that without the post-synthetic humidity treatment the amorphous iron oxide either directly transforms to the crystalline hematite or the intermediate phase is not stable and rapidly converts to the hematite. Moreover, we found that the DHT facilitates the crystallization of the oxyhydroxide species in the composite based on both Fe(II) and Fe(III) chlorides, though it is not the case for the nitrate hydrate precursor treated at the same conditions (Figure A6.5b in the Appendix). It has been previously shown that at certain conditions the hydrolysis of iron chlorides proceeds through the formation of $\alpha, \beta\text{-FeOOH}$ oxyhydroxide phases prior to a full conversion to $\alpha\text{-Fe}_2\text{O}_3$.^{40,41,42,43}

To elucidate the effect of the post-synthetic treatment, the iron chloride-NCC composites were dried at different conditions and studied by X-ray photoelectron spectroscopy (XPS). Figure 6.6 and Figure A6.6 in the Appendix show the evolution of the peaks arising from oxygen, chlorine, iron and carbon depending on the film drying conditions.

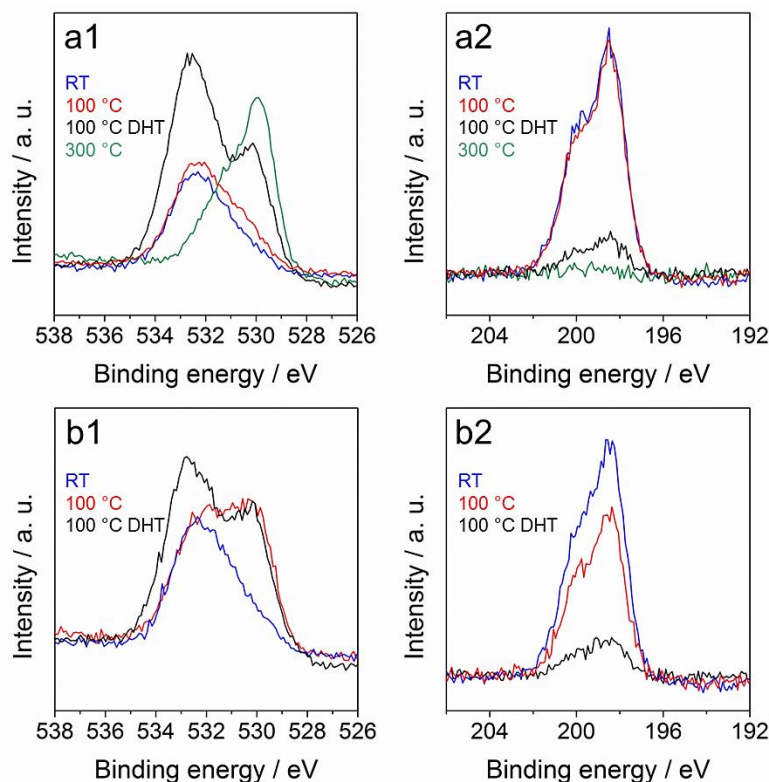


Figure 6.6. XPS spectra of O 1s (a1, b1) and Cl 2p (a2, b2) measured on iron chloride-NCC composite films coated on silicon wafers, resulting from $\text{FeCl}_3 \cdot 6\text{H}_2\text{O}$ (a1, a2) and $\text{FeCl}_2 \cdot 4\text{H}_2\text{O}$ (b1, b2) precursors and dried at different conditions: at room temperature (RT), at 100 °C in humid air (assigned as 100 °C DHT) and at 100 °C and 300 °C in ambient humidity conditions.

The most significant changes were observed for oxygen and chlorine peaks shown in Figure 6.6. The oxygen peak shifts towards lower binding energies (Figure 6.6-a1) with increasing temperature from RT to 300 °C, indicating the release of H_2O , degradation of cellulose and the formation of iron species containing OH^- and O^{2-} (the fitting is shown in Figure A6.6-a3 in the Appendix).^{44,45} In addition, chloride completely degrades at 300 °C (Figure 6.6-a2).

The heating at 100 °C under hydrothermal conditions (DHT) leads to a significant decrease in the chloride contents, whereas after the heating in air at the same temperature the chloride is well-preserved (the black and red lines in Figure 6.6-a2, respectively). This behavior indicates a higher degree of hydrolysis of iron chlorides due to the presence of water vapor, which is also consistent with the shape of the oxygen spectra recorded for the DHT samples. The black spectra in Figure 6.6-a1,b1 demonstrate a doublet with pronounced signal corresponding to water and cellulose at

532.5 eV, and the less intense peak at lower binding energies (530.1 eV) related to O^{2-} in iron oxide.

The spectra point to hydration of cellulose and formation of oxygen bridges in the inorganic part of the composites. We found that the iron(II) chloride composite loses some chlorine already after ambient heating at 100 °C and contains iron oxide O^{2-} species, which was not the case for the iron(III) chloride sample (red spectra in Figure 6.6-b2,a2, respectively). To conclude, the XPS analysis points to the accelerated hydrolysis and nucleation of crystalline phase due to the DHT. Additionally, the increase of the signal at about 533 eV implies high contents of water in the samples, which may reduce the shrinkage of the cellulose species due to swelling at high relative humidity.⁴⁶

Notably, we found that the induced crystallization of iron oxyhydroxide during the post-synthetic treatment significantly affects the film morphologies after calcination as demonstrated in Figures 6.7 and A6.7 in the Appendix.

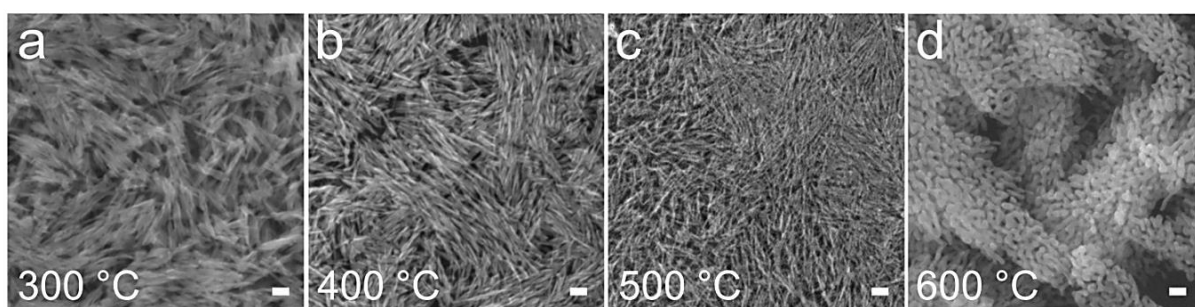


Figure 6.7. SEM top view images revealing the effect of calcination temperature on the morphology of the NCC-templated $\alpha\text{-Fe}_2\text{O}_3$ thin films post-synthetically treated in humid air at 100 °C prior to calcination at 300 °C (a), 400 °C (b), 500 °C (c), and 600 °C (d). The films were coated on silicon wafers from solutions containing NCC and $\text{FeCl}_2\cdot 6\text{H}_2\text{O}$. The scale bars correspond to 100 nm.

The DHT treatment results in an anisotropic geometry of iron oxide species, which is especially pronounced for the films calcined at low temperatures of 300–400 °C (Figure 6.7a,b). However, the thermal treatment at higher temperatures leads to recrystallization of the nanorods to form intergrown roundly shaped species (Figure 6.7d). A more detailed investigation of the DHT effect on crystal formation is shown in Figure 6.8.

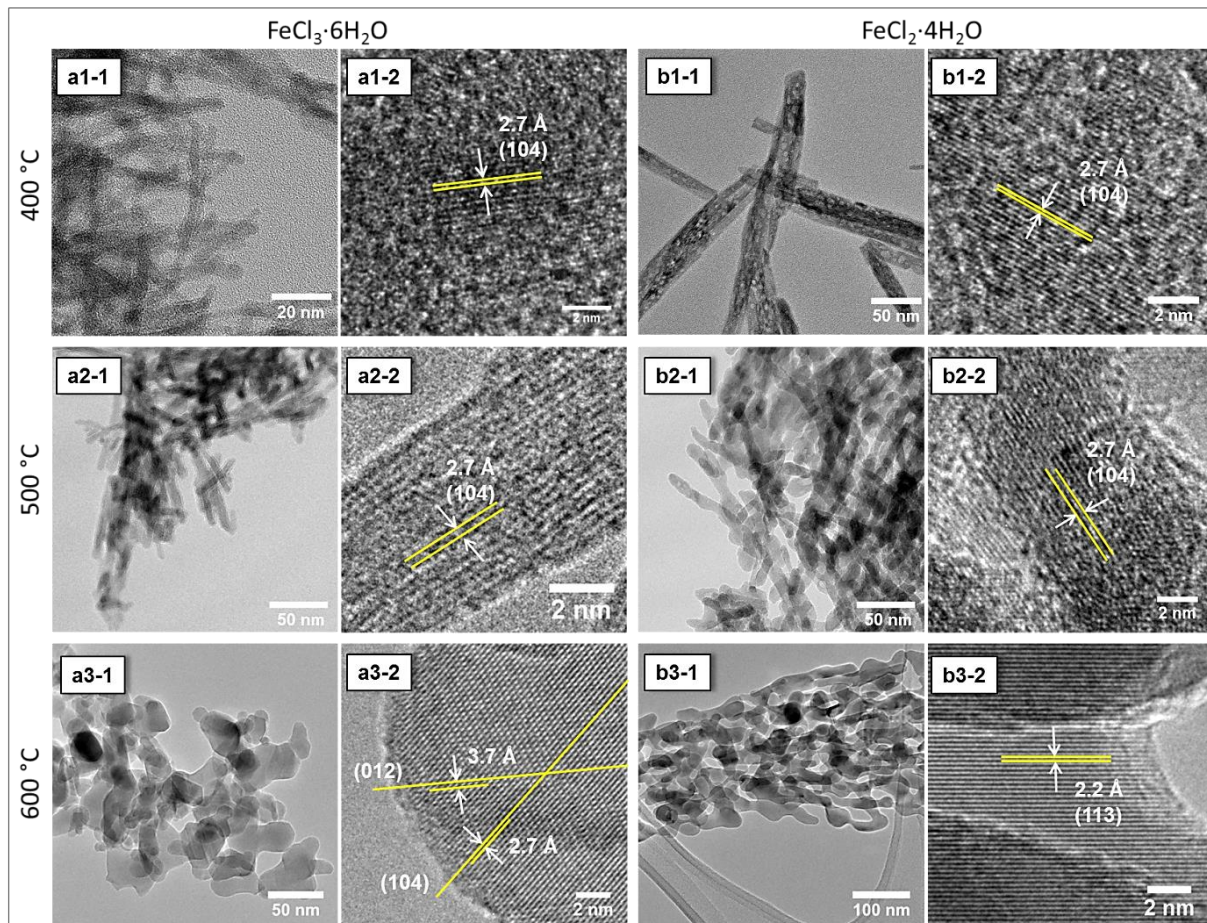


Figure 6.8. TEM images at low and high magnifications of iron oxide thin films prepared from iron chloride/NCC solutions coated on silicon wafer, obtained from $\text{FeCl}_3 \cdot 6\text{H}_2\text{O}$ (a) and $\text{FeCl}_2 \cdot 4\text{H}_2\text{O}$ (b) precursors. The composites were exposed to humidity treatment at 100 °C and subsequently calcined at 400 °C (a1, b1), 500 °C (a2, b2), and 600 °C (a3, b3).

TEM analysis in Figure 6.8 reveals a similar trend in the crystallization pathway for both $\text{FeCl}_3 \cdot 6\text{H}_2\text{O}$ and $\text{FeCl}_2 \cdot 4\text{H}_2\text{O}$ precursors. Calcination at the moderate temperature of 400 °C leads to the formation of crystalline species showing a pronounced anisotropic shape, with a length of around 55 nm and a width of around 5 nm (Figure 6.8a1–1). Additionally, the crystals obtained with $\text{FeCl}_2 \cdot 4\text{H}_2\text{O}$ (Figure 6.8b1–1) show a porous structure, which can be attributed to the dehydration during the thermal conversion from $\beta\text{-FeOOH}$ to $\alpha\text{-Fe}_2\text{O}_3$.⁴⁷ At 500 °C the elongated shape of the features is still present, although it is clearly visible that the particles start to recrystallize forming a polycrystalline network with the formation of additional more spherically-shaped species. The length of the rods is around 30 nm while the rod width remains approximately 5 nm. The preferred growth orientation of the crystals is the (104) direction, as can be seen in the HRTEM images in Figure 6.8. At 600 °C the

recrystallization step is more pronounced and the species have a nearly spherical geometry with a size of ca. 25 nm in length and 20 nm in width. Accordingly, the aspect ratio of the rods decreases with increasing calcination temperature from 12.3 to 1.3.

Fe(III) nitrate does not undergo the oxyhydroxide-to-hematite transformation, therefore the DHT treatment does not have a pronounced effect on the NCC-templated hematite morphology (Figure A6.7 in the Appendix). We note that all obtained NCC-templated hematite scaffolds exhibit a rather similar specific surface area of about 65 m²/g (Figure A6.8 in the Appendix).

6.3 Conclusions

We have established a facile method for the synthesis of crystalline porous iron oxide thin films with various nano-morphologies by employing the biogenic template nanocellulose. Different iron salts, namely FeCl₃·6H₂O, FeCl₂·4H₂O and Fe(NO₃)₃·9H₂O can be successfully employed for the NCC-assisted synthesis. The nature of the calcination procedure of the NCC/iron-oxide-precursor composites has a strong influence on the morphology of the porous hematite films.

Furthermore, we show that a post-synthetic humidity treatment at elevated temperature drastically affects the morphology of porous scaffolds prepared from FeCl₃·6H₂O and FeCl₂·4H₂O. Upon exposure to the humidity treatment at 100 °C, the crystallization of hematite proceeds through the formation of iron oxyhydroxide (β -FeOOH) species of highly anisotropic shape.

Due to the shape-persistence of cellulose nanocrystals, the film homogeneity and porosity is well preserved despite the complex behavior of hematite crystallization. We show that a great variety of iron oxide networks can be achieved and the morphology of the films can be tuned by facile nanocellulose templating. The above synthesis approach is particularly advantageous for the fabrication of homogeneous porous coatings of iron oxide on different types of substrates.

6.4 Experimental

6.4.1 Synthesis

Extraction of cellulose nanocrystals. The nanocrystalline cellulose (NCC) was extracted from cotton linters CP20 (Peter Temming AG) by hydrolysis in sulfuric acid.⁴⁸ The cotton fibers were washed with water and dried at 60 °C. Then 64% H₂SO₄ was added to cotton fibers at the ratio of 1 mL acid to 8.75 g cellulose. The mixture was kept at room temperature for 25 min. Then it was heated at 55 °C for 45 min under vigorous stirring until large cellulose aggregates dissolved. Afterwards the suspension was tenfold diluted with de-ionized water and stored overnight. The upper liquid phase was decanted and the NCC-rich lower phase was washed three times with water via repeated centrifugation at 47808 g relative centrifugal force (RFC) for 15 min. The last centrifugation step was performed at 70 g RFC for 10 min in order to sediment cellulose aggregates and to collect the suspension of finely dispersed NCC. Finally, the suspension was concentrated in a rotary evaporator to 8.15 wt % at pH 2.55.

Preparation of precursor solutions. 1.229 g of the above 8.15 wt % dispersion of cellulose crystals was added to 0.37 mmol iron salt corresponding to 0.100 g, 0.0736 g and 0.1495 g of FeCl₃·6H₂O, FeCl₂·4H₂O and Fe(NO₃)₃·9H₂O salts, respectively. The viscous mixture was vigorously stirred for about 2 min. Then 3.6 g of water was added in order to dilute the cellulose suspension and to dissolve the iron precursor. The precursor solutions contained concentrations of 0.076 M iron and 2 wt % NCC. The solutions were stirred for 2 hours prior to film coating.

Film fabrication. Free-standing films were cast from precursor solutions on a Teflon surface (5 g precursor solution on 6 × 6 cm² area) and dried at 35 °C overnight prior to calcination. After calcination, pulverized cast films were analyzed by using X-ray diffraction, nitrogen sorption measurements and thermogravimetric analysis.

Thin films were deposited on a 1.5 × 2.0 cm² silicon wafer or on 1.5 × 2.5 cm² FTO glass by spin-coating a 100 μL precursor solution at 1500 rpm for 25 s followed by drying with a heat gun set at 100 °C for 10 s. The spin-coating and drying cycles were repeated seven times to achieve ca. 1 μm film thickness of the composites for the XRD

degradation experiments and for the XPS analysis. For SEM imaging, two layers were coated on silicon wafers.

For the delayed humidity treatment (DHT), the free-standing films or films coated on substrates were placed into a 2 L desiccator containing 80 mL KCl saturated aqueous solution resulting in 85% relative humidity at RT and kept in an oven at 100 °C overnight prior to calcination.

The free-standing films and thin films were heat-treated at 100 °C/overnight, at 300 °C/30 min, 400 °C/30min and 600 °C/30 min with a heating ramp of 3 °C/min. The calcination at 500 °C was performed by using a 2 °C/min ramp with 2 h continuous heating steps at 100 °C and 360 °C and a final step at 500 °C/30 min.

6.4.2 Characterization

Thermogravimetric analysis of the samples was performed on a Netzsch STA 440 C TG/DSC instrument (heating rate of 2 °C min⁻¹ in a stream of synthetic air of about 25 mL min⁻¹).

XRD analysis of the free-standing films was performed on a STOE powder diffractometer in transmission geometry (Cu-K_{α1}, $\lambda = 1.5406 \text{ \AA}$) equipped with a position-sensitive Mythen-1K detector. XRD patterns were collected in a 2 θ range from 5 ° to 70 ° with a step of 1 ° and fixed counting time of 45 s per step. *In-situ* XRD heating measurements of the films on Si substrates were carried out in reflection mode (Bragg-Brentano) using a Bruker D8 Discover with Ni-filtered CuK_α-radiation and a position-sensitive detector (LynxEye). The instrument was equipped with a heating stage operated by an Anton Paar TCU 200 temperature control unit. The films were heated with the ramp of 1 °C/s and 10 min continuous heating at the set temperatures.

SEM images were obtained with a Jeol JSM-6500F scanning electron microscope equipped with a field emission gun operated at 5 kV. The films were prepared on silicon substrates and glued onto a sample holder with silver lacquer.

TEM analysis was performed with thin films removed from the substrate and deposited on a carbon-coated copper grid. The analysis was carried out on a FEI Titan 80–300 (S)TEM equipped with a field emission gun operated at 300 kV.

X-ray photoelectron spectroscopy (XPS) analysis was performed with a VSW TA10 X-ray source, providing non-monochromated Mg K_{α} radiation, and a VSW HA100 hemispherical analyzer. The samples were cleaned before measurement by 15 min Ar^{+} sputtering (1 kV, $\sim 7 \mu A$). Peak shifts due to charging of the sample were corrected by setting the Cl $2p_{3/2}$ peak to 198.4 eV. The recorded elemental peaks were fitted with a Doniach-Sunjic line shape convoluted with a Gaussian and linear background subtraction.⁴⁹

The nitrogen sorption isotherms were obtained at $-196 \text{ }^{\circ}C$ using a Quantachrome Autosorb-1. The specific surface area was determined with the Brunauer-Emmett-Teller method at $p/p_0 = 0.05-0.2$.

6.5 References

- (1) Sivula, K.; Le Formal, F.; Grätzel, M. *ChemSusChem* **2011**, *4*, 432–449.
- (2) Wu, C.; Yin, P.; Zhu, X.; OuYang, C.; Xie, Y. *J. Phys. Chem. B* **2006**, *110*, 17806–17812.
- (3) Chen, J.; Xu, L.; Li, W.; Gou, X. *Adv. Mater.* **2005**, *17*, 582–586.
- (4) Sivula, K.; Zboril, R.; Le Formal, F.; Robert, R.; Weidenkaff, A.; Tucek, J.; Frydrych, J.; Grätzel, M. *J. Am. Chem. Soc.* **2010**, *132*, 7436–7444.
- (5) Srivastava, D. N.; Perkas, N.; Gedanken, A.; Felner, I. *J. Phys. Chem. B* **2002**, *106*, 1878–1883.
- (6) Mitra, A.; Vázquez-Vázquez, C.; López-Quintela, M. A.; Paul, B. K.; Bhaumik, A. *Micropor. Mesopor. Mat.* **2010**, *131*, 373–377.
- (7) Brezesinski, T.; Groenewolt, M.; Antonietti, M.; Smarsly, B. *Angew. Chem. Int. Ed.* **2006**, *45*, 781–784.
- (8) Brezesinski, K.; Haetge, J.; Wang, J.; Mascotto, S.; Reitz, C.; Rein, A.; Tolbert, S. H.; Perlich, J.; Dunn, B.; Brezesinski, T. *Small* **2011**, *7*, 407–414.
- (9) Zhang, R.; Dai, H.; Du, Y.; Zhang, L.; Deng, J.; Xia, Y.; Zhao, Z.; Meng, X.; Liu, Y. *Inorg. Chem.* **2011**, *50*, 2534–2544.
- (10) Jiao, F.; Harrison, A.; Jumas, J.-C.; Chadwick, A. V.; Kockelmann, W.; Bruce, P. G. *J. Am. Chem. Soc.* **2006**, *128*, 5468–5474.
- (11) Lee, J.; Christopher Orilall, M.; Warren, S. C.; Kamperman, M.; DiSalvo, F. J.; Wiesner, U. *Nat. Mater.* **2008**, *7*, 222–228.
- (12) Klemm, D.; Kramer, F.; Moritz, S.; Lindström, T.; Ankerfors, M.; Gray, D.; Dorris, A. *Angew. Chem. Int. Ed.* **2011**, *50*, 5438–5466.
- (13) Ranby, B. G. *Acta Chem. Scand.* **1949**, *3*, 649–650.
- (14) Beck-Candanedo, S.; Roman, M.; Gray, D. G. *Biomacromolecules* **2005**, *6*, 1048–1054.
- (15) Kelly, J. A.; Giese, M.; Shopsowitz, K. E.; Hamad, W. Y.; MacLachlan, M. J. *Acc. Chem. Res.* **2014**, *47*, 1088–1096.
- (16) Liu, S.; Luo, X.; Zhou, J. *Magnetic Responsive Cellulose Nanocomposites and Their Applications*; InTech, 2013.
- (17) Ma, M.-G.; Zhu, J.-F.; Li, S.-M.; Jia, N.; Sun, R.-C. *Mat. Sci. Eng. C* **2012**, *32*, 1511–1517.
- (18) Zhou, J.; Li, R.; Liu, S.; Li, Q.; Zhang, L.; Zhang, L.; Guan, J. *J. Appl. Polym. Sci.* **2009**, *111*, 2477–2484.
- (19) Xiong, R.; Lu, C.; Wang, Y.; Zhou, Z.; Zhang, X. *J. Mater. Chem. A* **2013**, *1*, 14910–14918.
- (20) Mahmoud, K. A.; Lam, E.; Hrapovic, S.; Luong, J. H. T. *ACS Appl. Mater. Interfaces* **2013**, *5*, 4978–4985.
- (21) Yu, X.; Tong, S.; Ge, M.; Zuo, J.; Cao, C.; Song, W. *J. Mater. Chem. A* **2013**, *1*, 959–965.
- (22) Liu, S.; Tao, D.; Zhang, L. *Powder Technol.* **2012**, *217*, 502–509.

- (23) Rafi, M. M.; Ahmed, K. S.; Nazeer, K. P.; Siva Kumar, D.; Thamilselvan, M. *Appl. Nanosci.* **2014**, 1–6.
- (24) Wu, Y.; Zhu, P.; Reddy, M. V.; Chowdari, B. V. R.; Ramakrishna, S. *ACS Appl. Mater. Interfaces* **2014**, 6, 1951–1958.
- (25) Fei, X.; Shao, Z.; Chen, X. *J. Mater. Chem. B* **2013**, 1, 213–220.
- (26) Sreeram, K. J.; Nidhin, M.; Nair, B. U. *Colloid. Surface. B* **2009**, 71, 260–267.
- (27) Singh, J.; Srivastava, M.; Dutta, J.; Dutta, P. K. *Int. J. Biol. Macromol.* **2011**, 48, 170–176.
- (28) Chang, M.-Y.; Wang, W.-H.; Chung, Y.-C. *J. Mater. Chem.* **2011**, 21, 4966–4970.
- (29) Tang, H.; Zhou, W.; Lu, A.; Zhang, L. *J. Mater. Sci.* **2014**, 49, 123–133.
- (30) Klem, M. T.; Young, M.; Douglas, T. *J. Mater. Chem.* **2010**, 20, 65–67.
- (31) Zhou, W.; He, W.; Ma, J.; Wang, M.; Zhang, X.; Yan, S.; Tian, X.; Sun, X.; Han, X. *Mat. Sci. Eng. C* **2009**, 29, 1893–1896.
- (32) Peng, W.; Zhu, S.; Wang, W.; Zhang, W.; Gu, J.; Hu, X.; Zhang, D.; Chen, Z. *Adv. Funct. Mater.* **2012**, 22, 2072–2080.
- (33) Liu, S.; Zhang, L.; Zhou, J.; Xiang, J.; Sun, J.; Guan, J. *Chem. Mater.* **2008**, 20, 3623–3628.
- (34) Ding, J.; Fan, T.; Zhang, D.; Saito, K.; Guo, Q. *Solid State Commun.* **2011**, 151, 802–805.
- (35) Sadakane, M.; Kato, R.; Murayama, T.; Ueda, W. *Mater. Lett.* **2012**, 81, 80–83.
- (36) Ivanova, A.; Fattakhova-Rohlfing, D.; Kayaalp, B. E.; Rathouský, J.; Bein, T. *J. Am. Chem. Soc.* **2014**, 136, 5930–5937.
- (37) Camarero Espinosa, S.; Kuhnt, T.; Foster, E. J.; Weder, C. *Biomacromolecules* **2013**, 14, 1223–1230.
- (38) Wang, N.; Ding, E.; Cheng, R. *Polymer* **2007**, 48, 3486–3493.
- (39) Swanson, H. E. *Standard X-ray diffraction powder patterns*; U.S. Dept. of Commerce, National Bureau of Standards U.S. G.P.O.: Washington, DC, 1953.
- (40) Musić, S.; Krehula, S.; Popović, S. *Mater. Lett.* **2004**, 58, 2640–2649.
- (41) Chaudhari, N. K.; Yu, J.-S. *J. Phys. Chem. C* **2008**, 112, 19957–19962.
- (42) Wang, W.; Howe, J. Y.; Gu, B. *J. Phys. Chem. C* **2008**, 112, 9203–9208.
- (43) Xavier, A. M.; Ferreira, F. F.; Souza, F. L. *RSC Advances* **2014**, 4, 17753–17759.
- (44) McIntyre, N. S.; Zetaruk, D. G. *Anal. Chem.* **1977**, 49, 1521–1529.
- (45) Johansson, L.-S.; Campbell, J. M. *Surf. Interface Anal.* **2004**, 36, 1018–1022.
- (46) Aulin, C.; Ahola, S.; Josefsson, P.; Nishino, T.; Hirose, Y.; Österberg, M.; Wågberg, L. *Langmuir* **2009**, 25, 7675–685.
- (47) Cui, X.; Liu, T.; Zhang, Z.; Wang, L.; Zuo, S.; Zhu, W. *Powder Technol.* **2014**, 266, 113–119.
- (48) Dong, X. M.; Kimura, T.; Revol, J.-F.; Gray, D. G. *Langmuir* **1996**, 12, 2076–2082.
- (49) Doniach, S.; Sunjic, M. *J. Phys. C* **1970**, 3, 285–291.

6.6 Appendix

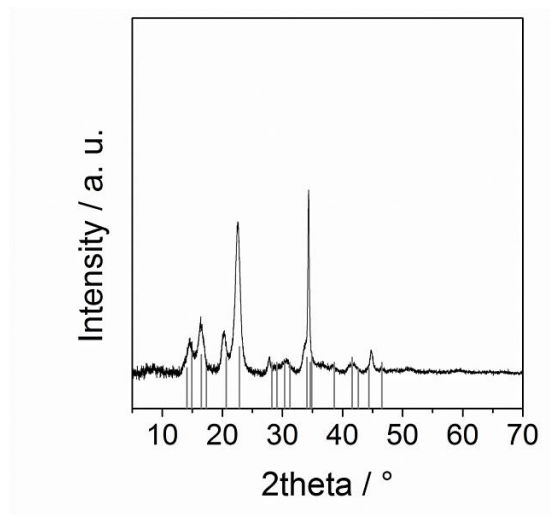


Figure A6.1. XRD pattern of an NCC free-standing film. The assigned signals correspond to native cellulose (ICDD pattern 00-003-0289).

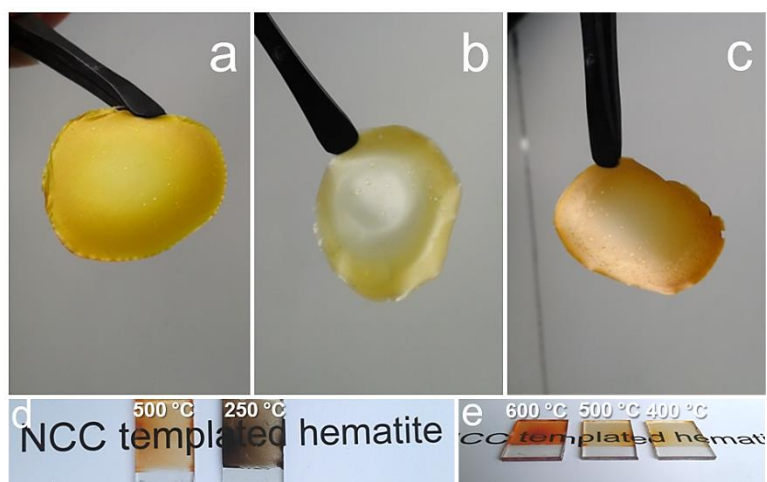


Figure A6.2. Photograph of free-standing nanocellulose-precursor composites prepared with (a) $\text{FeCl}_3 \cdot 6\text{H}_2\text{O}$, (b) $\text{FeCl}_2 \cdot 4\text{H}_2\text{O}$, and $\text{Fe}(\text{NO}_3)_3 \cdot 9\text{H}_2\text{O}$ (c) dried at 35 °C. (d, e) NCC/iron oxide precursor thin films coated on FTO glass from precursor solutions based on $\text{FeCl}_3 \cdot 6\text{H}_2\text{O}$ (d), and $\text{Fe}(\text{NO}_3)_3 \cdot 9\text{H}_2\text{O}$ (e) and calcined at different temperatures.

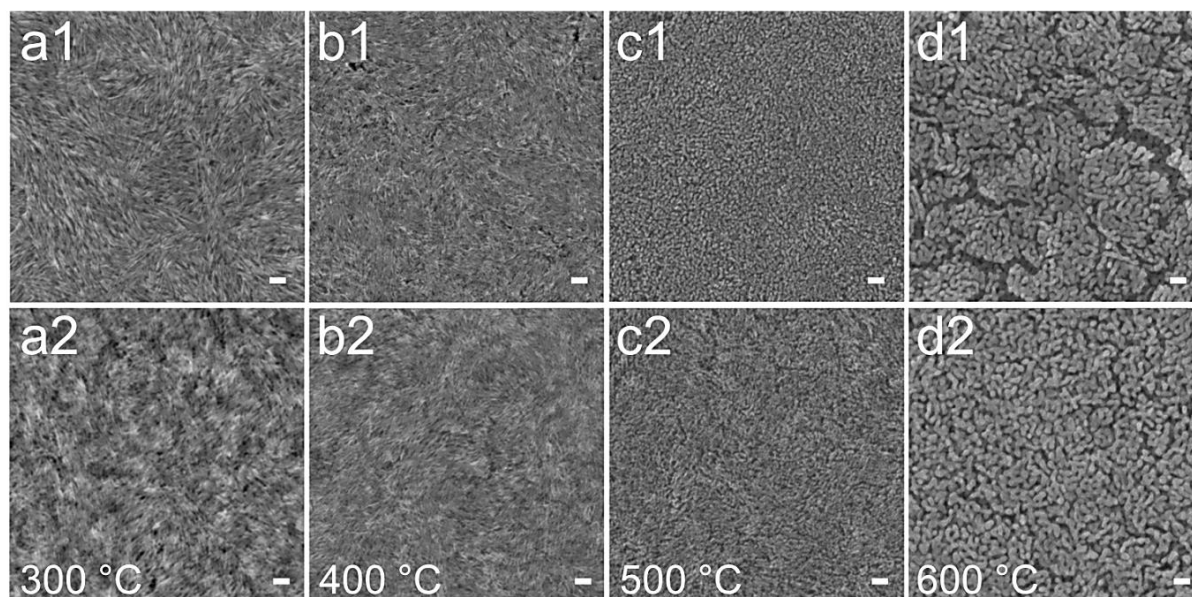


Figure A6.3. SEM top view images revealing the effect of the iron precursor and calcination temperature on the morphology of NCC-templated α - Fe_2O_3 thin films. The films were prepared from precursor solutions containing $\text{FeCl}_2 \cdot 4\text{H}_2\text{O}$ (top row: a1, b1, c1, d1) or $\text{Fe}(\text{NO}_3)_3 \cdot 9\text{H}_2\text{O}$ (bottom row: a2, b2, c2, d2) and calcined at 300 °C (a1, a2), 400 °C (b1, b2), 500 °C (c1, c2), and 600 °C (d1, d2). The scale bars correspond to 100 nm.

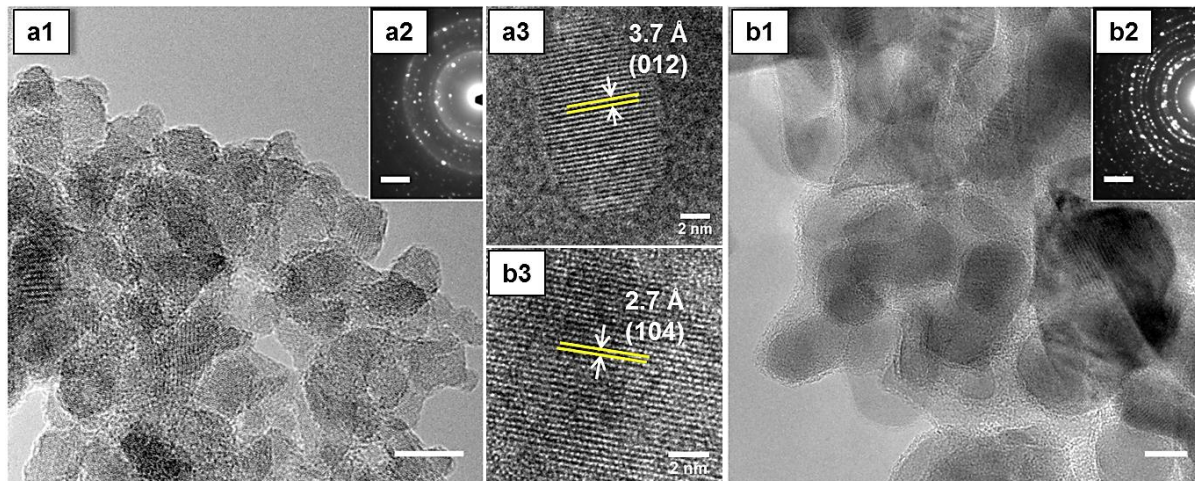


Figure A6.4. TEM images a1, b1 (scale bars correspond to 10 nm), a3, b3 and SAED patterns a2, b2 (scale bars correspond to 2.5 $1/\text{nm}$) of NCC-templated iron oxide thin films prepared from precursor solutions containing $\text{FeCl}_3 \cdot 6\text{H}_2\text{O}$ and calcined at 500 °C (a1, a2, a3) and 600 °C (b1, b2, b3).

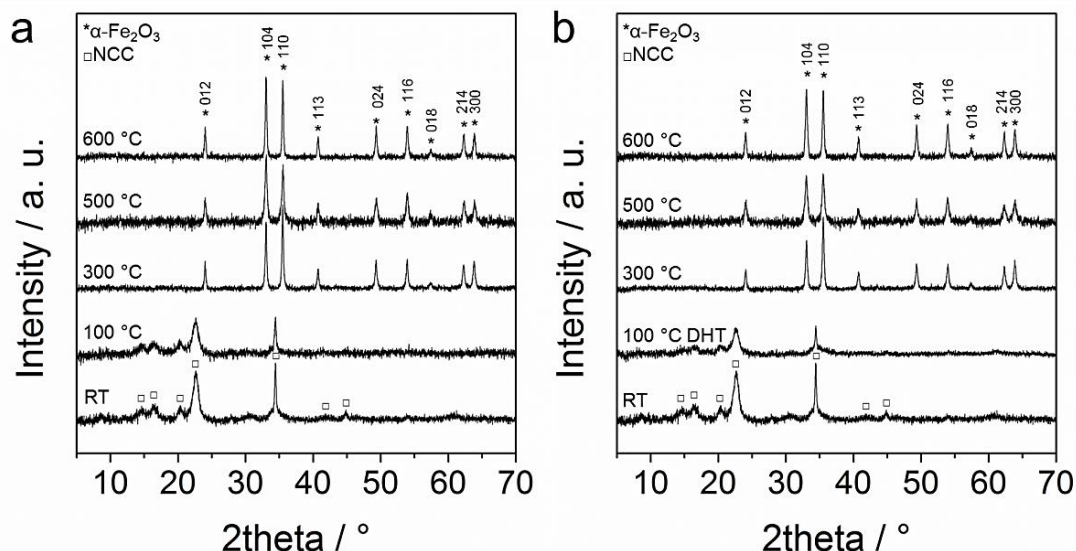


Figure A6.5. XRD patterns revealing the temperature-dependent development of phase composition of NCC/ $\text{Fe}(\text{NO}_3)_3 \cdot 9\text{H}_2\text{O}$ composites calcined at different temperatures after drying at 35 °C (assigned as RT) (a) and after DHT treatment (b). The assigned signals correspond to native cellulose (ICDD pattern 00-003-0289) (\square) and hematite (ICDD pattern 00-033-0664) (*).

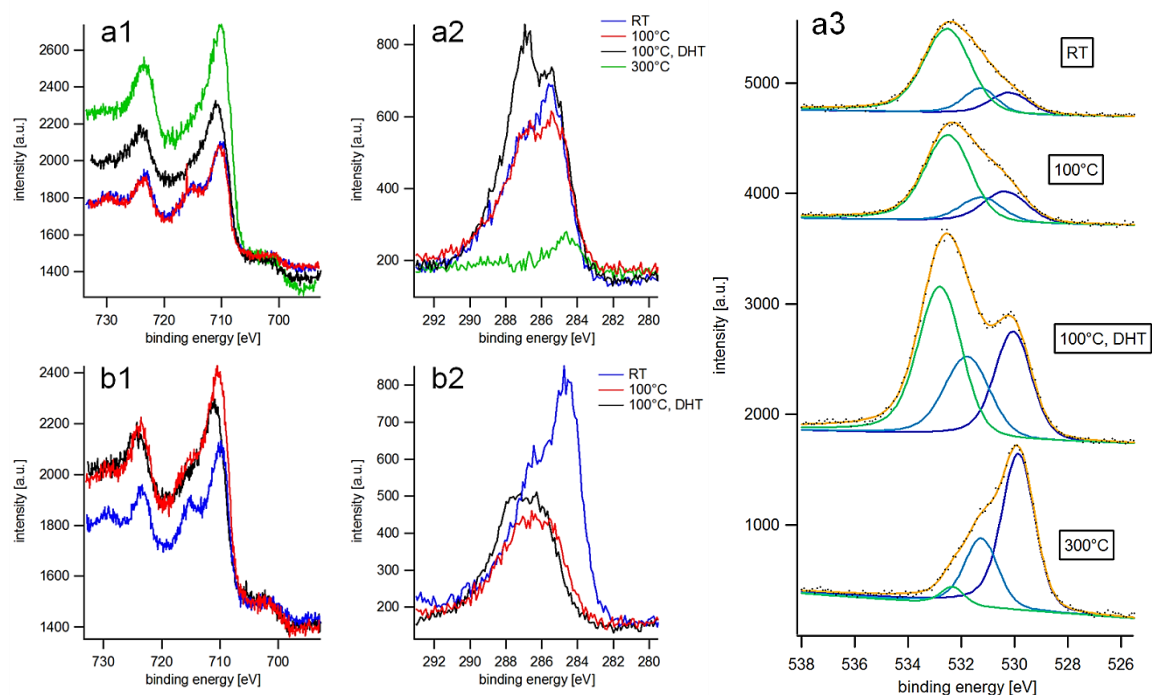


Figure A6.6. X-ray photoelectron spectra of iron chloride/NCC composite films coated from $\text{FeCl}_3 \cdot 6\text{H}_2\text{O}$ (a1, a2, a3) and $\text{FeCl}_2 \cdot 4\text{H}_2\text{O}$ (b1, b2) precursors and dried at different conditions: at room temperature (RT), at 100 °C at high humidity (100 °C DHT) and at 100 °C and 300 °C in ambient humidity conditions. The spectra reveal the development of Fe 2p (a1, b1), C 1s (a2, b2) and O 1s (a3) peaks. The points in figure a3 show the recorded oxygen spectra fitted with a Doniach-Sunjc line shape convoluted with a Gaussian and linear background subtraction. The three peaks with maxima at 530.1 eV, 531.3 eV and 532.5 eV correspond to oxygen in iron oxide, iron hydroxide and water/cellulose, respectively. Spectra were taken using a Mg K_{α} source.

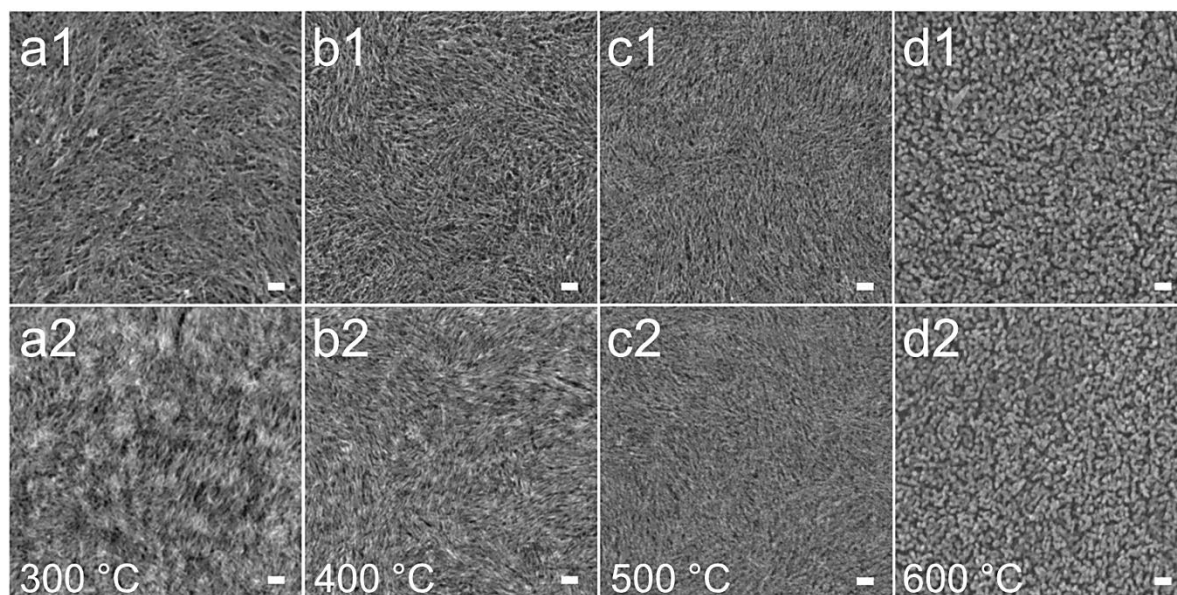


Figure A6.7. Top view SEM images of NCC-templated α - Fe_2O_3 thin films calcined at 300 °C (a1, a2), 400 °C (b1, b2), 500 °C (c1, c2), and 600 °C (d1, d2) after humidity treatment at 100 °C. The films were spin-coated on silicon wafers from aqueous precursor solutions containing NCC and $\text{FeCl}_3 \cdot 6\text{H}_2\text{O}$ (a1, b1, c1, d1) or $\text{Fe}(\text{NO}_3)_3 \cdot 9\text{H}_2\text{O}$ (a2, b2, c2, d2). The scale bars correspond to 100 nm.

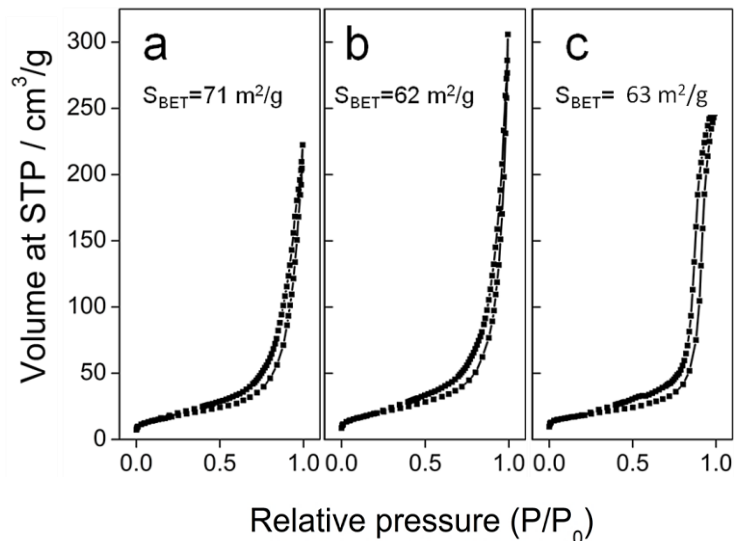


Figure A6.8. Nitrogen sorption isotherms measured on NCC-templated α - Fe_2O_3 powders after calcination at 500 °C. The samples were prepared from precursors containing NCC and $\text{FeCl}_3 \cdot 6\text{H}_2\text{O}$ (a), $\text{FeCl}_2 \cdot 4\text{H}_2\text{O}$ (b) and $\text{Fe}(\text{NO}_3)_3 \cdot 9\text{H}_2\text{O}$ (c) without delayed humidity treatment.

7 Conclusion and Outlook

The aim of this thesis was the development of a straightforward method for the synthesis of metal oxide thin films with various porous nano-morphologies by employing the biogenic template, nanocrystalline cellulose (NCC).

The present study reveals the novel synthetic strategies toward highly porous mesoporous titania and hematite supported coatings. Furthermore, we demonstrate that the NCC-templated titania films can be successfully applied in energy conversion and photocatalytic applications, namely as a photocatalyst for the degradation of water and air pollutants, as well as an active anode material in a dye sensitized solar cell.

Chapter 3 discusses the extraction of cellulose nanocrystals from pristine bulk celluloses. Our studies show that cotton is the most suitable cellulose source for the release of nanocrystalline domains via sulphuric acid hydrolysis, compared to other celluloses, such as dry wood pulps and microcrystalline cellulose. Hydrolysis of cotton linters provides NCC of high crystallinity, purity, defined shape and assures high reaction yields. Furthermore, we demonstrate that differential centrifugation improves the homogeneity of NCC suspensions and narrows down the size distribution of cellulose nanocrystals.

A typical optimized suspension of cotton NCC consists of elongated cellulose nanocrystals with dimensions of about 10 ± 2 nm in width and 117 ± 34 nm in length. The NCC derived from cotton shows a crystallinity of about 90%, as estimated with the XRD peak-height method, and high thermal stability.

Nanostructuring of titanium dioxide was achieved by aqueous hydrolysis of titanium alkoxide precursor in the presence of cotton-based cellulose nanocrystals (Chapter 4). The obtained NCC-templated titania networks feature well-defined, narrow pore size distributions with mean mesopore dimensions of about 8–13 nm.

The present study showed that the adjustment of precursor composition, i.e., variation of component concentrations, enabled morphology tuning of NCC-templated titania. Thus, the NCC-templated titania showed specific surface areas in the range from 85 to

175 m²/g, depending on the amount of template in the precursor solutions. Additionally, the concentration of titania precursor affected the growth of anatase crystallites, providing mean crystallite dimensions in the range of 9–13 nm after calcination at 500 °C. Furthermore, a pronounced pore widening was achieved by applying post-treatments at high humidity to NCC/titania-sol composites prior to their calcination. This treatment also promoted the formation of porous titania with significantly higher pore volume, larger specific surface area and slightly smaller titania crystallites, as compared to the untreated samples.

NCC-templated titania with tailored properties was deposited by spin- or dip-coating on glass, silicon and transparent conducting oxide substrates as transparent, homogeneous and mechanically stable thin films. Such coatings demonstrated profound activity in the photocatalytic NO (nitrogen(II) oxide) conversion and in the degradation of 4-chlorophenol, serving as model reactions for the purification of air and water, respectively. Furthermore, the high surface area of NCC-templated films enabled high dye loadings in thin films and consequently provided better performance in dye-sensitized solar cells compared to reference anodes of similar thickness made of commercial titania nanoparticles.

In Chapter 5 we describe an extension of the NCC templating approach. In particular, the photocatalytic properties of NCC-templated titania films were significantly improved by introducing hydrothermally presynthesized crystalline anatase to the titania-NCC sol-gel precursors.

The experimental data showed that the addition of preformed crystalline anatase nanoparticles promoted the enlargement of the mean dimensions of crystalline domains from 8 to 15 nm, depending on the fraction of added nanoparticles. Owing to the rigid and shape-persistent nature of the template, the crystalline anatase did not distort the porous morphology of the NCC replicated scaffolds. Pore volumes and surface areas remained almost intact, providing values in the ranges of 0.28–0.40 cm³/g and 113–157 m²/g, respectively.

The synergy of high crystallinity and high porosity increased the photocatalytic performance of NCC-templated titania films incorporating preformed nanocrystals. Quantitatively, the rate constant of the 4-chlorophenol degradation reaction was

improved from 0.19 h^{-1} to 0.53 h^{-1} for films without and with 75% preformed titania, respectively.

Nanostructuring of iron oxide (hematite) was also developed, following an approach that was analogous to the synthesis of NCC-templated titania. Chapter 6 describes in detail the preparation pathway towards NCC replicated porous hematite nanostructures and reveals the impact of iron oxide precursor salt and calcination temperature on the final morphology of the NCC-templated hematite.

Highly porous homogeneous hematite morphologies were achieved at calcination temperatures $\leq 500 \text{ }^\circ\text{C}$. However, a further increase of calcination temperatures to $600 \text{ }^\circ\text{C}$ promoted the uncontrolled recrystallization of hematite resulting in poorly porous scaffolds made of large fused hematite crystallites.

Furthermore, we found that a post-synthetic hydrothermal treatment affected the formation of hematite in the confined matrix of NCC. The hydrothermal treatment of NCC-iron chloride composites promoted the growth of anisotropic iron oxyhydroxide species already at low temperatures. Consequently, after calcination the porous nanomorphology of post-treated samples drastically differed from the non-treated ones. Thus, in the case of hematite, it was demonstrated that by adapting the synthesis conditions to the specific properties of the target metal oxide, it was possible to achieve novel NCC-derived nanomorphologies.

To summarize, we have developed a highly effective templating strategy by incorporating natural cellulose nanocrystals in the synthesis of porous titania and hematite thin films. The findings of this study demonstrate that the sacrificial replication with nanocrystalline cellulose offers many intriguing possibilities to tailor the morphology of various crystalline oxides, thereby improving their functionality.

Sacrificial nanostructuring with nanocellulose permits tailoring the morphology of metal oxide thin films by adjusting the composition of the precursor mixture, the processing conditions, and post-deposition treatments. The main advantages of the NCC compared to conventional structure directors include shape persistence, suitable thermal stability, natural origin and anisotropic nanodimensions. The synergy of these features enables the straightforward integration of NCC into the wet-chemical synthesis of porous metal oxides.

Future developments could aim at the detailed characterization of NCC and metal precursor interactions on a molecular level, in order to establish the mechanism of oxide formation in the presence of nanocellulose. Additionally, suitable surface modification of cellulose nanocrystals could extend their application, for example in the non-aqueous templating synthesis of metal oxides. We anticipate that future investigations will significantly expand the scope of the NCC-assisted sacrificial nanostructuring and broaden the application areas of NCC-derived functional nanomaterials.

8 Appendix

8.1 List of Abbreviations

NCC	nanocrystalline cellulose
DSC	dye-sensitized solar cell
TCO	transparent conducting oxide
IUPAC	International Union of Pure and Applied Chemistry
UV	ultraviolet
VB	valence band
CB	conduction band
TEOT	titanium(IV) ethoxide
CTABr	cetyltrimethylammoniumbromide
EISA	evaporation-induced self-assembly
MCC	microcrystalline cellulose
HPC	hydroxypropyl cellulose
BET	Brunauer-Emmett-Teller
DFT	density functional theory
NLDFT	non-local density functional theory
XRD	x-ray diffraction
WAXS	wide angle x-ray scattering
SAXS	small angle x-ray scattering
ICDD	International Centre for Diffraction Data
TEM	transmission electron microscopy
SEM	scanning electron microscopy
SAED	selected-area electron diffraction
STEM	scanning transmission electron microscopy
HAADF	high-angle annular dark field
HRTEM	high resolution transmission electron microscopy
XPS	X-ray photoelectron spectroscopy

UV-Vis	ultraviolet-visible
NMR	nuclear magnetic resonance
FID	free-induction decay
MAS	magic angle spinning
CP	cross-polarization
TGA	thermogravimetric analysis
TG	thermogravimetric
DSC	differential scanning calorimetry
DLS	dynamic light scattering
FTO	fluorine-doped tin dioxide
ECF	elemental chlorine free
DHT	delayed humidity treatment
RFC	relative centrifugal force
TRMC	time resolved microwave conductivity

8.2 List of Symbols

g	packing parameter
V_{hc}	volume of a hydrophobic core
A_0	area of a head group
L	chain length
P	pitch size
λ	wavelength
n_{avg}	average refractive index
p/p_0	relative pressure
p	equilibrium pressure
p_0	saturation vapor pressure
a_s	specific surface area
n_m^a	monolayer capacity
N_A	Avogadro constant
a_m	molecular cross-sectional area
m_s	sample mass
n^a	amount of adsorbed gas
C	BET constant
θ	Bragg angle
d	interplanar atomic distance
Δ	path difference
n	integer
D_{hkl}	crystallite size
k	numerical shape factor
β_{hkl}	diffraction broadening
h	Plank's constant
m	mass
v	velocity
E_s	kinetic energy

$h\nu$	photon energy
E_b	binding energy
ϕ	workfunction
I	light intensity
I_0	incident light intensity
T	transmittance
A	absorbance
l	path length
ε	absorptivity
E_g	band gap energy
α	reciprocal absorption length
D_T	translational diffusion coefficient
d_n	hydrodynamic diameter
k_B	Boltzmann's constant
T	temperature
η_m	viscosity
V	voltage
I_{SC}	short-circuit current
J_{SC}	short-circuit current density
V_{OC}	open circuit voltage
FF	fill factor
η	power conversion efficiency
MPP	maximum power point
P_{MPP}	power at maximum power point
I_{mpp}	current density at the maximum power point
V_{mpp}	voltage at the maximum power point
P_{in}	incident power
P_{out}	output power

9 Curriculum Vitae

Name **Alesja Ivanova**
Date of Birth 02.11.1985
Place of Birth Riga, Latvia

EDUCATION

2010–present **PhD Physical Chemistry**
Department of Chemistry, Ludwig-Maximilians-University Munich
PhD thesis: Nanoporous Metal Oxides Templated by Nanocrystalline Cellulose – Synthesis and Applications in Photocatalysis and Photovoltaics, under the supervision of Prof. Thomas Bein

2008–2010 **MSc Advanced Materials Science**
Joint master program within the Elite Network of Bavaria, Technical University of Munich, Ludwig-Maximilians-University Munich, University of Augsburg
MSc thesis: Characterization of Lithium Sulfur Cell at the first Cycle

2004–2008 **Honours BSc Chemical Engineering and Technology**
St. Petersburg State Institute of Technology
BSc thesis: Effect of Co-activator Concentration on Luminiscent Properties of ZnS: Cu,Cl Phosphors

HONOURS AND AWARDS

2015 Center for NanoScience (CeNS) **Travel Award**

2011–2013 German Academic Exchange Service (DAAD) **Research Grant**

2009–2010 German Academic Exchange Service (DAAD) **Graduate Scholarship**

2006–2007 St. Petersburg Government **Distinguished Student Scholarship**

WORK EXPERIENCE

2010–present **Research Assistant, Ludwig-Maximilians-University Munich**

2009 **Intern, Robert Bosch GmbH** Advanced Research Analytics, Gerlingen

2007 **Intern, BASF** Agricultural Products Global Operations, Ludwigshafen

TEACHING

- 2010–2014 **Teaching Assistant**, Ludwig-Maximilians-University Munich
Physical Chemistry, General and Inorganic Chemistry lab courses
- 2012–2013 **Research Mentor**, Ludwig-Maximilians-University Munich
Practical training in Physical Chemistry for master students
- 2012/2011 **Research Mentor**, Nanosystems Initiative Munich (NIM)
Summer School for international exchange students

ADDITIONAL TRAINING

- 2012–present **SEM Operator**, Ludwig-Maximilians-University Munich
- 2012 **Quantsol International Summer School**, Hirschegg
- 2009 **Helion Battery School**, Justus Liebig University Giessen
- 2009 **Entrepreneurship and Business Planning**, Unternehmer TUM,
Wacker Chemie AG, Garching
- 2006–2012 **German Language Course**, Goethe-Institut, St. Petersburg/Munich

LANGUAGES

- Russian Native
- English Fluent
- German Fluent
- Latvian Fluent

10 Publications and Presentations

10.1 Publications

1. Ivanova, A.; Fravventura, M.; Fattakhova-Rohlfing, D.; Rathouský, J.; Movsesyan, L.; Ganter, P.; Bein, T. Nanocellulose-templated porous titania scaffolds incorporating pre-synthesized titania nanocrystals.
Chem. Mater. **2015**, DOI:0.1021/acs.chemmater.5b00770.
2. Ivanova, A.; Fominykh, K.; Fattakhova-Rohlfing, D.; Zeller, P.; Döblinger, M.; Bein, T. Nanocellulose-assisted formation of porous hematite morphologies.
Inorg. Chem. **2015**, *54*, 1129–1135.
3. Ivanova, A.; Fattakhova-Rohlfing, D.; Kayaalp, B. E.; Rathouský, J.; Bein, T. Tailoring the morphology of mesoporous titania thin films through biotemplating with nanocrystalline cellulose. *J. Am. Chem. Soc.* **2014**, *136*, 5930–5937.
4. Docampo, P.; Hanusch, F. C.; Giesbrecht, N.; Angloher, P.; Ivanova, A.; Bein, T. Influence of the orientation of methylammonium lead iodide perovskite crystals on solar cell performance. *APL Mater.* **2014**, *2*, 081508/1–081508/6.
5. Fried, D. I.; Ivanova, A.; Muller, V.; Rathousky, J.; Smarsly, B. M.; Fattakhova-Rohlfing, D. A facile synthesis of mesoporous crystalline tin oxide films involving a base-triggered formation of sol–gel building blocks.
Nanoscale **2011**, *3*, 1234–1239.
6. Kondofersky, I.; Müller, A.; Dunn, H. K.; Ivanova, A.; Scheu, C.; Štefanić, G.; Ehrensperger, M.; Parkinson, B. A.; Fattakhova-Rohlfing, D.; Bein, T. Nanostructured ternary FeCrAl oxide photocathodes for water photoelectrolysis.
Submitted to J. Am. Chem. Soc.
7. Jumabekov, A. N.; Cordes, N.; Siegler, T. D.; Docampo, P.; Ivanova, A.; Fominykh, K.; Medina, D. D.; Peter, L.M.; Bein, T. Passivation of PbS quantum dot surface with L-glutathione in solid-state quantum-dot-sensitized solar cells.
Submitted to ACS Appl. Mater. Interfaces.

10.2 Oral Presentations

1. Nanocellulose-assisted nanostructuring of porous metal oxide thin films. Ivanova, A.; Fominykh K.; Fattakhova-Rohlfing, D.; Rathousky, J.; Kayaalp, B. E.; Fravventura, M.; Zeller, P.; Döblinger, M.; Movsesyan, L.; Ganter, P.; Bein, T.
MRS 2015 Materials Research Society Spring Meeting, San-Francisco, CA, USA
2. Biotemplated porous titania scaffolds with incorporated pre-synthesized titania nanocrystals. Ivanova, A.; Fravventura, M.; Fattakhova-Rohlfing, D.; Rathouský, J.; Movsesyan, L.; Ganter, P.; Bein, T.
EMRS 2014 European Materials Research Society Spring Meeting, Lille, France
3. Tailoring the morphology of titania thin films by biotemplating with nanocrystalline cellulose. Ivanova, A.; Fattakhova-Rohlfing, D.; Kayaalp, B. E.; Rathouský, J.; Bein, T.
EMRS 2013 European Materials Research Society Fall Meeting, Warsaw, Poland

10.3 Poster Presentations

1. Dual-source titania templated by biogenic nanocrystals. Ivanova, A.; Movsesyan, L.; Ganter, P.; Fravventura, M.; Rathouský, J.; Fattakhova-Rohlfing, D.; Bein, T.
FEZA 2014 Federation of European Zeolite Associations International Conference, Leipzig, Germany
2. Tailoring the morphology of inorganic oxide thin films through templating with biogenic nanocrystals. Ivanova, A.; Fattakhova-Rohlfing, D.; Kayaalp, B. E.; Movsesyan, L.; Ganter, P.; Rathouský, J.; Bein, T.
SolTech 2014 Solar Technologies Go Hybrid Meeting, Wildbad Kreuth, Germany
3. Tailoring the morphology of titania thin films by direct shape-persistent nanocrystalline cellulose templating approach. Ivanova, A.; Kayaalp, B. E.; Movsesyan, L.; Ganter, P.; Bein, T.
HOPV 2013 International Conference on Hybrid and Organic Photovoltaics, Seville, Spain

4. Tuning the morphology of titania thin films by direct shape-persistent nanocrystalline cellulose templating approach. Ivanova, A.; Bein, T.
SolTech 2013 Solar Technologies Go Hybrid Meeting, Kloster Banz, Germany
5. Tuning the morphology of titania thin films by direct nanocrystalline cellulose templating. Ivanova, A.; Bein, T.
DZT 2013 Deutsche Zeolith-Tagung, Hamburg, Germany
6. Highly porous titania systems for photovoltaics. Mandlmeier, B.; Ivanova, A.; Feckl, J.; Szeifert, J. M.; Fattakhova-Rohlfing, D.; Bein, T.
SolTech 2013 Solar Technologies Go Hybrid Meeting, Munich, Germany
7. Synthesis and characterization of biotemplated titania porous films.
Ivanova, A.; Bein, T.
HOPV 2013 International Conference on Hybrid and Organic Photovoltaics, Uppsala, Sweden
8. Synthesis and characterization of biotemplated titania porous films.
Ivanova, A.; Bein, T.
DZT 2012 Deutsche Zeolith-Tagung, Magdeburg, Germany
9. Biotemplated mesoporous titania films. Ivanova, A.; Bein, T.
CeNS 2011 Center for NanoScience Workshop, Venice, Italy